FLOW OF SELF-COMPACTING CONCRETE

Rola Deeb

Ph.D. 2013

FLOW OF SELF-COMPACTING CONCRETE

Rola Deeb

B.Sc., M.Sc.

Submitted for the degree of

Doctor of Philosophy

School of Engineering

Cardiff University, UK

October 2013

There are no shortcuts to any place worth going…

DECLARATION

This work has not previously been accepted in substance for any degree and is not concurrently submitted in candidature for any degree.

Signed……(candidate)
Date……

STATEMENT 1

This thesis is being submitted in partial fulfilment of the requirements for the degree of Doctor of Philosophy.

Signed……(candidate)
Date……

STATEMENT 2

This thesis is the result of my own independent work/investigations, except where otherwise stated. Other sources are acknowledged by explicit references.

Signed……(candidate)
Date……

STATEMENT 3

I hereby give consent for my thesis, if accepted, to be made available for photocopying and for inter-library loan, and for the title and summary to be made available to outside organisations.

Signed……(candidate)
Date……

ACKNOWLEDGEMENT

I would like to express my deepest appreciation to all those who gave me the chance to complete this thesis.

Foremost, I would like to express my sincere gratitude to my supervisor, Prof. Karihaloo for the continuous support unwavering guidance throughout the course of this work. I can't say thank you enough for his tremendous support and help. I have learned a lot from him. Without his guidance and persistent help this thesis would not have been possible.

My sincere thanks also goes to my co-supervisor Dr. Kulasegaram, he has been always helpful. I am deeply grateful to him for valuable discussions we had during my research project.

I would like also to dedicate this thesis to my beloved husband for his help, love and support during the preparation of this research.

And finally, my special tribute goes to my parents, for their love and encouragement.

SYNOPSIS

This thesis describes the steps taken to develop self-compacting concrete (SCC) mixes with and without steel fibres. For the self-compacting concrete mixes without steel fibres the fulfilment of the flow and cohesiveness criteria are found to be sufficient for the mix design. However, for the design of self-compacting concrete mixes with steel fibres it is found that they must additionally meet the passing ability criterion.

The plastic viscosity of SCC mixes with and without fibres so developed is accurately estimated using a micromechanical procedure based on the measured viscosity of the cement paste alone and on the mix proportions.

A Lagrangian particle based method, the smooth particle hydrodynamics (SPH), is used to model the flow of SCC mixes with or without short steel fibres in slump and L-box tests. An incompressible SPH method is employed to simulate the flow of such non-Newtonian fluids whose behaviour is described by a Bingham-type model, in which the kink in the shear stress versus shear strain rate diagram is first appropriately smoothed out. The basic equations solved in the SPH are the incompressible mass conservation and momentum equations.

The simulation of the SCC mixes emphasised the distribution of large aggregate particles of different sizes throughout the flow in the 3-dimensional configurations. On the other hand, the simulation of high strength SCC mixes which contain steel fibres focused on the distribution of fibres and their orientations during the flow in the 3-dimensional configuration. The capabilities of this methodology were validated by comparing the simulation results with the slump flow and L-box tests carried out in the laboratory.

A simple method is developed to assess the orientation and distribution of short steel fibres in self-compacting concrete mixes during the flow. A probability density function (PDF) is introduced to represent the fibre orientation variables in three dimensions. Moreover, the orientation variables of each individual fibre in an arbitrary two dimensional cross-section have been calculated using the geometrical data obtained from the three dimensional simulations. This is useful to determine the fibre orientation factor (FOF) in practical image analysis on cut sections.

The simulations of SCC mixes are also used as an aid at the mix design stage of such concretes. Self-compacting concrete mixes with and without steel fibres are proportioned to cover a wide range of plastic viscosity. All these mixes meet the flow and passing ability criteria, thus ensuring that they will flow properly into the formwork.

TABLE OF CONTENTS

LIST OF FIGURES

LIST OF TABLES

Chapter 1

Introduction

1.1 Scope of the research

Concrete is the most consumed construction material for buildings at present. The achievement of designed strength and durability of concrete relies largely on sufficient compaction during placement. Inadequate compaction can dramatically lower the performance of mature concrete in-situ. Therefore, to ensure adequate compaction and homogeneity of the cast concrete and to facilitate its placement especially in structures with congested reinforcement and restricted areas, self-compacting concrete has been introduced.

It all started around 1988 at Tokyo University when Okamura et al. (1998) established the basic description of SCC. The history of self-compacting concrete (SCC) dates back to late 1980s. SCC concepts originally were thought to be a tool to enhance long-term durability of structures having members with congested reinforcements. It has generated tremendous interest since its inception. It has been considered as the greatest breakthrough in concrete technology for many decades due to the improved performance and working environment.

SCC is a concrete that is capable of self-compacting, occupies all the space in the formwork without any external effort (in the form of mechanical vibration, floating, poking etc.). For the concrete to occupy the full space, flowing through the formwork, without any external effort, it has to have an acceptable level of passing ability, filling ability and stability. Because of the heterogeneous nature of concrete, its high fluidity and the fact that it contains materials with different specific gravities, cohesiveness becomes an issue, as it is very difficult to keep its constituents in a cohesive form where higher mass particles tend to settle down. This problem however can be tackled by adding larger amounts of finer material. Owing to its excellent user-friendly characteristics, SCC is a highly attractive alternative today in traditional construction industry.

Depending on its composition, SCC can have a wide range of different properties; from a normal to an ultra-high compressive strength, from a poor to an extremely high durability. The mixture of SCC is strongly dependent on the composition and characteristics of its constituents in its fresh state. The properties of SCC in its fresh state have a great influence on its properties in the hardened state. Therefore it is critical to understand its flow behaviour in the fresh state. Since the SCC mix is essentially defined in terms of its flow-ability, the characterisation and control of its rheology is crucial for its successful production.

This is even more relevant if the fibres are added to SCC. Self-compacting high and ultra-high performance fibre reinforced concretes (SCHPFRC/SCUHPFRC) must maintain their flow- ability and passing ability despite the presence of a large volume fraction of fibres. This presents a challenge which makes the control of rheology crucial for the successful production of SCHPFRC/SCUHPFRC. The definition of SCHPFRC/SCUHPFRC changes from country to country and from time to time. However, SCHPFRC has a characteristic strength in excess 100 MPa and that of SCUHPFRC is in excess of 140 MPa.

The flow of SCC with or without fibres is best described by the Bingham constitutive model. This model contains two material properties, namely the yield stress and the plastic viscosity. It is known however that the yield stress of SCC mixes is low in comparison with normal vibrated concretes and remains nearly constant over a large range of plastic viscosities. The viscosity of a homogenous viscous fluid such as the cement paste can be measured accurately which cannot be said of any SCC.

The prediction of SCC filling behaviour is very difficult especially in the presence of reinforcing steel and in formworks of complex shapes. However, an understanding of the behaviour and the flow characteristics is crucial to achieving a high quality SCC. The most cost-effective way to gain such an understanding is by performing numerical simulations, which will enable us to fully understand the flow behaviour of SCC with or without steel fibres and to reveal the distribution of larger aggregate particles and of fibres and their orientations inside the formworks. The accurate picture can only be gained by using the three-dimensional flow simulation which shows the actual distribution of fibres and their orientations during the flow.

1.2 Research objectives

The objectives of this thesis are as follows:

- To produce self-compacting concrete (SCC) mixes of varying strengths and performances with or without steel fibres. The aim is to investigate how the proportions of solids and liquids, the amount of super-plasticiser, and the steel fibres need to be selected in order to produce SCC mixes with the right flow-ability, passing ability and segregation resistance.

- To estimate the plastic viscosity of the developed SCC mixes using micromechanical principles. This plastic viscosity, together with the yield stress of the mix, is needed in the numerical simulation of SCC flow in moulds of different shapes and sizes.

- To simulate the 3-dimentional flow of the non-Newtonian viscous SCC mixes using smooth particle hydrodynamic approach in two standard test configurations, namely the slump flow and L-box tests using appropriate computational strategies. To simulate also the slump flow test as a homogenous mass in axisymmetric configuration.

- To monitor the distribution of larger aggregate particles of different sizes during the flow.

- To provide a simple method to assess the orientation and distribution of short steel fibres in self-compacting concrete mixes during flow.

- To proportion self-compacting mixes of varying strengths and performance with and without steel fibres that have the correct flow and passing ability using the computational flow modelling technique at the mix design stage.

1.3 Research methodology

To achieve the above objectives research was undertaken in four stages:

- First, self-compacting concrete (SCC) mixes of varying strengths and performances were developed to meet the flow-ability, passing ability and segregation resistance criteria. The design of SCC mixes followed the traditional trial-and-error approach,

using the slump cone, J-ring and L-box tests on trial mixes, until the mix was found that met the flow-ability and passing ability criteria and had no visible signs of segregation. The plastic viscosity of the SCC mixes so developed with or without fibres was then estimated using a micromechanical procedure and the known plastic viscosity of the cement paste which can be measured accurately. For this, concrete was regarded as two-phase suspension of solid and liquid phases, and the plastic viscosity was estimated from a two-phase model in several stages until all the ingredients of SCC have been accounted for. By adding steel fibres, the plastic viscosity increases significantly; this increase was quantified using a micromechanical model.

- Second, a three-dimensional and an axisymmetric Lagrangian smooth particle hydrodynamics (SPH) method has been used to model the flow of self-compacting concrete (SCC). The constitutive behaviour of this non-Newtonian viscous fluid is described by a Bingham-type model. The 3D simulations of SCC without fibres are focused on the distribution of large aggregates (larger than or equal to 8 mm) during the flow. The simulation results are in very good agreement with available experimental data.

- Third, a simple method has been developed to assess the orientation and distribution of short steel fibres in self-compacting concrete mixes during flow. In this stage, a three-dimensional Lagrangian smooth particle hydrodynamics (SPH) method has been used to model the flow of self-compacting concrete (SCC) with short steel fibres. This simulation is focused on the distribution of fibres and their re-orientation during the flow.

- Fourth, the SPH simulation technique was used at the mix design stage to proportion the mixes of SCC mixes of different strength and performance that meet the flow ability, passing ability requirements and have the desired plastic viscosity.

1.4 Outline of the thesis

This thesis is organised into 8 chapters, followed by bibliographical references and Appendixes. Each chapter is further divided into Sections and Sub-sections for the clarity of presentation. A brief overview of the contents of each chapter follows:

Chapter 2 gives a general overview of SCC, its properties, applications, and the influence of materials used on its characteristics in the fresh and hardened states. Fibre reinforced SCC is also reviewed with an emphasis on steel fibres. Finally, a review of the methods for testing SCC in its fresh state is presented.

Chapter 3 reviews the different computational methods used for simulating the flow of concrete mixes available in literature by considering either the homogenous or the heterogeneous approach. An overview of smooth particle hydrodynamic approach, its concept, particle interpolation, kernel functions, density and gradient evaluation will be also presented together with a corrected particle interpolation. The three-dimensional Lagrangian form of the governing equations of flow used to model the flow of SCC namely, the mass and momentum conservation equations was also been reported in Chapter 3.

Chapter 4 (Stage 1 of research) describes the steps taken to develop self-compacting concrete (SCC) mixes of varying strengths and performance with or without steel fibres, and how the proportions of solids and liquids, the amount of super-plasticiser, and the steel fibres need to be selected in order to produce SCC mixes with the right flow-ability, passing ability and have no sign of segregation. The plastic viscosity of the SCC mixes so developed will then be estimated by the micromechanical procedure. This plastic viscosity, together with the yield stress of the mix, will then be used in the numerical simulation of SCC flow.

Chapter 5 (Stage 2 of research) presents the results of the three-dimensional and axisymmetric simulation of the non-Newtonian viscous SCC mixes. Here, an incompressible Lagrangian SPH method is adopted. The formulations relating to incompressible SPH and coupling of SPH formulation with a suitable Bingham-type model to represent the rheological behaviour of SCC is also been presented in this Chapter. The basic equations solved in SPH are the incompressible mass conservation and momentum equations. The simulation of SCC without fibres focuses on the distribution of large aggregates (larger than or equal to 8 mm) during the flow. This simulation was conducted in 3-dimentional configurations using 2 different test apparatuses namely, slump cone and L-box. The simulation results are in very good agreement with available experimental data.

Chapter 6 (Stage 3 of research) is devoted to the development of a simple method to assess the orientation of short steel fibres in self-compacting concrete mixes during flow, using three-dimensional Lagrangian smooth particle hydrodynamics (SPH). A probability density function (PDF) has been introduced to represent the fibre orientation variables in three

dimensions. Moreover, the orientation variables of each individual fibre in an arbitrary two dimensional cross-section have been calculated using the geometrical data obtained from the three dimensional simulations.

Chapter 7 (Stage 4 of research) uses the SPH simulation technique as a practical aid in the proportioning of SCC mixes that may contain coarse aggregates or/and short steel fibres.

Chapter 8 will then summarise the conclusions of this research work embodied in Chapters 4 to 7. Recommendations for future research work will be also provided.

Finally, an alphabetic list of references to the works in the literature cited in the text will be reported. Some of the work described in this thesis has been published or is in the process of publication. For easy reference, the publications are listed below.

1. Kulasegaram, S., Karihaloo, B. L., Deeb, R. , (2011). Application of SPH method for modelling the flow of ultra-high performance fibre reinforced self-compacting concrete, II International Conference on Particle-based Methods Fundamentals and Applications, Barcelona.
2. Deeb, R., Ghanbari, A., Karihaloo, B. L., (2012). Development of self-compacting high and ultra- high performance concretes with and without steel fibres, Cement and Concrete Composites, 34(2): 185-190.
3. Deeb, R., Kulasegaram, S., Karihaloo, B. L., (2012). Modelling the flow of self-compacting high and ultra-high performance fibre-reinforced concretes, The 8th RILEM International Symposium on Fibre Reinforced Concrete: Challenges and Opportunities. BFIB2012, Portugal.
4. Deeb, R., Karihaloo, B. L., (2013). Mix proportioning of self-compacting normal and high strength concretes, Magazine of Concrete Research, 65(9): 546–556.
5. Deeb, R., Kulasegaram, S., Karihaloo, B. L., (2013). 3D modelling of the flow of self-compacting concrete with or without steel fibres. Part I: slump flow test, Computational Particle Mechanics (submitted).
6. Deeb, R., Karihaloo, B. L., Kulasegaram, S., (2013). Reorientation of short steel fibres during the flow of self-compacting concrete mix and determination of the fibre orientation factor, Cement and Concrete Research (accepted).
7. Kulasegaram, S., Karihaloo, B. L., Deeb, R., (2013). Simulation of fibre orientation during the flow of ultra-high performance self-compacting concrete, International

Conference on Particle-Based Methods Fundamentals and Applications, Stuttgart, Germany.

8. Deeb, R., Karihaloo, B. L., Kulasegaram, S., (2013). Simulation of fibre orientation during the flow of ultra-high performance self-compacting concrete, EMI2013 conference, Evanston (IL), USA.

Chapter 2

Self-compacting concrete

2.1 Introduction

Reinforced concrete is one of the most versatile and widely used construction materials. With the demand increasing for reinforced concrete structures in the modern society to meet the needs of new developments, increasing population and new ambitious structural design ideas, the reinforcement in concrete structures is becoming more dense and clustered. The heavy and dense reinforcement can raise problems of pouring and compacting the concrete. The concrete must be able to pass the dense rebar arrangement without blocking or segregating. The design of such concrete is very challenging because poor placement and the lack of good vibratory compaction can lead to the inclusion of voids and loss of long term durability of concrete structures. This has been a concern for engineers for many years.

During the last decade, concrete technology has made an enormous advance through the introduction of self-compacting concrete (SCC). Self-compacting or self-consolidating concrete is a relatively new generation of high-performance concrete that is able to achieve impressive deformability and homogeneity in its fresh state, filling all the space around the reinforcement, passing through dense reinforcing steel bars while compacting under its own weight without any external vibration.

SCC with its outstanding properties, impressive deformability, gives designers and architects more freedom of creativity that was not possible previously. Lighter and slender members can be made from SCC, larger span bridges can be developed, and underwater structures can be built, making SCC a highly promising material for the future of the in-situ and pre-cast construction industries. Since its early use in Japan, SCC has now started to be an alternative to vibrated concrete across the world in such areas where normal vibrated concrete is difficult or impossible to pour and vibrate. However those applications are still few and vibrated concrete is still considered as the standard concrete. As more and more investigations are done into SCC, it is likely to move from being a fringe technology to becoming a concrete of choice for construction because of reduced health concerns, i.e. no vibration-induced noise.

In this chapter, a general overview of the properties and applications of SCC will be given, highlighting the influence of materials used on its characteristics in the fresh and hardened states. Fibre reinforced SCC will also be reviewed with an emphasis on steel fibres. Finally, the testing methods of SCC in its fresh state will be summarised, together with its rheological properties.

2.2 History of development

In the mid-1980s, research undertaken into underwater placement technology within the UK, North America and Japan led to the development of concrete mixes with a high degree of washout resistance. However, the creation of durable structures from such mixes required adequate compaction by skilled workers. At the same time in Japan, a gradual reduction in the number of skilled workers in the construction industry was leading to a reduction in the quality of construction work, with subsequent knock-on effects on concrete durability (Okamura et al., 1998). One solution to overcome the durability problems in concrete structures independently of the quality of construction work was to use self-compacting concrete (SCC) (Okamura and Ouchi, 2003).

Its use was first proposed by Okamura (1986) who also conducted a fundamental study on the workability of SCC. The first prototype SCC was completed in 1988 at Tokyo University, using constituent materials readily used in conventional vibrated concrete (Ozawa et al., 1989). The main reasons for the employment of SCC were to shorten the construction time, to avoid vibrating the confined zones which are rather difficult to reach and to eliminate noise caused by vibration (Okamura and Ouchi, 2003).

Although Japan was the predominant user in the early years of development, the technology spread then to Europe starting from Sweden to other Scandinavian countries at the end of the 1990s (Billberg, 1999) . In Denmark, SCC has been applied in both ready-mix and pre-cast industry with an annual production reaching approximately 20% and 30%, respectively of the total concrete production (Thrane et al., 2004). Other countries, such as UK, France, Germany, USA and the Netherlands have also been developing and using the material (Ouchi et al., 2003; Bennenk, 2005) with a temporary stagnation. One reason for this stagnation appears to be the lower segregation resistance of SCC compared with vibrated concrete (Thrane et al., 2004).

In the last two decades, self-compacting concrete has been developed further, utilizing various materials such as pulverized-fuel ash (PFA), ground granulated blast furnace slag (GGBS) and condensed silica fume (CSF). SCC has gained wide interest especially for structures with very complicated shapes, difficult casting process and congested reinforcement. In spite of this, the overall production is still relatively small compared to conventional concrete (Gaimster and Dixon, 2003), the global gap that has been always

present in the market for such a concrete indicates that in the future there is likely to be an even greater demand for all types of SCC.

2.3 Self-compacting concrete definition

The British Standard (BS EN 206-9, 2010) defines "SCC is the concrete that is able to flow and compact under its own weight, fill the formwork with its reinforcement, ducts, boxouts etc, whilst maintaining homogeneity".

Other researchers (Ozawa et al., 1989; Bartos and Marrs, 1999; Khayat, 1999) have defined SCC in almost the same terms as a highly flow-able concrete that should meet the following requirements:

- **Flow-ability**: SCC should flow under its own weight and fill all parts of formwork without any external aid or vibration.
- **Passing ability**: SCC should pass through heavy reinforcing steel bars.
- **Segregation resistance:** SCC should maintain its homogeneity without any migration or separation of its large components (aggregates or/and fibres).

2.4 Advantages and disadvantages of using SCC

The use of SCC on site offers many advantages:

- **Eliminating vibration and lower noise level:** This will certainly put less physical demands on site workers, something that is clearly a desirable objective, including preventing "white finger" syndrome, which is mainly related to the vibrating equipment.
- **Easy placement and filling:** the impressive filling ability, flow-ability and passing ability of SCC eases placement significantly even with very complex shaped structures and where heavy reinforcement or very long formwork is involved, and eliminate honeycombing, blow holes and grout loss.
- **Better surface finish:** SCC ensures a uniform architectural surface finish with little to no remedial surface work as illustrated in Figure 2.1.

Figure 2.1: Surface finish for a column using SCC with no repairs or "rubbing down"

- **Reduce manpower and construction time:** SCC can be placed at a faster rate with no vibration and less screeding resulting in reducing manpower and saving construction time.
- **Improve durability:** due to the dense matrix of SCC and the high consolidation and bond around reinforcement, the structural durability is improved.

Among sixty eight case studies of the applications of self-compacting concrete (SCC), which were published from 1993 to 2003, the period of increasingly widespread use of SCC in many countries, Domone (2006) reported that 67% were using SCC for technical advantages where vibration is either difficult or impossible due to the heavy reinforcement or inaccessibility, 14% were for economical reason to reduce labour work and construction time, while 10% were for new types of structure such as thin sections, pre-cast units and steel/concrete composite. The rest of the cases involved environmental causes including reducing noise level and improving working conditions.

We should however also mention the possible disadvantages of using SCC compared with conventional concrete can include the high cost of materials which can subsequently be overcome by the low cost of labour. Another disadvantage can be related to the nature of SCC, because of its high fluidity, handling and transporting SCC becomes a bit delicate, although the outstanding results would definitely overcome these disadvantages.

2.5 Fresh state properties of self-compacting concrete

2.5.1 Deformability (flow and filling ability)

Deformability refers to the ability of SCC mix to deform and undergo changes in shape with completely filling all areas and corners of the formwork horizontally and vertically while

maintaining its homogeneity. The deformability of SCC is characterized by the concrete's fluidity and cohesion, and mainly assessed using the slump flow test described later in this Chapter.

Kennedy (1940) proposed the 'Excess Paste Theory' as a way to explain the mechanism governing the workability of concrete. Kennedy states that there must be enough paste to cover the surface area of the aggregates, and that the excess paste serves to minimize the friction among the aggregates and give better flow-ability. Without the paste layer, too much friction would be generated between the aggregates resulting in extremely limited below workability.

Figure 2.2: Excess paste layer around aggregates (After: Oh et al., 1997)

Figure 2.2 shows the formation of cement paste layers around aggregates. The thickness of the paste layer can be best related to the diameter of the aggregates (Oh et al., 1997).

2.5.2 Passing ability

Passing ability refers to the ability of SCC mix to pass through congested reinforcement without blocking, whilst maintaining good suspension of coarse particles in the matrix, thus avoiding arching near obstacles and blockage during flow. The J-ring and L-box tests are the most common methods used to assess this property (see Figures 2.25 and 2.26).

The probability of blocking increases when the volume fraction of large aggregates and/or fibres increases. The size of aggregates, their shapes and their volume fraction influence the passing ability of SCC, moreover, the presence of fibres especially long and hooked or crimped ends make self-compacting fibre reinforced concrete (SCFRC) more difficult to pass through reinforcement.

Okamura and Ouchi (1999) reported that the potential of collision and contacts between particles increases as the distance between particles decreases; which therefore results in an increase in the internal stresses when concrete is deformed, particularly near obstacles causing blockage. Research shows that the energy required for flowing is consumed by the increase of internal stresses. Limiting the coarse aggregate content whose energy consumption is high can effectively reduce the risk of blockage. Figure 2.3 shows how normal stress can be generated due to the approach of coarse aggregate particles near obstacles.

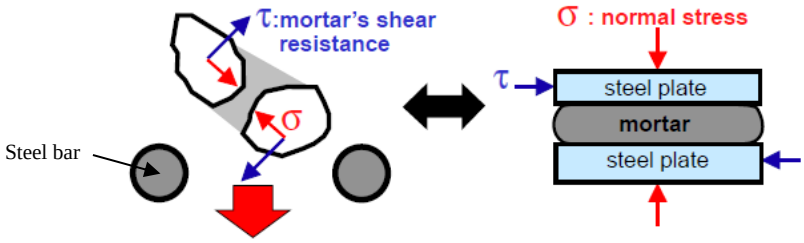

Figure 2.3: Normal stress generated in mortar due to approaching coarse aggregate particles (After: Okamura and Ouchi, 1999)

Highly viscous paste also prevents localized increases in internal stress due to the approach of coarse aggregate particles (Okamura and Ouchi, 1999) and therefore increases the passing ability of SCC. Roussel et al. (2009) state that highly fluid SCC could be more prone to have its coarsest particles blocked in highly reinforced zones, which is related to the instability of the material, and to the increases in the local volume fraction of coarse aggregates near an obstacle as shown in Figure 2.4; in this case, the material is too fluid to carry its own particles during the flow.

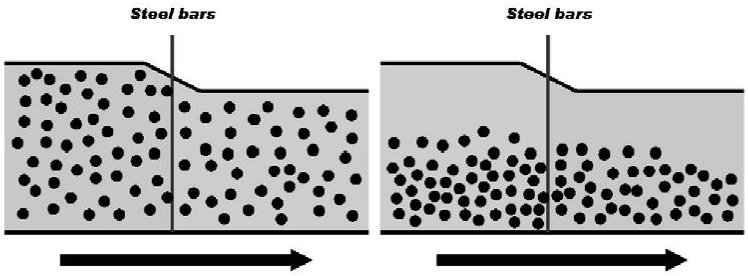

Figure 2.4: Local increase of the aggregate volume fraction due to dynamic segregation. A low viscosity cement paste could increase the risk of blocking by allowing for a strong segregation within the material (After: Roussel et al., 2009)

Blocking can be also increased as the gaps between steel bars are reduced. The spacing between bars is typically recommended to be 3 times the maximum aggregate size (EFNRC, 2005). For fibre-reinforced concrete, the bars should be placed 1 to 3 times the maximum fibre length (Koehler and Fowler, 2003).

2.5.3 Segregation resistance (homogeneity/cohesiveness)

Segregation resistance refers to the ability to retain the coarse components of the mix and the fibres in suspension in order to maintain a homogeneous material. Stability is largely dependent on the cohesiveness and the viscosity of the concrete mixture which can be increased by reducing the free water content and increasing the amount of fines (Khayat et al., 1999).

Segregation resistance is largely controlled by viscosity; therefore ensuring a high viscosity can prevent a concrete mix from segregation and/or bleeding. Bleeding is a special case of segregation in which water moves upwards by capillary action and separates from the mix. Some bleeding is normal for concrete, but excessive bleeding can lead to a decrease in strength, high porosity, and poor durability particularly at the surface (Douglas, 2004).

Two basic methods can ensure adequate stability; the first approach is based on the Japanese method. It uses a super-plasticiser (SP), low water/cement ratio, high powder content, mineral admixtures, and low aggregate content. The second approach is based on incorporating a viscosity-modifying admixture (VMA), low or moderate powder content and super-plasticiser (Bonen, 2004).

2.6 How does SCC defer from vibrated concrete

SCC consists of cement, aggregates, water and admixtures which are quite similar to the composition of conventional vibrated concrete, however, the reduction of coarse aggregates, the large amount of fines, the incorporation of super-plasticizer, the low water to cement ratio, is what led to self-compactability. Figure 2.5 shows a general comparison between mix proportions of self-compacting concrete (SCC) and vibrated concrete (VC).

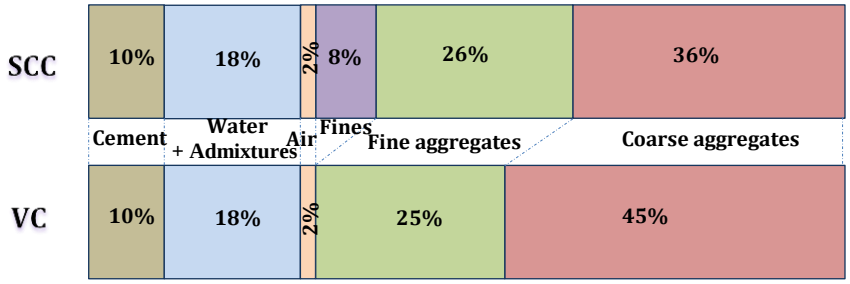

Figure 2.5: Comparison between VC and SCC mixes (After: Okamura and Ouchi, 2003)

What makes SCC unique is the migration of air bubbles to the surface without any vibration which is mainly due to the dense matrix, mix proportion and the material characteristics. The smooth passing ability through reinforcement bars and the impressive filling ability of all the formwork without any segregation or bleeding are remarkable, even in narrow structural elements with complicated shapes and heavy reinforcement, thanks to the balance between high fluidity and moderate viscosity. All these properties in the fresh state would lead to a high strength and durable concrete in the hardened state; especially after adding steel fibres, the performance becomes distinctly high.

2.7 Mechanisms of achieving SCC

In the fresh state, SCC should achieve high flow-ability as well as rheological stability (see section 2.15), which means it must be as fluid as possible in the fresh state to fill under its own weight all the far reaching corners in the form work and pass through heavy reinforcement without segregation. The methodology of selecting the right amount of materials and admixtures is crucial to achieve this goal. The following three main rules have been suggested by Okamura and Ouchi (2003):

- Limiting aggregate content.
- Using super-plasticiser.
- Reducing water-powder ratio.

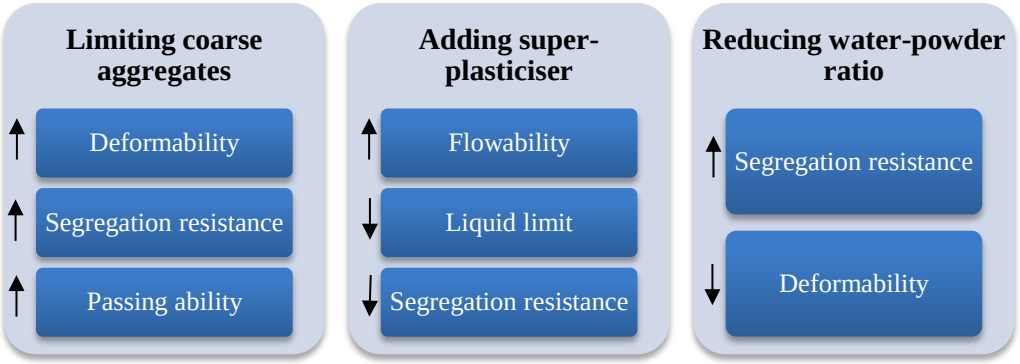

Figure 2.6: Mechanisms of achieving self-compactability. ↑ increases, ↓decreases

Figure 2.6 illustrates the three main rules of achieving self-compactability and the influence of each rule on the mechanism of achieving self-compactability.

Limiting aggregate content: The friction between the aggregates limits the spreading and the filling ability of SCC. By reducing the volume and the maximum size of coarse aggregates, and replacing crushed aggregates with round ones the passing ability of SCC in congested areas can be increased, thus improving the workability and optimizing the packing density of skeleton.

High amount of super-plasticiser: Achieving a highly flowable mix would conflict with keeping the homogeneity at an acceptable level. The mechanism of achieving this is by the dispersion effects of super-plasticiser on flocculated cement particles, by reducing the attractive forces among them. An optimum amount is necessary as a high amount would result in segregation and a low amount would compromise the fluidity. Obtaining a good degree of cohesiveness can guarantee a considerable improvement in the overall performance (Kwan and Ng, 2010).

High paste volume: SCC contains a high volume of paste, the role of which is to maintain aggregate separation (Tviksta, 2000). Okamura and Ouchi (2003) indicated that the internal stresses can increase when concrete is deformed, particularly near obstacles. The energy required for flowing is consumed by those increased internal stresses, resulting in blockage. Also, paste with high viscosity prevents localized increases in internal stresses due to the approach of coarse aggregate particles. A high amount of fine particles increases the workability and cohesiveness while simultaneously reducing the interlocking of coarse particles which could result in a blocking behaviour (Khayat, 2000). The necessity of including this large amount of fines requires that there should be cement replacement

materials such as GGBS, silica fume, fly ash...etc., in order to avoid excessive heat generation.

Using viscosity modifying agents (VMA): These products are generally cellulose derivatives, polysaccharides or colloidal suspensions. The use of VMA gives the same effect as the fine particles in minimising bleeding and coarse aggregate segregation by thickening the paste and retaining the water in the skeleton. For normal strength SCC with high water to binder content, the introduction of such products seems to be justified. On the other hand, they may be less useful for high performance SCC with low water to binder ratio. Viscosity agents are assumed to make SCC less sensitive to water variations. Because of the small quantities of viscosity agents required, however, it may be difficult to achieve accuracy of dosage (Tviksta, 2000).

2.8 SCC Mix design

Over the last decade, extensive research has been devoted to achieve self-compactability. Three different types of mixes can be distinguished: "Powder- type" by increasing the powder content, "VMA-type" using viscosity modifying admixture (VMA) and "Combined- type" by increasing powder content and using a viscosity agent in consideration of structural conditions, constructional conditions, available material, restrictions in concrete production plant, etc.

2.8.1 Powder-Type SCC

Okamura and Ozawa (1995) proposed a simple mix proportioning system for SCC mix (Figure 2.7). Their main ideas were to fix the coarse aggregate content at 50% of solid volume and the fine aggregate content at 40% of mortar volume. Depending on the properties of mortar, the water to powder ratio is in the range of 0.9-1. This ratio should be carefully selected due to the high sensitivity of SCC to it. The self-compactability is achieved by adjusting the super-plasticiser dosage and the final water to powder ratio. This independent consideration of gravel and sand, results in a relatively high content of paste. The Japanese method has been adopted and used in many European countries as a starting point for the development of SCC (Brouwers and Radix, 2005).

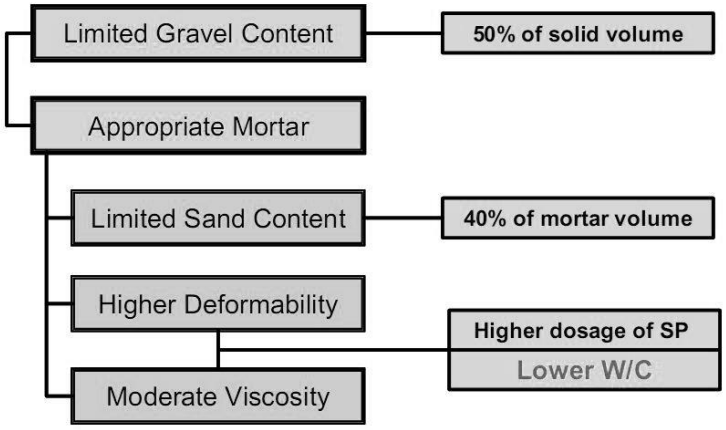

Figure 2.7: A typical mix design of SCC (After: Ouchi et al., 1996)

Su and Miao (2003) then developed an alternative method, henceforth referred to as 'the Chinese method' which starts with packing all coarse and fine aggregates, and then filling of the aggregate voids with paste. This easier method can result in less paste and hence saving the most expensive constituents, namely cement and filler. With this method, concrete with normal strength is obtained, while in Japanese method a higher strength than actually required can be attained (Brouwers and Radix, 2005).

2.8.2 VMA-type SCC

By adding a high dosage of VMA to the mix of SCC, plastic viscosity can be controlled and increased without adding extra powder. To achieve flow-ability using this method a higher amount of super-plasticiser or higher water-powder ratio is required compared with the powder-type method.

2.8.3 Combined-type SCC

This type of mix was developed to improve the robustness of powder-type SCC by adding a small amount of VMA. In such mixes, the VMA content is less than that in the VMA-type SCC and the powder content and water to powder ratio are less than those in the powder-type SCC. The viscosity is provided by the VMA along with the powder. This type of SCC was reported to have high filling ability, high segregation resistance and improved robustness (Roziere et al., 2007).

2.9 Cement replacement materials (CRMs)

Stability and flow-ability are the main characteristics of SCC. They are achieved by limiting the coarse aggregate content, the maximum aggregate size and reducing water–powder ratios together with using super-plasticisers (SP) (Okamura et al., 1998). During the transportation and placement of SCC the increased flow-ability may cause segregation and bleeding which can be overcome by enhancing the viscosity of concrete mix, this is usually supplied by using a high volume fraction of paste, by limiting the maximum aggregate size or by using viscosity modifying admixtures (VMA) (Khayat, 1999). However, chemical admixtures are expensive and may contribute to increasing the cost of concrete. On the other hand, achieving high powder content by increasing the cement content is not feasible, and may lead to a significant rise in material cost and some negative impacts on concrete properties associated with the rise in temperature during hydration and higher drying shrinkage. Alternatively, incorporating cement replacement materials (CRMs) in concrete can impart many advantages to concrete through enhancement of particle distribution, cohesiveness, and reduction of the risk of thermal cracking as well as the improvement of certain mechanical and rheological properties.

All CRMs have two common features; their particle size is smaller or the same as Portland cement particle and they become involved in the hydration reactions mainly because their ability to exhibit pozzolanic behaviour. By themselves, pozzolans which contain silica (SiO_2) in a reactive form, have little or no cementitious value. However, in a finely divided form and in the presence of moisture they will chemically react with calcium hydroxide at ordinary temperatures to form cementitious compounds (Lewis et al., 2003; Domone and Illston, 2010). The most common CRMs used are ground granulated blast furnace (GGBS), micro-silica or silica fume (SF) and pulverised fuel ash or fly ash (FA).

2.9.1 Ground granulated blast-furnace slag (GGBS)

Ground granulated blast-furnace slag (Figure 2.8) is a by-product from the blast-furnaces used to make iron. It has been successfully used in many countries around the world achieving many technical benefits in construction industries (Uysal and Sumer, 2011; Boukendakdjia et al., 2012; Dinakar et al., 2013).

Adding GGBS to self-compacting concrete offers many advantages related to increasing its compactability, workability and retaining it for a longer time, while protecting cement against

both sulphate and chloride attack (Russel, 1997). Because GGBS has 10% lower density than Portland cement, replacing an equal mass of cement by GGBS will result in a larger paste volume, which substantially increases the segregation resistance and flow-ability.

Figure 2.8: Ground granulated blast-furnace slag (GGBS)

Water demand tends to be less for concrete made with GGBS, owing to the smoother surface texture of the slag particles compared to cement, and to the delay in the chemical reaction (Lewis et al., 2003). Oner and Akyuz (2007), in their experiments on 32 different mixtures of SCC containing GGBS, indicated that as GGBS content increases, water-to-binder ratio decreases for the same workability and thus GGBS has a positive effect on the workability. They proved further that the strength gain when using GGBS is more steady than concrete made with only cement with the same binder content. Although it tends to have lower strength at an early stage but as the curing period is extended (Figure 2.9), the strength increase was higher for the GGBS concretes. The reason is that the slow pozzolanic reaction and that the formation of calcium hydroxide requires time.

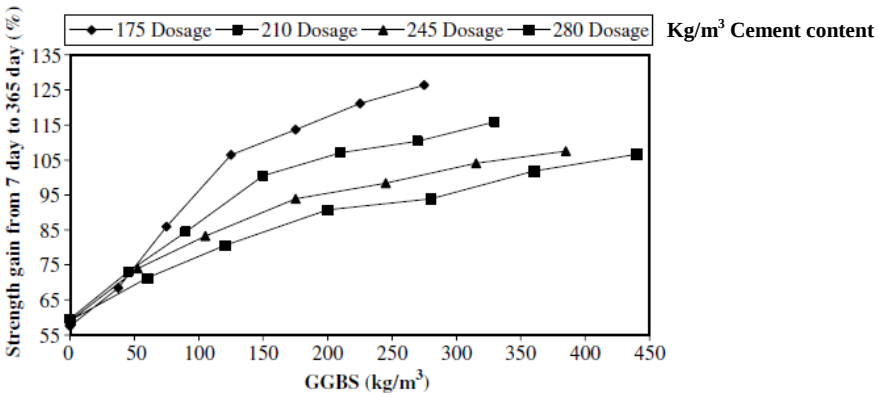

Figure 2.9: Strength gain from 7 to 365 days in concrete containing GGBS (After: Oner and Akyuz, 2007)

Ramachandran et al. (1981) reported that depending on the desired properties, the amount of GGBS by the total mass of cementitious material content can be as high as 50 per cent. Oner and Akyuz (2007) indicated further that the compressive strength of concrete mixtures containing GGBS increases as the amount of GGBS increases. After an optimum point, at around 55% of the total binder content, the addition of GGBS does not improve the compressive strength (Figure 2.10), which can be explained by the presence of unreacted GGBS, acting as a filler material in the paste.

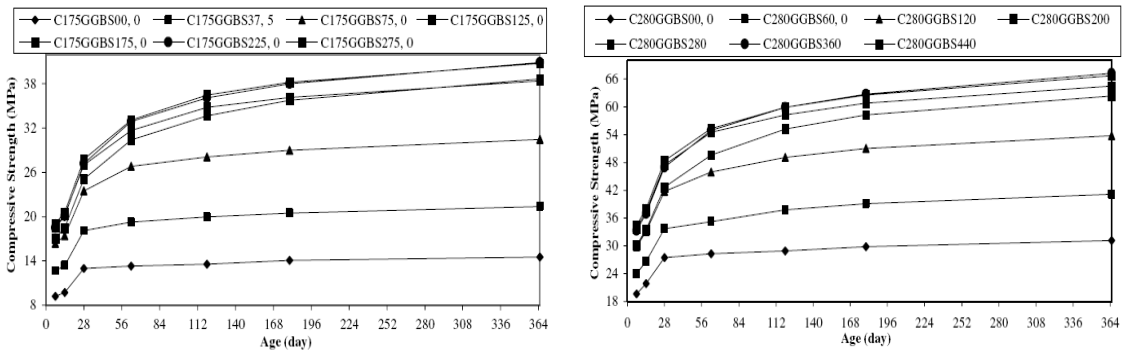

Figure 2.10: Compressive strength development of 175 dosage cement (left) and 280 (right) (After: Oner and Akyuz, 2007)

2.9.2 Micro-silica

The terms micro-silica, condensed silica fume, and silica fume are often used to describe by-products extracted from the exhaust gases of ferrosilicon, silicon, and other metal alloy smelting furnaces. However, the terms of silica fume and micro-silica are used for those condensed silica fumes that are of high quality for use in the cement and concrete industry.

Micro-silica (Figure 2.11) consists primarily of amorphous (non-crystalline) silicon dioxide (SiO_2); when added to Portland cement concrete it improves its properties, in particular its compressive strength, bond strength, and abrasion resistance. The individual particles are extremely small, approximately $1/100^{th}$ the size of an average cement particle. Because of its fine particles, large surface area, and the high SiO_2 content, silica fume is a very reactive pozzolan when used in concrete.

Figure 2.11: Micro-silica

Silica fume performs two roles in concrete (Siddique and Khan, 2011):

- **Pore-size refinement and matrix densification**: The presence of silica fume in the Portland cement concrete mixes causes considerable reduction in the volume of large pores at all ages. It basically acts as filler due to its fineness and because of which it fits into the spaces between grains.

- **Pozzolanic reaction**: When Portland cement in concrete begins to react chemically, it releases calcium hydroxide (CH); these CH crystals are a source of weakness because cracks can easily propagate through or within these crystals without any significant resistance affecting the strength, durability and other properties of concrete. Silica fume reacts with this CH to form additional binder material called Calcium Silicate Hydrate (C-S-H) which is very similar to the Calcium Silicate Hydrate formed from Portland cement and water and therefore reduces the CH content.

Fresh concrete containing silica fume is more cohesive and less prone to segregation and bleeding than concrete without silica fume. By studying the influence of silica fume on the workability, it is evident based on the results of Rao (2003) that the workability of mortar slightly decreases as the silica fume content is increased. This is due to the higher specific surface of silica fume, which needs more water for complete hydration and for workability.

Katkhuda et al. (2010) investigated 4 types of concrete M1, M2, M3, M4 with micro-silica content 0%, 10%, 15% and 20%, respectively. They observed a significant reduction in slump as the micro-silica content increases; their results were illustrated in Figure 2.12. The same was also been reported by Khayat and Guizani (1997) who revealed that the addition of small percentages of micro-silica, usually less than 10%, and of a proper amount of high

range water reducing admixture (super-plasticiser) could decrease the viscosity of the paste, thus reducing the water demand and the risk of bleeding.

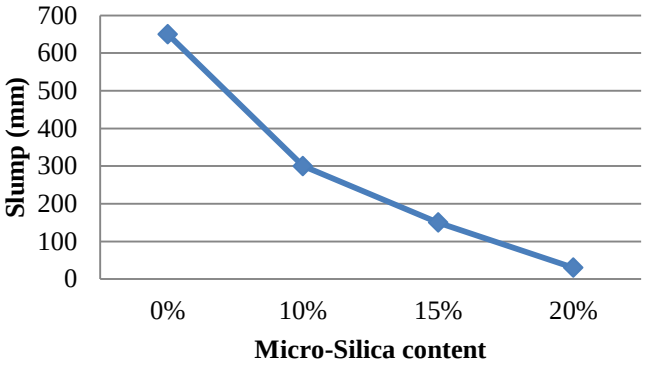

Figure 2.12: Reduction in slump as the micro-silica content increases (After: Katkhuda et al., 2010)

The addition of silica fume also reduces the permeability of concrete to chloride ions, which protects the reinforcing steel from corrosion, especially in chloride-rich environments such as coastal regions (Mazloom, et al., 2004).

Duval and Kadri (1998) studied the influence of micro-silica on the workability and compressive strength of concretes. It was found that micro-silica increased the compressive strength at most by 25%, but the workability of concretes was best when its content was between 4% and 8%. However, Duval and Kadri (1998) found out that if micro-silica exceeds 15% of the cementitious material, both compressive and tensile strengths are reduced.

Carlsward et al. (2003) also reported that micro-silica increases the yield stress of a SCC mix thus decreasing the slump flow and segregation. Vikan and Justnes (2003) also observed the same effect of micro-silica on the yield stress.

2.9.3 Fly ash (FA)

Fly ash (or pulverised fuel ash) is a by-product of coal-fired electricity generating plants. Because of its pozzolanic properties, fly ash (Figure 2.13) can be used as a partial replacement of Portland cement in SCC. The use of fly ash in SCC mixtures generally improves both its fresh and hardened properties. It can replace up to 30% by mass of Portland cement increasing the strength of SCC and its chemical resistance and durability. However, the maximum strength is reached more slowly than concretes made with only Portland cement.

Figure 2.13: Fly ash

Due to its small spherical shape, adding FA to SCC mix can improve its workability while reducing water demand (Koehler et al., 2007). Bouzoubaa and Lachemib (2001) reported that the use of fly ash and GGBS in SCC reduces the amount of super-plasticiser needed to obtain slump flow spread as compared with concrete made with only Portland cement. Furthermore, Kim et al. (1996) studied the effect of fly ash on the workability of super-flowing concrete and reported that replacing 30% of cement with FA can result in excellent workability.

FA increases the reactivity of SCC, leading to increased compressive strength, improved durability and reduced drying and autogenous shrinkage (Obla et al., 2003).

In terms of rheological properties, Sonebi (2004) reported that the use of fly ash reduced both the yield stress and plastic viscosity of SCC. However Park et al. (2005) found that fly ash slightly reduced yield stress but increased the plastic viscosity of super-plasticised pastes. Fly ash can also reduce bleeding and improve stability (Shadle and Somerville, 2002).

2.10 Using limestone powder in SCC

Fillers, such as limestone powder (Figure 2.14) are used as a portion of total CRMs to enhance certain properties of SCC.

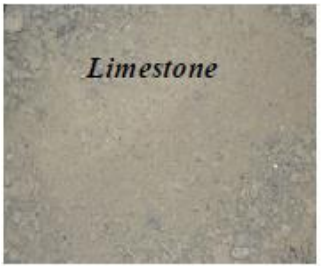

Figure 2.14: Limestone powder

The use of limestone powder particularly in self-compacting concrete has been widespread in France and Sweden. Ground limestone is not a pozzolanic material and its action can be related to a change in the microstructure of the cement matrix associated with the small size of the particles, showing an enhancement in the packing density of powder, increasing the stability and the cohesiveness of fresh SCC and reducing the interstitial void thus decreasing entrapped water in the system.

Surabhi et al. (2009) reported that for a given water to binder ratio, replacing up to 20% of cement with limestone powder can enhance fresh and hardened properties of SCC. Figure 2.15 shows that replacing cement with 20% of limestone powder can increase the slump flow spread and can result in a moderate flow time t_{500}.

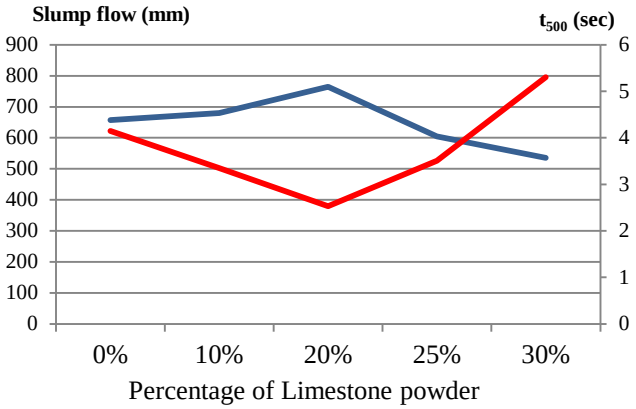

Figure 2.15: Fresh properties of SCC using limestone powder (After: Surabhi, et al., 2009)

However, excessive amounts of fine particles can result in a considerable rise in the surface area of powder and an increase in inter-particle friction, due to solid-solid contact, which may affect the ability of the mixture to deform under its own weight, pass through obstacles and also a substantial rise in the viscosity (Yahia et al., 2005).

2.11 Effect of super-plasticiser (SP) on SCC

The hardened properties of self-compacting concrete are affected by its fresh behaviour which is dominated primarily by the dispersing of its components. With conventional concrete the cement particles group together to form flocs and therefore internal friction

occurs within the mix, hindering its flow-ability as the particles will not be able to flow past each other with ease. Super-plasticisers or high-range water-reducing admixtures (HRWRAs) contribute to the achievement of denser packing and lower porosity in concrete by increasing the flow-ability and improving the hydration through greater dispersion of the cement particles, and thus assisting in producing SCCs of high strength and good durability.

Figure 2.16: Polycarboxylate-based super-plasticiser (left) and sulfanate-based super-plasticiser (right)

HRWRAs (Figure 2.16) have been used to improve the flow-ability of concrete with low water to binder ratio by deflocculating the cement particles and freeing the trapped water through their dispersing action as illustrated in Figure 2.17. However, a high amount could cause segregation and bleeding.

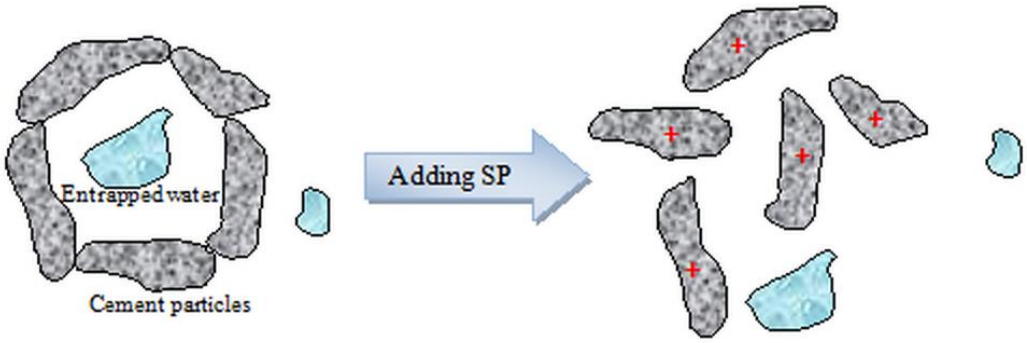

Figure 2.17: Method of deflocculation and water liberation with use of Super-plasticiser

Although SCC can be made with naphthalene sulfonate formaldehyde condensate (NSFC), melamine sulfonate formaldehyde condensate (MSFC), and lignosulfonate based HRWRAs (Assaad et al., 2003; Lachemi et al., 2003) but it is most commonly produced with

polycarboxylate-based HRWRAs. Polycarboxylate-based HRWRAs with its different structure and mode of action, represents an improvement over the other older sulfonate-based HRWRAs.

Sulfonate-based HRWRAs consist of anionic polymers that adsorb onto the cement particles and impart a negative charge, resulting in electrostatic repulsion.

Figure 2.18 illustrates the effect of sulfonate-based polymer on the dispersion of cement paste by electrostatic repulsion (Koehler et al., 2007).

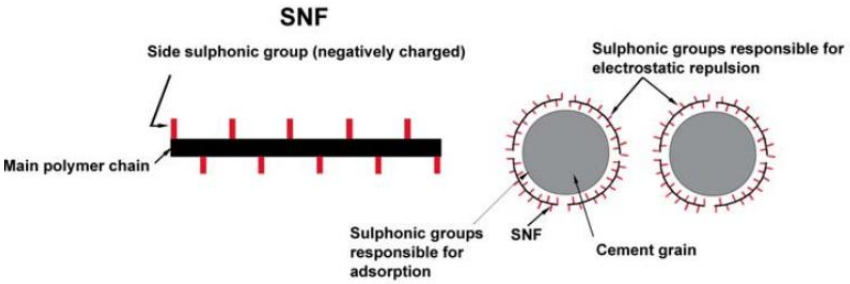

Figure 2.18: Schematic picture of sulfonate-based HRWRAs and the related electrostatic repulsion effect on the dispersion of cement particles (After: Collepardi, 2005)

By contrast, polycarboxylate-based HRWRAs consist of flexible, comb-like polymers with a main polycarboxylic backbone and grafted polyethylene oxide side chains. The backbone, which includes ionic carboxylic or sulfonic groups, adsorbs onto a cement particle and the nonionic side chains extend outward from the cement particle. The side chains physically separate cement particles, which is referred to as steric hindrance as illustrated in Figure 2.19 (Koehler et al., 2007). Polycarboxylate-based HRWRAs may function by both electrostatic repulsion and steric hindrance (Bury and Christensen, 2002; Li et al., 2005) or only by steric hindrance (Blask and Honert, 2003; Li et al., 2005) depending on the structure of the polymer.

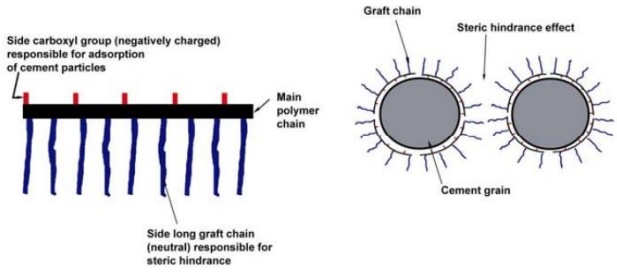

Figure 2.19: Schematic picture of the polycarboxylate-based super-plasticiser and its steric hindrance effect on the dispersion of cement particles (After: Collepardi, 2005)

Polycarboxylate-based super-plasticisers are more sensitive than sulfonate-based super-plasticiser to the amount of mixing energy (Koehler et al., 2007).

2.12 Viscosity modifying agents (VMA)

VMA, also known as anti-washout admixtures, can be added to the concrete mixtures to improve segregation resistance, cohesiveness and reduce bleeding. In general these admixtures increase yield stress and plastic viscosity. They may be also used as an alternative to increasing the powder content or reducing the water content of a concrete mixture (Koehler et al., 2007).

Acrylic- or cellulose- based water-soluble polymers or polysaccharides of microbial sources, such as welan gum are the commonly used viscosity-modifying agents in concrete. Water-soluble polymers can imbibe some of the free water in the system, thus increasing the viscosity of the cement paste which, in turn, enables the paste to hold aggregate particles in a stable suspension.

When using VMAs in SCC mixtures we should take into account its compatibility with the super-plasticiser used. For instance, cellulose derivatives are incompatible with a naphthalene-based super-plasticiser, whereas welan gum is compatible (Khayat, 1995).

Adding VMAs to SCC mixtures can alter cement hydration, resulting generally in a decrease in the compressive strength, flexural strength and modulus of elasticity of hardened concrete (Khayat, 1995).

2.13 Fibre reinforced self-compacting concrete

Cracks can be initiated in concrete at three main areas:

- ‘The interfacial transition zone’ which represents the interface between aggregates and mortar in concrete;
- In the cement paste or mortar matrix;
- In the particles of aggregates.

The point where the crack can be initiated will depend on the relative strengths of these three phases.

Coarse aggregates increase the toughness of concrete mix. However, the presence of sharp particles in a mix relatively close to each other can prevent the easy flow of SCC. Due to this reason, coarse aggregate content need to be reduced in SCC mixes. However, one of the major drawbacks in doing so is the brittle nature of the mix. This is because all the energy that was previously consumed by micro-cracking, debonding and crack coalescence is now available for the propagation of pre-existing cracks in the material.

Inherently, self-compacting concrete is a brittle material with low strain capacity under tensile loading. By adding randomly oriented discrete fibres, the performance (strength and toughness) of SCC can be improved and concerns related to SCC brittleness and poor resistance to crack growth addressed by preventing or controlling initiation, propagation or coalescence of cracks (Sahmaran et al., 2005).

The concept of using fibres as reinforcement is not new. Fibres have been used as reinforcement since ancient times. They have been produced from a wide range of materials, shapes and characteristics (Figure 2.20); glass (Ferreira and Branco, 2007), PVA (Poly Vinyl Alcohol) (Bezerra et al., 2004), polypropylene (Richardson and Dave, 2008), carbon (Bayasi and Kaiser, 2003), Asbestos (Murali et al., 2012) and steel fibres (Benson and Karihaloo, 2005a)...etc.

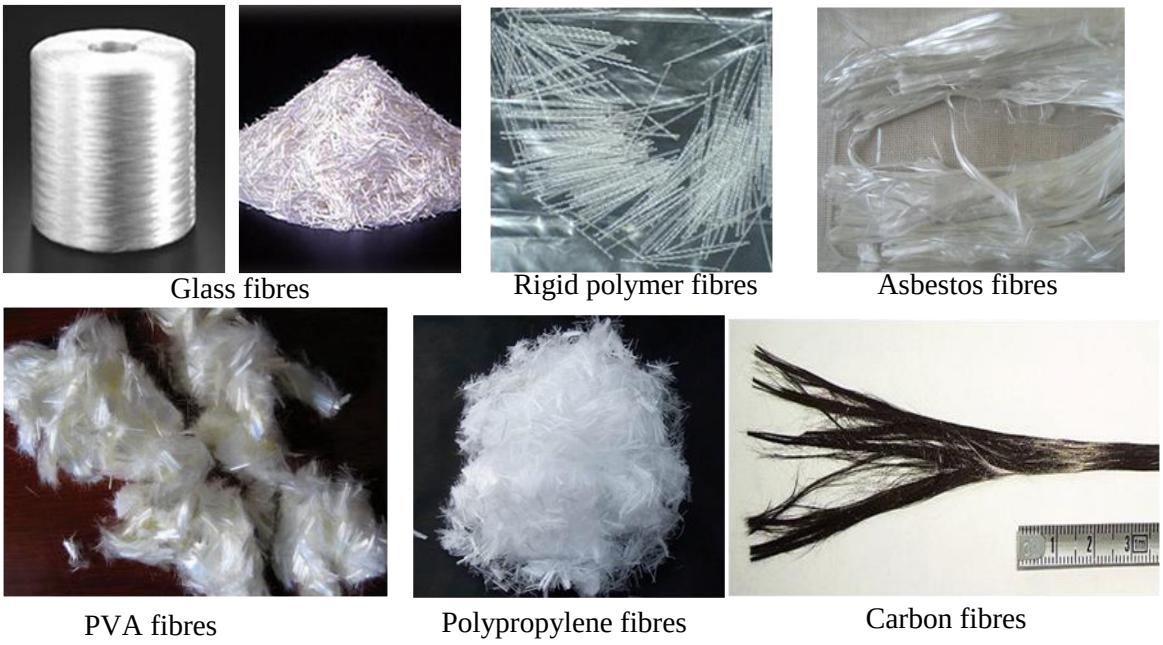

Figure 2.20: Different type of fibres used in concrete reinforcement

The characteristics and performance of fibre reinforced concrete depend on the properties of concrete and the fibres. The properties of fibres that are usually of interest are fibre volume fraction V_f, fibre geometry (fibre length L_f /fibre diameter d_f), fibre orientation, and fibre distribution. Fibre length and volume fraction are selected based on the maximum aggregate size used. It is recommended to choose fibres not shorter than the maximum aggregate size (Vandewalle, 1993; Johnston, 1996).

Usually, the fibre length is 2-4 times that of the maximum aggregate size (Grünewald and Walraven, 2009). Johnston (1996) indicates that the maximum coarse aggregate size is important because the number of rigid straight fibres like steel that can be accommodated within a unit volume reduces with an increase in the maximum aggregate size as shown schematically in Figure 2.21.

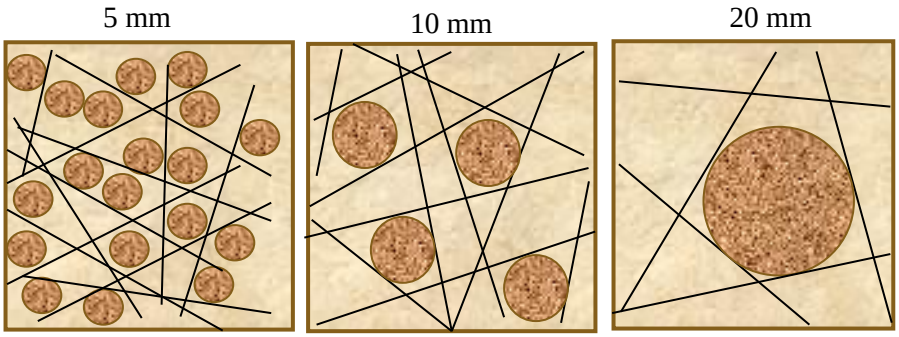

Figure 2.21: Max aggregate size when fibre length is 40mm (After: Johnston, 1996)

When the ratio ($V_f L_f / d_f$) is high, concrete performance increases, however, workability can significantly decrease. Therefore a minimum of 600 mm slump flow is ensured before adding fibres to the concrete mixture to avoid the risk of blocking especially when fibres are used in conjunction with normal reinforcement (Schutter, 2005).

Grünewald and Walraven (2009) reported three different observations of slump flow which indicates that the maximum fibre content was surpassed:

- The fibres are homogeneously distributed but the contour of the flown-out concrete is not round and less than 600 mm; this is associated with the use of fibre with a large surface area which affects the workability of concrete (Figure 2.22a).

- Fibres and/or aggregates tend to cluster along the flow without affecting the flow diameter (Figure 2.22b).

- A combination of the two previous flow patterns can be associated with the use of fibres with intermediate aspect ratio (L_f/d_f: 45-65).The free flow is obstructed and a cluster of fibres and/or aggregates remains in the centre of the flow table (Figure 2.22c).

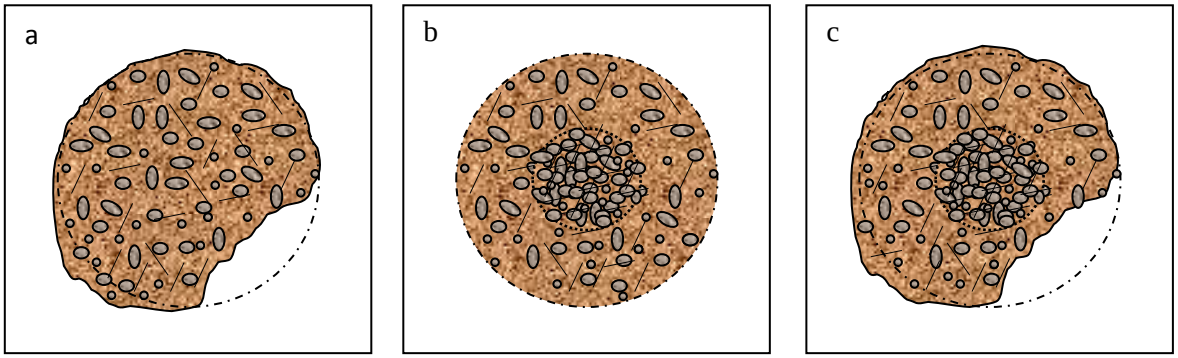

Figure 2.22: Three different observations of slump flow (After: Grünewald and Walraven, 2009)

a: Spread area for fibres having a large surface area (exp: Dramix 80/60 BP)

b: Spread area for long fibres (exp: Dramix 80/60 BP)

c: Spread area for fibres having low to intermediate aspect ratio (exp: Dramix 65/40 BP)

Fibres affect the workability of SCC due to the following main reasons (Grünewald and Walraven, 2009):

- The elongated shape of fibres; therefore the surface area of fibres is larger than aggregates for the same volume.

- The stiffness of fibres; stiff fibres push apart particles that are relatively large compared to fibre length which therefore increases the porosity, whereas flexible fibres fill the space between the particles.

- The surface characteristics of fibres differ from that of cement and aggregates, for instance some fibres might be hydrophilic or hydrophobic.
- The deformed shape of fibres (in case of steel fibres) which on one hand improve the anchorage between them and the surrounding matrix, and on the other hand affect the workability.

Steel fibre is the most common fibre type in the building industry (Figure 2.23). Other types of fibre take a smaller section of the market share. Since its invention in the early 1960s, steel fibre reinforced concrete has been successfully used in many types of construction such as airports, highways, slabs, bridges, tunnels...etc.;

Figure 2.23: Different types of steel fibres used in reinforced concrete

One of the important properties of steel fibre reinforced concrete is its superior resistance to cracking and crack propagation. As a result of this ability to arrest cracks, fibre composites possess increased extensibility and tensile strength, both at first crack and at ultimate, particularly under flexural loading; and the fibres are able to hold the matrix together even after extensive cracking. The transformation from a brittle to a ductile type of material due to the addition of steel fibres increases substantially the energy absorption characteristics of the fibre composite and its ability to withstand repeatedly applied shock or impact loading.

The fluid properties in the fresh SCC formulations are beneficial for the inclusion and homogeneous dispersion of steel fibres. However, fibres affect the characteristics of SCC in the fresh state. They are rigid needle-like particles, consequently, they do not easily accommodate to the dynamically changing shape of the bulk paste located between the particles constituting the granular skeleton structure which therefore increases the resistance to flow and contributes to an internal structure in the fresh state (Grünewald and Walraven, 2009).

Steel fibre reinforced concrete is stiffer than conventional concrete. In order to optimise the performance of the single fibres, fibres need to be homogeneously distributed; clustering of fibres has to be avoided. As a result, the design procedure and the optimization technique followed to achieve self-compacting requirements must be sensitive to the fibre content, as well as to the geometrical and material properties of the fibres.

Different types of fibre can also be simultaneously introduced in to self-compacting concrete. The concept of hybridization with two or more different types of fibre provides attractive engineering properties in terms of strength and toughness of materials (Benson and Karihaloo, 2005a; Sahmaran et al., 2005).

2.14 Testing self-compacting concrete

Assessing the workability of SCC mix can be divided into three categories as proposed by Tattersall (1991):

- Qualitative assessment; it is a general description of concrete behaviour such as workability, flow-ability, stability, compactability, pump-ability…etc. without any attempt to quantify. This was discussed previously in this Chapter.

- Quantitative empirical assessment to be used as a simple description of quantitative behaviour such as slump flow test, L-box test…etc.
- Quantitative fundamental assessment; it is a description related to rheological terms of concrete, e.g. plastic viscosity, fluidity and yield value.

For SCC mix, the quantitative fundamental rheological tests can be performed using rheometers of different types. However, these tests suffer for some drawbacks; they are not suited for use at the working site, and they can be rather time-consuming (Utsi et al., 2003). Therefore, it is important to find suitable workability test methods for continuous use outside the laboratory, and to calibrate them with the rheological parameters. For the SCC mix, a number of quantitative empirical workability assessment tests have been proposed and established in practice, such as slump flow test, J-ring test, L-box test, V-funnel test, U-box test and wet sieve stability…etc. In this section, the workability tests which are recommended by the British standard (BS EN 206-9, 2010) are discussed, namely the slump flow test for flowing ability, L-box and J-ring tests for passing ability, and visual inspection or sieve stability test can be used for segregation resistance.

2.14.1 Flow-ability using slump test

The slump test with its simple and rapid procedure is used to evaluate the deformability of SCC in the absence of obstacles. This test measures two different aspects; the filling ability by measuring the horizontal flow diameter *SF* and the viscosity of mix by measuring the time needed for SCC to reach 500 mm flow (t_{500}). The segregation resistance in this test can be detected visually. Because of its simplicity, the slump test can be done either on site or in the laboratory with inverted or upright Abram's cone.

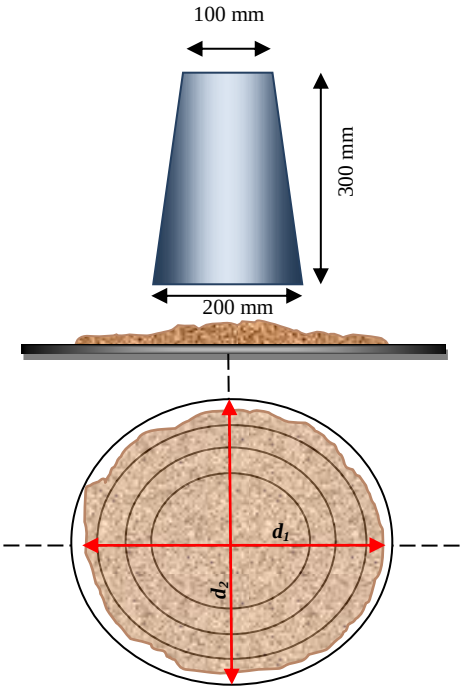

Figure 2.24: Slump test apparatus with upright cone

The cone is placed on a non-absorbing levelled flat steel surface with a plane area of at least 900 mm x 900 mm, filled with SCC, and lifted in 2 to 4 sec to a height of 15 to 30 mm; SCC flows out under the influence of gravity. Two horizontal perpendicular diameters d_1 and d_2 as illustrated in Figure 2.24 are recorded and the average flow spread diameter *SF* is calculated using Equation (2.1)

$$SF = \frac{(d_1 + d_2)}{2} \tag{2.1}$$

Criteria of acceptance (BS EN 12350-8, 2010)

- Achieving a large diameter with no segregation indicates a good deformability and a low yield stress.
- t_{500} 'the time needed for SCC to reach a diameter of 500 mm' should be recorded.
- This test is not acceptable when the largest aggregate size in more than 40 mm.
- The difference between d_1 and d_2 should be less than 50 mm otherwise the test should be repeated.

- Segregation can be detected by visually inspecting a ring of cement paste/mortar in the edge of flow, and /or ensuring that no coarse aggregates and fibres have lifted in the centre of flow.

According to the latest mix design guidelines for self-compacting concretes (BS EN 206-9, 2010) two viscosity classes are introduced: viscosity class 1 (VS1) and viscosity class 2 (VS2) depending on whether t_{500} < 2 sec or ≥ 2 sec.

2.14.2 Passing ability tests

2.14.2.1 J-ring test

J-ring is a test used in conjunction with a slump test to assess the passing ability of SCC with or without fibres through gaps in the obstacles, e.g. reinforcement. For this test, the slump test apparatus is used with an open steel rectangular section ring with 16 steel rods (ϕ16 mm) and 100 mm height, as shown in the Figure 2. 25. The gap between the bars is 42 mm±1. Wider gaps can be used when fibres are introduced to the mix which should be 1-3 times the maximum length of fibres used (Tviksta, 2000).

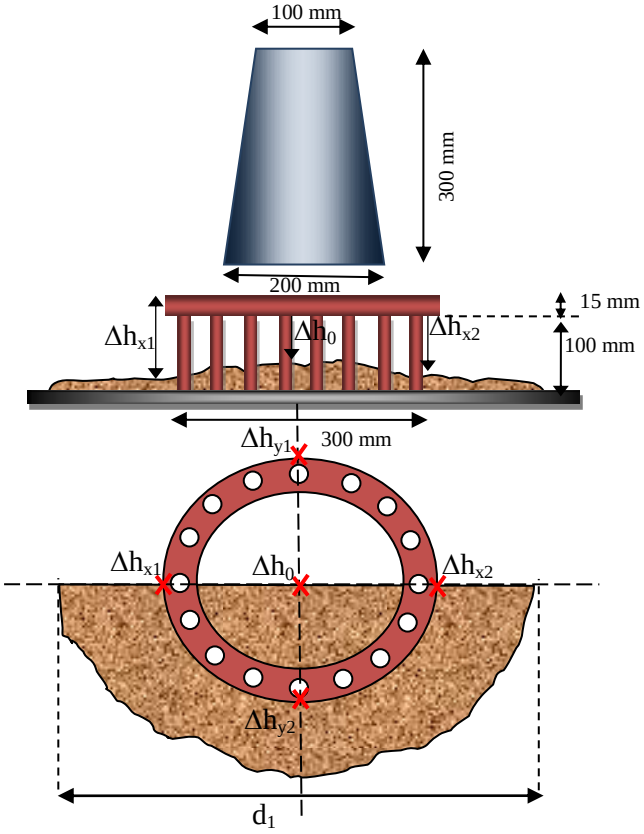

Figure 2.25: J-ring test apparatus

After filling the cone with concrete without using any vibration or rodding, the cone is lifted perpendicular to the steel base plate allowing the concrete to flow freely. The time needed for the flow to reach 500 mm diameter is recorded as $t_{500J,}$ and the flow allowed to stop before recording the remaining measurements.

- Flow spread of the J-ring (SF_J) indicates the restricted deformability of SCC and can be expressed using Equation (2.2)

$$SF_J = \frac{(d_1 + d_2)}{2} \tag{2.2}$$

- Flow time t_{500J} has been recorded.

- Blocking step P_J is calculated using Equation (2.3).

$$P_J = \frac{\Delta h_{x1} + \Delta h_{x2} + \Delta h_{y1} + \Delta h_{y2}}{4} - \Delta h_0 \tag{2.3}$$

where:

$\Delta h_{0:}$ is the height measurement at the centre of flow.

Δh_{x1}, Δh_{x2}, Δh_{y1}, Δh_{y2} are the four measurement heights at positions just outside the J-ring.

Criteria of acceptance

❖ According to (Chan et al., 2010), the flow spread (SF_J) of SCC, with or without steel fibres using the J-ring can be assessed relative to the flow spread (SF) of the same mix using the slump test as described in Table 2.1

Table 2.1. Passing ability criteria

(SF-SF_J)	Passing ability rate	Notes
< 25 mm	0	No visible blocking
25 mm - 50 mm	1	Minimal to noticeable blocking
> 50 mm	2	Noticeable to extreme blocking

❖ The blocking step P_J should be less than 10 mm based on EFNRC.

- t_{500J} which is the time needed for SCC to reach a diameter of 500 mm should be recorded.
- This test is not acceptable when the largest aggregate size in more than 40mm.
- The difference between d_1 and d_2 should be less than 50 mm otherwise the test should be repeated.
- Segregation can be detected by visually inspecting a ring of cement paste/mortar in the edge of flow, and /or ensuring that no coarse aggregates or fibres have lifted in the centre.

2.14.2.2 L-box test

The L-box test is used to assess the filling and passing ability of SCC, or in other words the ability of concrete to pass though reinforced bars without blocking or segregation. After filling the vertical column of the L-box, the gate is lifted to allow SCC to flow into the horizontal part after passing through the rebar obstructions. Two measurements are taken, (H_1, H_2) heights of concrete at the beginning and end of the horizontal section, respectively. The ratio H_2/H_1 represents the filling ability, and typically, this value should be 0.8~1, while the passing ability can be detected visually by inspecting the area around the rebar.

In L-box, 2 or 3 smooth steel bars with 12 mm diameter can be used to represent light or dense reinforcement with distance between them 59 and 41 mm, respectively.

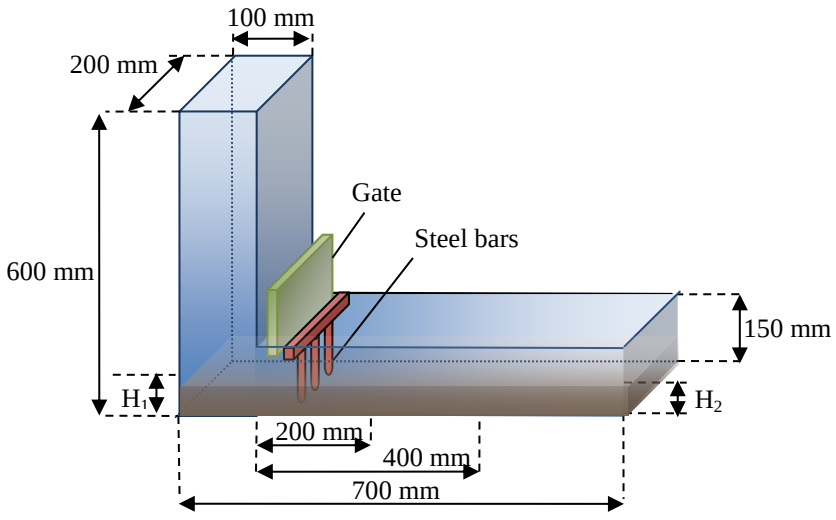

Figure 2.26: L-box test apparatus

The passing ability ratio *PL* should be calculated:

$$PL = \frac{H_2}{H_1} \quad (2.4)$$

H_1 is the mean depth of concrete in the vertical section of the box

H_2 is the mean depth of concrete at the end of the horizontal section of the box.

t_{200} and t_{400} are also recorded which represent the time of SCC to reach 200 mm and 400 mm from the gate, respectively as illustrated in Figure 2.26.

Criteria of acceptance

- For this test, at least 14*l* of SCC should be prepared in accordance with (BS EN 12350-10, 2010).
- No signs of segregation or bleeding.
- Passing ability ratio *PL* should be between 0.8 and 1; a value more than 1 means an error.
- There is no recommendation for t_{200} and t_{400} values, but larger values represent higher viscosity.

It should be mentioned that this test is very sensitive to the operators in terms of the speed of lifting the gate. Slow lifting could result in an increase in t_{200} and $t_{400.}$

2.14.3 Segregation resistance tests

Several empirical tests have been proposed to evaluate SCC segregation.

2.14.3.1 Visual examination

The visual examination method is carried out by inspecting the periphery of the concrete after measuring the slump flow spread and rating it from 0 to 3 (PCI, 2003). However it is an inadequate method because it relies on the experience of the individual and fails to evaluate segregation quantitatively.

2.14.3.2 Sieve stability test

The potential for static segregation can be evaluated by a simple sieve stability test, which measures the amount of grains passing through a 5 mm sieve after a standard period, which is called sieve segregation or segregation index. In this test, 10 litres of fresh SCC are placed

into a test container and allowed to settle over a 15 minute period. The coarse aggregate settles at the bottom and the upper part of the concrete in the container is then wet sieved and the volume of mortar calculated. The more the segregation has occurred the more mortar passes through the sieve, indicating a higher risk of segregation after the placement of SCC.

2.15 Rheology of SCC: Quantitative fundamental study

Quantitative fundamental study deals with the rheological characteristics of concrete such as plastic viscosity, fluidity or yield stress. Rheology has been studied for many years through the development of SCC. Self-compacting concrete which is dominated by its fluid-like behaviour is a viscous non-Newtonian fluid, described by a bi-linear Bingham-type rheological model, in which the fluid flow only initiates once the shear stress has reached a critical value called the yield stress τ_y. This model contains two material properties, namely the yield stress τ_y and the plastic viscosity, η (Papanastasiou, 1987). The mixture of self-compacting concrete is strongly dependent on the composition and characteristics of its constituents in the fresh state which have a great effect on its hardened state. The basic property influencing its performance in the fresh state is its rheological behaviour.

Understanding its rheological parameters, namely the plastic viscosity and the yield stress, provides a quantitative and fundamental way of characterizing the deformability, passing ability and stability of SCC, which are critical for concrete industry as they affect all the mechanical properties in the hardened state.

2.15.1 Measuring the rheological parameters of Bingham model

Plastic viscosity η can be considered to be the internal friction of a fluid. It is the ability of this fluid to resist shear or angular deformation, which is mainly due to the interaction between fluid particles. Yield stress can be considered as the minimum force required to initiate the flow. Flow initiates when the shear stress becomes higher than the yield stress, however, when its value becomes equal or lower than the yield stress, the flow stops. This suggests that the yield stress must be the dominant factor that governs the slump flow spread.

It is known however that the yield stress of SCC mixes is very low (around 200 Pa) in comparison with normal concretes (thousands of Pascal) and remains nearly constant over a large range of plastic viscosities as shown in Figure (2.27).

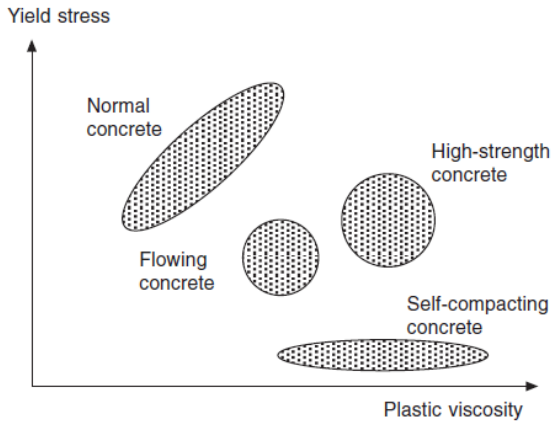

Figure 2.27: Rheology of several types of concrete (After: Domone, 2003)

To measure the rheological parameters of general viscous liquids (such as cement pastes) and solid-liquid suspensions (such as self-compacting concretes), a rheometer is used. When choosing a rheometer, it should take into account the small size of aggregate used in self-compacting concrete compared with conventional vibrated concrete, the presence of yield stress, moderate plastic viscosity, the potential of segregation and the high sensitivity to small changes in materials and their proportions. Although it is difficult to account all these factors in one rheometer, but basically, two types of rheometer can be used, namely those that impose a controlled shear rate on SCC and measure its shear stress, and those that do the opposite. A wide range of rheometers is commercially available such as the coaxial cylinder rheometers, parallel plate rheometers and impeller rheometers (Domone, 2003).

Domone (2003) reported that for a given concrete mix, logically, any rheometer should give the same values of these two fundamental parameters. But in practice that is not the case. This was indeed proved by Banfill et al. (2001) using a series of comparative tests in which three instruments were taken to the same laboratory and used simultaneously to test a series of fresh concrete mixes with a wide different range of rheological characteristics. Figure 2.28 shows an example of how two different rheometers gave totally different responses for the same mix.

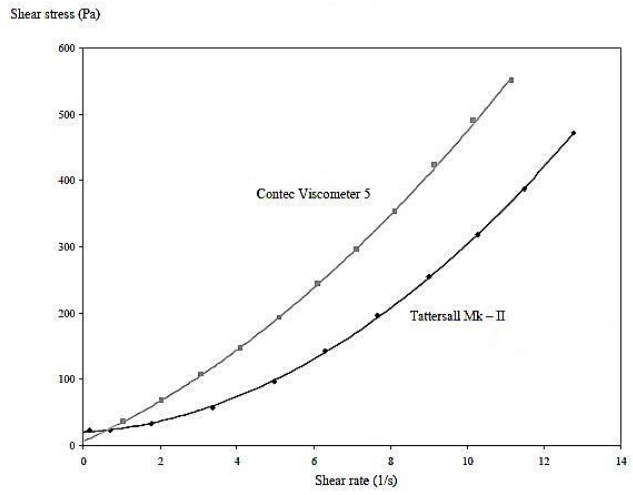

Figure 2.28: Two different responses for a single SCC mix tested by two rheometers (After: Feys et al., 2007)

In both cases the yield stress values were somewhat more consistent than those of plastic viscosity. These inaccurate results, which are often have a large scatter with mixes containing long fibres, have triggered research in to alternative prediction techniques for plastic viscosity (Krieger and Dougherty, 1959; Struble and Sun, 1995).

Ghanbari and Karihaloo (2009) have developed a micromechanical procedure for estimating the plastic viscosity of SCC with or without steel fibres from the knowledge of the plastic viscosity of cement paste alone or of the cement paste with SP and/or VMA. This procedure has been shown to predict the plastic viscosity of SCC mixes with or without fibres that agree very well with measured values. Details about this micromechanical procedure will be explained in Chapter 4.

Many researchers (Grünewald, 2004; Roussel, 2006; Thrane, 2007; Tregger et al., 2007) have investigated the potential of a relationship between the rheological characteristics of self-compacting concrete mix (yield stress and plastic viscosity) and the measured parameters in the slump flow test (namely, slump flow diameter and t_{500}). They all agreed that the time t_{500} can be related to the plastic viscosity but that the slump flow spread is a function of both the yield stress and the density of SCC. In general, both the yield stress and the plastic viscosity increase with time, as the concrete hardens (Castro and Liborio, 2006).

2.15.2 Effects of materials and mixture proportions on the Bingham constants

Irrespective of their absolute values, it is very important to understand how the yield stress and the plastic viscosity of concrete mixes vary with different mix proportions and material components. There is a considerable amount of published information on this which can be summarised as follows:

- An increase in water to powder ratio in a concrete mix decreases both its yield stress and the plastic viscosity. Similar results have been reported by many researchers (Ramachandran and Beaudoin, 2001; Banfill, 2006). Figure 2.29 shows the effect of water to cement ratio on both the plastic viscosity and yield stress.

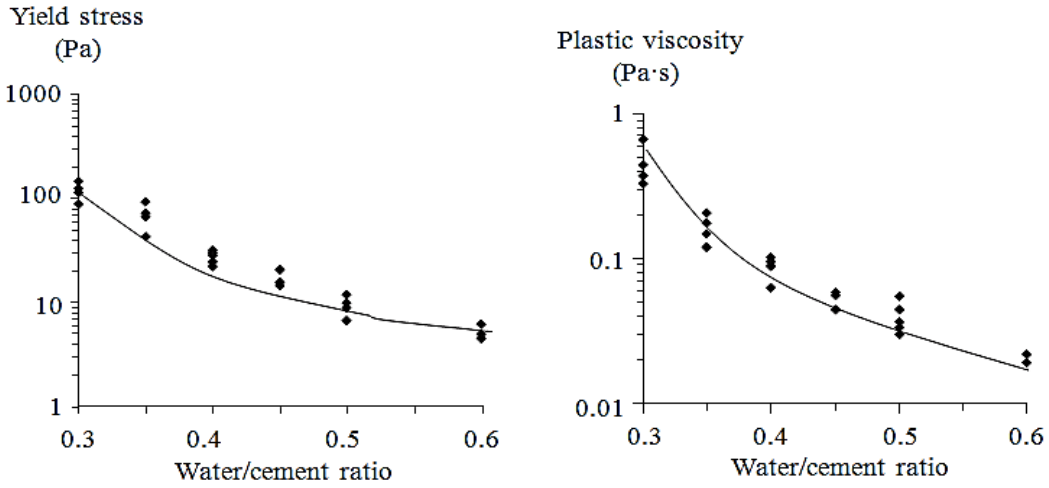

Figure 2.29: Typical effect of water-cement ratio on Bingham constants for cement paste (After: Domone and Thurairatnam, 1988)

- Yield stress decreases with increasing super-plasticiser concentration (Domone and Thurairatnam, 1988; Banfill, 2006) as illustrated in Figure 2.30, while plastic viscosity effects are linked to the type of super-plasticiser. For instance, solid-based super-plasticisers like naphthalene-based, lead to an increase in the plastic viscosity, while the liquid-based super-plasticisers such as Gelenium ACE 333 have the opposite effect.

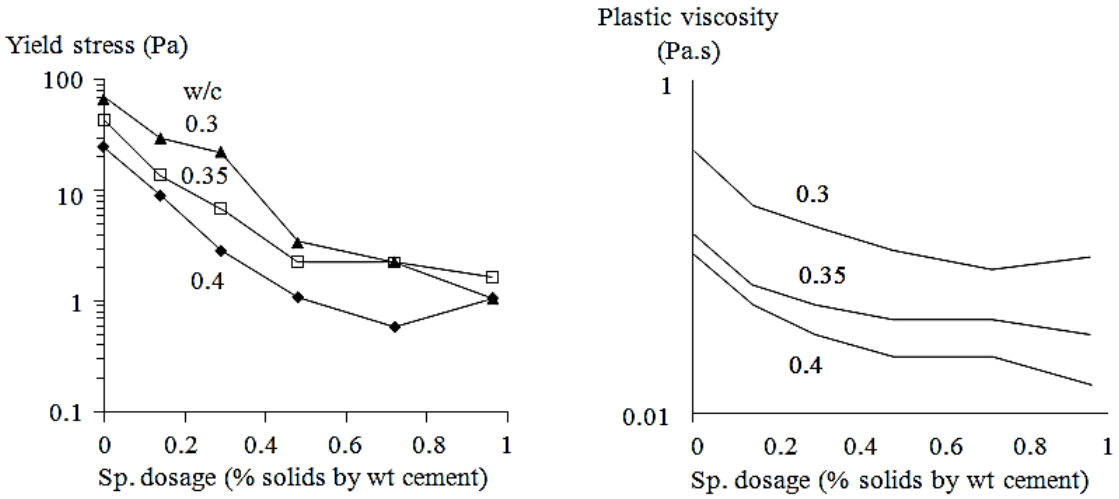

Figure 2.30: Typical effect of superplasticiser on Bingham constants for cement paste (After: Domone and Thurairatnam, 1988)

- Although increasing the total aggregate content (with angularity) results in a high plastic viscosity and yield stress, aggregate with round and smooth surface tends to have opposite effects on both plastic viscosity and yield stress (Ramachandran and Beaudoin, 2001; Koehler and Fowler, 2007).

- Ground granulated blast furnace slag (GGBS) reduces the yield stress, but leads to an increase in the plastic viscosity.

- Banfill (2006) reported that pulverized-fuel ash (PFA) reduces both the yield stress and plastic viscosity. However, Ramachandran and Beaudoin (2001) have different results; yield stress increases with low fly ash contents and decreases with high contents of fly ash.

- Increasing paste content reduces the yield stress and has the opposite effect on the plastic viscosity.

- Silica fume considerably increases yield stress and initially reduces plastic viscosity (Ramachandran and Beaudoin, 2001). Small amounts of silica fume reduce the plastic viscosity, with almost no effect on the yield stress; however, above a threshold level of SF, which depends on the cement content, there is a substantial increase in the yield stress, followed by an increase in the plastic viscosity.

2.16 SCC applications

Following its success in Japan with more than 400,000 m^3 of annual production for bridges and buildings, other parts of the world have embraced SCC.

- At over 828 meters (2,716.5 ft) and 166 stories, Burj Khalifa (2010) in Dubai (Figure 2.31) holds the record of the tallest building and free standing structure in the world with the largest number of stories. Self-compacting concrete is playing a greater role in high-rise construction to overcome the problem of congested reinforcement and ease of placement. The groundwater in which the Burj Dubai substructure is constructed is particularly severe, with chloride concentrations of up to 4.5%, and sulfate of up to 0.6%. The chloride and sulfate concentrations found in the groundwater are even higher than the concentrations in seawater. Accordingly, the primary consideration in designing the piles and raft foundation was durability. The concrete mix for the piles which are 1.5 m in diameter and 43 m long with design capacity of 3000 tonnes each was a 60 MPa mix based on a triple blend with 25% fly ash, 7% silica fume, and a water to cement ratio of 0.32. A viscosity modifying admixture was used to obtain a slump flow of 675 +/- 75 mm to limit the possibility of defects during construction.

Figure 2.31: Burj Khalifa in Dubai

- The 800 million dollar Sodra Lanken (1997) Project in Sweden (Figure 2.32) notably was one of the largest infrastructure projects that used SCC. The six kilometres long four-lane highway in Stockholm involved seven major junctions, and rock tunnels totalling over 16 km partly lined with concrete and over 225,000 cubic meters of concrete. Incorporating SCC was ideal to cope with the density of reinforcement required and the highly uneven rock surfaces.

Figure 2.32: The Sodra Lanken Project links east and west of Stockholm's southern side

- Another example can be found in the UK at St George Wharf (2004), London Docklands where SCC has been used to save time and manpower (Figure 2.33). SCC was used in limited areas on two floors in lift shaft walls, upstand beams and columns and for stairs precast on site.

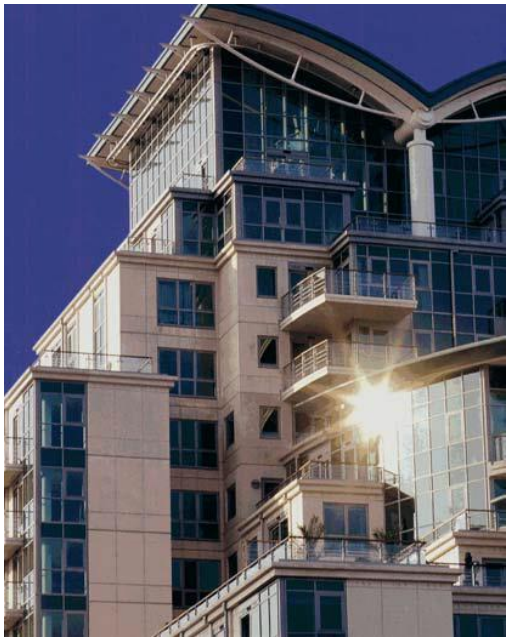

Figure 2.33: St George Wharf, London Docklands

- Dragon Bridge (2012), Alcalá De Guadaira, Seville, Spain (Figure 2.34). This spectacular 124 m long bridge, distributed in four spans, stands out due to its unique shape. The concrete structure represents a dragon that seems to emerge from the Guadaira river in the province of Seville.

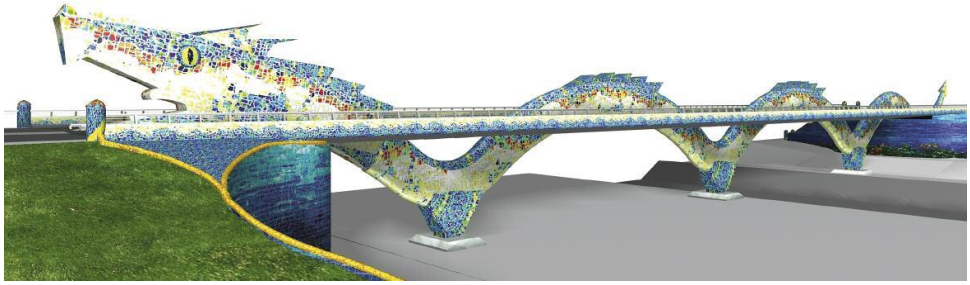

Figure 2.34: Dragon Bridge, Alcalá De Guadaira, Seville, Spain

The dragon's body is made up of an egg-shape section, 4 meters high and 2 meters wide, of self-compacting reinforced concrete. Its shape was clad in "trancadis" using more than 4,500 square meters of mosaic tiles.

2.17 Concluding remarks

Self-compacting concrete (SCC) is an advanced type of concrete that can flow and compact under its own weight without external aid or vibration, pass through intricate geometrical configurations without showing any segregation. The use of SCC has many advantages including increased construction productivity, improved jobsite safety, and enhanced concrete quality. These benefits, however, must be measured against the potentially higher material costs and the need for greater technical expertise and quality control measures. It has been successfully used for a wide range of precast and ready mixed concrete applications.

This chapter gave a general overview of SCC including its properties, the basic principle of its mix design, the mechanism of achieving self-compacting ability and the influence of cement replacement materials and admixtures on the characteristics of SCC in the fresh state. It was concluded that in the fresh state, CRMs enhance self-compacting ability, fluidity and cohesiveness while improving its performance in the hardened state.

A review of the effect of fibres on the SCC was also given. Although the fibres greatly impair the workability of SCC because of their elongated shape and large surface area, the addition of fibres to SCC will lead to great benefits and improve its performance in the hardened state.

Fibres bridge cracks and retard their propagation. They contribute to an increase in the energy absorption compared with plain concrete. In order to make the best use of the fibres, they need to be homogeneously distributed in the mix without clustering.

Finally, the rheology of SCC was introduced, with an overview of the rheological parameters and the effects of materials and mixture proportions on the Bingham constants. The most popular methods of testing SCC were introduced including the slump flow test, J-ring test, L-box test and sieve stability test.

As we have seen above, there is a lot of research available in the literature of an ad-hoc nature. Often the conclusions are contradictory (one example was reported in Section 2.9.3). As a result, there is a scope for a systematic development of SCC mixes. We will develop in a systematic manner SCC mixes ranging in compressive strength from 35 MPa to 160 MPa. Some of these mixes will contain fibres.

The aim is to identify the role of paste to solids ratio in SCC mixes and to check how much this ratio defers from that used in the vibrated concrete mixes of corresponding compressive strength. Then, we shall accurately estimate the plastic viscosity of the SCC mixes so produced using a micromechanical procedure based on the measured viscosity of the cement paste and the mix proportions. This plastic viscosity together with the yield stress is the main parameter controlling the behaviour of SCC mixes. They will be used later for simulating the flow of SCC mixes with and without fibres in different configurations.

The next Chapter will report on the modelling the flow of fresh self-compacting concrete.

Chapter 3

Modelling the flow of fresh self-compacting concrete

3.1 Introduction

Computer modelling nowadays is an indispensable tool for solving complicated engineering problems replacing expensive experimental tests in order to save time, effort and materials. Simulation algorithms translate the mathematical description of different physical problems into a discrete form and exploit the enormous capabilities of modern computers.

The modelling of fresh concrete flow is increasingly becoming an important issue for the construction industry. Since concrete is put into place in its plastic form, its fresh properties have a direct influence on the strength and durability in the hardened state. Concrete which is not been properly cast and consolidated may be prone to defects such as honeycombs, air voids and aggregate segregation (Patzák and Bittnar, 2009) which are a major problem affecting the durability of concrete structures. For aesthetic reasons the defective surfaces may be repaired after the casting if the cost of repair is not prohibitive, but detecting problems that occur inside the formwork can be very difficult (Dufourn and Pijaudier-Cabot, 2005). Therefore, modelling the flow of concrete in its plastic form can significantly contribute to the durability and strength of a structure because it allows us to predict:

- Whether or not the formwork is completely filled;
- The blocking and passing behaviour of the mix as particles migrate through reinforcements, especially when fibres and/or large aggregates are present;
- The minimum workability of the fresh concrete that could ensure the proper filling of a given formwork, thus avoiding the use of highly flowable mixes with a tendency to static and dynamic segregation;
- The rheological behaviour of concrete and a potential tool for improving mix proportioning;
- The distribution of large aggregates during the flow of concrete and therefore avoiding segregation and ensuring the homogeneity of the mix;
- The distribution of fibres and their orientation in the formwork, therefore optimizing the durability and strength of concrete.

This Chapter will report on the various computational methods used in the past to model concrete flow, highlighting their advantages and disadvantages. The numerical strategy used in the simulation techniques will be also discussed. An overview of the smooth particle hydrodynamics as a mesh-free computational method able to take into account special

features such as large deformations, large heterogeneity and free surfaces flow of SCC will be reported, as these features pose big challenges to the mesh-based methods.

3.2 Previous attempts to model fresh concrete flow

When it comes to fresh concrete, many attempts have been made to represent its motion. From a computational point of view the modelling of concrete flow can be divided into two main categories. In the first category are methods that treat concrete as a homogeneous medium; in the second category the concrete is treated as a heterogeneous medium. Choosing the right technique depends on the purpose of the simulation and whether the solid components of concrete are considered as separate particles or are embedded inside the matrix.

3.2.1 Simulation of concrete as a homogeneous medium

In this simulation concrete is regarded as a fluid without particle inclusions. Although single fluid simulation can be considered as the fastest way to simulate fresh concrete flow with a large choice of constitutive laws which allows simulating different types of phenomena such as thixotropy, it is difficult to predict particle blocking and segregation (Roussel et al., 2007). Mori and Tanigawa (1992) have treated concrete as a single fluid with specific rheological properties using the Viscoplastic Finite Element Method (VFEM) and the Viscoplastic Divided Element Method (VDEM). In the former, the fresh concrete is divided into elements and the deformation and the displacements of the nodal points representing the flow are calculated, while in the latter, the fresh concrete is divided into elements and cells which are either full or empty, and a cell marker describes the flow. Although both methods can model various problems, but using nodal points can be more useful when representing reinforcement bars at fixed positions of nodes.

Thrane et al. (2004) have simulated SCC as a single fluid flow with Bingham behaviour using the Galerkin FEM formulation of the Navier–Stokes equations with the code Fidap©. The code did not have the means to treat discrete particles and hence couldn't assess the blocking resistance. They concluded that it is necessary to use a 3-dimensional model for simulating SCC in the L-box. According to their results the viscous contribution due to the shear introduced by the horizontal boundaries of the L-box contributes to a delay in the flow; the

times needed for the flow to reach 700 mm from the gate for 2-dimensional and 3-dimensional simulations were 0.7 sec and 1.2 sec, respectively. The difference can be further increased if the SCC mix has higher viscosity.

Kitaoji et al. (1996) used VDEM in 2-dimensions and 3-dimensions to simulate the flow of fresh concrete cast into formwork confirming a good correlation between the experiment and simulation results. Kurokawa et al. (1996) used VFEM to evaluate factors affecting the slump flow of fresh concrete. They used the Bingham model and determined the rheological properties from the best fit to experimental results of slump flow.

Roussel and Coussot (2005) and Roussel (2006) have simulated the 3D flow behaviour of concrete in the slump test with yield stress between 25 Pa and 5500 Pa using the computational fluid mechanics code Flow 3D®. Good agreement between the numerical and experimental results was obtained for the mini cone test and for the ASTM slump test, as reported by Roussel and Coussot (2005) (where ASTM stands for the American Society for Testing and Materials).

Patzák and Bittnar (2009) have simulated the 2D flow of concrete in the L-box using the finite element method (FEM) and the interface-capturing method to track the position of a free surface.

3.2.2 Simulation of concrete as a heterogeneous medium

This type of simulation considers the differences in the physical properties between the liquid and granular components used in the concrete and their effects on the flow. Concrete is naturally dominated by a fluid-like behaviour or granular medium-like behaviour. For instance, when the amount of coarse aggregates is limited SCC behaves like a fluid suspension, while for ordinary concrete the behaviour is dominated by the granular nature of materials.

Gram (2009) used the Discrete Element Method (DEM, sometimes also called Distinct Element Method) commercial software PFC3D to model the flow of SCC as a homogeneous and a heterogeneous fluid. Martys (2005) used the Dissipative Particle Dynamics method (DPD) to cementitious materials which allowed for much larger time steps, as opposed to DEM.

Mori and Tanigawa (1992) used the so-called Viscoplastic suspension element method (VSEM) to simulate the flow of SCC where concrete is divided between coarse aggregates represented as monosize spheres, and mortar. By testing concrete with a minimum yield stress 100 Pa, they claimed that such a method is only applicable to study the complex behaviour concrete, such as collapse, separation and mixing.

Dufourn and Pijaudier-Cabot (2005) used a finite element method with Lagrangian integration points (FEMLIP) to numerically model the flow of concrete in L-Box.

Svec et al. (2012) have modelled the free surface flow of suspension of rigid particles in a non-Newtonian fluid using the Lattice Boltzmann method combined with Immersed Boundary Method and particle dynamics. This model is efficient and robust allowing simulations of tens of thousands of particles.

In the present research, the Smooth Particle Hydrodynamics (SPH) will be used. Due to the fact that SCC goes through large deformations during the flow and the fact that it contains particles of different sizes, SPH is an ideal computational method to represent with a good margin of accuracy its rheological behaviour. Hence, unlike the mesh-based methods, SPH as a particle-based method does not require re-meshing. This method has been tested and proved to be efficient and accurate in modelling SCC without fibres by Kulasegaram et al. (2011) and SCC with fibres by Kulasegaram and Karihaloo (2013) in the 2D configuration. The goal in this thesis is to extend its application to cover 3D configurations which will give a highly accurate picture of SCC flow behaviour both as a homogeneous and a heterogeneous medium allowing to reveal the actual distribution of coarse aggregates and/or fibres (and their orientations) during the flow and therefore the ability to predict the fibre orientation factor, FOF.

3.3 Numerical solution strategy of simulation techniques

There are in principle some basic steps in the procedure of numerical simulation as shown in Figure 3.1. The first step of the investigation will focus on the observed physical phenomenon, which will be represented by a mathematical model driven in the form of governing equations with limited conditions (boundary conditions). To numerically solve the governing equations, the next step involves dividing the continuum problem domain into a discrete number of elements or components. This will form the computational frame for the numerical approximation which is based on a theory of function approximations and includes discrete representation of the governing equations according to the discretization technique used, before coding or translating the decomposed domain and numerical algorithms into a computer code in one of the programming languages.

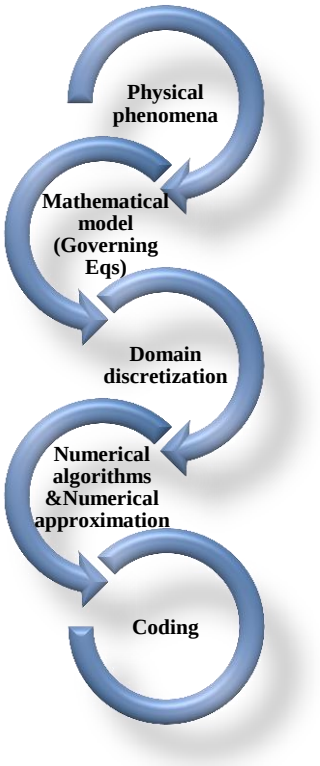

Figure 3.1: The numerical strategy of the simulation technique

3.4 Mathematical Model - The governing equations of concrete flow

The second step in the numerical strategy is to identify the mathematical model of the studied phenomenon which represents here the flow behaviour of self-compacting concrete. The flow of SCC can be described as a non-Newtonian flow like a liquid. Due to its extreme fluidity, the behaviour of SCC can be best described using the governing equations of a fluid. Fluid dynamics uses the concept of fluid particles whose motion is described by Newton's second law of motion. The basic governing equations of fluid motion are the continuity, momentum and energy equations which are based on the fundamental physical laws of conservation. However, in the absence of heat flux in a continuum, the energy can be assumed to be identically conserved. In the case of incompressible flow when the viscosity and density are not affected by the temperature, energy conservation equations can therefore be ignored.

3.4.1 Continuity equation (the mass conservation)

Let us consider an infinitesimal moving fluid element with fixed mass δm, density ρ and volume δV, so that

$$\delta m = \rho \delta V \tag{3. 1}$$

Since the mass is conserved, we can state that the time-rate-of-change of the mass of the fluid element is zero as the element moves along with the flow

$$\frac{D(\delta m)}{Dt} = 0 \tag{3. 2}$$

The substantial derivative in Equation (3.2) can be written as

$$\frac{D(\delta m)}{Dt} = \frac{D(\rho \delta V)}{Dt} = \delta V \frac{D\rho}{Dt} + \rho \frac{D(\delta V)}{Dt} = 0 \tag{3. 3}$$

Rearranging Equation (3.3) gives

$$\frac{D\rho}{Dt} + \rho \frac{1}{\delta V} \frac{D(\delta V)}{Dt} = 0 \tag{3. 4}$$

The second term in Equation (3.4) is the divergence of the velocity $\nabla.\mathbf{v}$ which is the time rate of change of the volume of a moving fluid element per unit volume (see Appendix A).

$$\frac{D\rho}{Dt} + \rho\nabla \cdot \mathbf{v} = 0 \qquad (3.5)$$

Equation (3.5) is the continuity equation or the mass conservation equation in the Lagrangian form. For an incompressible fluid, the density is constant, and therefore the continuity equation becomes

$$\nabla.\mathbf{v} = 0 \qquad (3.6)$$

3.4.2 The momentum equations

The momentum equations are the fundamental governing equations that describe flow of fluids by applying Newton's second law of motion which states that the total force on a fluid element **F** is equal to its mass *m* times the acceleration ***a*** of the considered fluid element

$$\mathbf{F} = m\,\boldsymbol{a} \qquad (3.7)$$

Let us consider a small moving fluid element; the total forces acting on that element are the surface forces $\mathbf{F_S}$ and body forces $\mathbf{F_B}$

- $\mathbf{F_S}$ are the surface forces which are applied directly on the surface of the fluid element; these forces can be caused by the pressure, shear or normal forces imposed by external fluid surrounding the fluid element;
- $\mathbf{F_B}$ are the body forces which act directly on the volume of the fluid element (e.g. gravitational, electrical or magnetic forces, etc…).

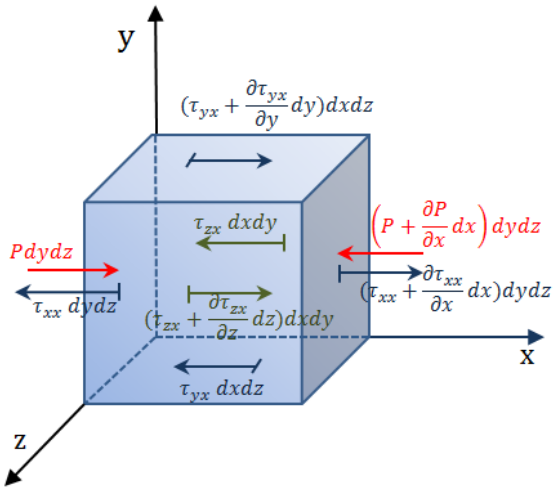

Figure 3.2: Surface forces acting on a fluid particle in x-direction

Consider first only the x-component of the forces acting on the fluid element. The surface forces acting on a surface area of fluid particle in x-direction are the pressure *P* from surrounding fluid , shear and normal stresses τ_{ix} applied in x-direction exerted perpendicular to the *i* axis (where *i* is *x*, *y* or *z*) . Figure 3.2 illustrates the x-component of surface forces acting on a fluid element

$$F_{sx} = P dydz - \left(P + \frac{\partial P}{\partial x} dx \right) dydz - \tau_{xx}\, dydz + \left(\tau_{xx} + \frac{\partial \tau_{xx}}{\partial x} dx \right) dydz - \tau_{yx}\, dxdz + \left(\tau_{yx} + \frac{\partial \tau_{yx}}{\partial y} dy \right) dxdz - \tau_{zx}\, dxdy + \left(\tau_{zx} + \frac{\partial \tau_{zx}}{\partial z} dz \right) dxdy \quad (3.8)$$

$$F_{sx} = -\frac{\partial P}{\partial x} dxdydz + \frac{\partial \tau_{xx}}{\partial x} dxdydz + \frac{\partial \tau_{yx}}{\partial y} dxdydz + \frac{\partial \tau_{zx}}{\partial z} dxdydz \quad (3.9)$$

where *P* is the pressure from the surrounding fluid.

Let us denote the body force per unit mass acting on the fluid element by ***f***, with f_x representing its x-component. The volume of the fluid element is (*dxdydz*); hence, the body force in x-direction

$$F_{Bx} = f_x \rho\, dxdydz \quad (3.10)$$

Therefore the total force acting on the fluid element in the x-direction is

$$F_x = -\frac{\partial P}{\partial x} dxdydz + \frac{\partial \tau_{xx}}{\partial x} dxdydz + \frac{\partial \tau_{yx}}{\partial y} dxdydz + \frac{\partial \tau_{zx}}{\partial z} dxdydz + f_x \rho\, dxdydz \quad (3.11)$$

Now we recall Equation (3.7), where the acceleration is equal to the time-rate-of-change of the velocity, denoted $\frac{Dv_x}{Dt}$ in x-direction;

$$F_x = m\, a_x = \rho\, dxdydz \frac{Dv_x}{Dt} \quad (3.12)$$

Substitute Equation (3.12) into Equation (3.11)

$$\rho dxdydz \frac{Dv_x}{Dt} = -\frac{\partial P}{\partial x} dxdydz + \frac{\partial \tau_{xx}}{\partial x} dxdydz + \frac{\partial \tau_{yx}}{\partial y} dxdydz + \frac{\partial \tau_{zx}}{\partial z} dxdydz + f_x \rho\, dxdydz \quad (3.13)$$

And hence the momentum equation in the x-direction is given by

$$\rho \frac{Dv_x}{Dt} = -\frac{\partial P}{\partial x} + \frac{\partial \tau_{xx}}{\partial x} + \frac{\partial \tau_{yx}}{\partial y} + \frac{\partial \tau_{zx}}{\partial z} + f_x \rho \quad (3.14)$$

Similarly, in the y- and z-directions

$$\rho \frac{Dv_y}{Dt} = -\frac{\partial P}{\partial y} + \frac{\partial \tau_{xy}}{\partial x} + \frac{\partial \tau_{yy}}{\partial y} + \frac{\partial \tau_{zy}}{\partial z} + f_y \rho \tag{3. 15}$$

$$\rho \frac{Dv_z}{Dt} = -\frac{\partial P}{\partial z} + \frac{\partial \tau_{xz}}{\partial x} + \frac{\partial \tau_{yz}}{\partial y} + \frac{\partial \tau_{zz}}{\partial z} + f_z \rho \tag{3. 16}$$

Equations (3.14) to (3.16) are the momentum balance equations.

If the body force acting on the continuum is only gravitational force **g**, the momentum Equations (3.14) to (3.16) in the Lagrangian form can be written in the compact vectorial form as

$$\frac{D\mathbf{v}}{Dt} = -\frac{1}{\rho}\nabla P + \frac{1}{\rho}\nabla.\boldsymbol{\tau} + \mathbf{g} \tag{3. 17}$$

where ρ, t, **v**, P, **g** and $\boldsymbol{\tau}$ represent the fluid particle density, time, particle velocity, pressure, gravitational acceleration, and shear stress, respectively.

3.4.3 Common models to describe a fluid flow

Self-compacting concrete satisfies the flow and cohesiveness criteria and can thus be modelled as a Bingham fluid (Vasilic et al., 2010). Most numerical simulations consider only the steady-state of the flow while the thixotropic state i.e. the loss of workability of concrete during the flow is not been taken into account. However, SCC can exhibit shear thickening behaviour which means the plastic viscosity η increases with the shear rate $\dot{\gamma}$ (e.g. in pumping and mixing); in this case, SCC can be modelled by the Herschel-Bulkley model (Vasilic et al., 2010). Over the years, some empirical models have been proposed. The two commonly used models are described below.

3.4.3.1 Bingham plastic model

The Bingham plastic model or simply the Bingham model is the simplest relation to show the behaviour of a fluid having a yield stress τ_y. It is written as:

$$\tau = \tau_y + \eta\dot{\gamma} \qquad \tau > \tau_y \tag{3. 18}$$

$$\dot{\gamma} = 0 \qquad \tau \leq \tau_y \tag{3. 19}$$

From a practical point of view, it is expedient to represent the bi-linear Bingham model with its associated discontinuity at zero shear rate by a continuous function (Papanastasiou, 1987)

$$\tau = \eta\dot{\gamma} + \tau_y\left(1 - e^{-m\dot{\gamma}}\right) \tag{3. 20}$$

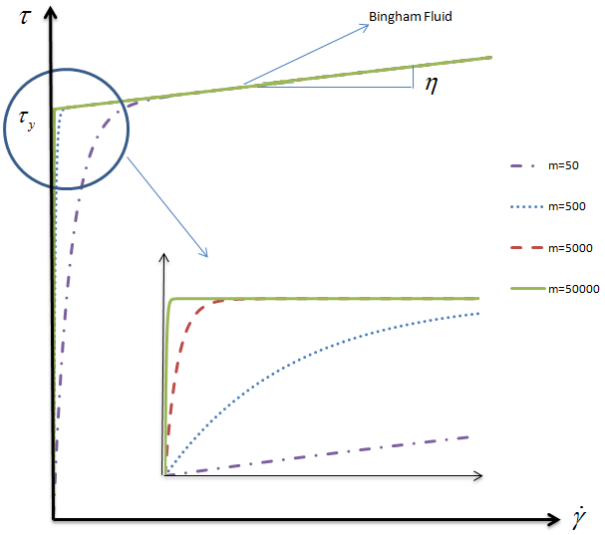

Figure 3.3: A bi-linear Bingham fluid constitutive model replaced by the continuous function (3.20) (After: Ghanbari, 2011)

where *m* is a very large number. It can be seen from Figure 3.3 that the continuous function in Equation (3.20) approaches the bi-linear function for large *m*. On the scale of the figure, the discontinuity at τ_y cannot be distinguished for *m* =5000 s and 50000 s. However, at a magnification of 100 on the horizontal scale as shown in the Figure 3.3, it is clear that the continuous approximation is better for *m* =50000 s.

3.4.3.2 Herschel-Bulkley model

This model is a generalization of the Bingham model in such a way that, upon deformation, the viscosity can be shear thinning or shear thickening. The constitutive equation is

$$\tau = \tau_y + \eta\dot{\gamma}^n \qquad \tau > \tau_y \tag{3. 21}$$

$$\dot{\gamma} = 0 \qquad \tau \le \tau_y \tag{3. 22}$$

For n <1, the fluid exhibits shear thinning properties

n =1, the fluid shows Bingham behaviour

n >1, the fluid shows shear thickening behaviour

In Equation (3.21), n is an empirical curve-fitting parameter known as the flow behaviour index. For a shear thinning fluid, the index may have any value between 0 and 1. The smaller the value of n, the greater is the degree of shear thinning. For a shear thickening fluid, the index n will be greater than unity.

3.5 Domain Discretization

Domain discretization represents the third step in the numerical strategy reported in the Section 3.2. In this step, the continuum problem domain needs to be divided into a finite number of discrete components in order to numerically solve the governing equations. This technique is different according to the numerical method used. From a graphical point of view, computational modelling can be divided into two main categories, grid and particle based methods. Figure 3.4 illustrates the two different discretizations of the same geometrical domain.

3.5.1 Grid based method

In the grid or mesh based method, the discretization of the problem domain is performed by dividing the continuum domain into small discrete domains called the mesh or grid. These discrete domains are connected to each other by nodes. Accuracy of the numerical approximation is closely related to the mesh topography (i.e. shape, size...etc.). Although grid based methods such as the finite element method (FEM), the finite difference method (FDM) are very commonly used, the difficulty of solving complicated problems namely free surfaces, large deformability, moving interfaces, difficult boundary conditions and complex geometries make them computationally costly and time consuming (Liu and Liu, 2010). Because the generation of the mesh for a grid method is a prerequisite, for complicated problems, it can be more difficult than solving the problem itself since all the formulation and their results are based on the quality of the mesh (Vesenjak and Ren, 2007). Therefore, mesh-

less methods become more attractive to treat problems where it is difficult to used grid based methods.

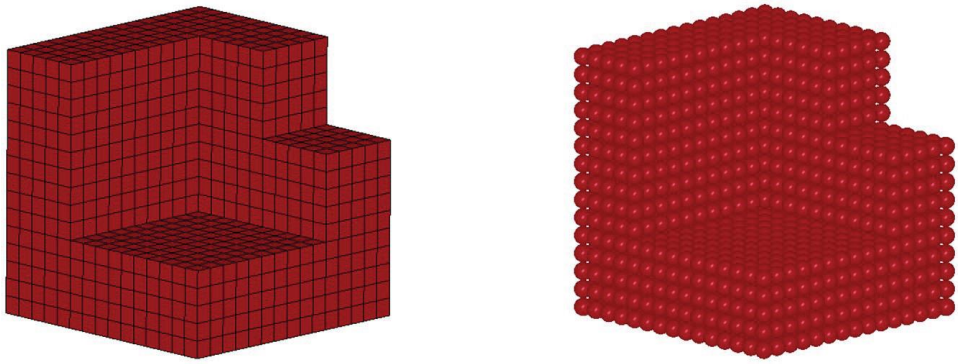

Figure 3.4: comparison between grid method (left) and particle method (right) for the same geometry (After: Vesenjak and Ren, 2007)

3.5.2 Particle based method

In particle (or mesh-less) methods the analysis domain is represented by a set of nodal points or particles without using any mesh that provides the connectivity of those nodes. Here it is easy to handle large deformations, moving interfaces, difficult boundary conditions and complex geometries, since the connectivity among nodes is generated as part of the computation. Moreover, it is easy to control accuracy by simply adding more particles and adjusting the shape function.

A number of mesh-free methods have been proposed for the analysis of fluid flow such as the smoothed particle hydrodynamics (SPH) (Kulasegaram and Karihaloo, 2013), Element Free Galerkin Method (EFGM) (Yang, 2013), Reproducing Kernel Particle Method (RKPM) (Xiong, 2005) and Cloud Method (Burke et al., 2010)...etc. These methods share some common features, but are different in the means of function approximation and the implementation process (Liu and Liu, 2003).

3.6 Eulerian and Lagrangian approaches

There are two fundamental approaches to describe the physical governing equations: Eulerian and Lagrangian.

The Eulerian approach is a spatial description; it is used to track a certain fixed location in the flow field and follows the change in properties, as different materials pass through that location.

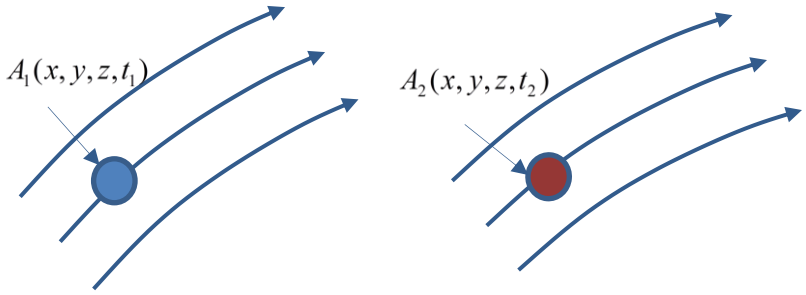

Figure 3.5: Different fluid elements at different times at a fixed location in the fluid flow

Let us say that the velocity is being followed at a location in the fluid flow through which different fluid elements pass at different times (Figure 3.5)

$t_1 \rightarrow \mathbf{v}_1$

$t_2 \rightarrow \mathbf{v}_2$

The time rate of change of the velocity in such a measurement is denoted as $\left.\frac{\partial \mathbf{v}}{\partial t}\right|_{(x,y,z)}$ which is called the partial derivative of the velocity with respect to time. Note that the suffix (x,y,z) implies that the observer records the change in the property at the fixed location (x,y,z). $\left(\frac{\partial \mathbf{v}}{\partial t}\right)$ is also called the local rate of change of that property (velocity in this case).

The Lagrangian approach is used to track a material element of the fluid as it moves and the change in its properties are monitored. The properties may be velocity, temperature, density, mass, or concentration, etc… in the flow-field.

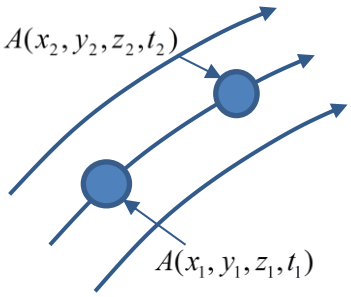

Figure 3.6: Fluid particle motion from time t_1 to time t_2

At time t_1, the 'material' or 'particle' of the fluid 'A' illustrated in Figure 3.6 has moved from location (x_1,y_1,z_1) to another location (x_2,y_2,z_2) at time t_2. Its property, say velocity, is recorded, as the material moves in the flow-field. The recorded property is associated with the same fluid particle, but at different locations and at different times

$$t_1 \rightarrow \mathbf{v}_1 \rightarrow (x_1, y_1, z_1)$$

$$t_2 \rightarrow \mathbf{v}_2 \rightarrow (x_2, y_2, z_2)$$

The time change of the velocity in such a measurement is denoted as $\frac{D\mathbf{v}}{Dt}$, which is called material derivative or substantial derivative. It reflects time rate of change in the velocity (or any other properties) of the tagged fluid particle as observed by an observer moving with the fluid. The Vortex method, Finite Point set Method (FPM), and smooth particle hydrodynamics (SPH) method, are examples of Lagrangian methods.

The two derivatives are related to each other

$$\frac{D\mathbf{v}}{Dt} = \frac{\partial \mathbf{v}}{\partial t} + (\mathbf{v}.\nabla)\mathbf{v} \qquad (3.\ 23)$$

where the term $\mathbf{v}.\nabla$ is the convective derivative, which defines the time rate of change as the fluid element moves from one location to another in the flow field. The substantial derivative can be used for any field variables, e.g. pressure (see Appendix A).

3.7 Numerical approximation- Smoothed particle hydrodynamics (SPH)

The fourth step in the numerical strategy is the numerical approximation which can be performed using different numerical methods. Despite the fact that mesh-based numerical methods are the primary computational methodology in engineering computational mechanics, the limited application efficiency of mesh-based methods in many complex problems (e.g. free surface problems, large deformations) have encouraged researchers to develop other computational methods, able to avoid the mesh dependence. One of the attractive mesh-free formulations is the Smoothed Particle Hydrodynamics (SPH).

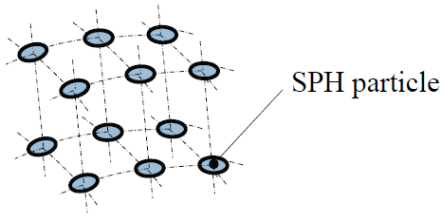

Figure 3.7: SPH model (After: Vesenjak & Ren, 2007)

The SPH is a Lagrangian particle-based numerical method (Figure 3.7). It was first independently proposed by Lucy (1977) and Gingold and Monaghan (1977) to solve particular astrophysical problems in three-dimensional open space. Since the collective movement of those particles is similar to the movement of a liquid or gas flow, it can be modelled by the governing equations of the hydrodynamics. The SPH was first conceived for compressible flow problems in confined flow simulations, until later Monaghan et al. (1994) proposed and developed a modified SPH formulation to model free surface inviscid liquid flow. Several other researchers have since contributed to the method and solved various engineering problems including multi-phase problems (Monaghan and Kocharyan, 1995), quasi-incompressible flow (Monaghan, 1994; Morris et al., 1997), incompressible fluid flow (Shao and Lo, 2003; Solenthaler and Pajarola, 2009), flow through porous media (Zhu et al., 1999) , viscous fluid flow (Takeda et al., 1994), shock simulations (Monaghan and Gingold, 1983), gravity currents (Monaghan, 1996), heat transfer (Chaniotis et al., 2002; Cleary et al., 2002), turbulent flows (Welton, 1998), interfacial flows, discontinuity and large deformability (Bui et al., 2008; Colagrossi and Landrini, 2003) and sloshing problems

(Kelecy and Fletcher, 1997; Koshizuka et al., 1995). The interaction between fluids, free surfaces and many other applications can be also simulated using SPH (Amini et al., 2011).

Benz and Asphaug (1994) extended the application of SPH to cover the fracture of brittle solids. Bonet and Kulasegaram (2000) applied SPH to simulate the metal forming. Libersky et al. (1993) introduced an approximation of the full stress tensor into the "classical" SPH formulation. This was a pilot application of the SPH method to the dynamics of elastic-plastic solids, and its success resulted in a number of applications in related fields. One of the drawbacks associated with the simulation of elastic problems was the tensile instability, which is the instability of the numerical solution that occurs when simulating material undergoing large tensile deformations. Several correcting techniques were proposed to overcome the problem of tensile or spatial instability (Chen et al., 1999; Dyka et al., 1997; Monaghan, 2000), including other notable modifications or corrections to the SPH method (Bonet and Kulasegaram, 2000; Dilts, 1999; 2000a). The tensile instability problem rarely occurs in fluid dynamics simulations, but can be very severe in solid body computations.

SPH is gaining more and more popularity, and with the continuing improvement and modifications the accuracy, stability and adaptability of the method have reached an acceptable level for practical engineering applications. Moreover, "the harmonic combination between the Lagrangian formulation and particle approximation" (Liu and Liu, 2003) allowed particles to carry material properties; therefore it becomes easier to model flows with complex geometry, free surfaces, discontinuity and large deformation. The Lagrangian nature of SPH allows the grid to be embedded in the material and thus reduces some of the material interface problems associated with Eulerian techniques. Nevertheless, as mentioned before because the motion of SPH particles is similar to liquid or gas flow, therefore those particles can be simulated using the governing equations of hydrodynamics (Liu and Liu, 2003).

3.7.1 SPH concept

SPH is an integral interpolation method to approximate values and derivatives of continuous field quantities by using discrete sample points (Gingold and Monaghan, 1977). The key characteristics employed to solve problems in SPH as reported by Liu and Liu (2003) are:

- **Domain discretisation**: the entire problem domain in the physical space is discretised into a finite number of macroscopic volumes of fluid. Each macroscopic volume fluid

is represented by a particle in SPH. These particles possess individual material properties and move according to the governing conservation equations.

- **Kernel approximation**: Each particle, say particle '*a*' as illustrated in the Figure 3.8, carries the field variables such as the mass m_a, density ρ_a, pressure P_a, velocity v_a, position r_a, temperature (T_a), internal energy (ϵ_a), colour (c_a) and any other quantities depending on the nature of the flow and of the fluid. The mass is constant through the simulations, however, the other physical quantities are updated every time step. These field variables are represented by integral functions, the so-called kernel functions.

- **Particle approximation**: The kernel is further approximated using particles, by replacing the integration in the integral representation of the field variable and its derivatives with summations over all the corresponding values at the neighboring particles in a local domain called the support domain. This means that any physical property can be obtained by summing the same property of particles that lie within the support domain Ω. This part is very important in terms of computational effort; for instance, problems with large deformation that require a huge number of particles could take unacceptably long CPU time to solve.

- **Adaptive:** The particle approximation is performed every time step and the contributions of the particles depend on their current locations.

- **Lagrangian:** The particle approximation is performed on all terms related to field variables to produce a set of ordinary differential equations (ODEs) in a discretized form with respect to time.

3.7.2 SPH support domain

The support domain for a particle '*a'* is the domain where all the information for all particles inside this domain is used to determine the information at the point '*a'* (see Figure 3.8). This means that any physical property of a particle '*a'* can be obtained by summing the same property of particles that lie in the support domain Ω within a radius *ch* of the observed particle *'a'* and multiplying the sum by a smoothing function, where *c* is a scaling constant related to the smoothing function (usually equal to 2). The smoothing length *h* is usually

small for a high density region and large for a low density one; on average the support domain should have 30-80 neighboring particles within the smoothing volume (Kalssen, 2002).

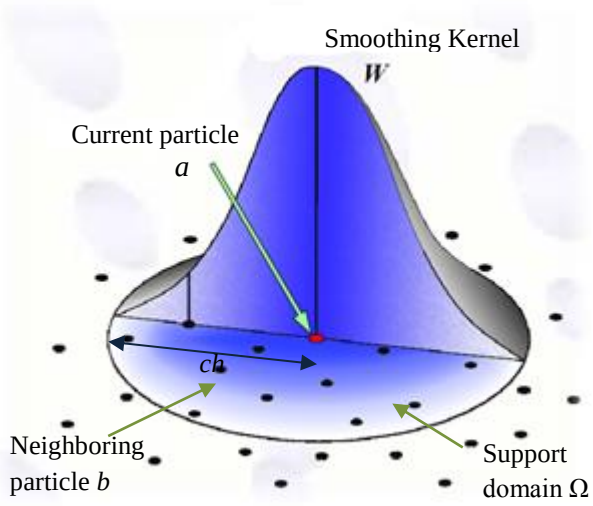

Figure 3.8: Distribution of physical properties of a particle

The smoothing radius *ch* is a key parameter in the SPH approximation. It defines the distance within which particles interact with each other or, in other words, the distance with a non-zero value of the smoothing kernel (the so-called support domain of the kernel). The value of the constant *c* is determined by the choice of the smoothing kernel. For a common case with *c* = 2, particles separated at a distance greater than two smoothing radii will have no influence on the parameters at the current particle. This is exactly correct when the value of the smoothing function is zero, if the distance to the neighboring particle is greater than or equal to *2h*.

Figure 3.8 shows the support domain of particle '*a*' and all the neighbouring particles that lie in the support domain. Particles which are closer to the centre have greater contribution to the property unlike particles outside the influence domain that have no contribution at all, the influence area of each particle will be therefore defined using the kernel function.

There are two main steps in the SPH formulation:

- Kernel approximation which includes the integral representation of a function and its derivatives.

- Particle interpolation or approximation.

3.7.3 Kernel approximation

SPH provides a concept to approximate the spatial derivative using particles, which therefore makes computing the spatial derivatives in particle-based method as easy as in the grid-based methods. SPH is based on integral interpolation; for instance, a continuous quantity $f(\mathbf{x})$ over a space Ω can be written as the convolution of the quantity and Delta function

$$f(\mathbf{x}) = \int_{\Omega} f(\mathbf{x}') \, \delta(\mathbf{x} - \mathbf{x}') \mathrm{d}\mathbf{x}' \tag{3. 24}$$

where Ω is the volume of the fluid domain, $\mathrm{d}\mathbf{x}'$ an elementary volume, and $\delta(\mathbf{x} - \mathbf{x}')$ is the Dirac Delta function i.e.

$$\delta(\mathbf{x} - \mathbf{x}') = \begin{cases} 1 & \mathbf{x} = \mathbf{x}' \\ 0 & \mathbf{x} \neq \mathbf{x}' \end{cases} \tag{3. 25}$$

The Delta function is approximated with the so-called smoothing kernel function *W* of limited support *h*

$$f(\mathbf{x}) \approx \int_{\Omega} f(\mathbf{x}') W(\mathbf{x} - \mathbf{x}', h) \, \mathrm{d}\mathbf{x}' \tag{3. 26}$$

W should be differentiable, normalised, and should converge to the Delta function.

3.7.4 Properties of the Kernel

- Normalisation condition

$$\int_{\Omega} W(\mathbf{x} - \mathbf{x}', h) \mathrm{d}\mathbf{x}' = 1 \tag{3. 27}$$

- Delta function property when the smoothing length *h* tends to 0 (Lucy, 1977)

$$\lim_{h \to 0} W(\mathbf{x} - \mathbf{x}', h) = \delta(\mathbf{x} - \mathbf{x}') \tag{3. 28}$$

- Compact support which means it is equal 0 outside the region *ch*

$$|\mathbf{x} - \mathbf{x}'| \leq ch \tag{3. 29}$$

where *c* is a scaling factor to normalise the kernel function.

3.7.5 SPH kernel

The choice of the kernel (or the smoothing function) plays a very important role in the SPH approximations, as it determines the accuracy of the function representation and the efficiency of the computation, as stated by Liu and Liu, 2003. Generally, the kernels can be divided into four categories based on the shape of kernel: bell shaped, parabolic shaped, hyperbolic shaped, or double hump. Figure 3.9 shows a sample for each of these kernels and their derivatives.

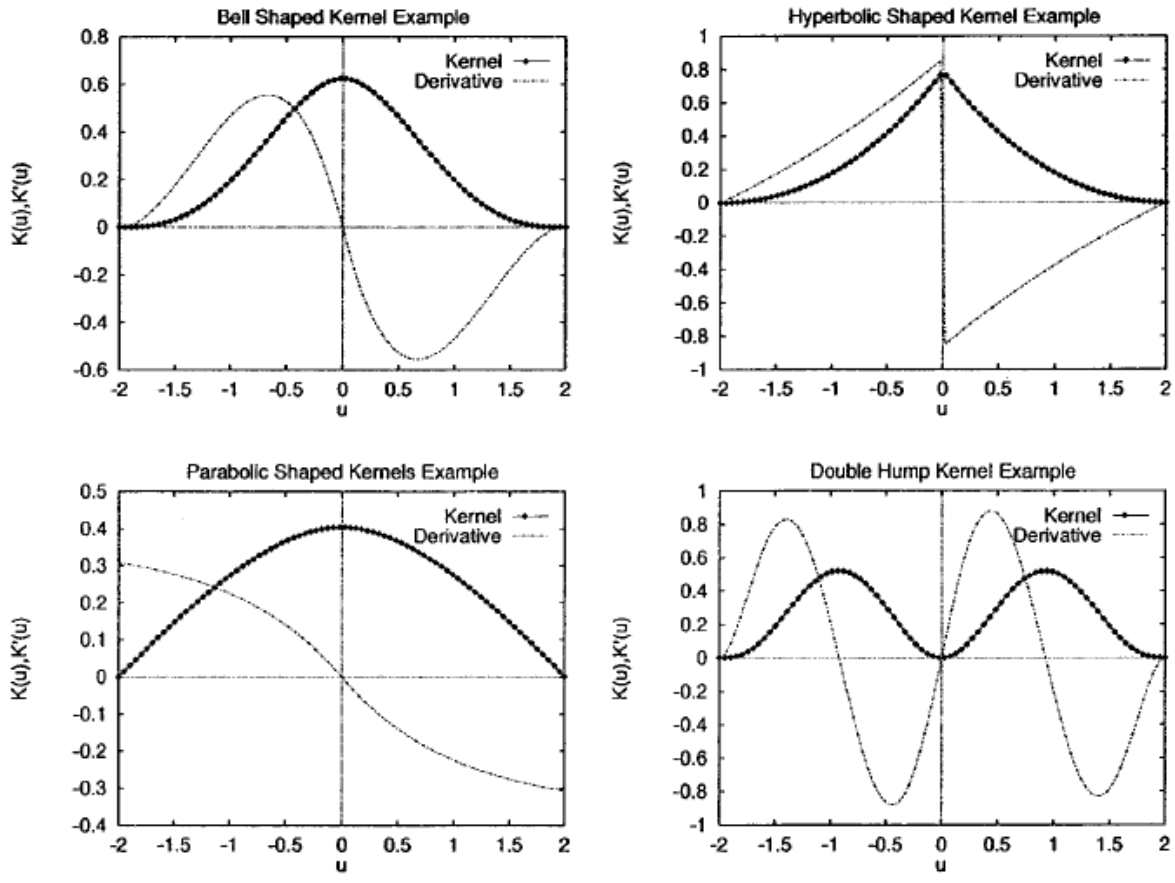

Figure 3.9: General shapes of kernels studied (After: Fulk and Quinn, 1996)

Amongst 20 different kernels used for analysing a hydrodynamic smooth test case and the classic Riemann shock tube test case, Fulk and Quinn (1996) show the tendency of bell

shaped kernel to outperform the other shapes in regions of smooth data. A wide range of kernel functions have been discussed in literature, ranging from Gaussian to polynomial functions and can be found in (Liu and Liu, 2003)). In the next paragraph, only the most common kernels will be reported.

Gaussian kernel: Although it is a very stable and accurate kernel, it is not really compact and therefore computationally more expensive since it needs a longer distance for the kernel to approach zero. Equation (3.30) represents the Gaussian kernel function.

$$W\left(\mathbf{x}-\mathbf{x}',h\right)=\begin{cases}\dfrac{1}{\sqrt{2\pi}h}e^{-\frac{\mathbf{x}^2}{2h^2}} & 1d\\ \dfrac{1}{2\pi\, h^2}e^{-\frac{\mathbf{x}^2+\mathbf{y}^2}{2h^2}} & 2d\\ \dfrac{1}{\left(\sqrt{2\pi}h\right)^n}e^{-\frac{|\mathbf{x}|^2}{2h^2}} & nd\end{cases} \qquad (3.30)$$

where d is the dimension, and h is the width of the Gaussian kernel.

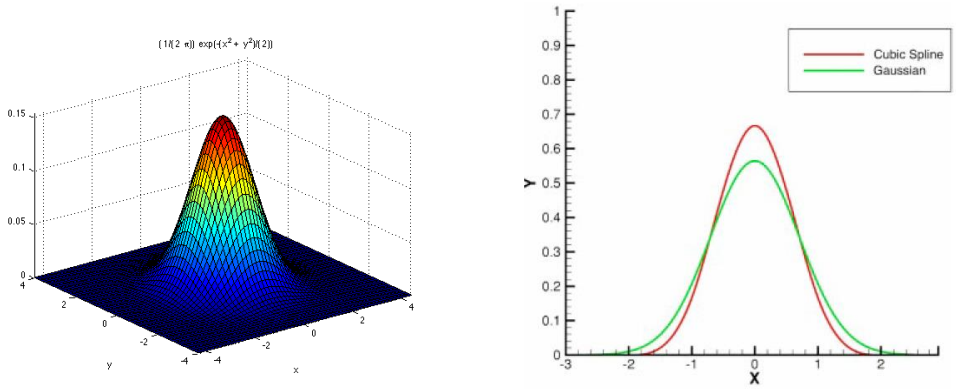

Figure 3.10: Gaussian and cubic spline shape functions (After: Li and Liu, 2002)

Figure 3.10 illustrates the Gaussian and the cubic spline functions; these functions look similar but the cubic spline function shows more compact support as compared with the Gaussian function.

Cubic-Spline kernel: "the cubic-Spline kernel" shown in Figure 3.10 resembles the Gaussian kernel except that the compact support is much narrower. In the spline kernel function (Equation (3.31) and Figure 3.11), the outer edges are well defined at a distance *h* from the particle, therefore everything outside these edges is ignored while in the Gaussian kernel the region of influence of each particle tends to infinity, which means more computational time.

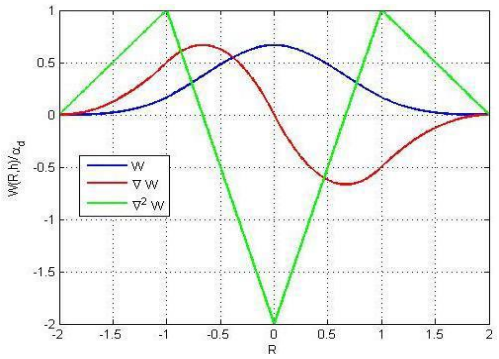

Figure 3.11: Cubic spline and its derivatives

$$W\left(\mathbf{x}-\mathbf{x}',h\right)=\frac{c}{h^d}\begin{cases}1-\frac{3}{2}\zeta^2+\frac{3}{4}\zeta^3 & if\ \ \xi\le 1\\ \frac{1}{4}\left(2-\zeta\right)^3 & if\ 1<\xi\le 2\\ 0 & if\ \ \xi>2\end{cases};\qquad \zeta=\frac{\left\|\mathbf{x}-\mathbf{x}'\right\|}{h} \tag{3. 31}$$

where *d* is the number of dimensions of the problem, *c* is a scaling factor to normalise the kernel function, and *h* the length parameter which has a similar interpretation to the element size in the finite element method.

The quartic spline: Morris (1994) introduced a higher order kernel "The quartic spline" (Equation (3.32)) which tends to be more stable and closely approximates the Gaussian kernel previously introduced.

$$W\left(\mathbf{x}-\mathbf{x}',h\right)=c\begin{cases}\left(\zeta+2.5\right)^4-5\left(\zeta+1.5\right)^4+10\left(\zeta+0.5\right)^4 & 0\le\zeta<0.5\\ \left(2.5-\zeta\right)^4-5\left(1.5-\zeta\right)^4 & 0.5\le\zeta<1.5\\ \left(2.5-\zeta\right)^4 & 1.5\le\zeta<2.5\\ 0 & \zeta\ge 2.5\end{cases} \tag{3. 32}$$

where *c* is a scaling factor.

3.7.6 Particle interpolation

Particle approximation in SPH involves discretising the entire domain problem into a limited number of particles *N*, and then approximately calculating all the field variables on these particles. First, the infinitesimal volume $d\mathbf{x}'$ at the location of particle '*b*' can be approximately replaced by the finite volume of the particle V_b where $V_b = \frac{m_b}{\rho_b}$. This inclusion of density ρ_b and mass m_b makes SPH the ideal numerical solution to simulate dynamic fluid flow applications such as the flow of self-compacting concrete. Then, the continuous integral in Equation (3.26) can be converted to a discretized form of summation over all the particles *N* in the support domain Ω. A quantity $f(\mathbf{x})$ at an arbitrary position **x** is approximated using quantities f_b at sample positions $\mathbf{x}_b$. The kernel function *W* realizes a diminishing influence of particles at larger distances.

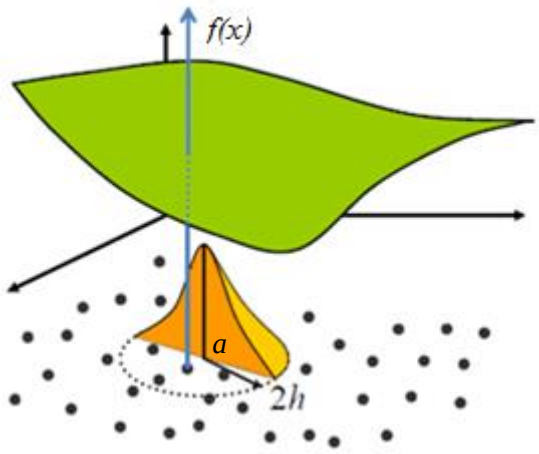

Figure 3.12: particle approximation of function *f(x)*

Therefore, the continuous integral in Equation (3.26) can be expressed in the equivalent forms of discretized particle approximation

$$f(\mathbf{x}) = \sum_{b=1}^{N} m_b \frac{f(\mathbf{x}_b)}{\rho_b} W(\mathbf{x} - \mathbf{x}_b, h) \tag{3. 33}$$

$$f(\mathbf{x}) = \sum_{b=1}^{N} V_b f(\mathbf{x}_b) W_b(\mathbf{x}) \tag{3. 34}$$

The differential of this function is given by

$$\nabla f(\mathbf{x}) = \sum_{b=1}^{N} V_b f(\mathbf{x}_b) \nabla W_b(\mathbf{x}) \tag{3. 35}$$

where the quantity $\nabla W_b(\mathbf{x})$ denotes the gradient of the kernel, which is taken as centred on the position of particle *a* (Figure 3.12). Equations (3.34) and (3.35) state that the value of any function (or its differential) at any position is approximated using the average of the values of the function at all the particles within the support domain (particles *b=1,2,…N*) of that particle weighted by the smoothing function $W_b(\mathbf{x})$.

The application of Equation (3.34) to compute the approximate value for the density of a continuum leads to the classical SPH equation

$$\rho(\mathbf{x}) = \sum_{b=1}^{N} m_b W_b(\mathbf{x}) \tag{3. 36}$$

3.7.7 Corrected SPH integration

The basic SPH approximations as given by equation (3.34) and (3.35) do not accurately reproduce or approximate the function $f(\mathbf{x})$ and its derivative $\nabla f(\mathbf{x})$ (see Appendix B). Therefore corrected SPH equations have been developed to address these issues (Bonet and Lok, 1999; Bonet and Kulasegaram, 2000). The main aim of the correction techniques is to satisfy the conservation of angular momentum which, unlike the linear momentum, is not automatically satisfied. In order to correct the SPH algorithms, some work was done on the gradient of the kernel directly (Bonet and Lok, 1999), whereas others have modified the kernel function itself (Li and Liu, 1996). Another possible way is to mix the kernel and gradient corrections (Bonet and Lok, 1999; Bonet and Kulasegaram, 2000).

Using the corrected gradient of the corrected kernel, the SPH equations (3.34) and (3.35) can be rewritten as

$$f(\mathbf{x}) = \sum_{b=1}^{N} V_b f(\mathbf{x}_b) \tilde{W}_b(\mathbf{x}) \tag{3. 37}$$

$$\nabla f(\mathbf{x}) = \sum_{b=1}^{N} V_b f(\mathbf{x}_b) \tilde{\nabla} \tilde{W}_b(\mathbf{x}) \tag{3. 38}$$

where $\tilde{W}_b(\mathbf{x})$ indicates that the kernel function is corrected to satisfy the consistency conditions (Appendix B), and '*b*' is the neighbouring particle within the support domain. Further, $\tilde{\nabla}$ above indicates that the gradient is corrected to reproduce linear consistency (Appendix B). The gradient correction used here is adopted from the mixed kernel and gradient correction to avoid unnecessary computational efforts. More details about this corrected SPH integration will be found in Appendix B.

3.7.8 Nearest neighbour search

In SPH, it is very important to know particles that interact with each other. In other words, when dealing with a specific particle *'a'*, a list of the entire neighbourhood particles should be defined at each time step. This neighbour particle search is the most computationally expensive part of the simulation (Bayraktar et al., 2009), therefore special care should be taken to reduce the time needed at this step. Many methods have been implemented to ensure an adequate way for neighbourhood search. For instance, (Wróblewski et al., 2007) compared two methods of neighbourhood search for the SPH algorithm, the Constant Cut-off Radius method and the Constant Number of Neighbours; the simulation results obtained by both methods are practically indistinguishable, while the computational costs favour Constant Cut-off Radius. Many other methods have been also reported such as Bucket Sort Algorithm method (Monaghan and Lattanzio, 1985), All Pair search and Linked-List methods (Liu and Liu, 2003). The method adopted here is the Alternative Digital tree (ADT) which was used by Bonet and Peraire (1991) and shown to be efficient for 3D problems.

3.7.9 Treatment of boundary conditions

In SPH, boundary conditions should be imposed to ensure balancing the inner particle forces thus preventing those particles from penetrating the wall. A range of methods is available in literature to impose boundary conditions in SPH method, e.g. repulsive forces (Monaghan et al., 1994), mirror particles (Takeda et al., 1994; Cummins and Murray, 1999) and dummy particles (Dalrymple and Knio, 2001; Shao and Lo, 2003; Lee et al., 2008; Amini et al., 2011). Figure 3.13 illustrates each of these three methods.

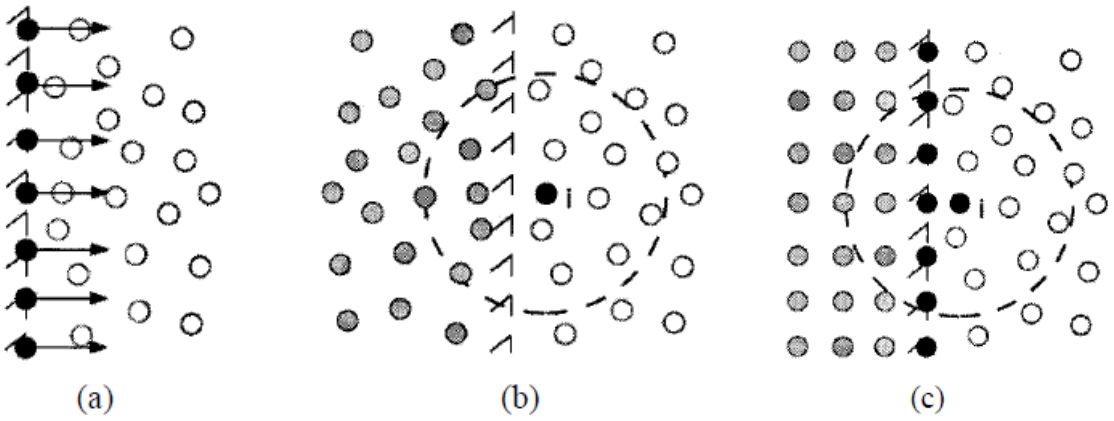

Figure 3.13: Solid boundary treatment: (a) Repulsive force, (b) Mirror particles and (c) Dummy particles. (After: Stamatelos and Anagnostopoulos, 2008)

Repulsive forces: Monaghan (1994) suggested that adding one layer of particles will be enough to represent the boundary conditions, and those particles exert high fictitious repulsive forces to prevent fluid particles penetrating walls (Zheng and Duan, 2010). Although this method is easy to implement its drawback is lack of accuracy when representing the interaction between solid and fluid (Amini et al., 2011).

Mirror particles can be placed either symmetrically or asymmetrically to fluid particle positions with a non-zero velocity. Cummins and Murray (1999) represented boundaries as a set of particles with velocity equal to the velocity of fluid particles but with opposite direction, i.e. $v_{fluid} = -v_{gost}$; the disadvantage of this method becomes obvious when dealing with curved or sharp cornered boundaries, because there will be a variation in density as a result of the homogeneous spacing between the particles being compromised (Robinson, 2009).

Dummy particles: In order to prevent particles from slip, it is necessary to impose non-slip boundary conditions. Dalrymple and Knio (2001) added several layers of fixed particles which are identical to the moving ones but with zero velocity. They proved by tests that only two rows are sufficient to maintain the boundary condition needed. Shao and Lo (2003), with their popular approach, indicated that boundaries in dummy particles could be represented by 4 lines of static particles. The velocity of these particles is set to be zero representing non-slip boundary conditions.

This easy approach does not need any extra computational or programming steps especially when dealing with irregular boundary contours. Pressure at these fixed particles is identical to the pressure on the particle edges and normal to the wall surface. What is important about these fixed particles is that they can satisfy all the fluid flow equations (momentum and continuity equations), but they retain their positions at the end of the loop if the problem involves a fixed boundary, or they change their positions in a prescribed manner if the boundary is moving, for instance at a gate (Amini et al., 2011). Dummy particles may not give an accurate representation of the wall boundaries with some difficult geometrical shapes, but an increase in the number of dummy particles should improve the accuracy.

Surface particles: In this situation the number of neighboring particles will be smaller since the support domain is truncated as shown in Figure 3.14 and the pressure on surface particles should be atmospheric pressure (Lee et al., 2008).

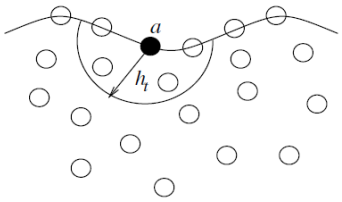

Figure 3.14: Free surface particles (Lee et al., 2008)

3.7.10 Incompressibility and weak compressibility in SPH approach

Enforcing incompressibility in SPH can be pursued using two different approaches - the weakly or quasi-compressible SPH will be referred to as WCSPH (Monaghan, 1994; Lee et al., 2008) and the truly incompressible SPH as ISPH (Kulasegaram et al. (2011). Although both strategies achieve the incompressibility, each one has got advantages and drawbacks.

3.7.10.1 Weak or quasi-compressibility in the SPH (WCSPH)

Monaghan (1994) proposed to treat a real fluid as a weakly compressible material. This approach leads to the replacement of a real fluid by an artificial quasi-compressible fluid having a small, user-defined, fluctuation in the density. His idea was very popular in many applications because it was easy to implement; the time-consuming solution of the Poisson equation can be avoided (Becker and Teschner, 2007), and the diffusion term can be fully calculated explicitly (Valizadeh et al., 2008). However, this method has some drawbacks as pointed out by Lee et al. (2008) related to the small time step associated with a numerical speed of sound which must be at least 10 times larger than the maximum velocity to reduce the density fluctuation down to 1%; a small density error always remains, causing significant, non-physical pressure fluctuations which can lead to numerical instability. Using WCSPH, as shown later in Figure 3.15, the fluid pressure can be obtained using the equation of state described by Bachelor (1967) for sound waves and modified by Monaghan (1994) to suit the simulation of bulk fluid flow

$$P = B\left(\left(\frac{\rho}{\rho_0}\right)^{\gamma} - 1\right) \tag{3. 39}$$

where γ is a power coefficient and depends on material property and ρ_0 is the reference density. To determine the constant *B* which governs the relative density fluctuation $\frac{|\Delta\rho|}{\rho_0}$ with $\Delta\rho = \rho - \rho_0$, Becker and Teschner (2007) show that the compressibility effects (the density variation in fluid flow) scale with $\propto M^2$ where $\boldsymbol{M}$ denotes the Mach number of flow, this results in the following relation

$$\frac{|\Delta\rho|}{\rho_0} \propto \frac{|v_f|^2}{c_s^2} \tag{3. 40}$$

where v_f is the speed of fluid flow, and c_s is the speed of sound in the fluid; the speed of sound is assumed to be large enough such that $\frac{|v_f|^2}{c_s^2}$ is typically 0.01 allowing the density variations of order of 1%. To enforce this condition, B is chosen as

$$B = \frac{\rho_0 c_s^2}{\gamma} \tag{3. 41}$$

Due to the power coefficient γ, small density fluctuations lead to large pressure fluctuations. The scheme is first order and fully explicit in time (Lee et al., 2008). The velocity is calculated from the momentum equation (Equation (3.17)) as

$$\mathbf{v}^{n+1} = \mathbf{v}^{n} + \left(-\frac{1}{\rho}\nabla P^{n} + \frac{1}{\rho}\nabla.\boldsymbol{\tau} + \mathbf{g} \right)\Delta t \tag{3. 42}$$

where superscripts ^{n} and $^{n+1}$ indicate, respectively, present and next time steps and Δt is the numerical time step. The position and density are updated at the next time step by

$$\mathbf{x}^{n+1} = \mathbf{x}^{n} + \mathbf{v}^{n+1}\Delta t \tag{3. 43}$$

From the continuity equation (Equation (3.5))

$$\rho^{\mathbf{n+1}} = \rho^{\mathbf{n}} - \rho^{\mathbf{n}}(\nabla.\mathbf{v}^{n+1})\Delta t \tag{3. 44}$$

Finally, the pressure is obtained from Equation (3.39) with the updated density.

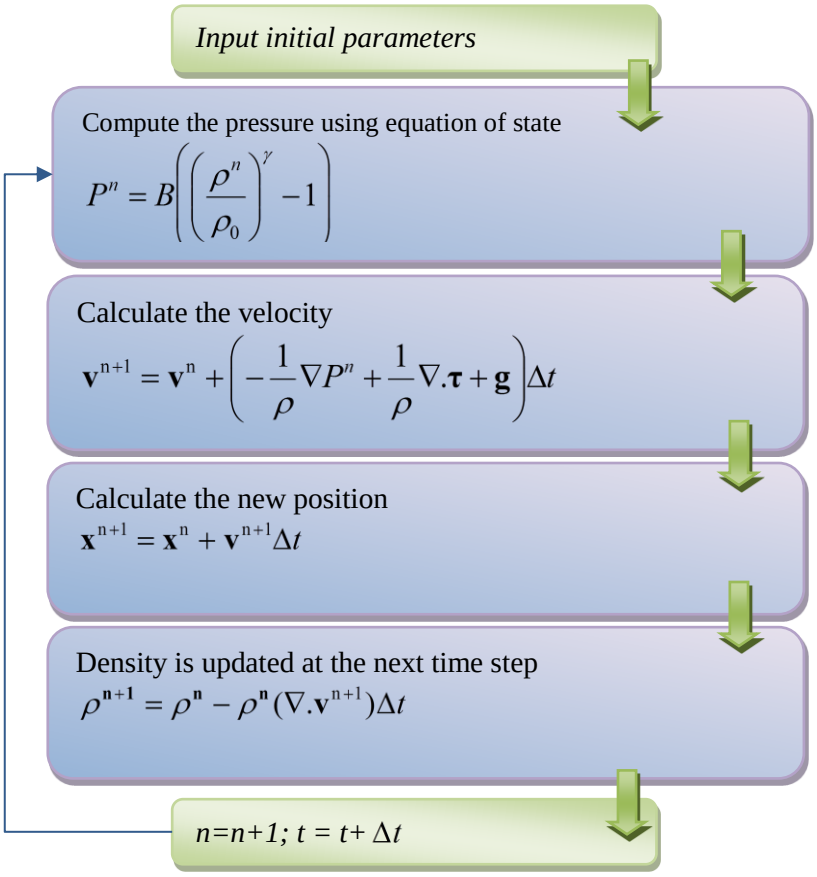

Figure 3. 15: Flow chart of quasi-compressible solution of the governing equations of the fluid flow

3.7.10.2 True incompressibility in SPH (ISPH)

The problems associated with the use of WCSPH can be circumvented by implementing ISPH. In ISPH, the pressure and velocity will be computed separately. Pressure can be solved implicitly using the Poisson equation (Shao and Lo, 2003; Kulasegaram and Karihaloo, 2013). Implementing the incompressible SPH approach is based on the prediction-correction time stepping scheme as illustrated in Figure 3.16. Further details will be provided in Chapter 5.

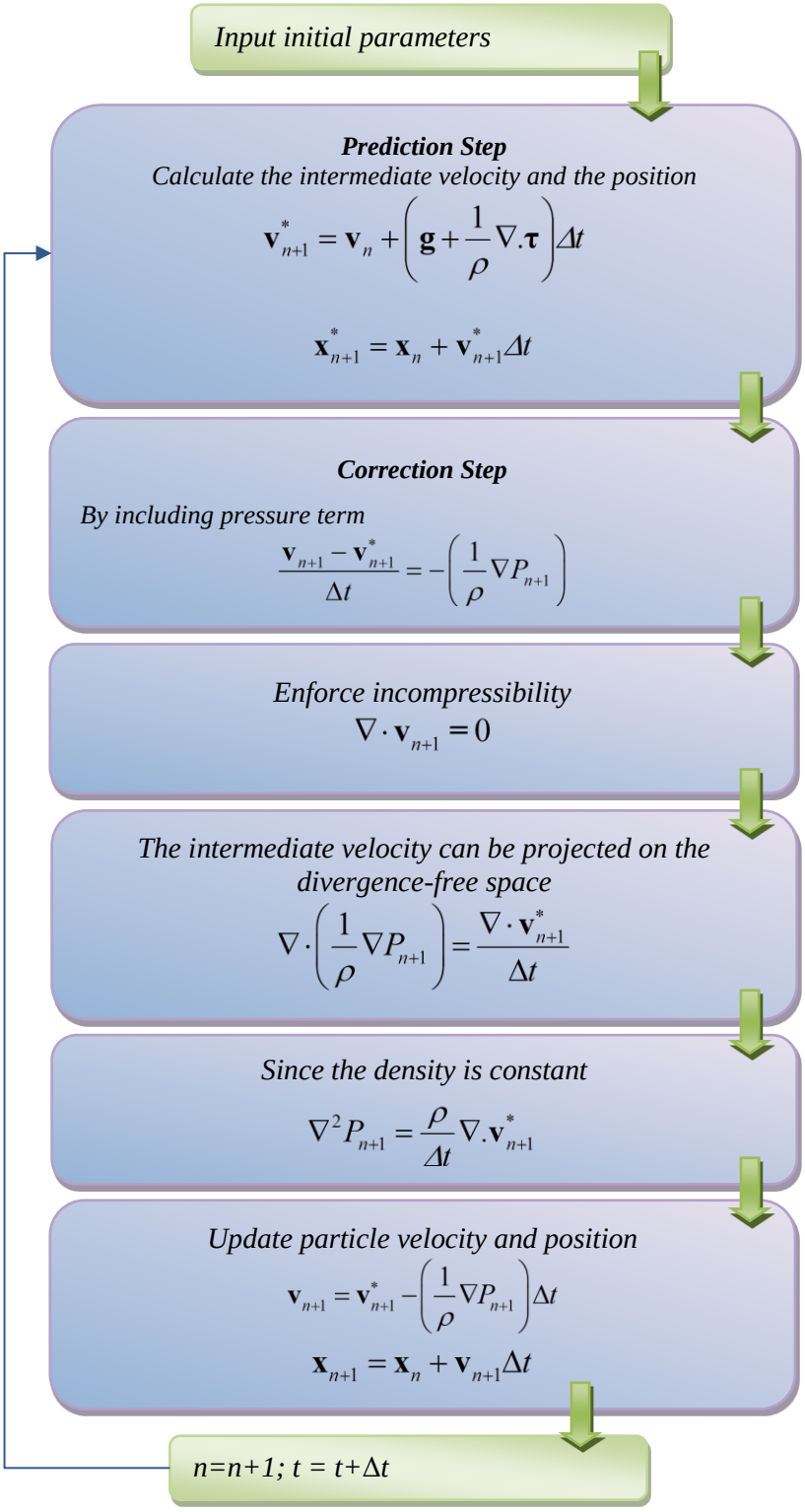

Figure 3.16: Flow chart of truly compressible solution of the governing equations of the fluid flow

3.8 Concluding remarks

Computational modelling of fresh self-compacting concrete flow is increasingly becoming of great interest for the researchers and the construction industry. The behaviour of concrete in its plastic form has a significant effect on the durability and strength of a structure and it is necessary to optimize the casting procedure, mix design through proportioning, predicting the total form filling and detailed flow behaviour such as particle migration and distribution throughout the flow, fibre re-orientation and distribution in the formwork.

We have described in this chapter the present status regarding computational modelling of fresh concrete flow. A review of SPH as a suitable method to model the flow behaviour of SCC has been given in detail. Through continuous modifications and improvement of SPH an acceptable level of accuracy and stability can be attained to meet all the practical engineering applications. Moreover, the adaptability of SPH, its simplicity, and Lagrangian nature make it more attractive to deal with the heterogeneous flow of SCC with and without fibres as compared with any other method.

An appropriate computational strategy using SPH method will be presented in Chapter 5 to simulate the flow behaviour of self-compacting concrete in different configurations and geometrical shapes. The same strategy will be used in Chapter 6 as a tool to simulate the flow of SCC mixes with fibres with a view to estimating the fibre orientation factor (FOF) in a cross section perpendicular to the principal direction of flow. Finally, the simulation will be used in Chapter 7 as a practical aid in the proportioning of SCC mixes that may contain coarse aggregates or/and short steel fibres.

Chapter 4

Development of self-compacting concrete mixes

4. 1 Introduction

The ideal design of a self-compacting concrete (SCC) mix is a compromise between two conflicting objectives. On the one hand, the SCC has to be as fluid as possible to ensure that it will fill the formwork under its own weight, but on the other, it has to be a stable mixture to prevent segregation of solids during the flow (Su et al., 2004; Roussel, 2007; Spangenberg et al., 2010). The former is ensured by using super-plasticiser and/or viscosity modifying admixtures, while the latter is achieved through the selection of the right amount and type of powders i.e. cement and cement replacement materials (CRM) and by striking the right balance between the solids and liquids in the mix.

The addition of steel fibres improves the mechanical properties and the ductility of SCC in much the same manner as in vibrated concrete. However, the fibres greatly impair the workability of SCC because of their elongated shape and large surface area. The amount of fibre that can be added to a SCC mix is therefore limited and depends on the fibre type used and the composition of the SCC mix. The maximum amount of fibre needs to be determined in such a way as to cause the least decrease in the workability, whilst maintaining good flow and passing ability. In order to make the best use of the fibres, they need to be homogeneously distributed in the mix without clustering (Grünewald and Walraven, 2003).

This Chapter describes the steps taken to develop self-compacting concrete (SCC) mixes of varying strengths and performance, with and without steel fibres. The aim is to investigate how the proportions of solids and liquids, the amount of super-plasticiser, and the steel fibres need to be selected in order to produce SCC mixes with the right flow and passing ability. For the self-compacting concrete mixes without steel fibres the fulfilment of the flow and cohesiveness criteria are sufficient for the mix design. However, for the design of self-compacting concrete mixes with steel fibres, they must additionally meet the passing ability criterion.

The plastic viscosity of the SCC mixes so developed will then be estimated by the micromechanical procedure described by (Ghanbari and Karihaloo, 2009). This plastic viscosity, together with the yield stress of the mix, is needed in the numerical simulation of SCC flow in moulds of different shapes and sizes.

The first part of this chapter has been published in the journal ‘Magazine of Concrete Research’ (see publication 4 in the list in Chapter 1), while the second part of this Chapter

has been published in the journal 'Cement and Concrete Composites' (see publication 2 in the list in Chapter 1).

4. 2 Experimental program flow-chart

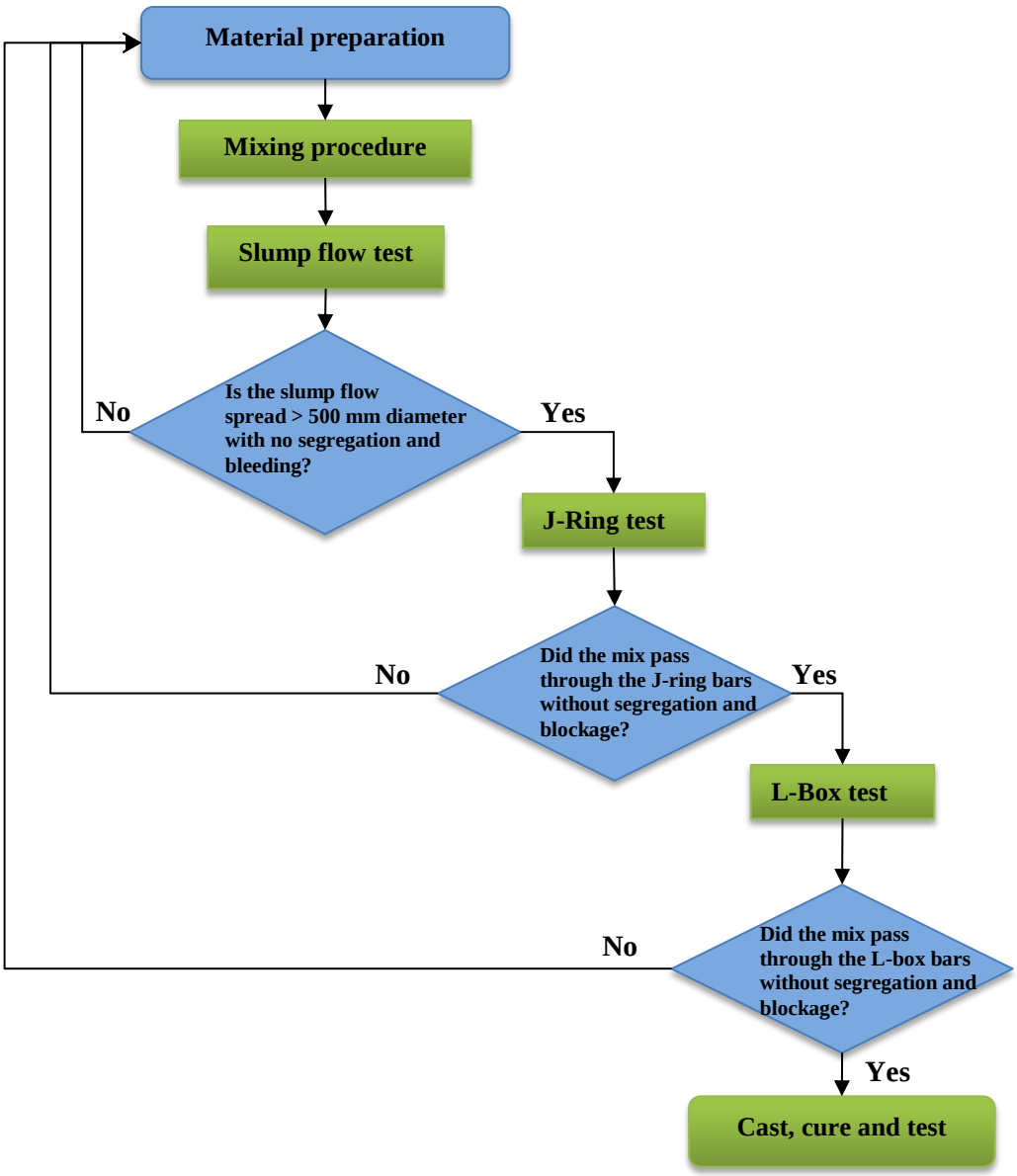

Figure 4.1: Experimental program flow chart

4. 3 Development of SCC base mixes with and without fibres

4.3.1 Self-compacting normal and high-strength concrete

An extensive laboratory investigation was conducted to produce different grades of self-compacting normal and high-strength concrete mixes (with nominal 28 day cube characteristic compressive strengths of 35 MPa, 45 MPa, 60 MPa, 80 MPa and 100 MPa) that on one hand were as fluid as possible to ensure that they filled the formwork under their own weight, passed through congested reinforcement cages without blockage, and on the other were stable to prevent segregation of solids during the flow. This investigation followed the traditional trial and error approach, using the slump cone test, J-ring test and L-box test on trial mixes, until the mix that met the flow-ability and passing ability criteria and had no visible signs of segregation according to the Code (BS EN 206-9, 2010) was found.

Although the mix proportions of vibrated mixes of the same compressive strength made in the same laboratory are available, we shall use only two of those vibrated mixes (40 MPa and 100 MPa vibrated mixes) to develop the full range of SCC mixes. However, later we shall compare the SCC mixes so developed with the corresponding vibrated mixes.

4.3.1.1 Mix preparation

The trial mixes were prepared in a planetary mixer by mixing the coarsest constituent (coarse aggregate) and the finest one (GGBS and/or micro-silica), followed by the next coarsest (sand) and next finest constituent (cement), and so on. Before each addition, the constituents were mixed for 2 minutes. To fluidize the dry mix, two-thirds of the super-plasticiser (SP) was added to the water. One-half of this water-SP mixture was added to the dry constituents and mixed for two minutes. One-half of the remaining water-SP mixture was then added and mixed for two minutes. This process was continued until all water-SP mixture was added. The remaining one-third of the SP was added and mixed for two minutes just before transferring the SCC mix into the slump cone. The horizontal spread up to 500 mm was timed. If any segregation was visible, the mix proportions were judiciously altered. This trial process was continued until the mix met the flow-ability criterion (BS EN 206-9, 2010) and was homogeneous with no visible segregation or bleeding. In this manner, all self-compacting normal and high-strength concrete mixes were developed.

The mix proportions of these mixes are shown in Table 4.1 and Table 4.2 below. The binder refers to cement plus GGBS and /or micro-silica.

4.3.1.2 Normal strength concrete

The trial mixes for normal strength concrete with 28-day cube compressive strengths of 35, 45 and 60 MPa (mixes 1, 2, and 3 in Table 4.1) were proportioned guided by the corresponding 40 MPa vibrated concrete mix proportions produced in the same laboratory and by the ad hoc guidance available in the literature (Chapter 2).

- Part of the cement was replaced by the lighter granulated ground blast furnace slag (GGBS) to increase the paste volume and lubricate the aggregate particles. For the same reason limestone powder (particle size range 0.05-2 mm) was added to all SCC mixes.
- The water to binder ratio was reduced from 0.56 for the 35 MPa mix to 0.5 for the 60 MPa, whereas the super-plasticiser to water ratio was increased from 0.009 for the 35 MPa mix to 0.025 for the 60 MPa SCC mix.
- The sand (particle size range 0.15-2 mm) content was slightly decreased (by 6% to 9%) in the SCC mixes in comparison with the corresponding vibrated mixes.
- The coarse aggregate (crushed limestone without dust, particle size range 4-10 mm), content was decreased by 8% for the 60 MPa mix to 14% for the 35 MPa mix in comparison with the vibrated mix, in order to reduce the inter-particle friction.

The mix proportions of the initial vibrated concrete mix and the normal strength SCC mixes (Mix 1, Mix 2 and Mix 3) are reported in Table 4.1.

Table 4.1. The mix constituents of the initial vibrated concrete mix and the normal strength SCC mixes (Mix 1, Mix 2 and Mix 3)

Constituents	Initial vibrated Mix	Mix 1	Mix 2	Mix 3
Cement (kg)	393	210	230	294
Ground granulated blast furnace slag (GGBS) (kg)	0	151.3	151.9	98
Coarse aggregates (kg)(crushed limestone) <10mm	982.5	839.3	842.6	896.3
Sand (kg)< 2mm	786	713.6	716.4	732.6
Water (kg)	220.1	203.3	210.3	196
Limestone (kg)	0	232	210.3	176
Super-plasticiser/water	0	0.009	0.013	0.025
Water/binder	0.56	0.56	0.55	0.50
Flow spread(mm)	-	710	700	680
t_{500} (sec)	-	2.42	2.65	2.35
t_{200} (sec)	-	0.45	0.51	0.36
t_{400} (sec)	-	0.95	1.04	0.80
Level-off (sec)	-	8.36	9.26	6.80
Compressive strength (MPa)	**40**	**35**	**45**	**60**

In the slump cone test, the time for the SCC mix to spread to a diameter of 500 mm after the cone filled with the mix has been suddenly lifted (t_{500}) was recorded, as well as the diameter of the spread when the flow stopped (BS 12350-8, 2010). The resistance to segregation was checked visually. Figures 4.1 , 4.2 and 4.3 show the horizontal spread of SCC Mix 1, Mix 2 and Mix 3, respectively. All mixes so proportioned fall into the viscosity class 2 (VS2) with $t_{500} \geq 2$ sec which indicates a moderate viscosity of SCC mixes (BS EN 206-9, 2010).

Figure 4.2: Horizontal spread of SCC Mix 1

Figure 4.3: Horizontal spread of SCC Mix 2

Figure 4.4: Horizontal spread of SCC Mix 3

4.3.1.3 Self-compacting high-strength concrete (SCHSC)

The aim of this part of the investigation was to develop a self-compacting counterpart of a high-strength vibrated concrete (with a nominal 28 day characteristic compressive strength of 100 MPa) that had been produced regularly in the same laboratory over many years using naphthalene sulfonate-based super-plasticiser. The mix proportions of this standard vibrated mix are shown in Table 4.2, the binder refers to cement plus micro-silica. To achieve this goal several trial mixes were made and tested as follows:

- The coarse aggregate (crushed limestone without dust, particle size range 4-10 mm) content was decreased by 24% in order to reduce the inter-particle friction and to achieve the desired flow-ability and resistance against segregation.
- Limestone powder (particle size range 0.05-2 mm) was added to increase the paste volume to lubricate the aggregate particles.
- Micro-silica (mean particle size 0.5 micron) content was increased by up to 36%.
- Super-plasticiser was increased from 1.8% to 3.8% by weight of cement.
- The sand (particle size range 0.15-2 mm) content was decreased modestly by 6%.
- The water to binder ratio was reduced from 0.29 to 0.24.

Following the same mix preparation as described in Section 4.3.1.1, the self-compacting high-strength concrete mix (designated Mix 4) shown in Figure 4.5 (left) was developed. The mix proportions of this SCHSC mix are reported in Table 4.2.

Table 4.2. The mix constituents of vibrated high-strength concrete. Mix 4 and Mix 5 are SCHSC mixes. Mix 6 is SCHSFRC mix that achieves both flow-ability and passing ability

Constituents	Initial vibrated Mix	Mix 4	Mix 5	Mix 6
Cement (kg)	500	500	500	500
Micro-silica (kg)	55	75	75	75
Limestone powder	-	200	105	200
Coarse aggregates (kg) (crushed limestone) <10mm	1105	833	990	833
Sand< 2mm	660	700	660	700
Water (kg)	161	138	133.5	138
Fibres (30mm long with crimped ends, volume fraction)	-	-	-	0.5%
Super-plasticiser/water	0.056	0.14	0.12	0.14
Water/(cement+micro-silica)	0.29	0.24	0.23	0.24
Flow spread (mm)	-	805	800	760
t_{500} (sec)	-	2.20	2.88	3
t_{200} (sec)	-	0.35	0.5	1.88
t_{400} (sec)	-	0.76	1.02	5.1
Level-off (sec)	-	7.23	9.20	38
Compressive strength (MPa)	**100**	**80**	**100**	**100**

Tests on specimens at the age of 28 days for Mix 4 reached a compressive strength of 80 MPa. That this mix fell short of the 28-day target compressive strength of 100 MPa is not surprising in view of the fact that the coarse aggregate content was reduced by nearly 24% in order to achieve the desired flow-ability and resistance against segregation.

A small quantity of steel fibres (0.5% by volume of 30mm long Z560 Dramix fibres with crimped ends) was added to the this SCHSC mix without altering any other mix proportions to examine whether it will still satisfy the flow-ability criterion. The fibres, which are supplied by the manufacturer as small flat packs containing more than 40 fibres temporarily held together by water-solvable glue, were added progressively to the wet SCHSC mix (i.e. after all the water-SP mixture had been added and mixed; see Section 4.3.1.1) and mixed until the glue had dissolved and the fibres had dispersed uniformly in the mix. The remaining one-third of the SP was added and mixed for two minutes just before transferring the fibre-reinforced mix into the slump cone. The horizontal spread up to 500 mm was timed at 3 sec, as desired, although the final spread was slightly less than that of the SCHSC without fibres (760 mm against 805 mm). This self-compacting high-strength fibre-reinforced concrete (SCHSFRC) is designated Mix 6 in Table 4.2. Just as the SCHSC, it meets the flow-ability

criterion and is very homogeneous with no visible segregation (Figure 4.6) and reached the target 28 day compressive strength of 100 MPa.

Mix 4 was further modified to develop a new mix with a 28-day compressive strength of 100 MPa without steel fibres. Therefore, a new trial mix was undertaken as follows:

- Coarse aggregate content was increased by 15% to increase concrete strength without any alteration in cement content.
- For the same reason, the water to binder ratio was slightly reduced to 0.23.
- SP to water ratio was modestly reduced.
- Limestone powder and sand contents were also decreased.

These alterations resulted in the SCHSC mix (Mix 5) illustrated in Figure 4.5 (right); the mix proportions of this mix are reported in Table 4.2. It met the flow-ability criterion and showed no signs of segregation. The mix also achieved the target 28-day compressive strength of 100 MPa.

However, not surprisingly, the flow characteristics of the 100 MPa mix achieved with the use of steel fibres (Mix 6) are somewhat sluggish compared to the 100 MPa mix (Mix 5) produced without the use of steel fibres in the sense that the flow times are longer and the plastic viscosity much higher (see Table 4.2).

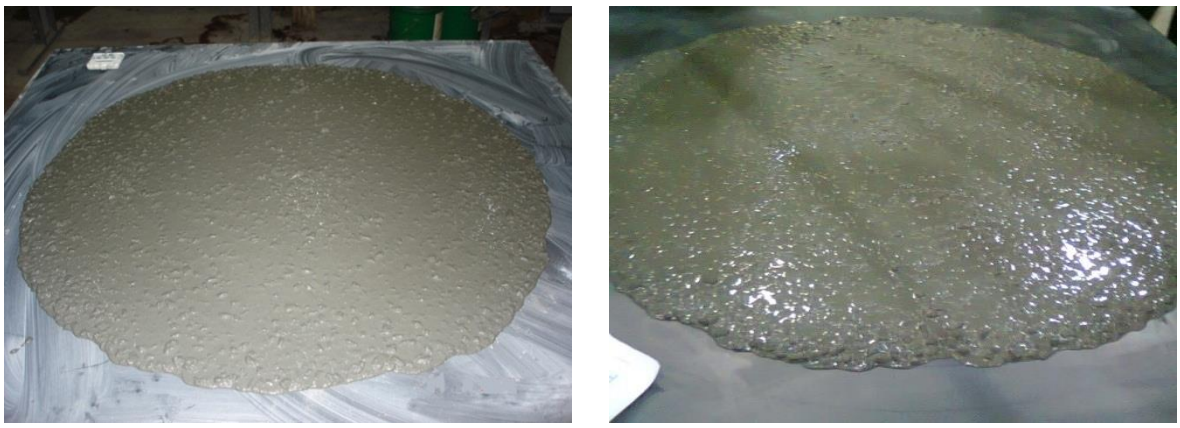

Figure 4.5: Horizontal spread of SCC Mix 4 (left) and Mix 5 (right)

Figure 4.6: Horizontal spread of SCC Mix 6

In this manner the mixes of different grades of SCC concrete were proportioned to meet all the requirements in the fresh state according to (BS EN 206-9, 2010). All mixes so proportioned fall into the viscosity class 2 (VS2) with $t_{500} \geq 2$ sec.

In the development of the above mixes, we found no need to add a viscosity modifying admixture (VMA) to reduce bleeding and blocking or to increase the resistance to segregation.

4.3.1.4 Passing ability test

All the above developed mixes (Mix 1, Mix 2, Mix 3, Mix 4, Mix 5 and Mix 6) that satisfied the flow-ability criterion and showed no signs of segregation, were subjected to the passing ability test using the J-ring and L-box to ensure that they were able to pass through the narrow gaps that exist between reinforcing bars in a real reinforced concrete structural element.

For this purpose, a 300 mm diameter J-ring apparatus with 16 steel rods (each of diameter 16 mm) was used, as recommended by The European Federation of National Trade Associations (EFNRC, 2005). Details of this test were fully described in Chapter 2.

Figure 4.7: Flow and passing ability of SCC Mix 2 (left) and Mix 3 (right)

Figure 4.8: Flow and passing ability of SCC Mix 4

Figure 4.9: Flow and passing ability of Mix 5 (left) and Mix 6 (right)

Mixes that pass the flow-ability test may not necessarily meet the passing ability criterion, especially when large aggregates and fibres are present in the SCC mix. Figure 4.10 shows fibres and large aggregates are nested around the steel rods in an earlier trial version of Mix 6

that had met the flow-ability criterion. In such instances, the paste content had to be increased. The final results of SCHSFRC (Mix 6 shown in Table 4.2) indicated that Mix 6 meets the flow-ability, passing ability and shows no signs of segregation (BS EN 12350-12, 2010). This mix reached the target 28-day compressive strength of 100 MPa.

Figure 4.10: Fibres and large aggregates are nested around the steel rods in an earlier trial version of Mix 6 that had met the flow-ability criterion

All the SCC mixes in Tables 4.1 and 4.2 met the passing ability criterion based on (BS EN 12350-12, 2010), EFNRC (EFNRC, 2005) and PCI (PCI, 2003) recommendations (Figures 4.7- 4.9).

It should be mentioned that slump cone and J-ring tests can be performed by using an upright or inverted cone. We have used both orientations and observed that in the inverted orientation the flow time t_{500} is slightly increased when large coarse aggregates are present. There was no discernible difference when such aggregates were absent, as in the mix of self-compacting ultra-high performance concrete which will be described later in this Chapter (Section 4.3.2).

4.3.1.5 L-box test

In order to test the ability of a SCC mix to fill the formwork containing reinforcement under its own weight, the L-box apparatus with adjustable steel rods (each of diameter 12mm) was used (BS EN 12350-10, 2010; EFNRC, 2005; PCI, 2003). The vertical leg of the L-box is filled with the SCC mix. At the bottom of this leg is a gate with two or three rods in front of it. When the gate is lifted, the mix flows into the horizontal part of the L-box through the gaps between the rods. The times for the mix to reach 200 mm (t_{200}) and 400 mm (t_{400}) from

the vertical leg are recorded, as well as the time it takes the mix to level off in the horizontal leg of the L-box. Again, it is required that no large aggregate particles or fibres be blocked by the rods.

The clearance between the bars when using 2 bars and 3 bars is 59 ∓ 1mm and 41 ∓ 1mm, respectively as illustrated in Figure 4.11.

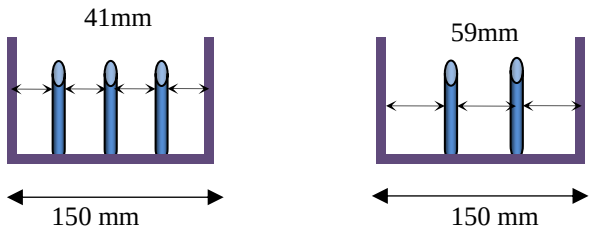

Figure 4.11: Clearance when using 3 or 2 steel rod bars

At least 14 litres (BS EN 12350-10, 2010) of concrete were prepared in a pan mixer and measurements were recorded.

Figure 4.12: Flow and passing ability of SCC Mix 1 (left) and Mix 2 (right)

Figure 4.13: Flow and passing ability of SCC Mix 3 (left) and Mix 4 (right)

Three steel rods were used for SCC mixes (Mix 1, Mix 2, Mix 3) and SCHSC mixes (Mix 4, Mix 5), while for the SCHSFRC mix with 30 mm steel fibres (Mix 6) only 2 rods were used based on the recommendation of (Tviksta, 2000) as wider gaps can be used when fibres are introduced to the mix which should be 1 -3 times the maximum length of fibres used.

Figure 4.14: Flow and passing ability of SCC Mix 5 (left) and Mix 6 (right)

All designated mixes that had passed the J-ring test also passed the L-box test without any alteration. The passing ability of the SCC mixes is evident from Figures 4.12 to 4.14. The

compressive strength of those mixes was measured in the hardened state at 28 days age. The results are reported in Table 4.1 and Table 4.2.

4.3.2 Development of Self-Compacting Ultra High-Performance Fibre-Reinforced Concrete (SCUHPFRC)

In this section, we describe the development of a SCUHPFRC. The base mix is CARDIFRC Mix I (Benson and Karihaloo, 2005a; Benson and Karihaloo, 2005b; Benson et al., 2005). This mix contains a total of 6% by volume of two types of fibre: 6mm (5% by volume) and 13mm (1% by volume) long steel fibres (diameter 0.15 mm). It is a very dense and highly viscous mix and is meant for vibratory compaction. However, the mix without the fibres is highly flow-able and thus has the potential for self-compaction. In the present development for cost, health and safety reasons, the 6% by volume brass-coated thin fibres (0.16 mm diameter) of the original CARDIFRC Mix I, will be replaced by 2.5% by volume of the cheaper 30 mm long steel Z560 Dramix fibres of 0.55 mm diameter. We expect that such a replacement will lead to a reduction in the compressive (200 MPa) and indirect tensile (25 MPa) strengths of the original CARDIFRC Mix I, but not in its toughness. However, as 85% of the cost of the original CARDIFRC Mix I is attributable to the expensive thin brass-coated fibres, we expect the cost of the self-compacting version using the much cheaper Dramix fibres with crimped ends to be substantially reduced, thus making it a highly competitive advanced cement-based construction material that can be used in many situations in which steel is currently the preferred option.

Trial mixes were prepared from the original CARDIFRC Mix I without fibres (for mix proportions, see Table 4.3) by replacing a part of the cement by granulated ground blast furnace slag (GGBS) (33%-37%) and using Glenium ACE333 super-plasticiser instead of the naphthalene sulfonate-based one. Various SP to water ratios (0.15-0.22) were tried to obtain highly flow-able trial mixes. Based on the experience with the SCHSFRC (Mix 6) reported above which contained only 0.5% by volume of the same type of fibres as envisaged in the present SCUHPFRC, it was reasonable to assume that the mix without fibres should have a larger horizontal spread than that of SCHSC, so that by the time 2.5% by volume of 30 mm long Z560 Dramix fibres with crimped ends were added to this mix, it would satisfy the target flow time t_{500} of 3 sec.

Table 4.3. Original CARDIFRC Mix I. Mix 7 and Mix 8 are mix proportions of SCUHPC and SCUHPFRC mixes, respectively meeting the flow-ability, passing ability and resistance to segregation criteria.

Constituents	CARDIFRC Mix I	Mix 7	Mix 8
Cement (kg)	855	543.5	543.5
Micro-silica (kg)	214	214	214
Ground granulated blast furnace slag (GGBS) (kg)	-	311.5	311.5
Limestone	-	-	-
Coarse aggregates (kg) (crushed limestone) <10mm	-	-	-
Sand< 2mm	-	-	-
Quartz Sand (kg)			
9-300 µm	470	470	470
250-600 µm	470	470	470
Water (kg)	188	188	188
Fibres 6mm (diameter 0.16 mm) (kg)	390		
Fibres 13mm (diameter 0.16 mm)(kg)	78		
Fibres (30mm long with crimped ends)(kg)		-	195
Super-plasticiser/water	0.15	0.28	0.28
Water/binder	0.18	0.18	0.18
Flow spread(mm)		910	850
t_{500} (sec)		3	3
t_{200} (sec)		0.3	1.9
t_{400} (sec)		0.75	5.6
Level-off (sec)		0.95	54
Compressive strength (MPa)	**200**	**140**	**160**

The composition of this mix with SP/water ratio of 0.28, designated Mix 7 is given in Table 4.3. The horizontal spread in the cone test is shown in Figure 4.15 (left) reaching a spread of 900 mm, with the spread t_{500} timed at 3 sec. 2.5% by volume of steel fibres were added to this mix. The fibres were evenly distributed in the mixer, as described above, and the resulting SCUHPFRC, designated Mix 8 in Table 4.3 and shown in Figure 4.15 (right), was found to satisfy the flow-ability, passing ability and resistance to segregation criteria , albeit with a reduced final flow spread (850 mm). Visual inspection showed that the fibres were evenly distributed throughout the slump spread.

Figure 4.15: Horizontal spread of SCUHPC Mix 7 (left) and SCUHPFRC Mix 8 (right)

As before, the mixes 7 and 8 were subjected to the passing ability test in the J-ring test apparatus. The mixes without and with fibres, easily and smoothly flowed through the gaps between the steel rods (Figure 4.16 and Figure 4.18). The compressive strength of SCUHPC (Mix 7) and SCUHPFRC (Mix 8) were measured at 140 MPa and 162 MPa, respectively.

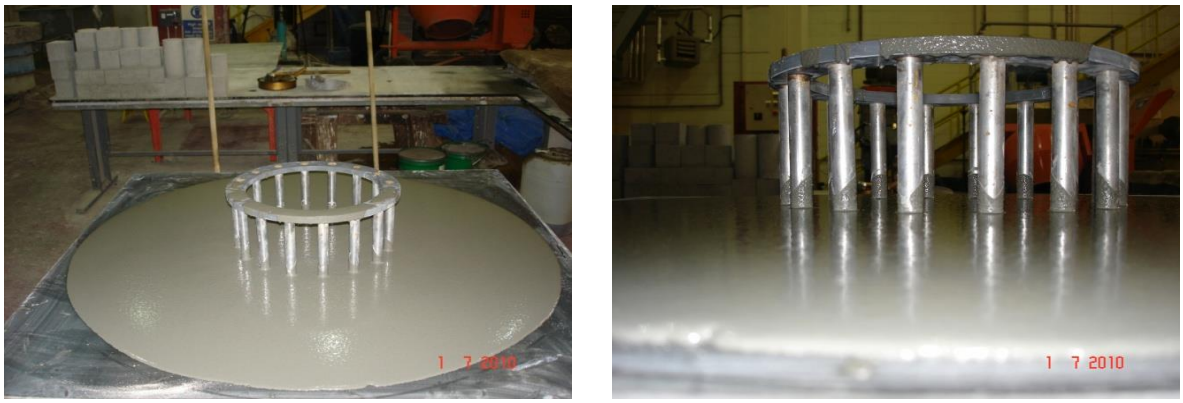

Figure 4.16: SCUHPC Mix 7 flows smoothly through the gaps between the steel rods

Figure 4.17: An earlier version of SCUHPFRC Mix 8 did not satisfy the passing ability test. The fibres are nested around the steel rods as seen clearly in the photo on the right

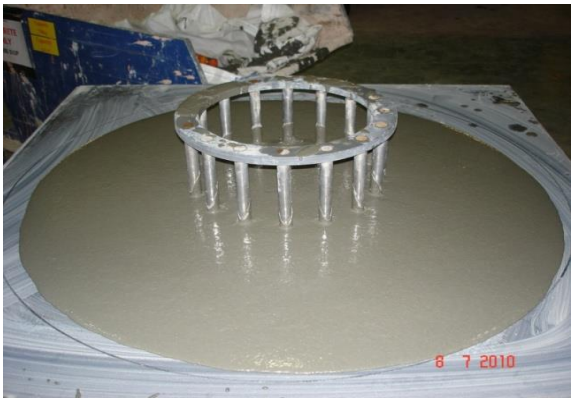

Figure 4.18: Flow and passing ability of SCUHPFRC Mix 8

Figure 4.17 illustrates an earlier version of SCUHPFRC Mix 8 that did not satisfy the passing ability test in the J-ring test. It is clearly seen in the photo how fibres are nested around the steel rods.

Finally, the mixes 7 and 8 were subjected to the passing ability test using L-box test apparatus to test the ability of a SCC mix to fill the formwork containing reinforcement under its own weight. As described before, the vertical leg of the L-box is filled with the SCC mix. When the gate is lifted, the mix flows into the horizontal part of the L-box through the gaps between the rods. Three or two rods were used to test SCUHPC and SCUHPFRC, respectively. The times for the mix to reach 200 mm (t_{200}) and 400 mm (t_{400}) from the vertical leg are recorded, as well as the time it takes the mix to level off in the horizontal leg of the L-box. Again, it is required that no particles or fibres be blocked by the rods

Figure 4.19: Flow and passing ability of SCUHPC (Mix 7)

The mixes without and with fibres flowed easily and smoothly through the gaps between the steel rods as illustrated in Figure 4.19 and Figure 4.20, respectively .

Figure 4.20: Flow and passing ability of SCUHPFRC (Mix 8)

4. 4 Comparison between self-compacting and vibrated concrete mixes

The paste to solids ratios by volume in the above self-compacting concrete (SCC), self-compacting high-strength (Deeb et al., 2012) and self-compacting ultra-high performance mixes (Deeb et al., 2012) (Tables 4.1, 4.2 and 4.3) are compared in Table 4.4 with their counterpart vibrated normal (Taylor, 1997), high strength (Taylor, 1997), and ultra-high performance (Karihaloo, 2012) concrete mixes (VC), ranging in the 28-day compressive strength from 35 to 160 MPa which were all developed in the same laboratory at Cardiff University over many years.

Table 4.4. Comparison of paste to solids ratio by volume between SCC and VC mixes of equal compressive strength (Deeb and Karihaloo, 2013)

Compressive strength (MPa)	35	45	60	80	100	140	162
Paste(SCC)	0.425	0.417	0.403	0.434	0.393	0.646	0.631
Solids(SCC)	0.574	0.583	0.597	0.566	0.607	0.353	0.369
Water/Binder (SCC)	0.56	0.55	0.50	0.24	0.23	0.18	0.18
Paste/Solids(SCC)	0.74	0.717	0.675	0.767	0.646	1.828	1.708
paste(VC)	0.353	0.337	0.316	0.309	0.366	0.628	0.613
Solids(VC)	0.647	0.663	0.684	0.691	0.634	0.371	0.387
Water/Binder (VC)	0.56	0.5	0.44	0.39	0.26	0.18	0.18
Paste/Solids(VC)	0.545	0.509	0.462	0.447	0.576	1.695	1.583

Table 4.4 shows that, for the same compressive strength and almost the same water to binder ratio, the paste to solids ratio in a SCC mix is much higher than in the counterpart vibrated concrete. However, the difference reduces as the strength of the mix increases.

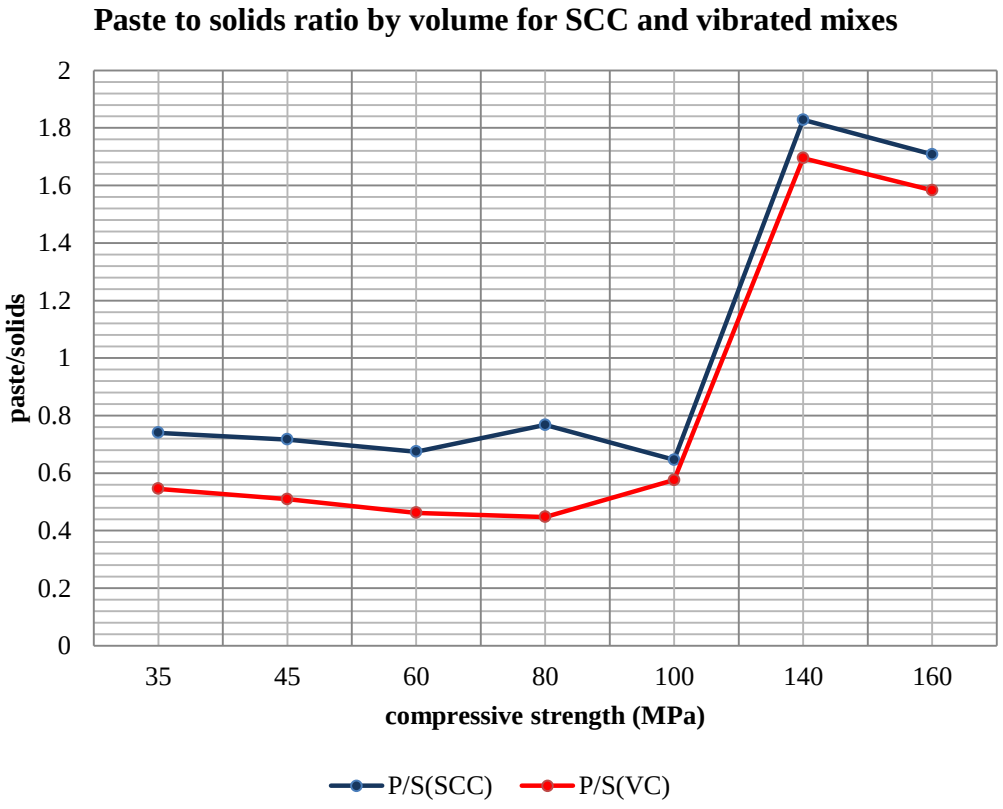

Figure 4.21: Paste to solids ratio by volume in SCC and vibrated concrete (VC) mixes.

It should be noted that the compressive strength of concrete can be increased by decreasing the water to binder ratio, which can be achieved by either increasing the binder content or decreasing the water content. These changes have an opposite effect on the volume of paste; an increase in the binder content increases this volume, whereas a decrease in the water content reduces it. This may explain why the paste to solids ratio of the 80 MPa SCC mix does not follow the expected trend (Figure 4.21). This mix contains a large amount of binder (Mix 4, Table 4.2) and therefore a large paste volume compared with the solids.

For SCUHPC and UHPVC with and without the fibres, the paste volume is almost double that of the solids (Table 4.4). This large paste to solids ratio distinguishes the ultra-high performance concrete mixes (both self-compacting and vibrated types) from the traditional vibrated normal and high strength mixes.

4. 5 Estimation of the plastic viscosity

The flow of SCC with or without fibres is best described by the Bingham constitutive model. This model contains two material properties, namely the yield stress τ_y and the plastic viscosity η. It is known however that the yield stress of SCC mixes is very low (around 200 Pa) in comparison with normal concretes (thousands of Pascal) and remains nearly constant over a large range of plastic viscosities (Dransfield, 2003). The viscosity of a homogenous viscous fluid such as the cement paste can be measured accurately which cannot be said about non-homogeneous viscous fluids such as SCC with and without fibres. However, Ghanbari and Karihaloo (2009) have developed a micromechanical procedure for estimating the plastic viscosity of SCC with or without steel fibres from the knowledge of the plastic viscosity of cement paste alone or of the cement paste with SP and/or VMA. This procedure has been shown to predict the plastic viscosity of SCC mixes with and without fibres that agree very well with measured values (Ghanbari and Karihaloo, 2009).

Based on the water to cement and the super-plasticiser to water ratios, the plastic viscosities of the cement pastes used in the SCC, SCHSC, SCHSFRC, SCUHPC and SCUHPFRC (Tables 4.1, 4.2 and 4.3) developed above, which is mainly influenced by water to cement ratio and super-plasticiser to water ratio, are estimated to be between 0.25 Pa s and 0.4 Pa s (Grzeszczyk and Lipowski, 1997; Nehdi and Rahman, 2004; Sun et al., 2006). In the procedure proposed by Ghanbari and Karihaloo (2009), a concrete mix is regarded as a

succession of two-phase suspensions. At each stage, the suspension consists of a liquid phase in which is suspended a discrete solid phase. Figure 4.22 shows the hierarchy of these two-phase liquid-solid suspensions used in the estimation of the plastic viscosity of all mixes developed above based on the viscosity of the cement paste used in them.

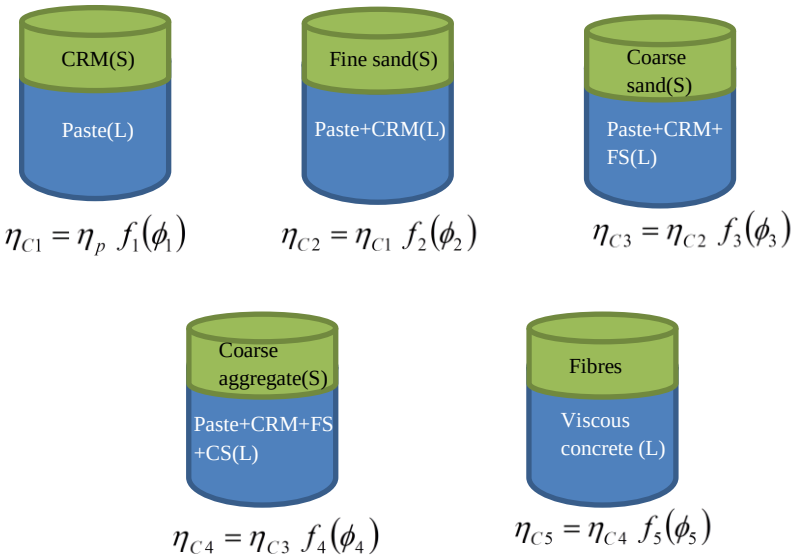

Figure 4.22: Hierarchy of two-phase liquid-solid suspensions constituting an SCC mix with fibres, showing the liquid (L) and solid (S) phases in each suspension. CRM stands for cement replacement material (e.g. GGBS)

The plastic viscosity of the *i*-th liquid-solid suspension can be estimated from the plastic viscosity of the preceding phase as follows

$$\eta_{Ci} = \eta_{Ci-1} f_i(\phi_i) \tag{4.1}$$

with $\eta_{C0} = \eta_p$ being the known plastic viscosity of the cement paste. For instance, cement replacement materials form the solid phase in the viscous cement paste in the first liquid-solid suspension. The plastic viscosity of this suspension is calculated from the known plastic viscosity of the cement paste. This process is repeated until all the ingredients of SCC have been accounted for.

The function $f_i(\phi_i)$ depends only on the volume fraction of solid phase ϕ_i

$$\phi_i = \frac{v_i}{v_i + v_0} \tag{4.2}$$

where

v_i: volume of solid phase i; v_0: volume of the continuous matrix phase in which the solid phase i is suspended;

If the volume fraction is less than 10%, the function $f_i(\phi_i)$ can be expressed by the Einstein equation (or many of its later modifications) in the following form

$$f_i(\phi_i) = 1 + [\eta]\phi_i \tag{4.3}$$

where $[\eta]$ is the so-called non-dimensional intrinsic viscosity which is a measure of the effect of individual particles on the viscosity (Struble and Sun, 1995). A value of $[\eta] = 2.5$ is adopted when the particles are rigid spheres and the distance between them is large compared to the mean particle diameter.

However, when the volume fraction of solid phase exceeds 10% but is less than the maximum possible volume fraction ϕ_m, then $f_i(\phi_i)$ depends not only on the volume fraction of the solid phase but also on how they are dispersed in the fluid and on their shape. ϕ_m represents the situation in which the particles have the minimum possible separation i.e. the void fraction (porosity) is the least and the viscosity is infinite. The value is 0.74 for hexagonal closed packing, 0.637 for random hexagonal packing, and 0.524 for cubic packing.

This dependence is captured in the formula proposed by Kreiger and Dougherty (1959) given below:

$$f_i(\phi_i) = \left(1 - \frac{\phi_i}{\phi_m}\right)^{-[\eta]\phi_m} \tag{4.4}$$

The intrinsic viscosity $[\eta]$ and ϕ_m depend up-on the shear rate; the former tends to decrease with increasing shear rate (i.e. shear thinning), whereas the latter shows the opposite trend. However $[\eta]$ and ϕ_m change in such a way that an increase in the one leads to a decrease in the other, but the product of the two changes remains practically the same and equal on average to 1.9 for rigid spheres.

In the final fluid-solid suspension, the increase in the viscosity induced by a dilute concentration of long steel fibres is estimated. For this the fibres are regarded as rigid slender bodies whose free translation and rotation are restrained by the viscous concrete mix (Ghanbari and Karihaloo, 2009). The plastic viscosity of SCC with fibres, designated η is given by

$$\eta = \eta_{NF}\left\{(1-\phi_f)+\frac{\pi\phi_f l_d^{\,2}}{3\ln(2l_d)}\right\} \tag{4.5}$$

where η_{NF} is the plastic viscosity of the viscous concrete mix without fibres given by Equation (4.1) above, ϕ_f is the fibre volume fraction, and l_d is the length to diameter ratio of the fibre.

4.5.1 Calculating the plastic viscosity of SCC mixes

In this section the plastic viscosity of mix compositions with and without fibres is determined using the above micro-mechanical model proposed by Ghanbhari and Karihaloo (2009). As mentioned above, this plastic viscosity together with yield stress is necessary to simulate the flow of SCC mixes with and without fibres which will be described in detail in Chapter 5.

The calculation of the plastic viscosity will be demonstrated on the example of Mix 6. The plastic viscosities of all SCC mixes developed above have been calculated in the same manner.

Step 1: Estimating the plastic viscosity of the liquid phase (cement paste (CP))

The plastic viscosity of the cement paste (cement +super-plasticiser +water) is estimated based on literature sources (Grzeszczyk and Lipowski, 1997; Nehdi and Rahman, 2004; Sun et al., 2006) to be:

$$f_{CP}(\phi_{CP}) = 0.4 \text{ Pa.s} \tag{4.6}$$

Step 2: Adding the first solid phase (micro-silica (MS)) as shown in Figure 4.23

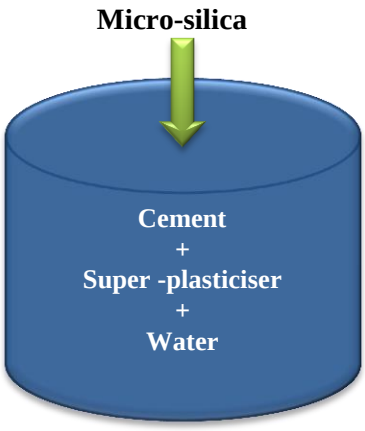

Figure 4.23: The first solid phase (micro-silica) is added to the liquid phase (Paste)

In this case micro-silica is considered to be the solid phase and cement + super-plasticiser + water is the liquid phase.

The volume fraction of the solid phase is determined using Equation (4.2)

$$\phi_{MS} = \frac{v_{MS}}{v_{MS} + v_{CP}} \tag{4.7}$$

where v_{MS} is the volume fraction of the solid phase (micro-silica), v_{CP} is the volume fraction of the continuous matrix phase in which the solid phase is suspended (i.e. the cement paste). After calculating the volume fraction of each ingredient in the mix, the volume of paste is $v_{CP} = 0.326$ m^3, and the volume of micro-silica $v_{MS} = 0.034$ m^3.

Therefore, the volume fraction of micro-silica is

$$\phi_{MS} = \frac{0.034}{0.034 + 0.326} = 0.0948 < 10\% \tag{4.8}$$

Using Equation (4.3)

$$f_{MS}(\phi_{MS}) = 1 + 2.5 * 0.0948 = 1.24 \text{ Pa.s} \tag{4.9}$$

Based on Equation (4.1) the plastic viscosity of the mix is:

$$f_{MS+CP}(\phi_{MS+CP}) = 1.24 * 0.4 = 0.50 \text{ Pa.s} \tag{4.10}$$

Step 3: Adding limestone powder (LS) (Figure 4.24)

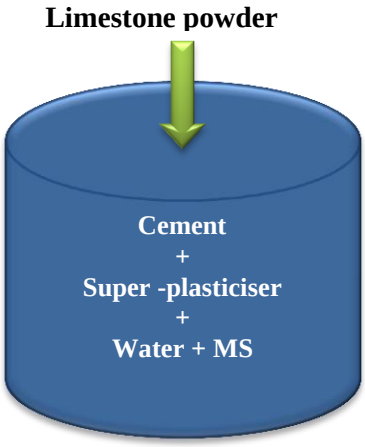

Figure 4.24: Adding the second solid phase (limestone powder)

Limestone powder is considered to be the solid phase and the components within the container are the liquid phase.

The volume fraction of LS, calculated as before, is

$$\phi_{LS} = 0.188 > 10\% \tag{4.11}$$

Using Equation (4.4) for hexagonal packing, the value of [η] = 2.5 and ϕ_m = 0.63 are used.

$$f_{LS}(\phi_{LS}) = (1 - \frac{0.188}{0.63})^{-2.5*0.63} = 1.74 \text{ Pa.s} \tag{4.12}$$

Based on Equation (4.1) the plastic viscosity of the mix so far is:

$$f_{LS+MS+CP}(\phi_{LS+MS+CP}) = 1.74 * 0.50 = 0.87 \text{ Pa.s} \tag{4.13}$$

Step 4: Adding the fine aggregates (FA) (Figure 4.25)

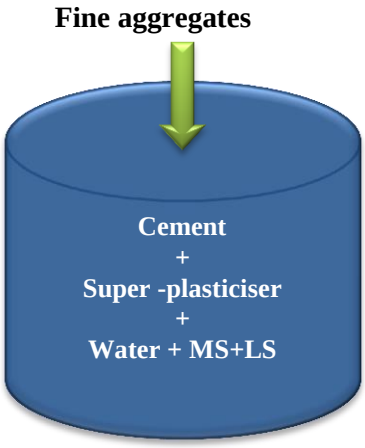

Figure 4.25: Adding the second solid phase (Fine aggregates)

Fine aggregates are now considered as the solid phase and the ingredients in the container as the liquid phase. The volume fraction of FA is

$$\phi_{FA} = 0.374 > 10\% \tag{4.14}$$

Using Equation (4.4)

$$f_{FA}(\phi_{FA}) = (1 - \frac{0.374}{0.63})^{-2.5*0.63} = 4.13 \text{ Pa.s} \tag{4.15}$$

Based on Equation (4.1) the plastic viscosity of the mix so far is:

$$f_{FA+LS+MS+CP}(\phi_{FA+LS+MS+CP}) = 4.13 * 0.87 = 3.59 \text{ Pa.s} \quad (4.16)$$

Step 5: Adding the coarse aggregates (CA)(Figure 4.26)

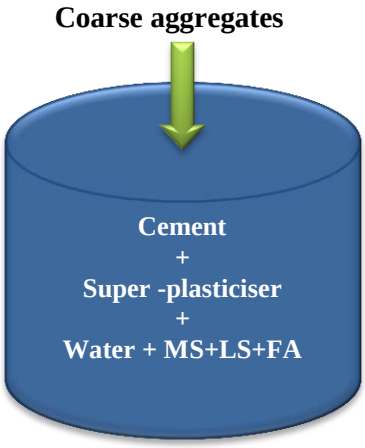

Figure 4.26: Adding the second solid phase (Coarse aggregates)

Coarse aggregates are now considered as the solid phase and the ingredients in the container as the liquid phase. The volume fraction of CA is

$$\phi_{CA} = 0.296 > 10\% \quad (4.17)$$

Using Equation (4.4)

$$f_{CA}(\phi_{CA}) = (1 - \frac{0.296}{0.63})^{-2.5*0.63} = 2.72 \text{ Pa.s} \quad (4.18)$$

Based on Equation (4.1) the plastic viscosity of the eventual SCHSC is:

$$f_{FA+CA+LS+MS+CP}(\phi_{FA+CA+LS+MS+CP}) = 2.72 * 3.59 = 9.76 \text{ Pa.s} \quad (4.19)$$

Note: This is the procedure used to determine the plastic viscosity of SCC mixes without fibres. For mixes with fibres (Mix 6 and Mix 8), the following additional step is needed to calculate the influence of fibres on the plastic viscosity of SCC mix.

Step 6: Adding fibres (Figure 2.27)

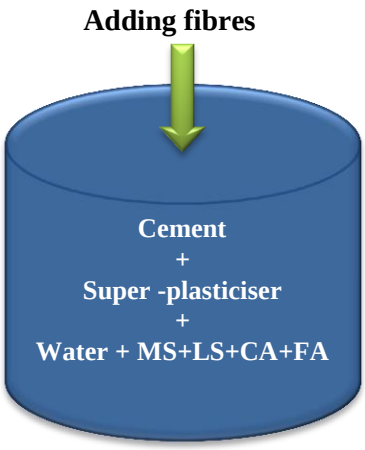

Figure 4.27: Adding steel fibres to SCC mix

The formula used to determine the plastic viscosity of a mix containing fibres represented in the Equation (4.5) as proposed by Ghanbari and Karihaloo (2009)

$$\eta = \eta_{NF}\left\{(1-\phi_f)+\frac{\pi\phi_f l_d^{\,2}}{3\ln(2l_d)}\right\}$$

where η_{NF} is the plastic viscosity of the self-compacting concrete (9.76 Pa.s) without fibres given by Equation (4.9), and

ϕ_f , volume fraction of fibres = 0.5%

l_d , fibres aspect ratio = (30/0.55) = 54.54

Substituting the values in the above Equation gives the plastic viscosity of SCHSFRC (Mix 6) =42.1 Pa.s

Table 4.5. Calculated plastic viscosity of SCC mixes

Mix	Plastic viscosity, Pa.s
Mix 1	10.50
Mix 2	11.30
Mix 3	9.90
Mix 4	9.76
Mix 5	12.40
Mix 6	42.10
Mix 7	3.10
Mix 8	54.30

The plastic viscosities of the SCC mixes with and without steel fibres reported above (see Table 4.1, Table 4.2 and Table 4.3) are estimated using the procedure just described, are given in Table 4.5. Judging by the excellent predictive capability of this procedure (Ghanbari and Karihaloo, 2009), it is reasonable to assume that the plastic viscosities given in Table 4.5 are very accurate. Table 4.5 shows that the plastic viscosity of the self-compacting normal and high strength mixes containing large aggregates (Mixes 1-5), the plastic viscosity varies only marginally from 9.76 Pa.s to 12.40 Pa.s. The plastic viscosity of SCUHPC (Mix 7) which contains no coarse aggregates is however much lower (3.1 Pa s).

The addition of steel fibres however increases the plastic viscosity significantly (Mixes 6 and 8) both in the high strength and the ultra-high performance mixes.

4. 6 Critical remarks

The development of self-compacting concrete mixes is a complex process requiring the resolution of conflicting demands of flow-ability and non-segregation. These demands can be reconciled by increasing the paste content and decreasing the large aggregate volume. The addition of long steel fibres with crimped ends can however compromise the ability of the mix to flow smoothly through gaps in the reinforcement and to cause segregation of the fibres. Our extensive investigations lead us to the following major conclusions.

Self-compacting normal, high-strength and ultra-high-performance concrete mixes without fibres may be designed to satisfy only the flow-ability and cohesiveness (i.e. resistance to

segregation) criteria using the slump cone flow test. The resistance to segregation was checked visually. In the mixes with fibres, it was noticed that the fibres were uniformly distributed in the slump spread right up to the edge. However, when long steel fibres are present in the mixes, it is additionally necessary to check that the mixes meet the passing ability criterion using the J-ring and L-box test apparatus. Our investigations show that although the mixes with fibres meet the flow-ability criterion and the resistant to segregation, as judged by the slump flow test, they may not meet the passing ability criterion. These mixes need to be more flow-able than required by the slump flow test, in order to satisfy the passing ability test.

The viscosity of SCC mixes so produced can be accurately estimated using a micromechanical procedure based on the measured viscosity of the cement paste and the mix proportions. This procedure is based on the rheology of concentrated suspensions (Phan-Thien and Huilgol, 1980; Krieger and Dougherty, 1959; Frankel and Acrivos, 1967) and it is known to predict accurately in a stepwise manner the plastic viscosity of heterogeneous SCC mixtures beginning with the plastic viscosity of the homogeneous cement paste. The latter can be measured accurately using the traditional rheometers (Heirman et al., 2008). The measurement of the plastic viscosity of heterogeneous SCC, especially those containing long fibres using the rheometers often gives inaccurate results with a large scatter. The 30mm long, 0.55 mm diameter steel fibres with crimped ends significantly increase the viscosity of SCC mixes with fibres.

Chapter 5

Modelling the flow of self-compacting concrete

5.1 Introduction

Due to the need for highly durable structures, self-compacting concrete (SCC) with its distinctive flow-ability, passing ability and segregation resistance has been developed, and is increasingly replacing conventional vibrated concrete in the construction industry. The mixture of SCC is strongly dependent on the composition and characteristics of its constituents both in its fresh and hardened states. The prediction of its filling behaviour is very difficult especially in the presence of reinforcing steel and in formworks of complex shapes. However, an understanding of the behaviour and the flow characteristics is crucial to achieving a high quality SCC. The most cost-effective way to gain such an understanding is by performing numerical simulations, which will enable us to fully understand the flow behaviour of SCC with and without steel fibres and to reveal the distribution of larger aggregate particles and of fibres and their orientations inside the formworks.

As the flow of self-compacting concrete mixes (Deeb et al., 2012; Deeb and Karihaloo, 2013) developed in Chapter 4 is Lagrangian in nature, and an SCC mix consists of particles of different sizes and shapes, it is simpler and more appropriate to use mesh-less particle based Lagrangian numerical techniques to simulate the flow. An incompressible SPH method is implemented to simulate the flow of these non-Newtonian fluids whose behaviour is described by a Bingham-type model, in which the kink in the shear stress vs. shear strain rate diagram is first appropriately smoothed out (as described in Chapter 3). The plastic viscosity of the self-compacting concrete mixes is predicted from the measured viscosity of the paste using micromechanical models in which the second phase aggregates are treated as rigid spheres and the short steel fibres as slender rigid bodies (see Chapter 4). The basic equations solved in the SPH are the incompressible mass conservation and momentum equations (Equations (3.5) and (3.17), Chapter 3).

In normal strength self-compacting concrete (compressive strength in the range 30-80 MPa) which do not normally contain any steel fibres, it is the distribution of large coarse aggregate particles (with size 8 and 10 mm) that needs to be monitored during the flow in order to ensure there is no segregation of these particles from the paste. The simulation of these SCC mixes will therefore emphasise the distribution of large aggregate particles of different sizes throughout the flow in the 3D configuration. On the other hand, the simulation of high strength SCC mixes (compressive strengths in the range 100-160 MPa) which contain between 0.5 and 2.5% by volume steel fibres will focus on the distribution of fibres and their

orientations during the flow in 3D configuration, this part will be reported in Chapter 6.

In the present Chapter, a novel but simple methodology has been developed to simulate the flow of SCC as a homogeneous or a heterogeneous medium containing coarse aggregate particles of various sizes in (a) slump cone test apparatus using three-dimensional and axisymmetric configurations (b) and L-box test apparatus using the actual three-dimensional configuration. A comparison between the experimental and simulation results is encouraging, thus improving our understanding of the flow and filling behaviour of SCC.

The first part of this chapter has been submitted for publication (see publication 5 in the list in Chapter 1), while the second part will be submitted to a journal at a future date.

5.2 Governing equations

In view of its shear rate-dependent response, SCC can be regarded as a non-Newtonian incompressible fluid. Its rheology is best described by the Bingham model which contains two material properties, the yield stress τ_y and the plastic viscosity η. It is known however that the yield stress of SCC mixes is very low (around 200 Pa) in comparison with normal vibrated concretes (~ 1000 Pa) and remains nearly constant over a wide range of plastic viscosities (Domone, 2003; Ghanbari and Karihaloo, 2009). From a practical computational point of view, it is expedient to approximate the bi-linear Bingham constitutive model with a kink at $\dot{\gamma} = 0$ by a smooth continuous function (Papanastasiou, 1987)

$$\tau = \eta\dot{\gamma} + \tau_y\left(1 - e^{-m\dot{\gamma}}\right) \tag{5.1}$$

in which m is a very large number (e.g. $m = 10^5$ s). This smooth function is practically indistinguishable from the original bi-linear relation. Equation (5.1) is applicable to each of the three independent shear components of the stress tensor. (see Chapter 3, Figure 3.3).

The Bingham type constitutive model of the mixes is coupled with the Lagrangian momentum and continuity equations to model the flow of SCC mixes. The isothermal, Lagrangian form of mass and momentum conservation equations are (see Chapter 3, Equations (3.5) and (3.17)):

$$\frac{1}{\rho}\frac{D\rho}{Dt} + \nabla.\mathbf{v} = 0 \tag{5.2}$$

$$\frac{D\mathbf{v}}{Dt} = -\frac{1}{\rho}\nabla P + \frac{1}{\rho}\nabla.\boldsymbol{\tau} + \mathbf{g} \tag{5.3}$$

where ρ, t, $\mathbf{v}$, P, $\mathbf{g}$ and $\boldsymbol{\tau}$ represent the fluid particle density, time, particle velocity, pressure, gravitational acceleration, and shear stress, respectively. Below we shall consider flows in which the density is constant, so that the first term in Equation (5.2) vanishes.

These equations govern both Newtonian and non-Newtonian fluid flows. However, the non-Newtonian fluids differ from Newtonian ones due to their shear rate-dependent viscosity.
For a non-Newtonian fluid, the shear stress is generally written as:

$$\boldsymbol{\tau} = 2\mu(\dot{\gamma})\boldsymbol{d} = \left(\eta + \frac{\tau_y}{\dot{\gamma}}\left(1 - e^{-m\dot{\gamma}}\right)\right)\boldsymbol{d}, \qquad (\dot{\gamma} > 0) \tag{5.4}$$

where $\boldsymbol{d}$ is the rate of deformation and μ is the effective plastic viscosity which is a function of shear rate. $\dot{\gamma}$ is the shear rate.

The three-dimensional (3D) and cylindrical forms of the vector Equations (5.2) and (5.3) are given in the following sections.

5.2.1 Mass and momentum conservation equations in 3D

5.2.1.1 Mass conservation equation

Multiplying both side of (5.2) by ρ and noting that the material derivative (or total time derivative) of density $\frac{D\rho}{Dt}$ can be decomposed into the normal derivative $\frac{\partial\rho}{\partial t}$ and the convective derivative $\mathbf{v}.\nabla\rho$ (see (3.23)) we can write

$$\left(\frac{\partial\rho}{\partial t}\right) + \mathbf{v}.\nabla\rho + \rho\nabla.\mathbf{v} = \left(\frac{\partial\rho}{\partial t}\right) + \nabla.(\rho\mathbf{v}) \tag{5.5}$$

For a steady-state flow, ρ does not change with respect to time hence the term $\frac{\partial\rho}{\partial t}$ vanishes. Therefore, in Cartesian coordinates (5.5) can be rewritten as

$$\frac{\partial(\rho v_x)}{\partial x}+\frac{\partial(\rho v_y)}{\partial y}+\frac{\partial(\rho v_z)}{\partial z}=0 \tag{5.6}$$

When additionally the flow is incompressible, ρ is constant and does not change with respect to space, therefore (5.6) is further simplified to

$$\frac{\partial v_x}{\partial x}+\frac{\partial v_y}{\partial y}+\frac{\partial v_z}{\partial z}=0$$

(5.7)

5.2.1.2 Momentum conservation equations

Multiplying both sides of (5.3) by ρ and noting that the substantial derivative (or total time derivative) of velocity $\frac{D\mathbf{v}}{Dt}$ can be decomposed into the normal derivative $\frac{\partial \mathbf{v}}{\partial t}$ and the convective derivative ($\mathbf{v}.\nabla\mathbf{v}$) (see (3.23)), we can write

$$\rho\left(\frac{\partial \mathbf{v}}{\partial t}\right)+\rho(\mathbf{v}.\nabla\mathbf{v})=-\nabla P+\rho\mathbf{g}+\nabla.\boldsymbol{\tau} \tag{5.8}$$

In Cartesian coordinates, (5.8) can be written explicitly as

$$\rho\left(\frac{\partial v_x}{\partial t}+v_x\frac{\partial v_x}{\partial x}+v_y\frac{\partial v_x}{\partial y}+v_z\frac{\partial v_x}{\partial z}\right)=-\frac{\partial P}{\partial x}+\rho g_x+\eta_{eff}\left(\frac{\partial^2 v_x}{\partial x^2}+\frac{\partial^2 v_x}{\partial y^2}+\frac{\partial^2 v_x}{\partial z^2}\right) \tag{5.9}$$

$$\rho\left(\frac{\partial v_y}{\partial t}+v_x\frac{\partial v_y}{\partial x}+v_y\frac{\partial v_y}{\partial y}+v_z\frac{\partial v_y}{\partial z}\right)=-\frac{\partial P}{\partial y}+\rho g_y+\eta_{eff}\left(\frac{\partial^2 v_y}{\partial x^2}+\frac{\partial^2 v_y}{\partial y^2}+\frac{\partial^2 v_y}{\partial z^2}\right) \tag{5.10}$$

$$\rho\left(\frac{\partial v_z}{\partial t}+v_x\frac{\partial v_z}{\partial x}+v_y\frac{\partial v_z}{\partial y}+v_z\frac{\partial v_z}{\partial z}\right)=-\frac{\partial P}{\partial z}+\rho g_z+\eta_{eff}\left(\frac{\partial^2 v_z}{\partial x^2}+\frac{\partial^2 v_z}{\partial y^2}+\frac{\partial^2 v_z}{\partial z^2}\right) \tag{5. 11}$$

where η_{eff} is the effective viscosity of the fluid such that $\boldsymbol{\tau}=\eta_{eff}(\dot{\gamma})\dot{\gamma}$. In the case of a Newtonian fluid it is constant.

To obtain η_{eff} for a Bingham fluid, both sides of (5.1) are divided by $\dot{\gamma}$ to give

$$\frac{\boldsymbol{\tau}}{\dot{\gamma}}=\eta+\frac{\tau_y\left(1-e^{-m\dot{\gamma}}\right)}{\dot{\gamma}} \tag{5.12}$$

The right hand side of (5.12) is η_{eff}

$\dot{\gamma}$ is the shear rate which is defined as

$$\dot{\gamma} = \sqrt{\frac{1}{2}\left(tr\ \boldsymbol{d}^2\right)} \tag{5.13}$$

(5.13) states that $\dot{\gamma}$ is the second invariant of the rate of deformation tensor $\boldsymbol{d}$, given by

$$\boldsymbol{d} = \frac{1}{2}\left(\nabla\mathbf{v} + \nabla\mathbf{v}^T\right); \qquad \nabla\mathbf{v} = \nabla \otimes \mathbf{v} \tag{5.14}$$

where $\nabla\mathbf{v}$ is velocity gradient and superscript *T* denotes transpose. In an explicit form $\boldsymbol{d}$ is

$$\boldsymbol{d} = \begin{pmatrix} \frac{\partial v_x}{\partial x} & \frac{1}{2}\left(\frac{\partial v_x}{\partial y} + \frac{\partial v_y}{\partial x}\right) & \frac{1}{2}\left(\frac{\partial v_x}{\partial z} + \frac{\partial v_z}{\partial x}\right) \\ \frac{1}{2}\left(\frac{\partial v_y}{\partial x} + \frac{\partial v_x}{\partial y}\right) & \frac{\partial v_y}{\partial y} & \frac{1}{2}\left(\frac{\partial v_y}{\partial z} + \frac{\partial v_z}{\partial y}\right) \\ \frac{1}{2}\left(\frac{\partial v_z}{\partial x} + \frac{\partial v_x}{\partial z}\right) & \frac{1}{2}\left(\frac{\partial v_z}{\partial y} + \frac{\partial v_y}{\partial z}\right) & \frac{\partial v_z}{\partial z} \end{pmatrix} \tag{5.15}$$

5.2.2 Mass and momentum conservation equations in the cylindrical co-ordinate system

When modelling the flow of SCC mixes in a slump test, in order to reduce the computational cost, axisymmetric configurations are used, which are a reduced versions of 3D and cylindrical coordinates respectively. The governing equations in the cylindrical co-ordinates and axisymmetric approximation are given below.

5.2.2.1 Mass conservation equation in the cylindrical co-ordinate system

A change of variables from the Cartesian equations gives the following mass conservation equation in the cylindrical co-ordinates *r*, ϕ, and *z*

$$\frac{1}{r}\frac{\partial}{\partial r}\left(rv_r\right) + \frac{1}{r}\frac{\partial v_\phi}{\partial \phi} + \frac{\partial v_z}{\partial z} = 0 \tag{5.16}$$

5.2.2.2 Momentum conservation equations in the cylindrical co-ordinate system

Similar to (5.16), the momentum conservation equations are given by

$$\begin{aligned} \textbf{\textit{r component :}}\ \rho\left(\frac{\partial v_r}{\partial t}+v_r\frac{\partial v_r}{\partial r}+\frac{v_\phi}{r}\frac{\partial v_r}{\partial \phi}+v_z\frac{\partial v_r}{\partial z}-\frac{v_\phi^2}{r}\right)= \\ -\frac{\partial P}{\partial r}+\eta_{eff}\left[\frac{1}{r}\frac{\partial}{\partial r}\left(r\frac{\partial v_r}{\partial r}\right)+\frac{1}{r^2}\frac{\partial^2 v_r}{\partial \phi^2}+\frac{\partial^2 v_r}{\partial z^2}+\frac{v_r}{r^2}-\frac{2}{r^2}\frac{\partial v_\phi}{\partial \phi}\right]+\rho g_r \end{aligned} \tag{5.17}$$

$$\begin{aligned} \textbf{\textit{}}\phi\textbf{\textit{ component :}}\ \rho\left(\frac{\partial v_\phi}{\partial t}+v_r\frac{\partial v_\phi}{\partial r}+\frac{v_\phi}{r}\frac{\partial v_\phi}{\partial \phi}+v_z\frac{\partial v_\phi}{\partial z}-\frac{v_r v_\phi}{r}\right)= \\ -\frac{1}{r}\frac{\partial P}{\partial \phi}+\eta_{eff}\left[\frac{1}{r}\frac{\partial}{\partial r}\left(r\frac{\partial v_\phi}{\partial r}\right)+\frac{1}{r^2}\frac{\partial^2 v_\phi}{\partial \phi^2}+\frac{\partial^2 v_\phi}{\partial z^2}-\frac{v_r}{r^2}+\frac{2}{r^2}\frac{\partial v_r}{\partial \phi}\right]+\rho g_\phi \end{aligned} \tag{5.18}$$

$$\begin{aligned} z\textbf{\textit{ component :}}\ \rho\left(\frac{\partial v_z}{\partial t}+v_r\frac{\partial v_z}{\partial r}+\frac{v_\phi}{r}\frac{\partial v_z}{\partial \phi}+v_z\frac{\partial v_z}{\partial z}\right)= \\ -\frac{\partial P}{\partial z}+\eta_{eff}\left[\frac{1}{r}\frac{\partial}{\partial r}\left(r\frac{\partial v_z}{\partial r}\right)+\frac{1}{r^2}\frac{\partial^2 v_z}{\partial \phi^2}+\frac{\partial^2 v_z}{\partial z^2}\right]+\rho g_z \end{aligned} \tag{5.19}$$

5.2.2.3 Axisymmetric mass and momentum conservation equations

A flow is axisymmetric, if the displacement takes place along the *r* and *z* axes but is independent of the ϕ direction. Therefore any derivative with respect to ϕ in the cylindrical co-ordinates vanishes. Furthermore in this case due to the irrotational nature of the flow the velocity in ϕ direction (v_ϕ) is also set equal to zero. Therefore (5.16), (5.17) and (5.19) become (5.20), (5.21) and (5.22), respectively.

$$\frac{1}{r}\frac{\partial}{\partial r}(rv_r)++\frac{\partial v_z}{\partial z}=0 \tag{5.20}$$

$$\textbf{\textit{r component}}: \rho\left(\frac{\partial v_r}{\partial t}+v_r\frac{\partial v_r}{\partial r}+v_z\frac{\partial v_r}{\partial z}\right)= -\frac{\partial P}{\partial r}+\eta_{eff}\left[\frac{1}{r}\frac{\partial}{\partial r}\left(r\frac{\partial v_r}{\partial r}\right)+\frac{v_r}{r^2}-\frac{\partial^2 v_r}{\partial z^2}\right]+\rho g_r \tag{5.21}$$

$$\textbf{\textit{z component}}: \rho\left(\frac{\partial v_z}{\partial t}+v_r\frac{\partial v_z}{\partial r}+v_z\frac{\partial v_z}{\partial z}\right)= -\frac{\partial P}{\partial z}+\eta_{eff}\left[\frac{1}{r}\frac{\partial}{\partial r}\left(r\frac{\partial v_z}{\partial r}\right)+\frac{\partial^2 v_z}{\partial z^2}\right]+\rho g_z \tag{5.22}$$

η_{eff} is obtained from (5.12) after replacing *x* and *y* by *r* and *z*, respectively.

5.3 Numerical solution procedure

A projection method based on the predictor-corrector time stepping scheme has been adopted to track the Lagrangian non-Newtonian flow (Chorin, 1968; Cummins and Murray, 1999; Koshizuka et al., 1998) and the incompressibility condition has been satisfied exactly through a pressure Poisson equation.

Prediction step

The prediction step is an explicit integration in time without enforcing incompressibility. Only the viscous stress and gravity terms are considered in the momentum Equation (5.3) and an intermediate particle velocity $\mathbf{v}_{n+1}^{*}$ and position are obtained as:

$$\mathbf{v}_{n+1}^{*}=\mathbf{v}_n+\left(\mathbf{g}+\frac{1}{\rho}\nabla.\boldsymbol{\tau}\right)\Delta t \tag{5.23}$$

where

$$\mathbf{x}_{n+1}^{*}=\mathbf{x}_n+\mathbf{v}_{n+1}^{*}\Delta t \tag{5.24}$$

Here, $\mathbf{v}_n$ and $\mathbf{x}_n$ are the particle velocity and position vectors at time *t*, $\mathbf{v}_{n+1}^{*}$ and $\mathbf{x}_{n+1}^{*}$ are the intermediate particle velocity and position vectors.

Correction step

Then the correction step is applied to enforce the incompressibility condition prior to

incrementing the time. This step is performed by considering the pressure term in Equation (5.3)

$$\frac{\mathbf{v}_{n+1} - \mathbf{v}^*_{n+1}}{\Delta t} = -\left(\frac{1}{\rho}\nabla P_{n+1}\right) \tag{5.25}$$

Rearranging Equation (5.25)

$$\mathbf{v}_{n+1} = \mathbf{v}^*_{n+1} - \left(\frac{1}{\rho}\nabla P_{n+1}\right)\Delta t \tag{5.26}$$

where $\mathbf{v}_{n+1}$ is the corrected particle velocity at the time step n+1. Computing Equation (5.26) requires the pressure P_{n+1}. This will be obtained by imposing the incompressibility condition in the mass conservation Equation (5.2) (as the particle density remains constant during the flow). The intermediate velocity $\mathbf{v}^*_{n+1}$ is usually not divergence-free but this condition is imposed on the corrected velocity $\mathbf{v}_{n+1}$ by enforcing the incompressibility condition from Equation (5.2):

$$\nabla.\mathbf{v}_{n+1} = 0 \tag{5.27}$$

Hence the intermediate velocity can be projected on the divergence-free space by writing the divergence of Equation (5.26), using (5.27), as

$$\nabla.\left(\frac{1}{\rho}\nabla P_{n+1}\right) = \frac{\nabla.\mathbf{v}^*_{n+1}}{\Delta t} \tag{5.28}$$

Since the density of particles remains constant in the present simulations, Equation (5.28) can be rewritten as:

$$\nabla^2 P_{n+1} = \frac{\rho}{\Delta t}\nabla.\mathbf{v}^*_{n+1} \tag{5.29}$$

where ∇^2 is the Laplacian.

Once the pressure is obtained from the Poisson Equation (5.29), the particle velocity is updated by the computed pressure gradient (see Equation (5.26))

And finally, the instantaneous particle position is updated using the corrected velocity:

$$\mathbf{x}_{n+1} = \mathbf{x}_n + \mathbf{v}_{n+1}\Delta t \tag{5.30}$$

Time step

The time step Δt is chosen based on the relevant stability conditions for the given problem. In the case of Bingham-type SCC fluid flow, the time step is primarily controlled by the effective plastic viscosity. Therefore, the time step size is generally decided by Shao and Lo (2003)

$$\Delta t = min\left(\frac{a_1 r_0}{\mathrm{v}_{max}}, \frac{a_2 r_0^2 \rho}{\mu}\right) \tag{5.31}$$

where r_0 is the initial particle spacing, v_{max} is the maximum particle velocity, α_1 and α_2 are the coefficients usually in order of 0.1. These coefficients depend on the choice of SPH kernel functions and the nature of the engineering application. Note that the term $\left(1 - e^{-m\dot{\gamma}}\right)$ was excluded from Equation (5.31), since its value is close to one when m is a very large number.

5.4 SPH discretisation of the governing equations

In the SPH, variables and their gradients are generally interpolated from values at a discrete set of particles by using the standard approximations (3.37) and (3.38). In the governing equations of SCC flow (Equations (5.2) and (5.3)), three terms need to be defined in the SPH formulation; these are the divergence of velocity field in the mass conservation equation (5.2), the gradients of pressure and viscous terms in the momentum conservation equation (5.3), and the Laplacian term $\nabla^2 P_{n+1}$ in the Poisson equation resulting from enforcing the incompressibility (5.29).

5.4.1 Divergence of velocity

The divergence of the velocity field can be obtained by identifying $f(x)$ in the Equation (3.38) (see Chapter 3) with the velocity term

$$(\nabla.\mathbf{v})_a = \sum_{b=1}^{N} V_b \mathbf{v}_b . \tilde{\nabla} \tilde{W}_b(\mathbf{x}) \tag{5.32}$$

where *a* and *b* are the reference particle and its neighbour, respectively. V_b is the volume of material assigned to a given particle. For particles representing heavier and/or larger constituents in the viscous continuum, the assigned volume is equal to the ratio of actual mass to the density of continuum and $\tilde{\nabla}\tilde{W}$ is the corrected gradient of the corrected kernel (see Chapter 3 and Appendix B). The accuracy of the approximation depends on the choice of the differentiable kernel function, especially on its closeness to the Delta function. The cubic spline function given by Equation (3.31) was used.

5.4.2 Gradient of pressure

The gradient of pressure in the momentum equations can be obtained in the similar manner as above

$$\left(\nabla P\right)_a = \sum_{b=1}^{N} V_b P_b \tilde{\nabla}\tilde{W}_b(\mathbf{x}) \tag{5.33}$$

5.4.3 Laplacian

The Laplacian in the pressure Poisson equation (5.29) can be formulated using the divergence and gradient operators of the SPH formulation to give

$$\left(\nabla^2 P\right)_a = \frac{\rho_a}{\Delta t}\sum_{b=1}^{N} V_b \mathbf{v}_b . \tilde{\nabla}\tilde{W}_b(\mathbf{x}) \tag{5.34}$$

5.4.4 Viscous term

The viscous term, $\frac{1}{\rho}\nabla\boldsymbol{\tau}$ in the momentum conservation equation can be written in a similar manner as

$$\left(\frac{1}{\rho}\nabla\boldsymbol{\tau}\right)_a = \sum_{b=1}^{N} \frac{m_b}{\rho_b^2}\boldsymbol{\tau}_b \tilde{\nabla}\tilde{W}_b(\mathbf{x}) \tag{5.35}$$

The pressure Poisson equation (5.29) can be solved using any suitable iterative method. In the present implementation a pre-conditioned conjugate gradient method is used. In addition to the numerical procedure and governing equations described above, a suitable method to treat the boundary conditions has to be developed.

5.5 Initial configuration and boundary conditions

When solving the momentum and continuity equations, appropriate initial and boundary conditions need to be applied.

Three types of boundary conditions need to be considered in the simulation of slump cone and L-box tests:

- Zero pressure condition (i.e. atmospheric pressure) on the free surfaces;
- Dirichlet (or first-type) boundary conditions have to be imposed on the normal component of the velocity field at the walls and the bottom plates to represent the sliding frictional boundary conditions;
- Neumann (or second- type) boundary condition has to be imposed on the pressure gradient;

For realistic simulations, the friction between the SCC mix and the contacting surfaces should be considered. A dynamic coefficient of friction equal to 0.55 Ns/m was chosen after several trials. The coefficient that gave the best match between the simulations and test results was chosen. The effect of friction boundary condition depends on the relative tangential velocity between the contacting surface and the fluid flow and ensures that slip with friction boundary condition is enforced along the tangential direction of the contacting surfaces.

In SPH, a number of techniques have been developed in the past to deal with boundary conditions. Some of these techniques have been explained in Chapter 3. In this research, the technique based on an array of dummy rigid particles was used to implement the wall and bottom plate boundaries (Koshizuka et al., 1998), as follows.

5.5.1 Slump cone test

Four arrays of rigid dummy particles placed outside the wall particles of the cone were used to implement the wall boundary conditions. The thickness of the array containing the dummy particles depends on the kernel smoothing length h. If the smoothing length $h=2r_o$, where r_o is the initial particle spacing, four arrays of dummy particles at a spacing r_o between the lines were used. The cone is lifted at a rate of 0.15 m/s.

The normal component of the velocities of both the wall and dummy particles has to be zero. Friction between SCC mix and boundaries was imposed on the cone wall and the bottom plate with a dynamic coefficient of friction between the SCC mix and steel equal to 0.55 Ns/m. These conditions mimic the actual discharge of the SCC mix from the slump cone. Despite the fact that the cone is lifted quickly, there is an inevitable time lapse before the entire contents of the cone stop being in contact with its surface. As a result, in the initial stage of the slump cone test, the contents lose contact with the cone surface progressively and flow along the base plate (Figure 5.1(d)).

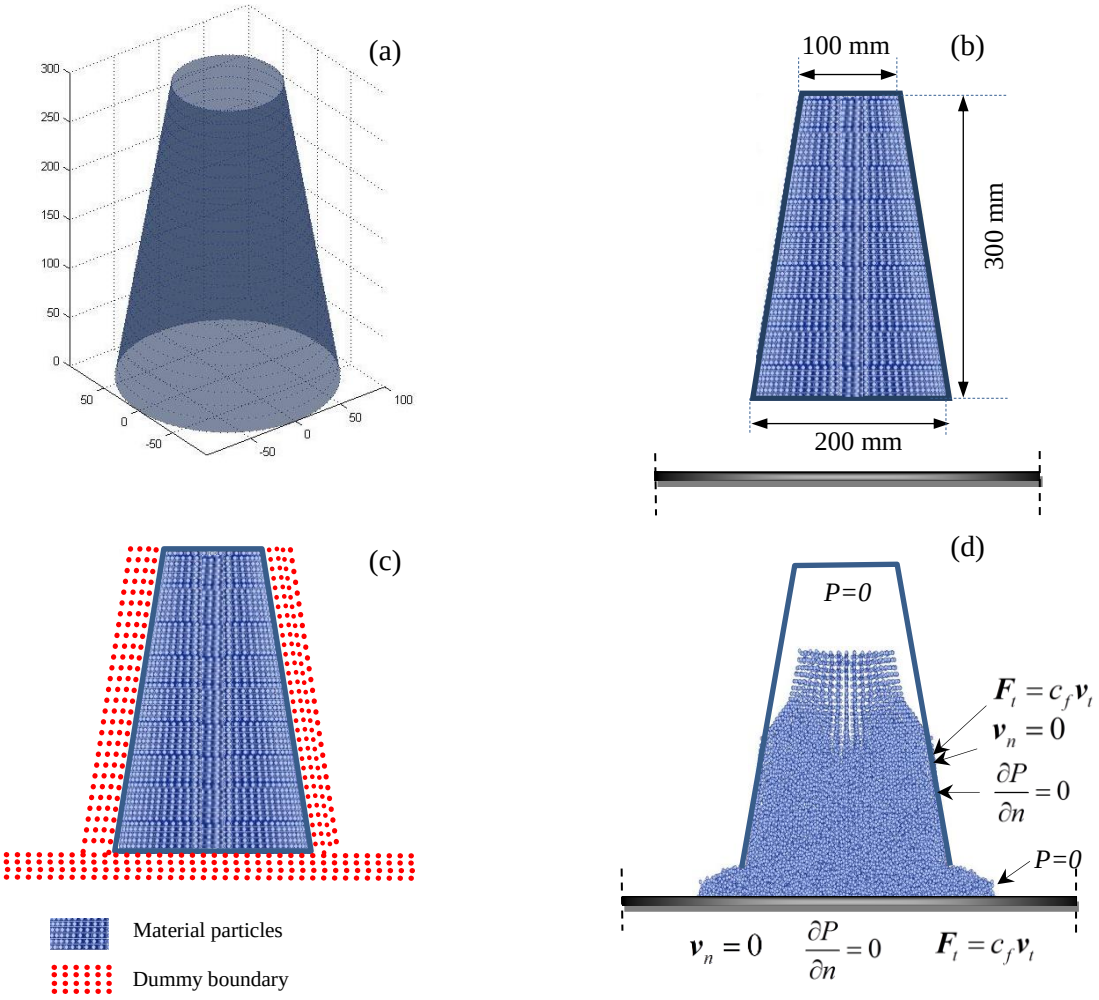

Figure 5.1: Slump cone test boundary conditions (P - pressure, v_n - normal velocity, v_t - tangential velocity, and c_f - the dynamic coefficient of friction). Pressure vanishes on a free surface. Note that the condition that the normal pressure gradient vanishes on rigid surfaces is only needed in the solution of the pressure Poisson Equation (5.29)

The boundary conditions along the slump wall are same as on the bottom plate. However, as

the cone is lifted, the condition $P=0$ is imposed on the newly formed free (exposed) surfaces of the flowing SCC mix. Figure 5.1d shows the slump cone test initial configurations and boundary conditions.

5.5.2 L-box test

As in the slump cone test, four arrays of rigid dummy particles placed outside the wall and the base particles of the L-box were used to implement the boundary conditions. Dirichlet and Neumann boundary conditions were imposed on the wall and the base of the L-box. Friction between SCC mix and boundaries was imposed as illustrated in Figure 5.2 with a dynamic coefficient of friction between the SCC mix and steel equal to 0.55 Ns/m. As the L-box gate is lifted, the condition $P=0$ is imposed on the newly formed free surfaces of the flowing SCC mix.

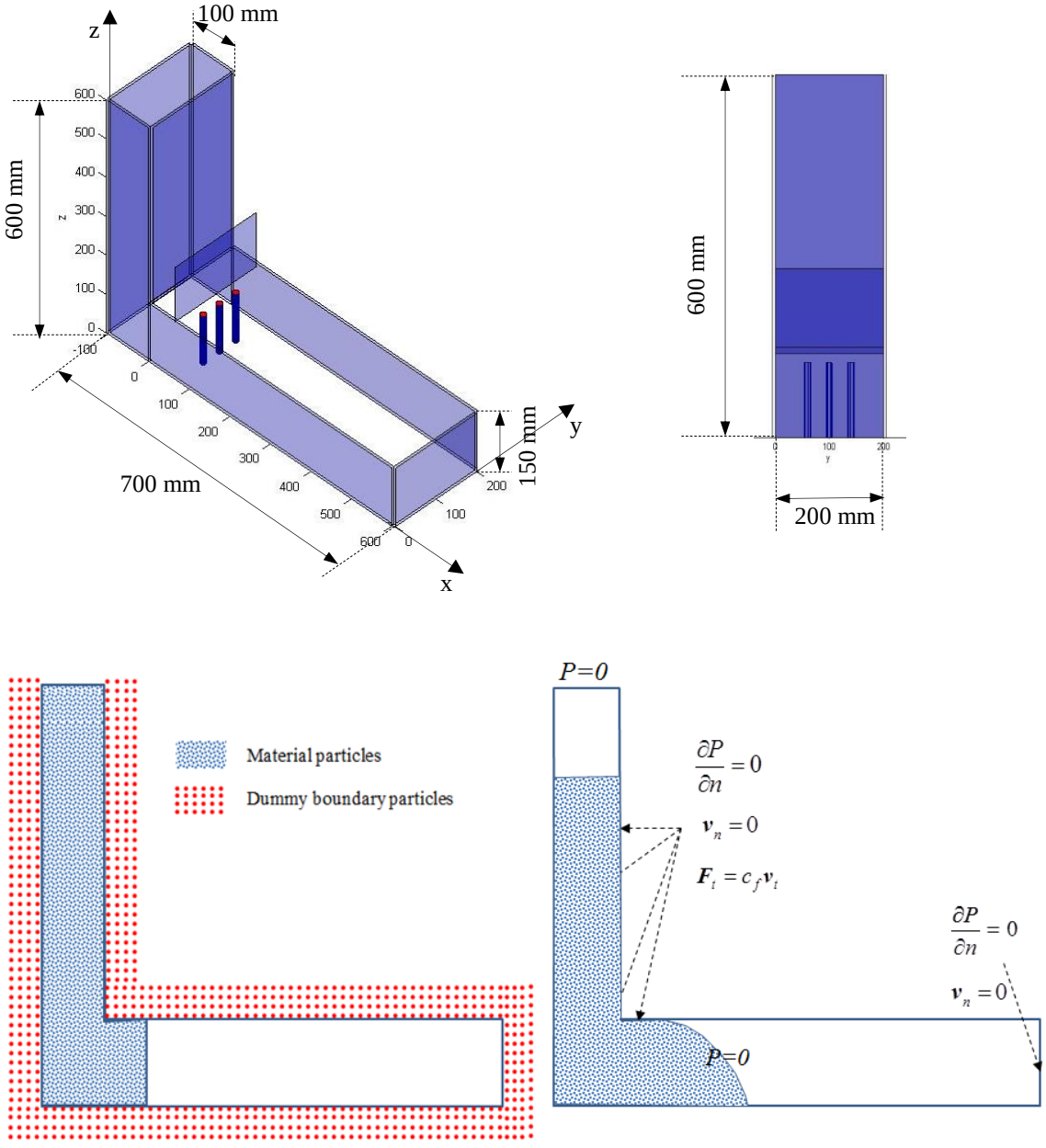

Figure 5.2: L-box test boundary conditions (*P* - pressure, v_n - normal velocity, v_t - tangential velocity, and c_f - the dynamic coefficient of friction). Pressure vanishes on a free surface. Similar to the slump test, note that the condition that the normal pressure gradient vanishes on rigid surfaces is only needed in the solution of the pressure Poisson Equation (5.29)

5.6 Treatment of aggregates

An essential requirement of a SCC mix is that heavier aggregate particles do not segregate from the paste during the flow. To investigate this, all aggregates larger than or equal to 8

mm in size have been modelled as separate particles suspended in the viscous paste containing the remaining particles less than 8 mm in size.

Sieve analysis was first performed to determine the grading curve of aggregate particle sizes within a given sample. According to the sieve analysis of a typical SCC mix (Mix 4 in Table 4.2), the volume fractions of aggregates 10 mm and 8 mm in size were 15% and 11%, respectively (Table 5.1). (The volume fractions were calculated from the measured mass fractions). The volume fraction of particles less than 8 mm in size which form the paste was therefore 74 %.

In order to be able to monitor the velocity vectors and positions of aggregates of different sizes, as well as those of the fluid particles representing the paste, the particles are represented by distinct colours as shown in Figure 5.3.

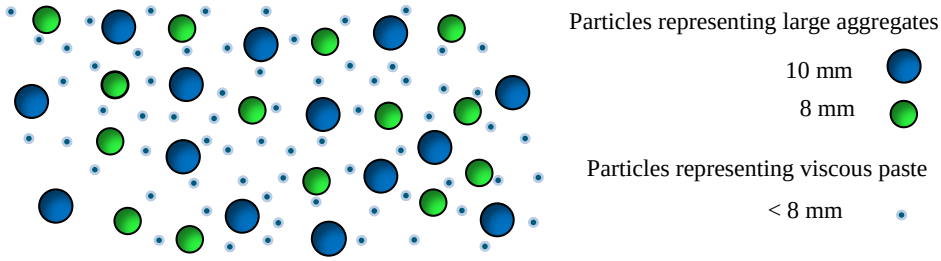

Figure 5.3: Schematic sketch of particle representation when simulating large aggregate distribution

The number of particles used to represent the volume of cone contents sets a lower limit on the volume element that can be distinguished from the homogeneous mass, i.e. the resolution of the modelling technique.

- In the 3D simulations of the slump flow, a total of 23581 particles have been used to represent the volume of mix in the cone (5.498×10^6 mm^3) giving a resolution of 233.15 mm^3 if all particles have the same density as the viscous continuum. The resolution may be somewhat different if the particles have different densities (see Table 5.1 below). Thus, in Mix 4 (Table 4.2) the large aggregates that can be distinguished from the homogeneous mass must have a volume exceeding this minimum. It is for this reason that only the aggregates of size 8 mm and above have been chosen.

  In the 3D Simulations of the L-box, a total of 59568 particles have been used to represent the volume of the mix (129×10^5 mm^3) giving a resolution of 216.56 mm^3 if all particles have the same density as the viscous continuum. This resolution again

will be different if the particles have different densities (Table 5.1) and only aggregates of size 8 mm and above can be distinguished from the homogeneous mass.

Further, the following steps were taken during the numerical simulations:

- All particles representing the mix were generated randomly.
- Particles representing the paste as well as the large aggregates form a homogeneous mass and have the same continuum properties except for their assigned volumes.
- The masses of the SPH particles representing the various aggregate particles in the SCC mix were calculated based on their respective volume fractions in the mix.
- Particles representing the large aggregates according to their assigned volumes were tagged (and colour coded as shown above) throughout the simulation in order to monitor their velocity vectors and positions.

Table 5.1. Volume fractions of aggregates larger than or equal to 8 mm in Mix 4 and the number of particles (N_p) representing them in the 3D simulation of slump cone and L-box tests and their assigned volume (V_a)

SCHPC (Mix 4)	**Particle diameter (mm)**	**Density (kg/m^3)**	**Volume fraction (%)**	**3D slump cone test**		**3D L-box test**	
				N_p	V_a **/ particle (mm^3)**	N_p	V_a **/ particle (mm^3)**
Particles < 8 mm	< 8 mm	2332.4	74	19750	195.79	50579	179.38
Aggregates ≥8 mm	10	2800	15	1575	597.42	3696	597.42
	8	2800	11	2256	305.88	5293	305.88
Total	-	2454	100	23581	-	59568	-

5.7 Numerical simulation results

A number of numerical tests were carried out to investigate the flow-ability, filling and passing ability of the SCC mix using two different test apparatuses: slump cone and L-box. The SCC mix studied in this section is the self-compacting concrete (SCC) Mix 4 developed in Chapter 4 (Table (4.2)). The plastic viscosity of this mix was calculated from the known plastic viscosity of the cement paste and the volume fractions of the various fine aggregates (see Tables (4.5)). As mentioned previously, the yield stress of SCC is low and practically

constant over a wide range of plastic viscosities (see Figure 2.27). For the present mix, τ_y was chosen to be 200 Pa.

5.7.1 Slump test

5.7.1.1 Simulating slump test for SCC mix in axisymmetric configuration

In this section, the axisymmetric numerical simulation of the slump cone test of a typical SCC mix (the SCHPC Mix 4, Table 4.2) is presented to investigate its flow characteristics and compared with the test results.

In this simulation, 7041 particles were used to represent the surface area of the diametrical vertical section of the slump cone (45000 mm^2) as a homogenous mix. The plastic viscosity of the SCC mix was first calculated using the micromechanical model proposed by Ghanbari & Karihaloo (2009) from the known plastic viscosity of the cement paste and the volume fractions of the various second phase particles (Table 4.5). All the material parameters of the mix, namely the yield stress and the plastic viscosity are of SCHPC Mix 4 in Table 5.2.

Table 5.2. The material parameters of the SCC mix (Mix 4).

Constituents	Mix 4
Flow spread (mm)	805
t_{500} (sec)	2.20
t_{200} (sec)	0.35
t_{400} (sec)	0.76
Level-off (sec)	7.23
Plastic viscosity (Pa s)	9.76
Yield stress (Pa)	200
Compressive strength (MPa)	**80**

The results of this simulation are illustrated in Figure 5.4.

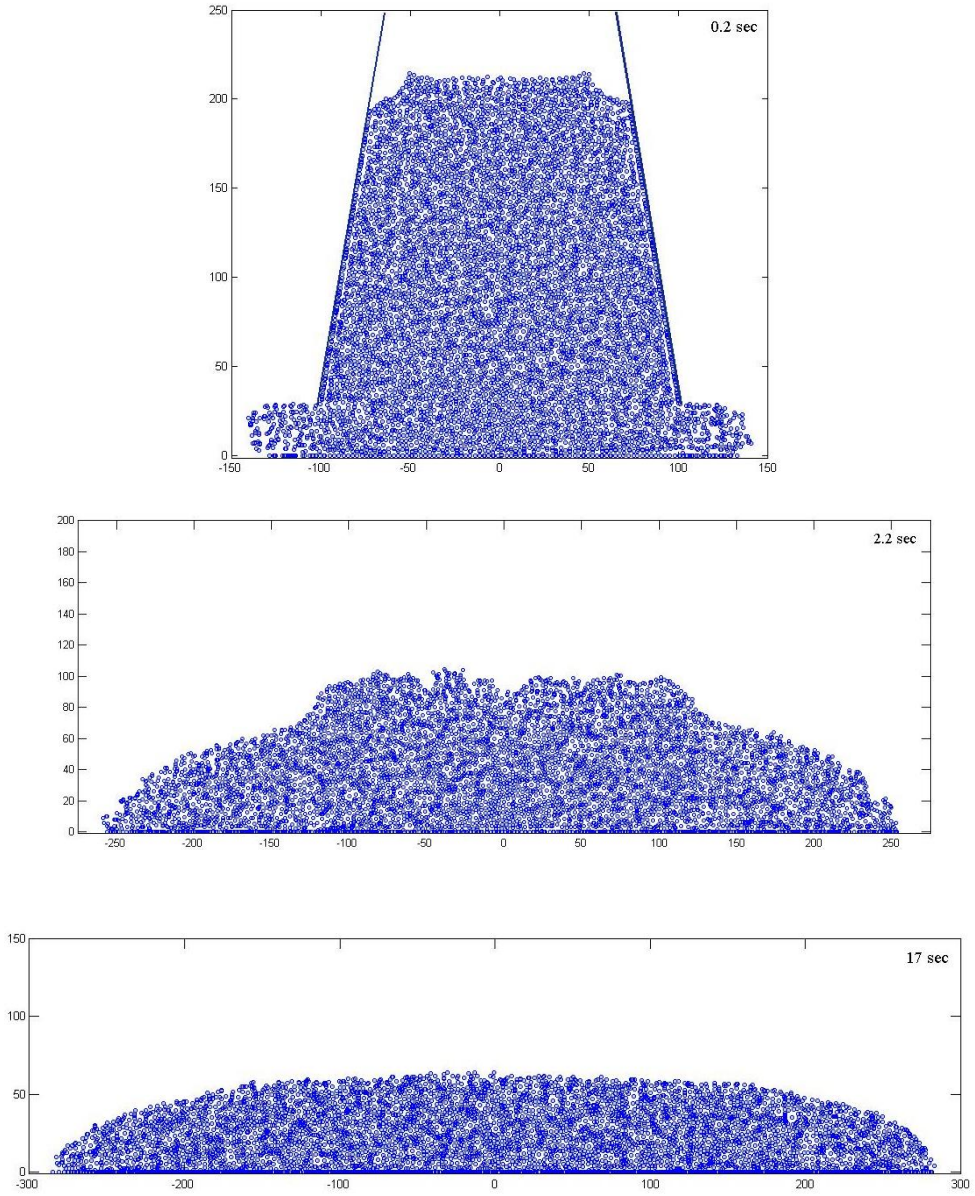

Figure 5.4: Horizontal flow of SCHPC Mix 4 after 0.2 sec, 2.2 sec and 17 Sec in axisymmetric configuration

It can be observed from the simulations illustrated in Figure 5.4 that the flow spread to a diameter of 500 mm in 2.2 sec, exactly as in the slump cone test in the laboratory. Equally importantly, the surface of the spread at 17 sec looks smooth as a 'pan cake' identical to that observed in the laboratory test on this mix (Mix 4, Figure 4.5 left). The only free variable that we altered in the simulation to get this exact fit was the dynamic coefficient of friction between the SCC mix and steel of the cone wall and of the base plate. The value which gave this excellent agreement with the test result was equal to 0.55 Ns/m. This value will remain unchanged in the 3D simulations below.

Here, and in the 3D simulations below, the simulations were stopped at 17 sec because of the excessive computational time involved. It should however be noted that the mix itself has not yet stopped flowing; it has only spread to a diameter of just about 600 mm after 17 sec, whereas it will only stop to flow when this diameter is 805mm (Table 5.2).

Despite the fact that the axisymmetric simulation reported above gave a good description of the flow behaviour of the SCC mix, the full and accurate picture can only be gained by a three-dimensional flow simulation; this will be presented in the following sections.

5.7.1.2 3D Slump cone test

In this section, 3D numerical simulations of the slump cone test of the same SCC mix (the SCHPC Mix 4, Table 4.2) are presented. These simulations highlight the distribution of the large aggregates in this mix (larger than or equal to 8 mm).

In the 3D simulations the volume of the mix in the cone was simulated by 23581 particles. Two simulations were performed; one in which the aggregates equal to or larger than 8 mm in size were treated separately from the viscous paste, and the second in which the entire volume of mix in the cone was treated as homogeneous.

Figure 5.5 illustrates the 3D simulation of the SCC mix (Mix 4, Table 4.2). It can be observed that the larger aggregates indeed stay homogenously distributed in the mix exactly as in the slump cone test in the laboratory at all times during the flow. Similar to the axisymmetric simulation, the surface of the spread at 17 sec looks smooth as a ‘pan cake’ identical to that observed in the laboratory test on this mix (Mix 4, Table 4.2). Moreover, the 3D simulation flow spread looks almost exactly as that in the actual test.

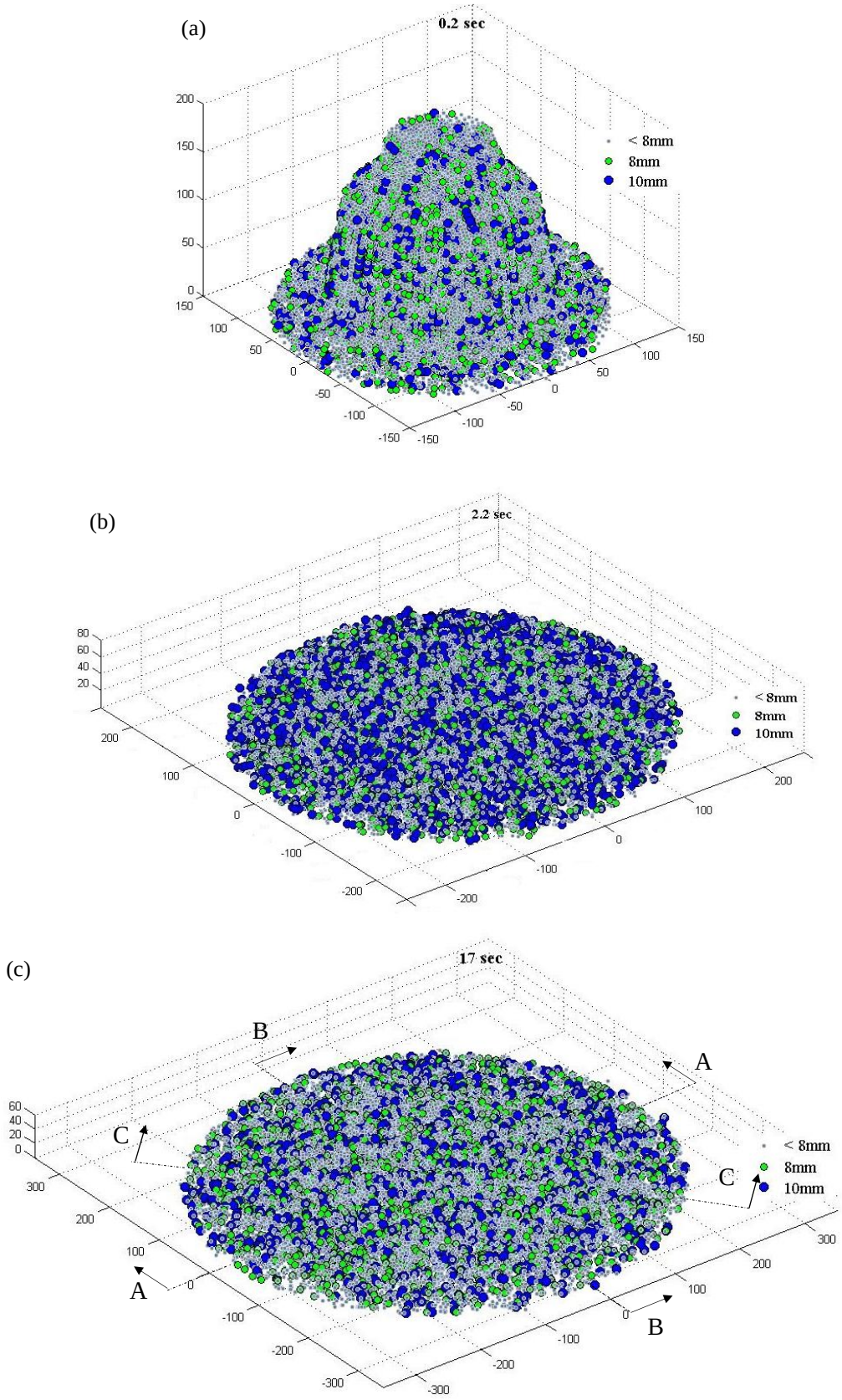

Figure 5.5. Horizontal flow of SCC Mix 4 after 0.2 sec, 2.2 sec and 17 sec in 3D configuration showing the large aggregates

By cutting the slump flow by diametrical planes (A, B and C as illustrated above in Figure 5.5(c)) after 17 sec flow time, the statistics of the large aggregates (≥ 8 mm) along these sections can be investigated.

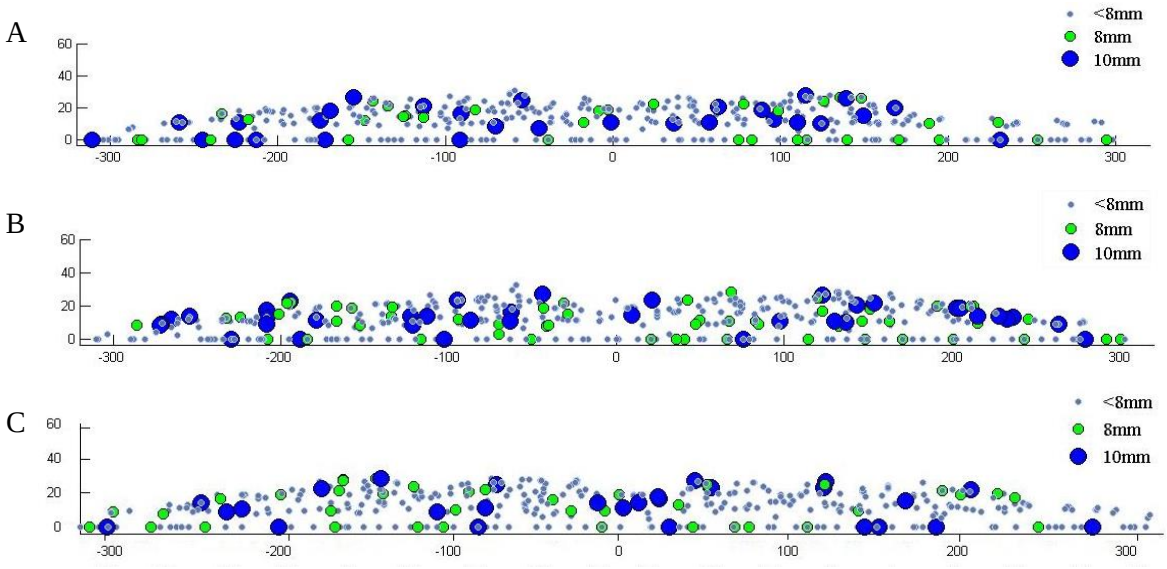

Figure 5.6. Diametrical cross-sections (A, B and C) of slump flow after 17 sec for Mix 4

Figure 5.6 shows how the aggregates are distributed in the diametrical cross-sections after 17 sec flow time with no visible settlement of the larger aggregates (≥ 8 mm).

That the larger aggregates are indeed distributed in an identical manner along these three sections can be ascertained by performing a statistical analysis of these aggregates using EasyFit software to estimate the best fit Probability Density Function (PDF) which in this case turns out to be the Weibull distribution function amongst the many distribution functions that were tried. It can be seen from the histograms in Figure 5.7 that the larger aggregate distribution is almost identical along the three cross-sections.

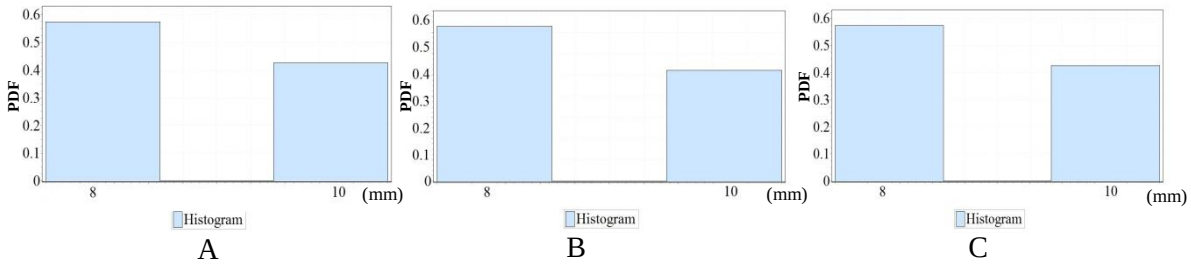

Figure 5.7. Histogram of larger aggregate distribution (≥ 8 mm) in Mix 4 along several diametrical cross-sections (A, B and C) after 17 sec flow time in the slump test

Figure 5.8 illustrates the numerical simulations of Mix 4 treated as a homogenous mass. As expected, in this case also, the flow spread to a diameter of 500 mm in 2.2 sec, exactly as in the slump cone test in the laboratory. Also, the top surface of the spread after 2.2 sec is smooth and looks similar to that observed in the laboratory test on this mix (Figure 4.5 left). A comparison of the simulations in Figures 5.5 and 5.8 confirms that Mix 4 is a good self-compacting mix in the sense that it flows as a homogeneous mass without any segregation of the heavier particles. Here, and in the simulations below, the simulations were stopped at 17 sec because of the excessive computational time involved. It should however be noted that the mix itself has not yet stopped flowing; it has only spread to a diameter of just over 600 mm after 17 sec, whereas it will only stop to flow when this diameter is 805mm (see, Mix 4, Table 4.2).

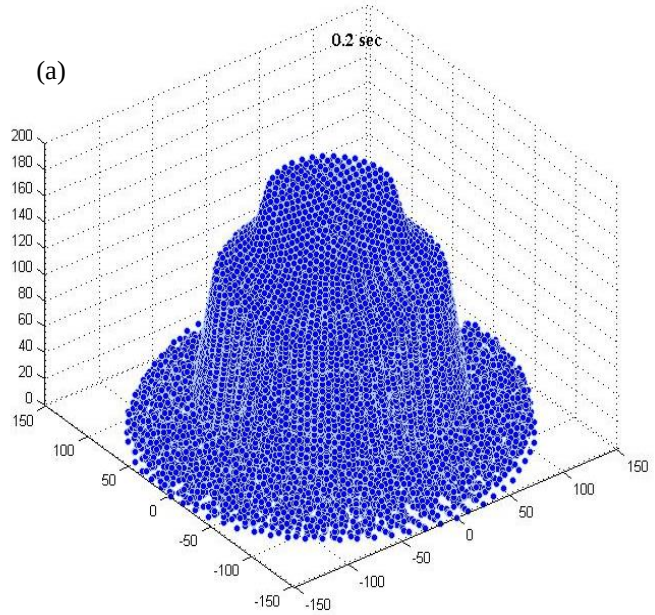

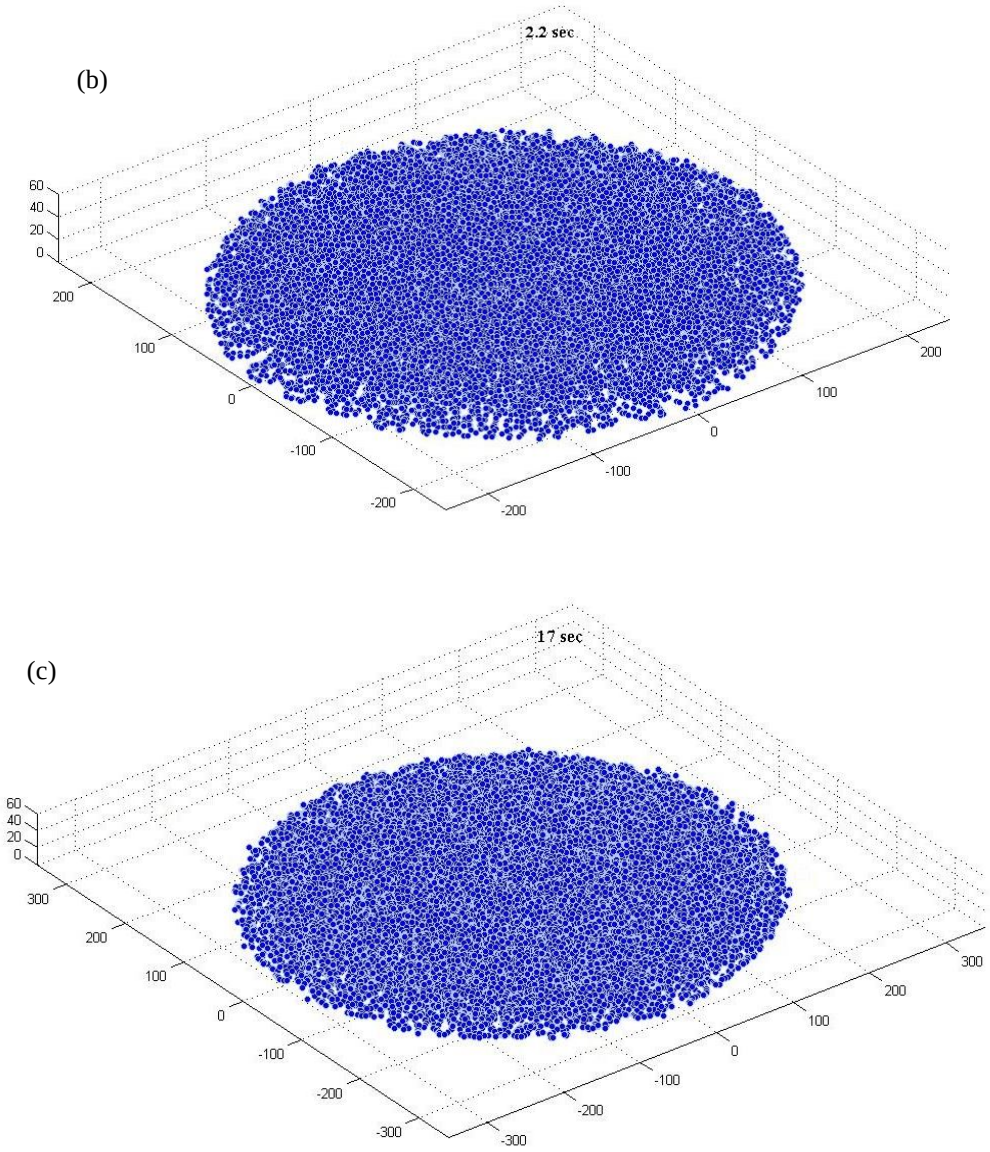

Figure 5.8. Horizontal flow of Mix 4 treated as a homogeneous mass after 0.2 sec, 2.2 sec and 17 sec in 3D configuration.

5.7.2 L-box test results

Other important properties of an SCC mix besides its flow-ability are the filling and passing ability. The filling ability, the blocking resistance and the segregation resistance are investigated in the L-box test. For that reason, 3-dimentional simulations of the same typical SCC mix (Mix 4, Table 4.2) were undertaken in the L-box configuration to examine the flow and filling characteristics of the SCC mix in a restricted area and its ability to pass through 3 steel bars without any segregation of its large components. The simulation results were also compared with the laboratory tests. In the 3D simulations the volume of the mix in the L-box

was simulated by 59568 particles. Similarly to the slump cone simulations, two simulations were performed; one in which the aggregates equal to or larger than 8 mm in size were treated separately from the viscous paste, and the second in which the entire volume of mix in the L-box was treated as homogeneous. The volume fractions of aggregates larger than or equal to 8 mm in SCHPC (Mix 4) and the number of particles representing them in the 3D L-box test simulation are reported in Table 5.1. The results of these simulations are illustrated in Figures 5.9 and 5.12.

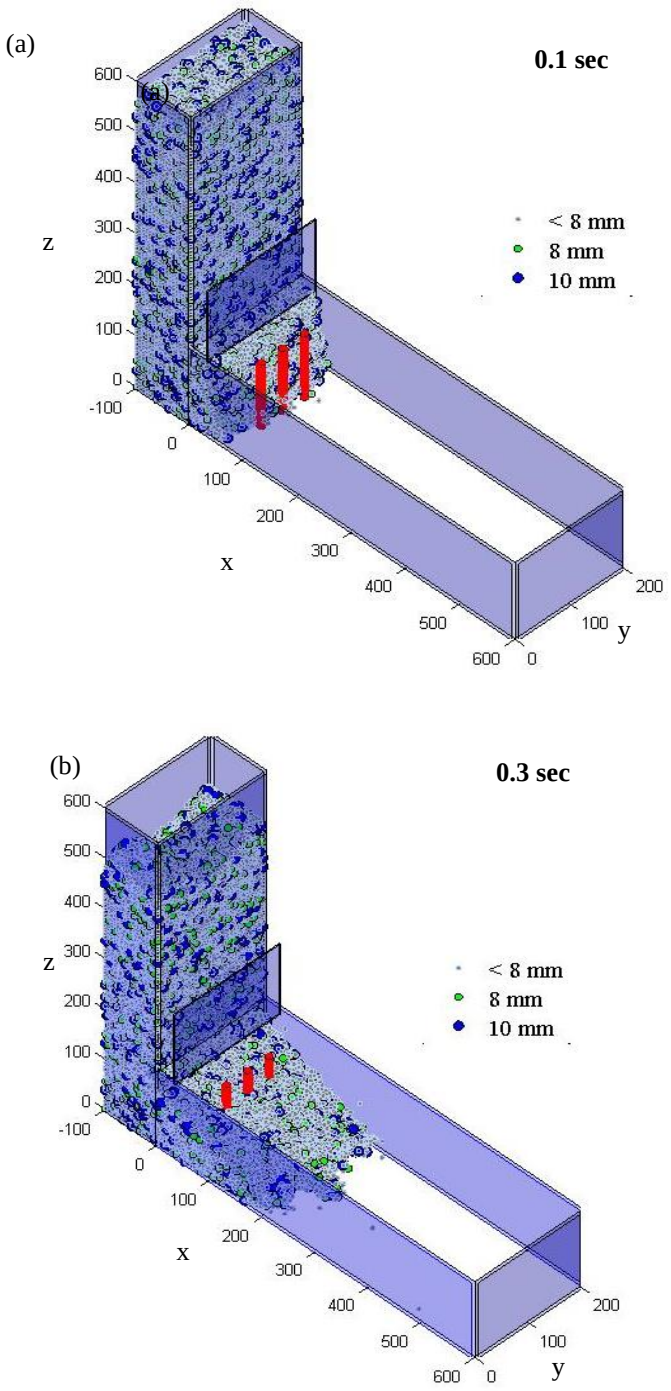

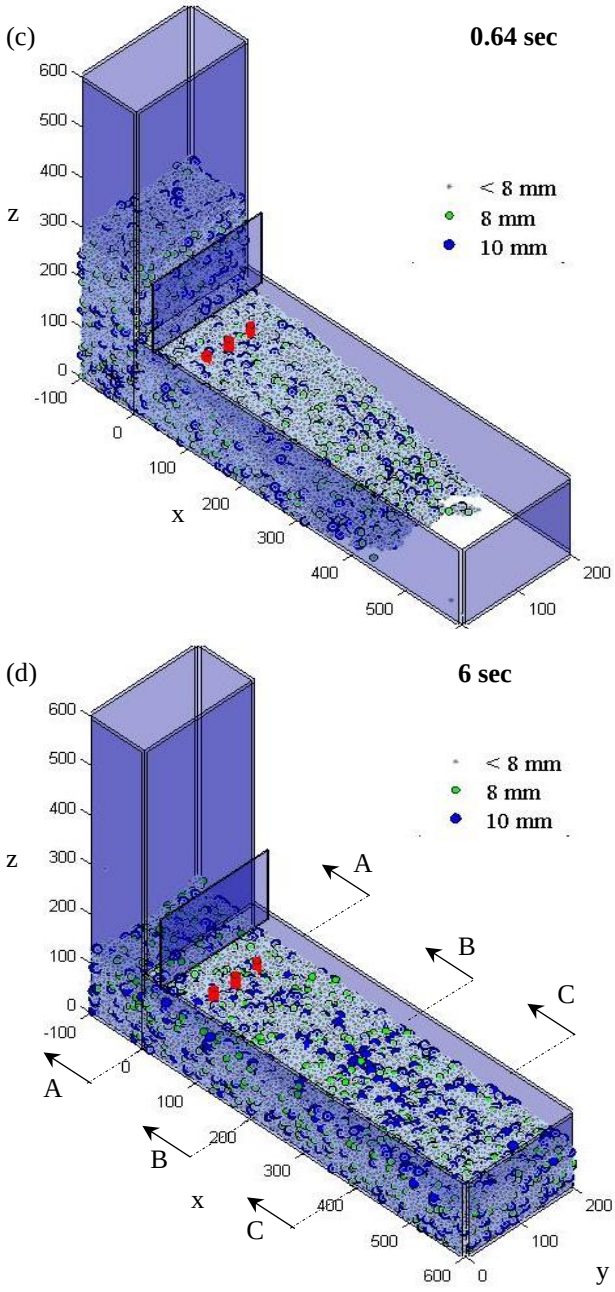

Figure 5.9: The flow of SCC mix 4 in the L-box test after 0.1 sec, 0.3 sec, 0.64 sec and 6 sec showing the large aggregates

As we can observed from the simulation results illustrated in Figure 5.9, the larger aggregates stay homogenously distributed at all times during the flow exactly as in the L-box test in the laboratory. The time needed for the mix to reach 200 mm and 400 mm were 0.3 sec and 0.64 sec, respectively. Furthermore, the ratio of the concrete height at the end of the horizontal section to the height of the remaining concrete in the vertical section is more than the minimum recommended value 0.8 (Tviksta, 2000); these results correlate very well with the

experimental results (Table 5.2).

By cutting the L-box by vertical planes (A, B and C as illustrated above in Figure 5.9(d)) after 6 sec flow time, the statistics of the large aggregates (≥ 8 mm) along these sections can be investigated.

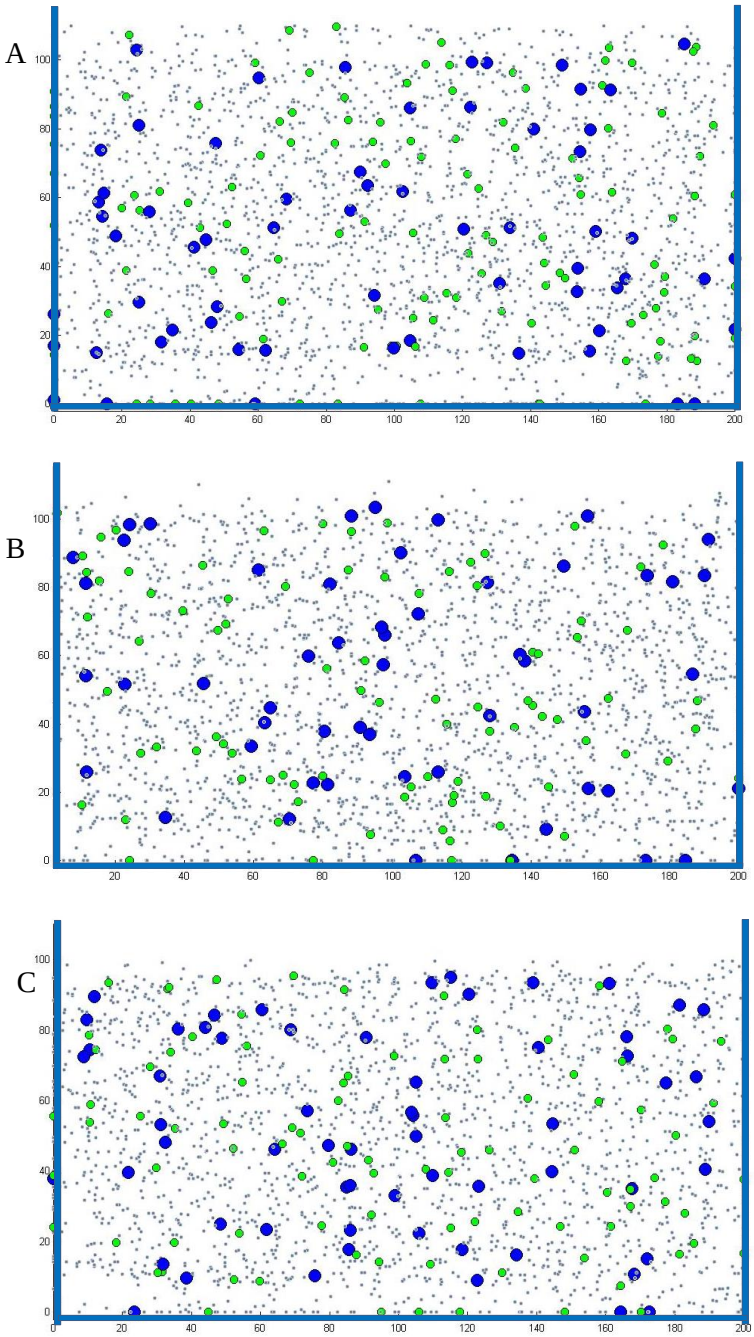

Figure 5.10. Vertical cross-sections (A, B and C) of L-box after 6 sec for Mix 4

Figure 5.10 shows how the aggregates are distributed in the vertical cross-sections after 6 sec flow time with no visible settlement of the larger aggregates (≥ 8 mm).

That the larger aggregates are indeed distributed in an identical manner along these three sections can be as in the case of slump test ascertained by performing a statistical analysis of these aggregates to estimate the best fit Probability Density Function (PDF) which in this case turns out to be the Weibull distribution function amongst the many distribution functions that were tried. It can be seen from the histograms in Figure 5.11 that the larger aggregate distribution is almost identical along the three cross-sections.

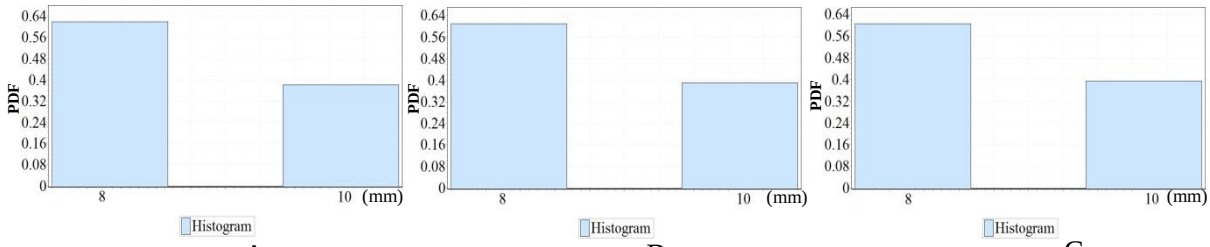

Figure 5.11. Histogram of larger aggregate distribution (≥ 8 mm) in Mix 4 along several vertical cross-sections (A, B and C) after 6 sec flow time in the L-box test

This 3-dimentional simulation notably presents an improvement over the 2-dimentional simulation results (Kulasegaram et al., 2011), thus achieving more realistic flow time of SCC in the horizontal section of the L-box. Table 5.3 compares the 2D and 3D simulation results of the L-box test with the laboratory results.

Table 5.3. A comparison between the flow time of the SCC mix (Mix 4) in the L-box in the 2D and 3D simulations with the laboratory test.

Flow times	2D simulation	3D simulation	Laboratory results
t_{200} (sec)	0.24	0.30	0.35
t_{400} (sec)	0.6	0.64	0.76
Level-off (sec)	5.9	6.00	7.23

In the 3D simulations, although the inclusion of the frictional resistance to the flow due to the vertical sides of the horizontal part of the L-box improves the flow time of SCC into the horizontal section of the L-box, and therefore gives more realistic flow times, there is an inevitable delay in manually lifting the gate to release the mix thus increasing the measured times. The larger the content of coarse aggregate and/or fibres in the mix, the more is the delay.

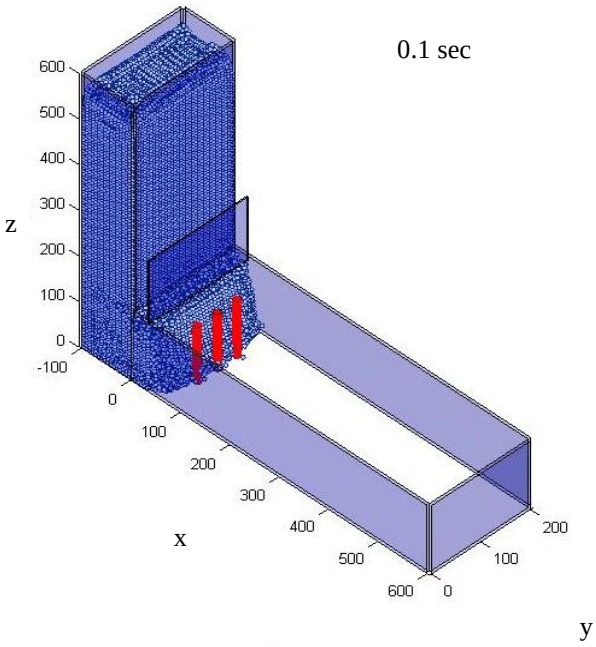
0.1 sec
z
600
500
400
300
200
100
0
-100
0
100
200
300
400
500
600
x
0
100
200
y

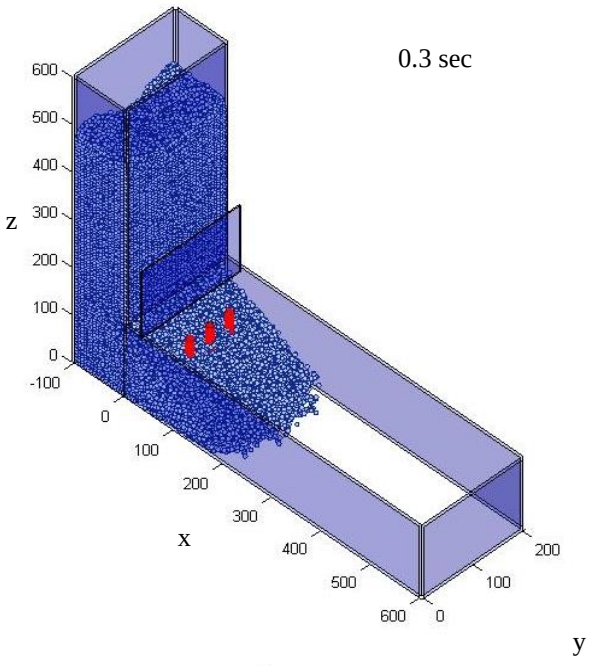
0.3 sec
z
600
500
400
300
200
100
0
-100
0
100
200
300
400
500
600
x
0
100
200
y

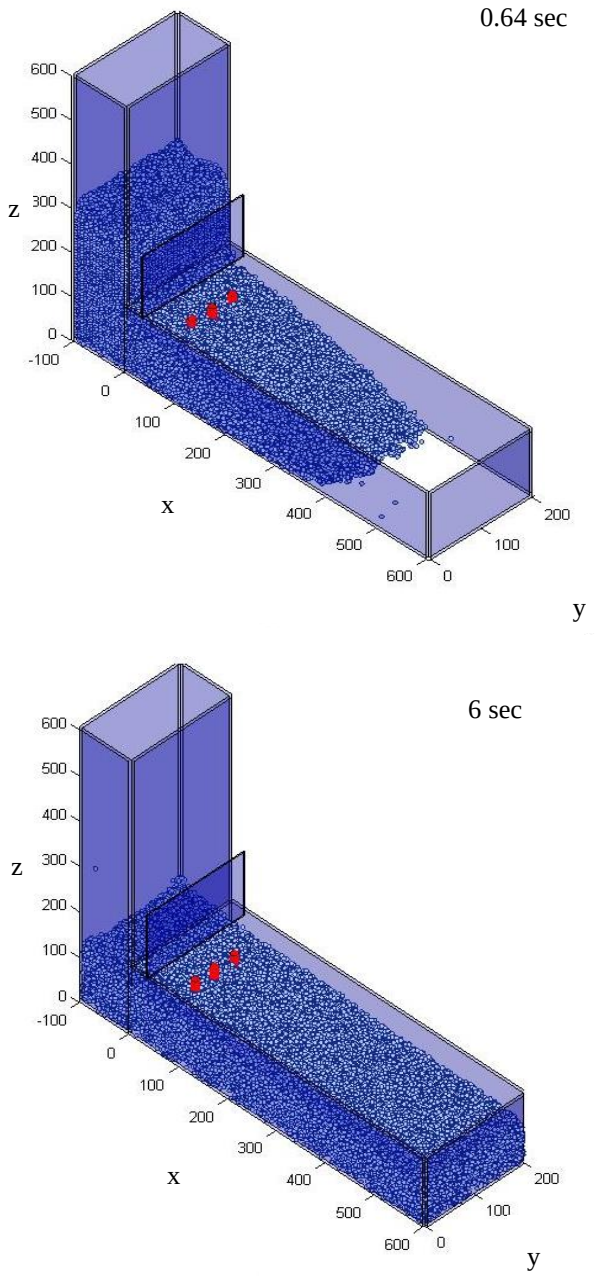

Figure 5.12: The flow of SCC mix 4 in the L-box test after 0.1 sec, 0.3 sec, 0.64 sec and 6 sec in as a homogeneous mass

Figure 5.12 illustrates the numerical simulations of SCHPC (Mix 4) treated as a homogenous mass. The filling behaviour of the 200 mm and 400 mm were undertaken in 0.3 sec and 0.64 sec, respectively, exactly as in the heterogeneous simulation illustrated above (Figure 5.9). Moreover, the surface of flow is smooth and looks identical to that observed in the laboratory test on this mix. The simulation results obtained here confirms that SCHPC Mix 4 is a good self-compacting mix in the sense that it flows as a homogeneous mass, fills all the far corners

of the box, and passes through reinforcement bars without any segregation of the heavier particles.

5.8 Critical remarks

A corrected Lagrangian SPH method has been used to simulate the flow of SCC mixes. A suitable Bingham model has been coupled with the Lagrangian momentum and continuity equations to model the flow. The mix characteristics of the SCC mix have been fully incorporated implicitly through the plastic viscosity, which has been calculated using the micromechanical model described in (Ghanbari & Karihaloo, 2009). All the self-compacting mixes developed in the Chapter 4 can be simulated in the slump cone test and the L-box test in 3D configurations in a similar manner of the simulations described in this Chapter. However, because of the excessive computational time involved in the 3-dimentional simulations, the simulations were performed only on one typical mix (Mix 4, Table 4.2). The simulation of SCC mixes without fibres followed the distribution of aggregates of different sizes (8 mm and 10 mm) throughout the flow. A comparison between the experimental and the simulation results is very encouraging. The developed numerical methodology is able to capture the flow behaviour of SCC mixes and to provide insight into the distribution of large aggregates during the flow.

In the 3D numerical simulations presented for SCC in both the slump test and L-box test, the total numbers of SPH nodal particles used were 23581 and 59568, respectively. This number of particles was chosen to obtain the results with adequate accuracy in a reasonable time. These simulations were carried out on a PC with 2GHz (XP850 Intel Core CPU) processor. For the slump test, the time taken for simulating the flow of SCC as a homogeneous mass or with various discrete coarse aggregates for 2.2 sec was approximately 40 hours. In the case of L-box, the time taken for the flow to reach 200 mm in 0.3 sec was about 9 hours. The lengthy computational time can be significantly reduced either by using high specification serial computers or by using high performance parallel computers. Since the particle methods such as SPH method are eminently suited for parallelisation, larger 3D configurations can be simulated within a reasonable computational time by the developed algorithms after appropriately parallelising them.

Chapter 6

Assessment of the orientation of short steel fibres during the flow of self-compacting concrete mix and determination of the fibre orientation factor

6.1 Introduction

With an increase in the compressive strength of concrete, its brittleness becomes an important structural integrity issue. To overcome this, short steel fibres are added to high strength concrete. They improve the ductility, toughness, and flexural and shear strengths of cement-based materials by bridging the micro- and macro-cracks and preventing their coalescence (Boulekbachea et al., 2010).

The properties of short steel fibre-reinforced composites are largely determined by the fibre content, the fibre aspect ratio, fibre orientation and the properties of the matrix itself. The efficiency of short fibres in a composite material decreases from 100 per cent when the fibres are all aligned along the major tensile stress to just 30 % when the fibres are randomly distributed (Martinie and Roussel, 2011). As the fibre orientation changes throughout the production of the composite, it is important to understand these changes. This has been the focus of scientific research for several decades. Most of the research has concentrated on the visual counting of cut concrete sections after casting in the hardened state (Zak et al., 2001; Bernasconi et al., 2012; Lee et al., 2002) and the prediction of the average orientation factor of fibres in the cut sections (Martinie and Roussel, 2011). In this Chapter, a simple method has been developed to assess the orientation of short steel fibres in self-compacting concrete mixes during flow. The flow of high strength SCC mixes (compressive strengths in the range 100-160 MPa; Mix 6 and Mix 8 developed in Chapter 4) which contain between 0.5 and 2.5% by volume steel fibres has been first modelled using three-dimensional Lagrangian smooth particle hydrodynamics (SPH) (Deeb et al., 2013a) in the slump cone and L-box configurations. These simulations will provide an insight into the distribution of fibres and their orientations during the flow. A two-dimensional or axisymmetric simulation of such mixes (Kulasegaram and Karihaloo, 2013) is rather misleading because all the fibres appear in a single plane. The accurate picture can only be gained by using the three-dimensional flow simulation which shows the actual distribution of fibres and their orientations during the flow.

A probability density function (PDF) has been introduced to represent the fibre orientation variables in three dimensions. Moreover, the orientation variables of each individual fibre in an

arbitrary two dimensional cross-section have been calculated using the geometrical data obtained from the three dimensional simulations. These will be useful to determine the fibre orientation factor in practical image analysis on cut sections, as will be demonstrated later in this Chapter (Deeb et al., 2013b).

6.2 Modelling the flow of self-compacting fibre-reinforced concrete

A number of computational modelling strategies have been attempted to model the distribution of fibres and their orientation during the flow. For instance, numerical techniques such as the discrete element method (Dupont and Vandewalle, 2005) or the lattice Boltzmann technique (Svec et al., 2012) can be used to model the SCC fluid flow with fibre suspensions. These numerical techniques or computational methodologies have their own merits and drawbacks in solving SCC flow with suspended fibres. However, it would seem natural, simpler and more appropriate to use mesh-less particle based Lagrangian numerical techniques to simulate the flow and to monitor the distribution of fibres and their orientation during the flow.

A three-dimensional Lagrangian smooth particle hydrodynamics (SPH) method, fully described in Chapter 5, has been used to simulate the flow of SCHPFRC/SCUHPFRC (Deeb et al., 2013a) in the slump cone and L-box configurations. The simulation of self-compacting high- and ultra-high-performance concrete containing short steel fibres is focused on the distribution of fibres and their orientation during the flow. The methodology based on SPH used here to monitor the fibres during the flow was proposed by Kulasegaram and Karihaloo (2013). The key points of this methodology are the following:

- The ends of a fibre are represented by two particles and the assigned volume of the fibre is equally divided between them. These particles are tagged throughout the simulation process and the distance between them is maintained equal to the fibre length. For particles representing heavier and/or larger constituents in the viscous continuum, the assigned volume is equal to the ratio of actual mass to the density of continuum.

- A fibre is regarded as a rigid body that undergoes only rotational and translational motion during the flow in a viscous fluid.
- Both fibre and fluid particles behave as a homogeneous mass and have the same continuum properties except their assigned volumes.
- Fibre orientation is mainly dictated by the fluid flow of the homogeneous SCC mix rather than the mass of fibres. It is therefore feasible to assume that the positions of the ends of fibre are largely controlled by the fluid particles surrounding them. This assumption will be later confirmed.
- Fibres are generated randomly, maintaining a constant distance between their ends equal to the fibre length L_0. The distance L_{n+1} at a subsequent time step t_{n+1} between the particles representing the ends of a fibre was calculated (Figure 6.1) and forced to be equal to L_0 within an acceptable error.

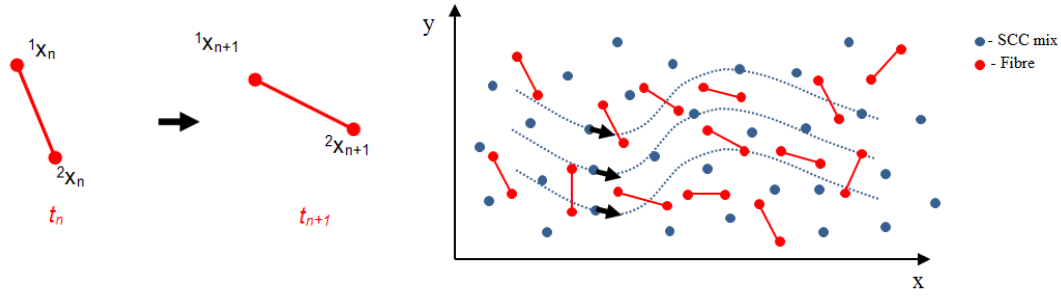

Figure 6.1: Fibre orientations at time steps t_n and t_{n+1}

The key steps involved in enforcing the constant distance between the pair of particles representing a fibre can be summarised as follows (Kulasegaram & Karihaloo, 2013), once the particle positions are updated using Equation (5.30) from time step t_n to t_{n+1}.

Step 1: Check whether the distance (L_{n+1}) between the pair of particles representing each and every fibre is equal to the fibre length (L_0) within an acceptable error.

Step 2: If $|L_{n+1} - L_0| > 10^{-5}$ for a certain fibre, then equal and opposite penalty forces F_P proportional to $|L_{n+1} - L_0|$ are introduced in Equation (5.23) on the pair of particles representing that fibre along the vector connecting this pair of particles. The penalty force can be calculated as

follows $F_p = \frac{\lambda mgH}{L_0^2}(L_0 - L)$ where λ represents a penalty factor (between 1 to 10), m particle mass, g gravitational acceleration, H maximum height (or depth) of the SCC mix as per initial configurations, L_0 fibre length and L distance between particles representing a given fibre. When $L < L_0$, F_p is a repulsive force otherwise it is an attractive force.

Step 3: The Equations ((5.23), (5.25), (5.29), (5.26) and (5.30)) are now solved again sequentially to determine the positions of all the particles.

Step 4: Steps 1 to 3 are repeated until the pairs of particles representing all the fibres satisfy the condition $|L_{n+1} - L_0| < 10^{-5}$.

Based on the formulation detailed above, suitable numerical schemes which integrate the Lagrangian SPH approximations of the governing equations with the rheological Bingham model for SCC have been developed. These numerical schemes have been utilised to understand the behaviour of SCC flow containing short steel fibres.

6.3 Modelling results of self-compacting fibre reinforced concrete

6.3.1 3-dimensional slump cone test for mixes with fibres

To investigate how the short steel fibres will distribute and orient themselves during the flow, the slump cone tests of two mixes with fibres (Mixes 6 and 8 in Tables 4.2 and 4.3) were simulated. In these simulations, the total number of particles used was also 23581. The short steel fibres were treated as explained above. The number of fibres in each of these mixes was calculated from their volume fraction (0.5% in Mix 6 and 2.5% in Mix 8) (see Table 6.1).

Table 6.1. Volume fraction of fibres in (Mix 6) and (Mix 8) and the number of particles representing them.

	Mix 6	**Mix 8**
Total number of particles	23581	23581
Volume fraction of fibres (%)	0.5	2.5
Number of fibres	118	590
Number of fibre end particles	236	1180
Assigned volume/particle (mm^3)	366.20	381.52

The plastic viscosity of these mixes is of course much larger than that of mixes without fibres (see Table 4.5). Apart from the different plastic viscosities of the mixes, their yield stress (200 Pa) and the dynamic coefficient of friction with the steel wall of the cone and the base plate (0.55 Ns/m) are the same as for an SCC mix without fibres. Table 6.2 shows the material parameters of Mix 6 and Mix 8.

Table 6.2. The material parameters of the SCC mix (Mix 6 and Mix 8).

Constituents	**Mix 6**	**Mix 8**
Flow spread (mm)	760	850
t_{500} (sec)	3.00	3.00
t_{200} (sec)	1.88	1.90
t_{400} (sec)	5.10	5.60
Level-off (sec)	38.00	54.00
Plastic viscosity (Pa.s)	42.10	54.30
Yield stress (Pa)	200	200
Compressive strength (MPa)	**100**	**160**

Figures 6.2 and 6.3 show the distribution of fibres and their orientation during the flow of SCHPFRC (Mix 6) and SCUHPFRC (Mix 8), respectively. The time for the mixes to spread to a diameter of 500 mm (t_{500} = 3 sec) matches exactly the time measured in the laboratory (Table 4.3). The surface of the spread is smooth and the fibres stay homogeneously distributed at all times during the flow.

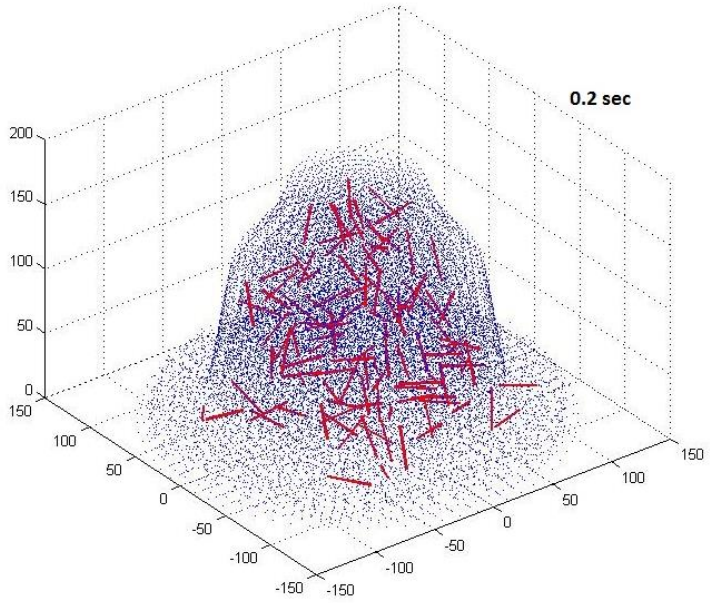
0.2 sec
200
150
100
50
0
150
100
50
0
-50
-100
-150
-150
-100
-50
0
50
100
150

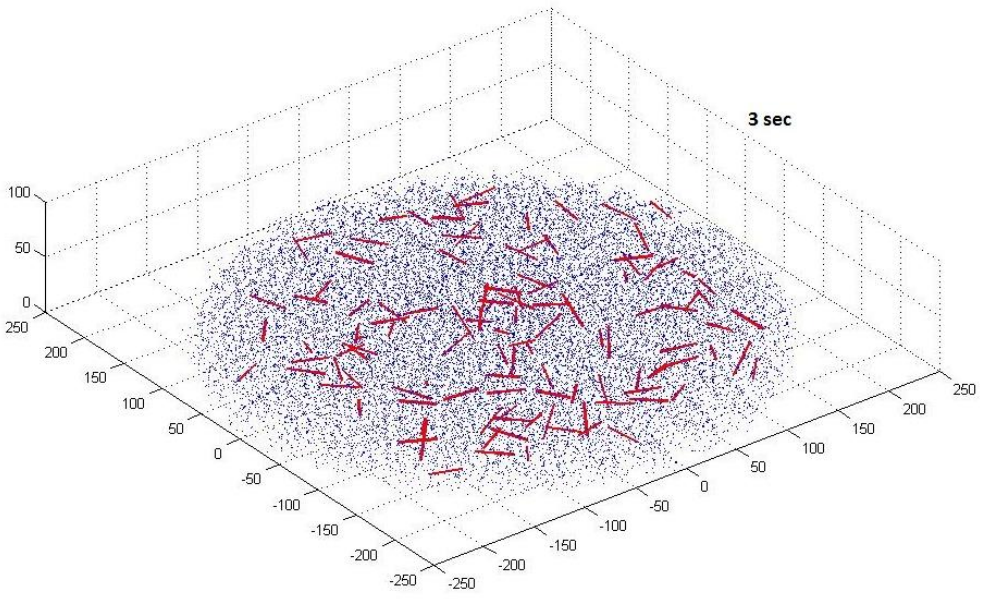
3 sec
100
50
0
250
200
150
100
50
0
-50
-100
-150
-200
-250
-250
-200
-150
-100
-50
0
50
100
150
200
250

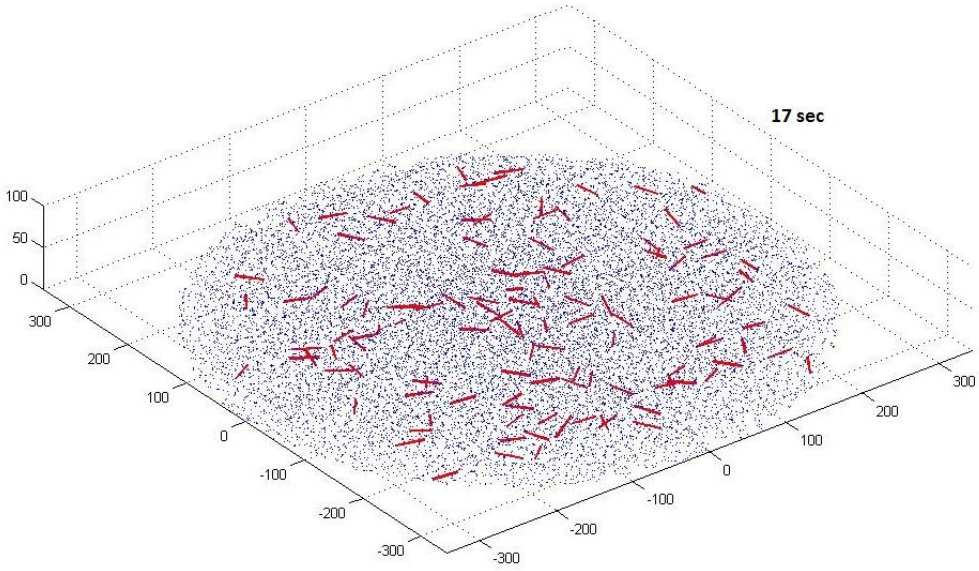

Figure 6.2: Horizontal flow of SCHPFRC (Mix 6) after 0.2 sec, 3 sec and 17 sec in 3D configuration

The simulation results illustrated in the Figures 6.2 and 6.3 which show the actual distribution of fibres and their orientation during the flow give a highly accurate picture of their rigid body motion compared with the 2D simulation (Ghanbari, 2011).

(a)

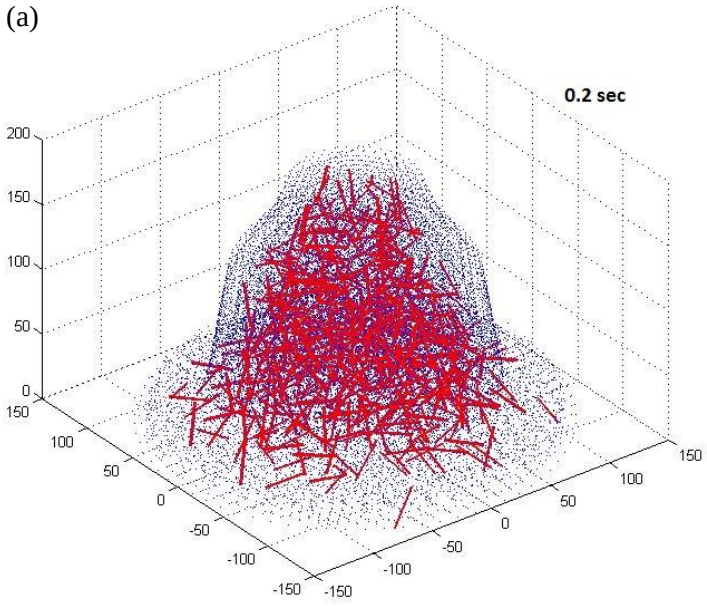

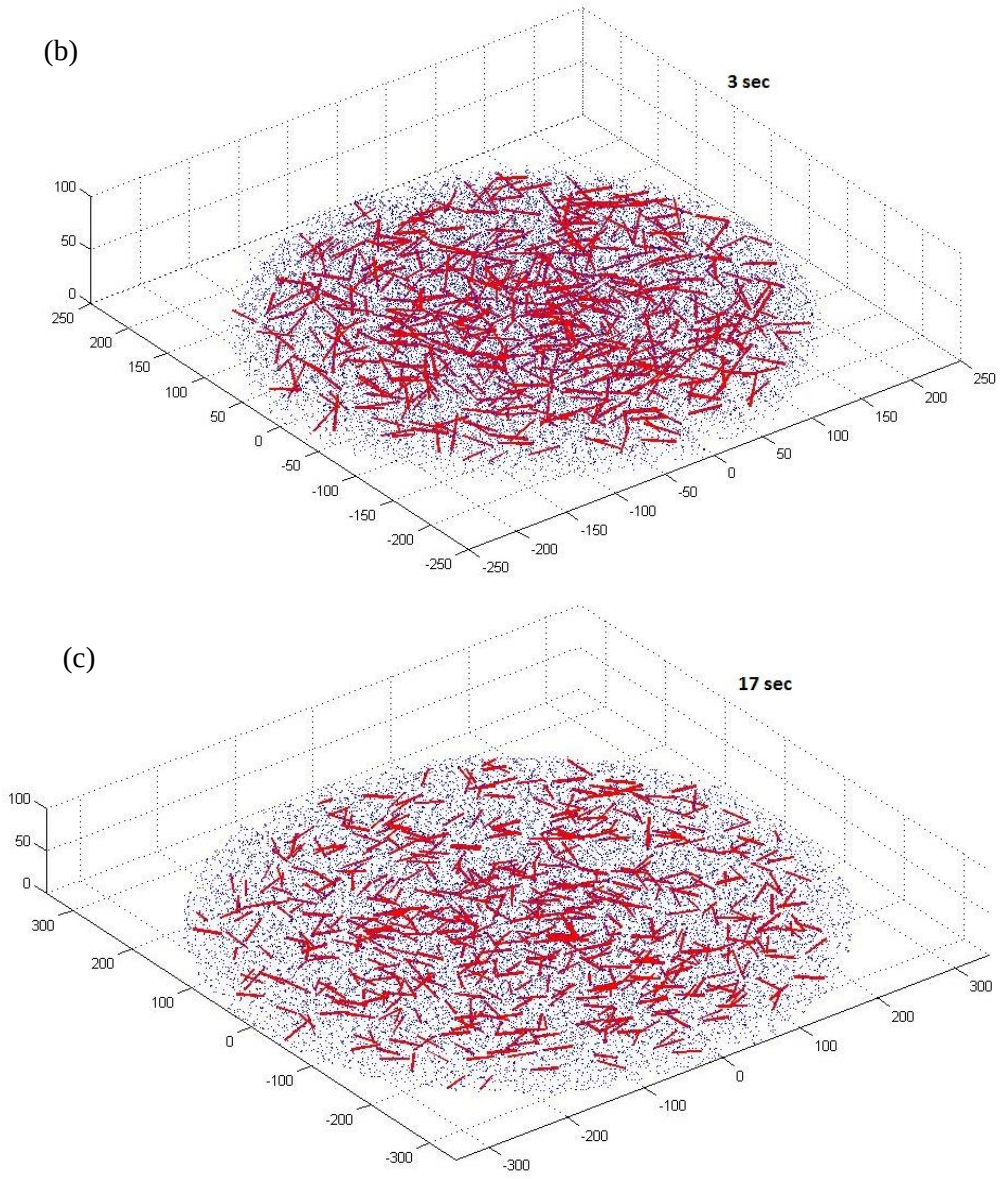

Figure 6.3: Horizontal flow of SCUHPFRC (Mix 8) after 0.2 sec, 3 sec and 17 sec in 3D configuration

The proposed method can be effectively applied in the numerical simulation of SCC flow to analyse the filling behaviour of these highly viscous fluids. The numerical results are in excellent agreement with test results and confirm that the 3D SPH methodology is capable of predicting accurately the flow of SCC with fibres.

In the numerical simulations presented above for SCC with fibres, the total number of SPH nodal particles used was 23581. As in the case of SCC without fibres, this number of particles was

chosen to obtain the results with adequate accuracy in a reasonable time. These simulations were carried out on the same serial computer (XP850 Intel Core CPU) and the time taken for simulating the flow for 3 sec was approximately 65 hours. The time taken for the simulation of SCC flow with fibres was longer than that of SCC without fibres by 15 to 20%. This is due to the iterative computation performed in the simulation of SCC flow with fibres to enforce the constant fibre length between particles representing fibre end points. In the numerical simulations shown above, to ensure that the front of the SCC flow has a smooth profile, the velocities of the particles obtained by Equation (5.26) were smoothed by the following equation

$$\bar{\mathbf{v}}(\mathbf{x}_a) = \sum_{b=1}^{N} V_b \mathbf{v}_b W_b(\mathbf{x}_a) \tag{6.1}$$

where $\bar{\mathbf{v}}(\mathbf{x}_a)$ is the smoothed velocity of particle '*a*'. This velocity was then used in Equation (5.30) to calculate the updated position of particle '*a*'. In a similar manner, all the particle velocities and positions were smoothed and updated. This smoothing procedure also adds to the total computational time taken by the numerical simulations.

In order to get a better understanding of how the mix flows just after its initiation, the velocity vector fields of the paticles are plotted for Mixes 4, 6 and 8 (Figure 6.4) at 0.2 sec flow time.

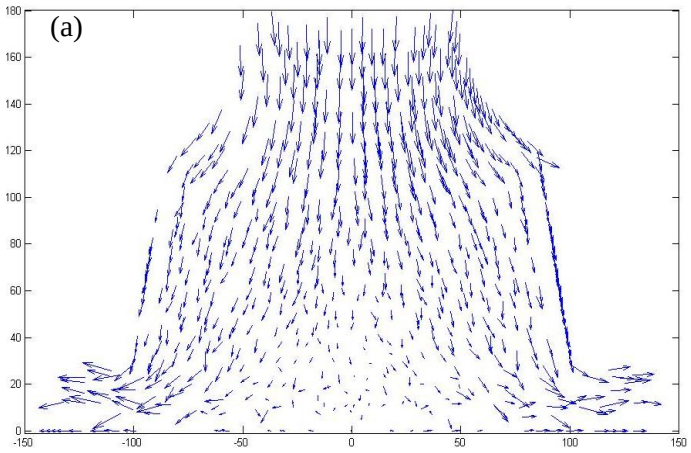

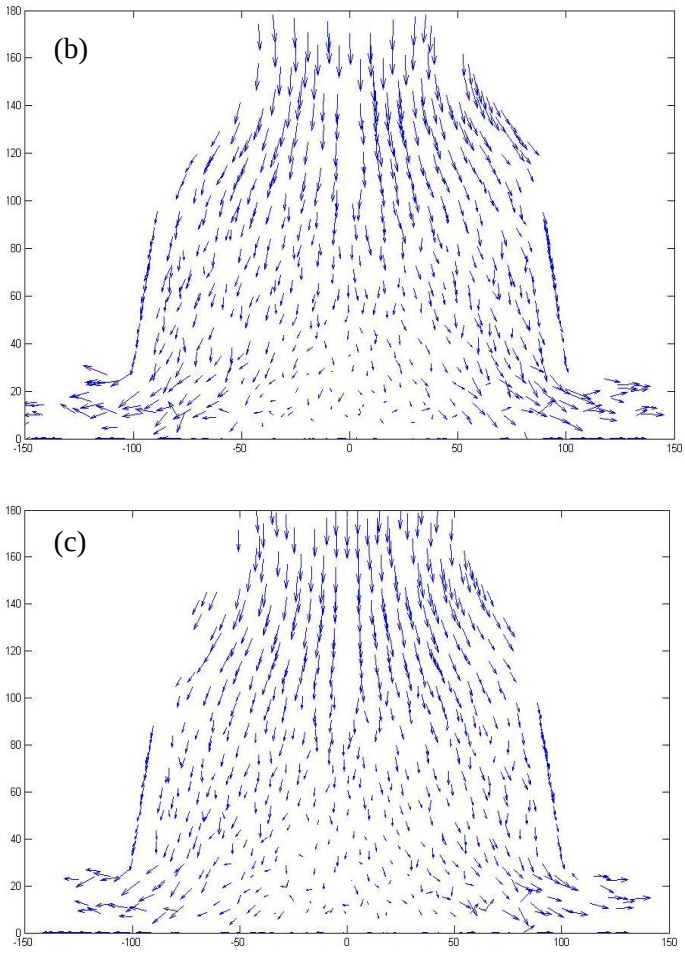

Figure 6.4. Velocity vectors of SCC particles for Mix 4 (a), Mix 6 (b) and Mix 8(c) at 0.2 sec flow time

As expected, the particles in the top portion of the cone are essentially in gravitational flow, (i.e. the vertical component of the velocity vector field is dominant) with negligible horizontal velocity components, so that these particles do not have enough time to make contact with the surface of the cone as it is being lifted. This explains why the top portion of the mix breaks off from the cone surface. However, as the plastic viscosity of the mix increases, the magnitude of the vertical component of the velocity vector field decreases (cf. Figure 6.4(a) and 6.4(c) or Figure 5.8(a) and Figure 6.3(a)) and the transition from no contact with cone surface to full contact is less pronounced.

6.3.2 3-dimensional L-box test for mixes with fibres

The two mixes (Mix 6 and Mix 8 in Tables 4.2 and 4.3) were further simulated in the L-box configuration to investigate how the short steel fibres will pass through reinforcement bars, redistribute and reorient themselves during the flow. In these simulations and because of the inclusion of 30 mm long steel fibres, only two steel bars will be used as obstacles in the L-box apparatus. The distance between the bars is shown in Figure 4.11. The number of particles used here was 59568, exactly as used in the simulation of the SCC mixes without fibres. This number of particles gives an adequate accuracy in a reasonable time. The short steel fibres were treated as explained above in the Section 6.2. The number of fibres in each of these mixes was calculated from their volume fraction (0.5% in Mix 6 and 2.5% in Mix 8) (see Table 6.3). The material properties of the two mixes were given in Table 6.2.

Table 6.3. Volume fraction of fibres in (Mix 6) and (Mix 8) and the number of particles representing them.

	Mix 6	**Mix 8**
Total number of particles	59568	59568
Volume fraction of fibres (%)	0.5	2.5
Number of fibres	298	1490
Number of fibre end particles	596	2980
Assigned volume/particle (mm^3)	340.46	354.66

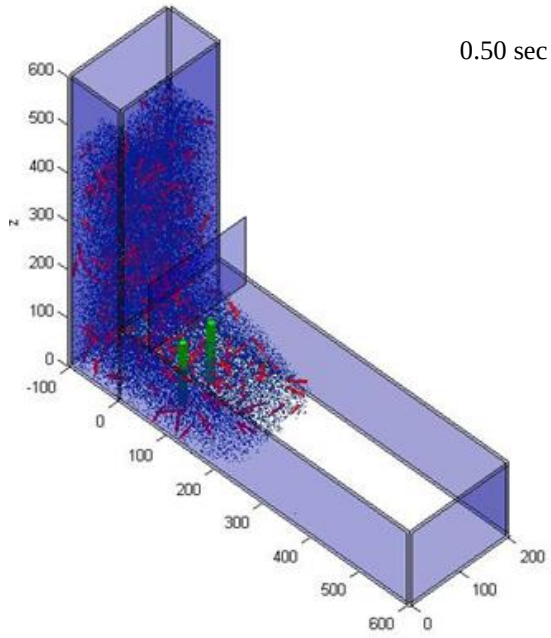
0.50 sec
z
600
500
400
300
200
100
0
-100
0
100
200
300
400
500
600
0
100
200

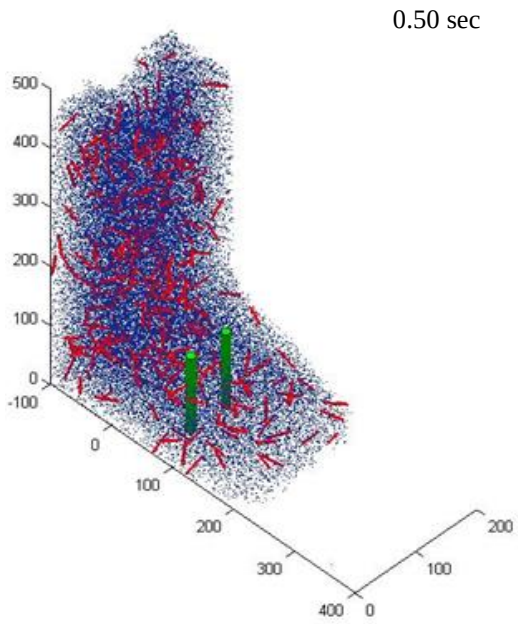
0.50 sec
500
400
300
200
100
0
-100
0
100
200
300
400
0
100
200

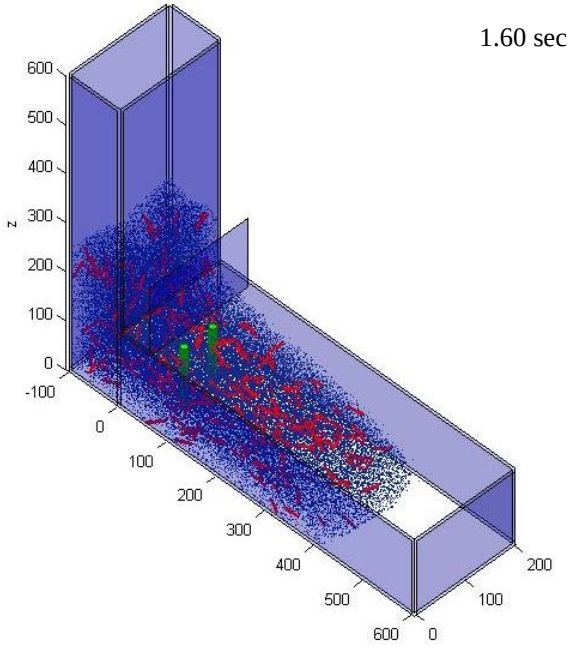
1.60 sec
z
600
500
400
300
200
100
0
-100
0
100
200
300
400
500
600
0
100
200

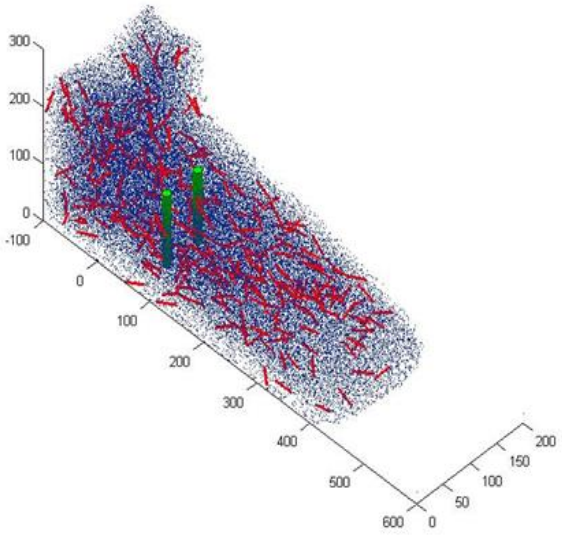
1.60 sec
300
200
100
0
-100
0
100
200
300
400
500
600
0
50
100
150
200

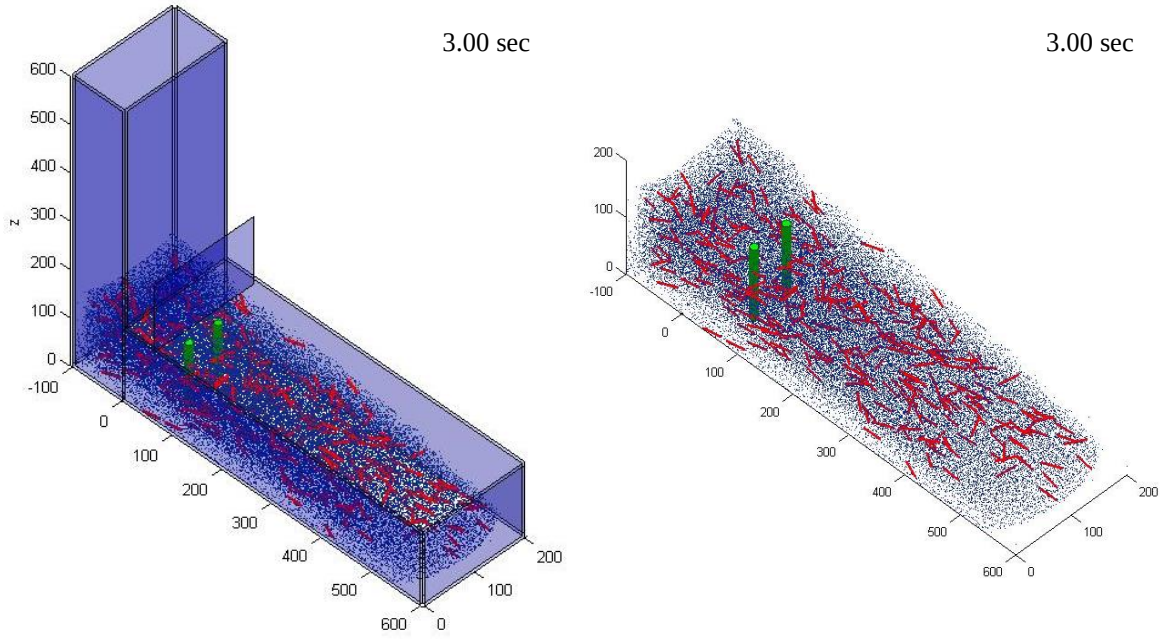

Figure 6.5: The flow of SCHPFRC mix (Mix 6) in the L-box test after 0.50 sec, 1.60 sec and 3.00 sec (For clarity of presentation, the images on the right show the flow without the box).

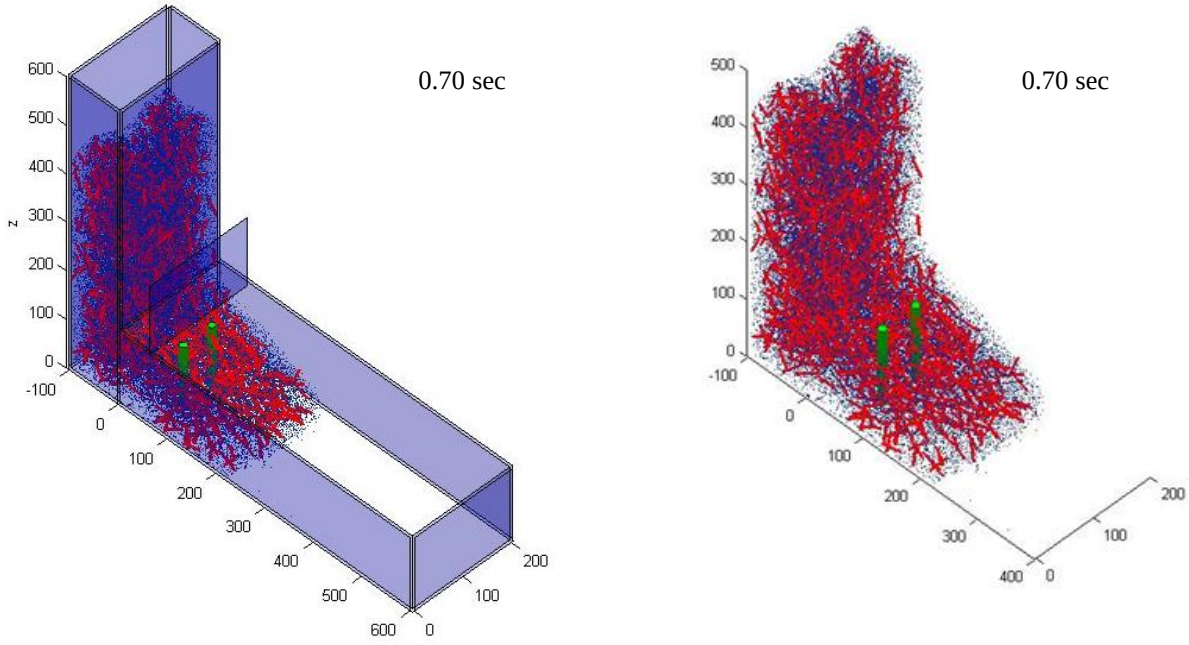

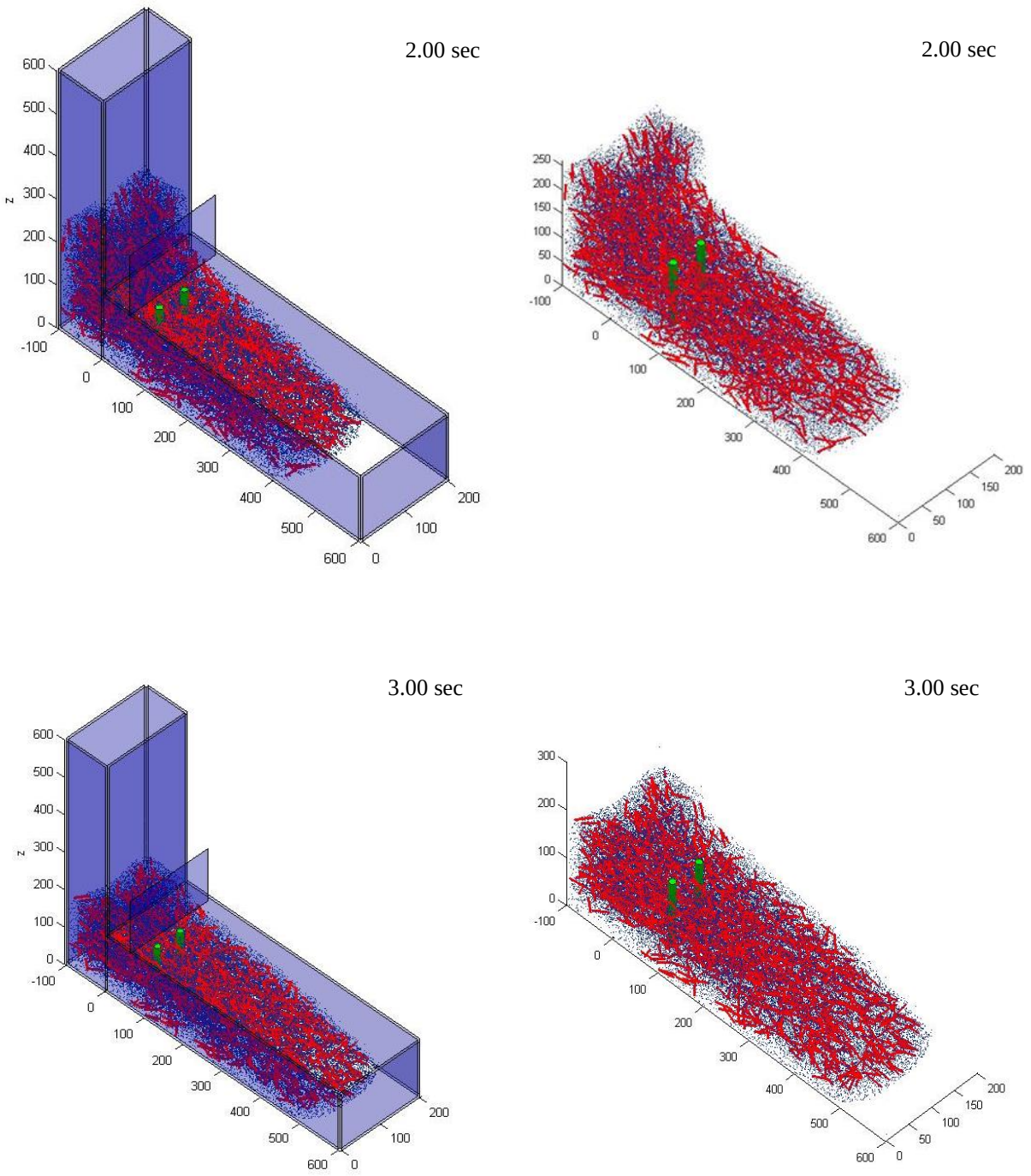

Figure 6.6: The flow of SCUHPFRC mix (Mix 8) in the L-box test after 0.70 sec , 2.00 sec and 3.00 sec (For clarity of presentation, the images on the right show the flow without the box).

The time needed for the Mix 6 to reach 200 mm and 400 mm from the gate was 0.5 sec and 1.6

sec, while for Mix 8, the time taken was 0.7 sec and 2 sec (Figures 6.5 and 6.6). Fibres are homogenously distributed in the mix at all times during the flow in both Mix 6 and Mix 8, exactly as observed on the same mixes in the laboratory, thus proving the effectiveness of the proposed method to analyse the filling and the passing ability of these highly viscous fluids. The 3D simulations of the two mixes with fibres represent an improvement over the 2D simulations, as is clear from Table 6.4, especially at t_{200}. Nevertheless, based on the simulation results of both mixes, the remark made in Chapter 5 about the inevitable delay associated with opening the gate and therefore an increase in the measured times has been borne in mind here, too. This delay appears to be longer with mixes containing fibres (Mix 6 and Mix 8), because of the increased pressure behind the gate and the friction between the gate and the mix, which make opening of the gate in a single lift very difficult. This problem needs to be solved by devising a new method for automatic opening of the gate.

Table 6.4. A comparison between the flow times of the SCC mixes (Mixes 6 and 8) in the 2D and 3D simulations with the laboratory test

Flow times	2D simulation		3D simulation		Laboratory results	
	Mix 6	Mix 8	Mix 6	Mix 8	Mix 6	Mix 8
t_{200} (sec)	0.40	0.50	0.50	0.70	1.88	1.90
t_{400} (sec)	1.60	2.00	1.60	2.00	5.10	5.60
Level-off (sec)	38.00	50.00	-	-	38.00	54.00

6.4 Fibre orientation distribution in the slump cone and L-box tests

Short steel fibres are distributed randomly during the production of a self-compacting concrete mix. However, they alter their orientations during the placement process. It is vital to know how they are distributed and oriented at the end of this process, because the performance of the fibre reinforced SCC in the hardened state is largely dictated by their alignment relative to the major tensile stresses in the cast structural element.

As mentioned above, two particles represent the ends of each fibre and these particles are tagged throughout the flow of the SCC and the distance between them is maintained equal to the fibre length. The coordinates of ends of each fibre i, $s_i(x_{si}, y_{si}, z_{si})$ and $e_i(x_{ei}, y_{ei}, z_{ei})$ are therefore known during the flow. It is thus easy to track the orientation of each individual fibre represented by angles θ_i and φ_i throughout the flow of SCC, where θ_i spans between 0 and 90°, and φ_i between 0 and 360°, as illustrated in Figure 6.7.

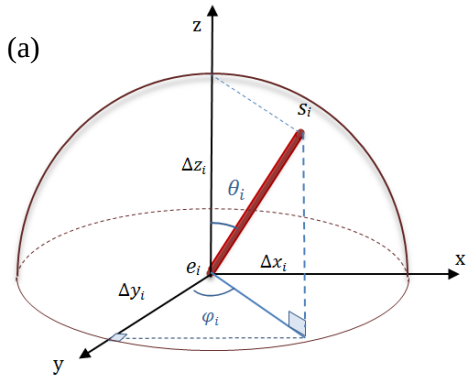

Figure 6.7: Fibre orientation in three dimensions

From Figure 6.7 it follows that

$$\tan\ \theta_i = \left(\sqrt{\Delta x_i^2 + \Delta y_i^2}\right)/\Delta z_i \tag{6.2}$$

$$\tan\varphi_i = \Delta x_i / \Delta y_i \tag{6.3}$$

We now introduce a Probability Density Function (PDF) of the fibre orientations $f(\theta,\varphi)$ at an arbitrary instant t during the flow. The PDF satisfies

$$\int_0^{2\pi}\int_0^{\frac{\pi}{2}} f(\theta,\varphi)\sin\theta\, d\theta\, d\varphi = 1.$$

Next, we perform a statistical analysis of the fibre orientations at different times during the flow to estimate the best fit PDF using EasyFit software. The Johnson SB distribution function (Johnson, 1949), which has been successfully used in marine (Fonseca et al., 2009) and forestry (Rennolls and Wang, 2005) science, was found to fit our simulated data the best from among 55

different distribution functions tried, including the Gamma, Gaussian, uniform, log-normal, Weibull distributions, etc.

$$f(x) = \frac{\delta}{\lambda\sqrt{2\pi}z(1-z)}\exp\left(-\frac{1}{2}\left(\gamma + \delta\ln\left(\frac{z}{1-z}\right)\right)^2\right) \tag{6.4}$$

$$z = \frac{x-\xi}{\lambda} \tag{6.5}$$

Equation (6.4), in which x stands for θ or φ represents the most probable fibre density function for each of the two uncorrelated variables θ, φ. Here, $\lambda > 0$ is a scale parameter and ξ is a location parameter. λ and δ are shape parameters of the PDF curve. The density function is skewed to the left, symmetric, or skewed to the right, if $\gamma > 0$, $\gamma = 0$, or $\gamma < 0$, respectively (Figure 6.8). δ represents the standardized measure of kurtosis of the curve; a high positive value means the curve is sharp, while a small value close to 0 means a nearly flat, wide curve (Figure 6.8).

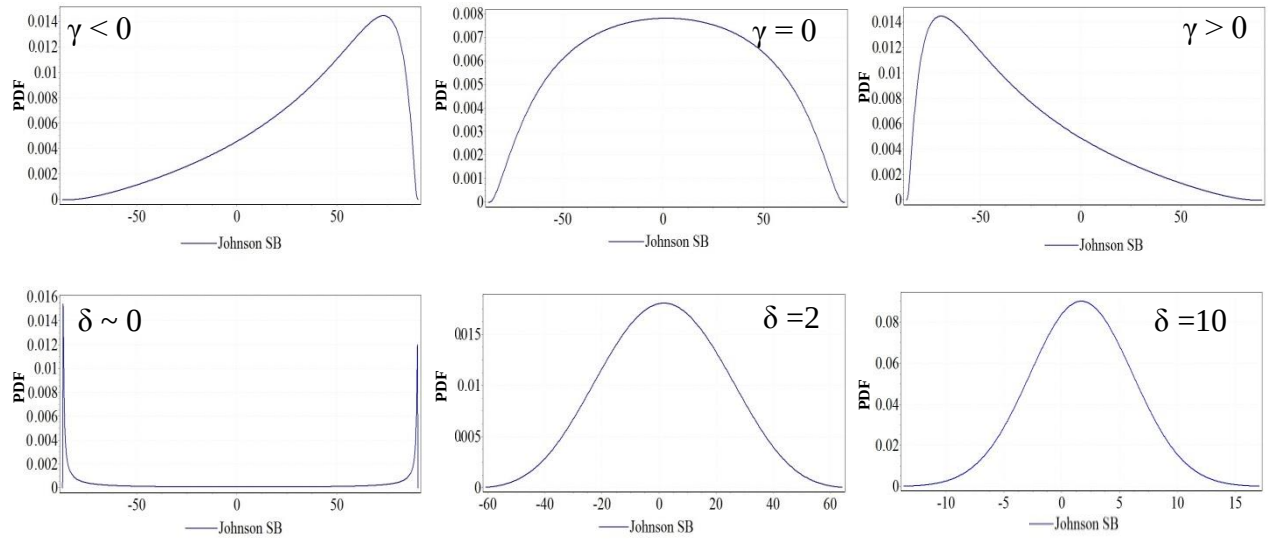

Figure 6.8: Different distribution function shapes based on different values of γ and δ

The Johnson SB distribution function possesses two properties that make it well suited to represent fibre orientation angles θ, φ. Firstly, because of the lower bound ξ and the upper bound λ, it can represent variables that have physical or natural constraints on their ranges. Secondly, the two parameters controlling the shape γ and δ allow a considerable amount of flexibility to fit a broad spectrum of distributions. This is clearly seen in Figures 6.9 to 6.16 which show the

PDFs of θ and φ at various instants during the flow of Mixes 6 and 8 in the slump test (up to 10 sec of flow time) and in the L-box test (up to 3 sec flow time).

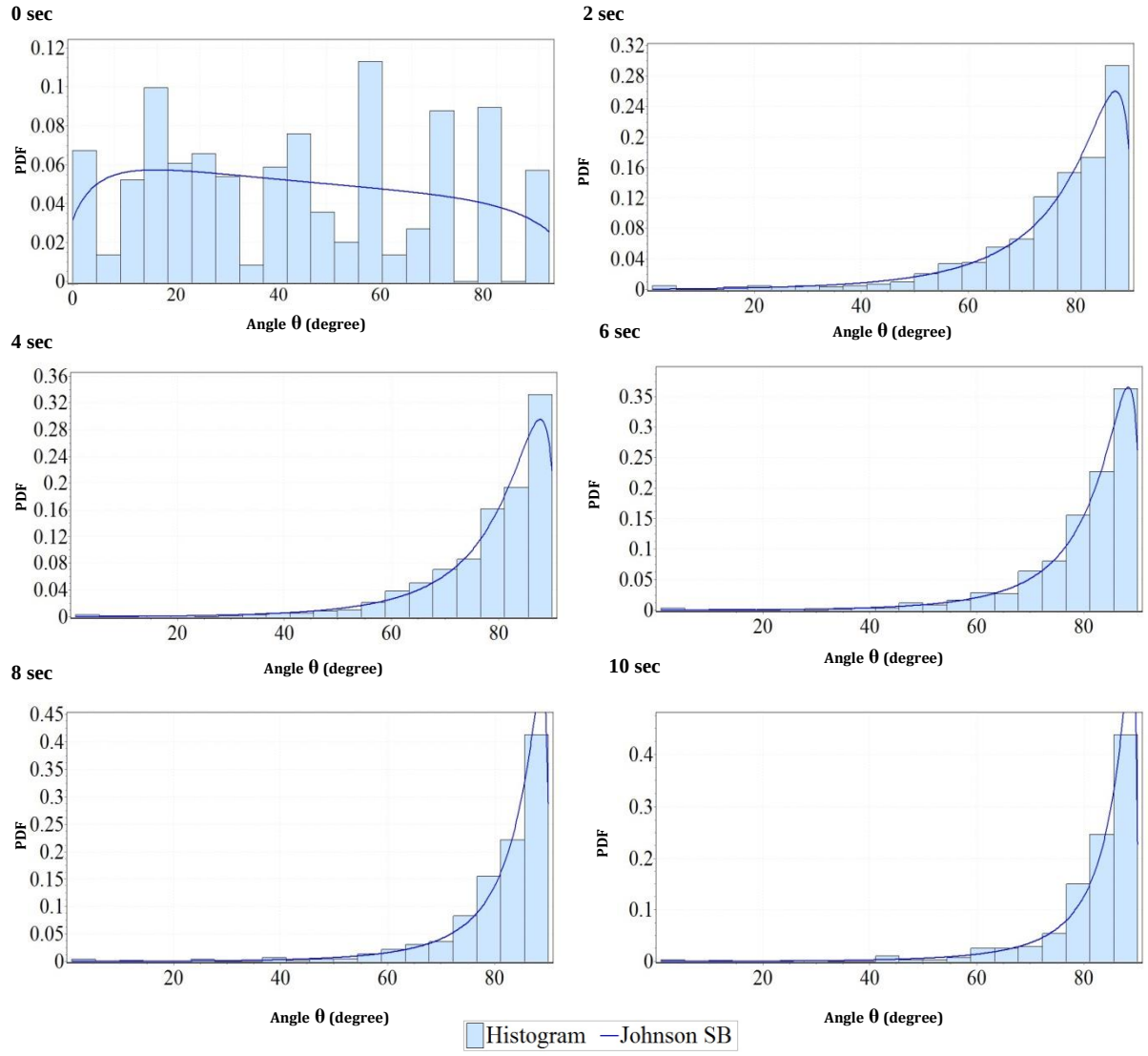

Figure 6.9: Probability density function *f* (θ) of Mix 8 at several instants during the flow in the slump test

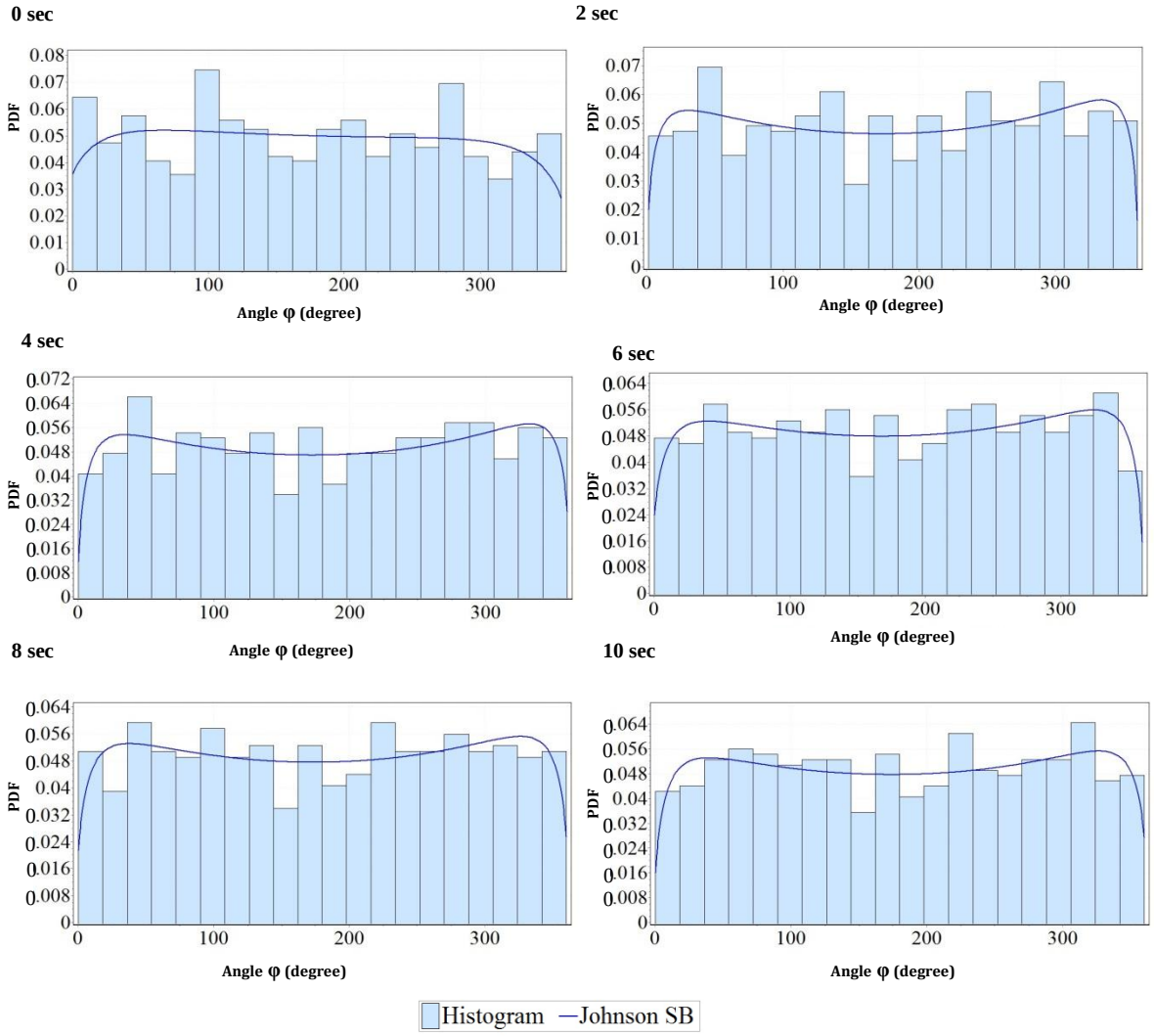

Figure 6.10: Probability density function *f* (φ) of Mix 8 at several instants during the flow in the slump test

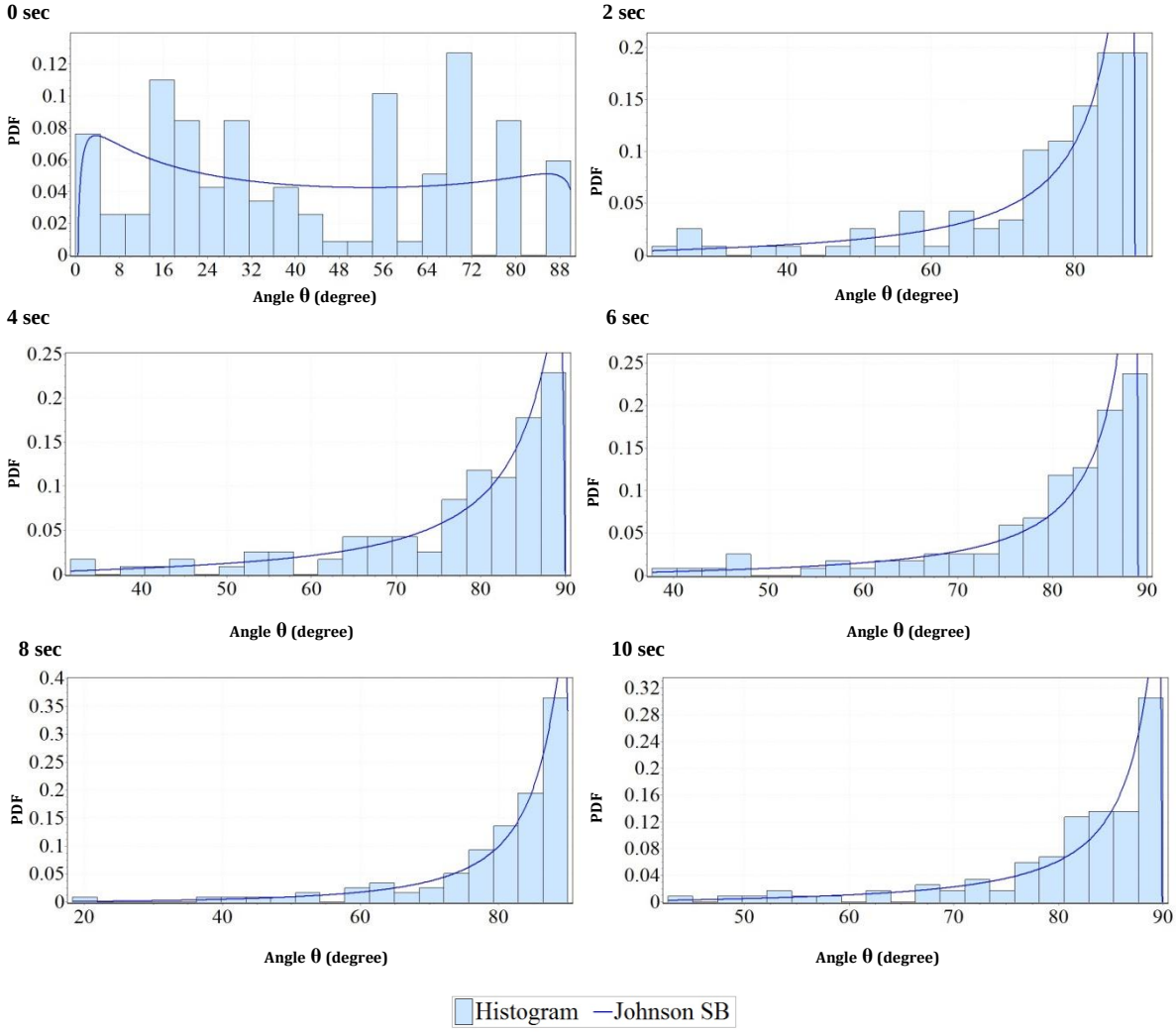

Figure 6.11: Probability density function *f* (θ) of Mix 6 at several instants during the flow in the slump test

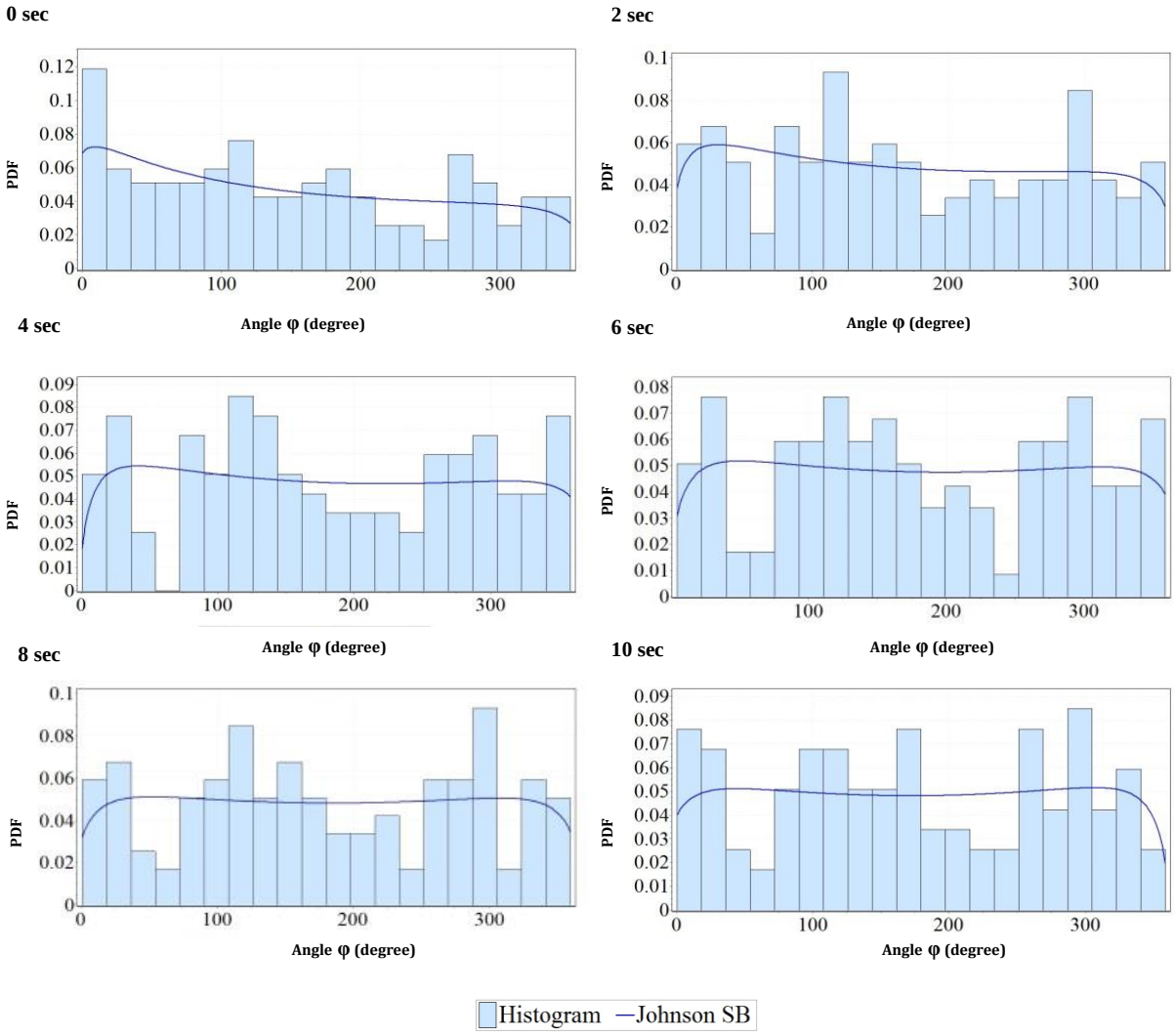

Figure 6.12: Probability density function *f* (φ) of Mix 6 at several instants during the flow in the slump test

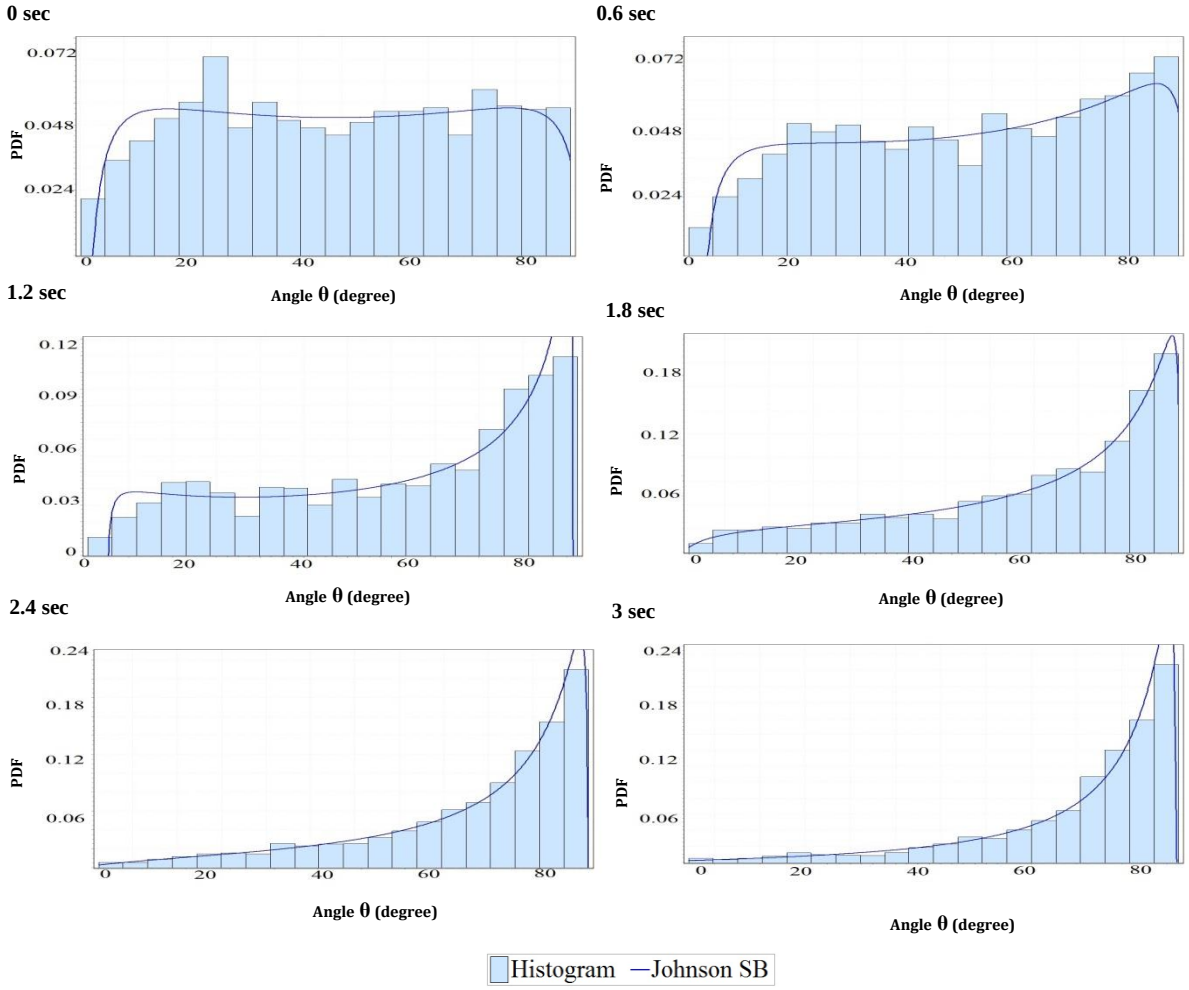

Figure 6.13: Probability density function *f* (θ) of Mix 8 at several instants during the flow in the L-box

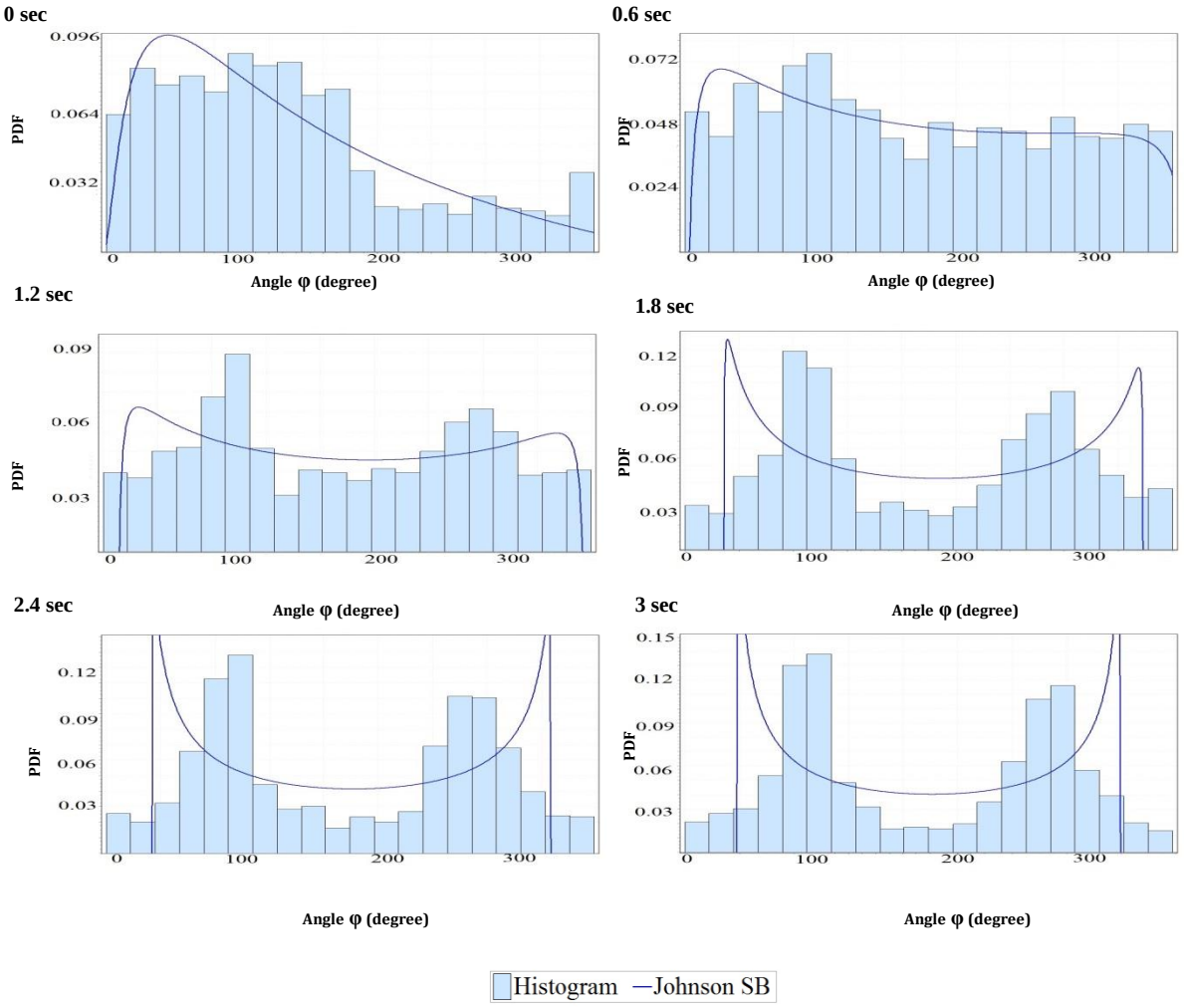

Figure 6.14: Probability density function *f* (φ) of Mix 8 at several instants during the flow in the L-box

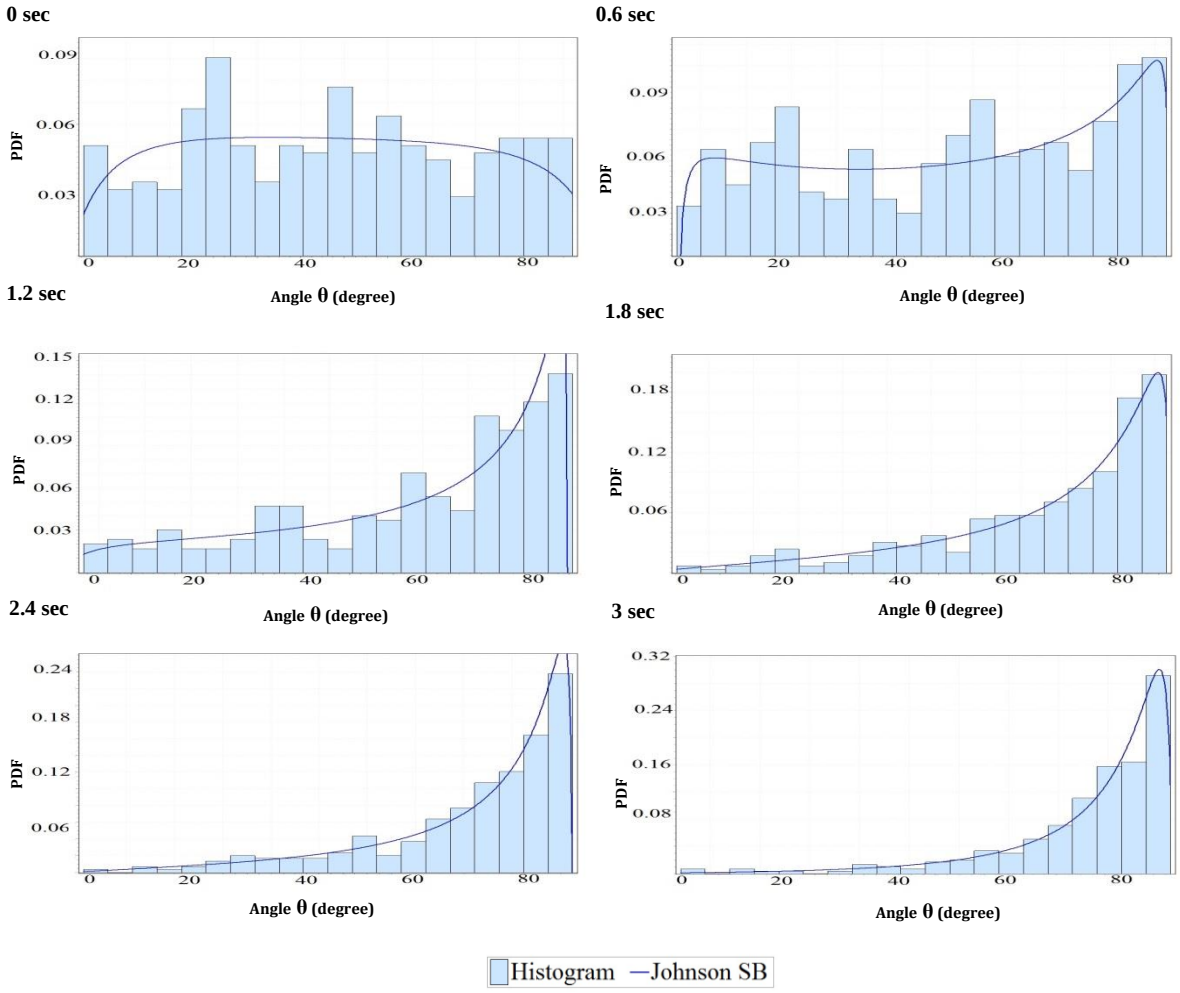

Figure 6.15: Probability density function *f* (θ) of Mix 6 at several instants during the flow in the L-box

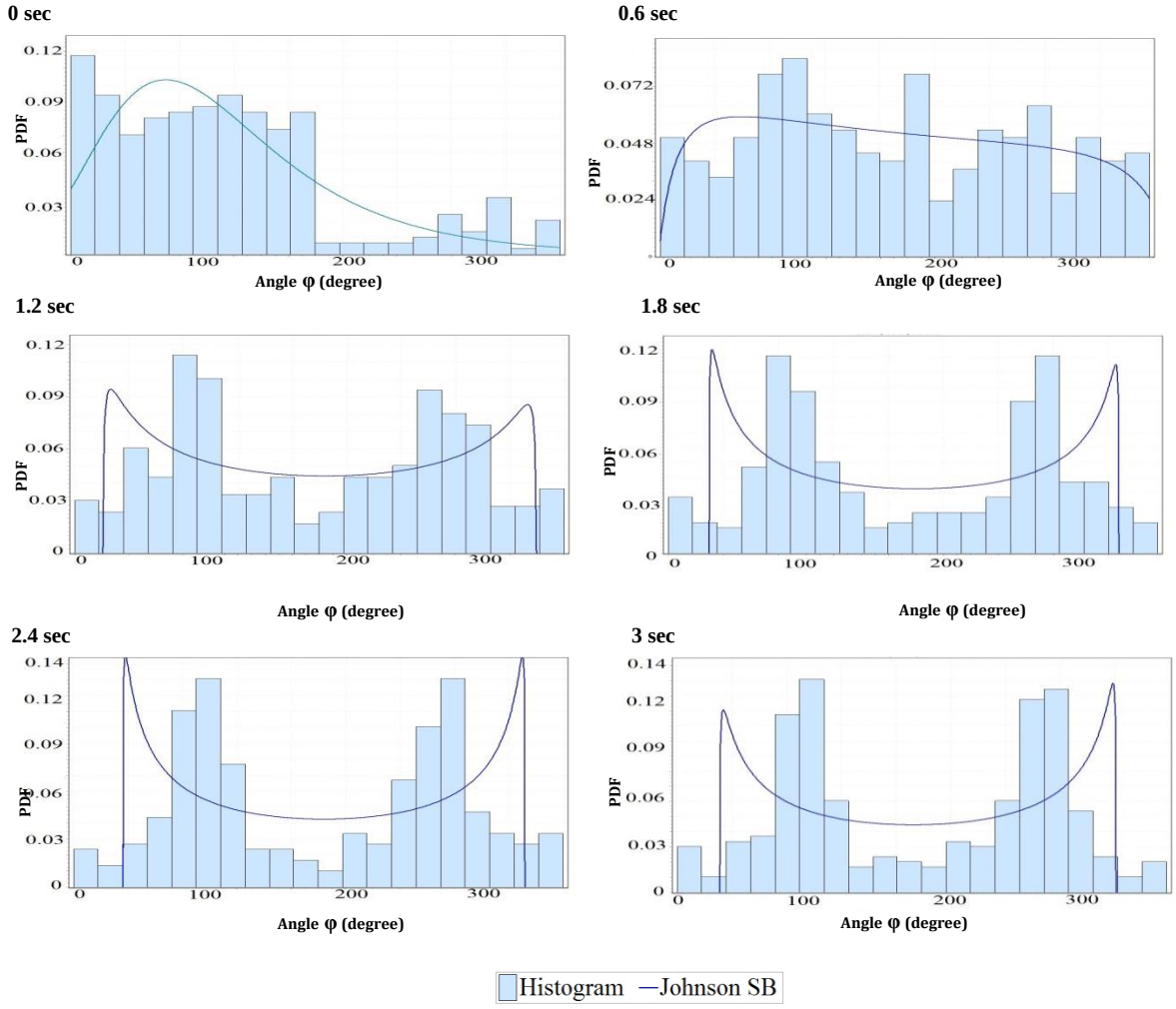

Figure 6.16: Probability density function *f* (φ) of Mix 6 at several instants during the flow in the L-box

The mean values of angles θ and φ at various instants of flow shown in Figures 6.17 and 6.18 are calculated using Equation (6.6), where *n* is the total number of fibres

$$\bar{x} = \sum_{i=1}^{n} f(x_i)x_i \tag{6.6}$$

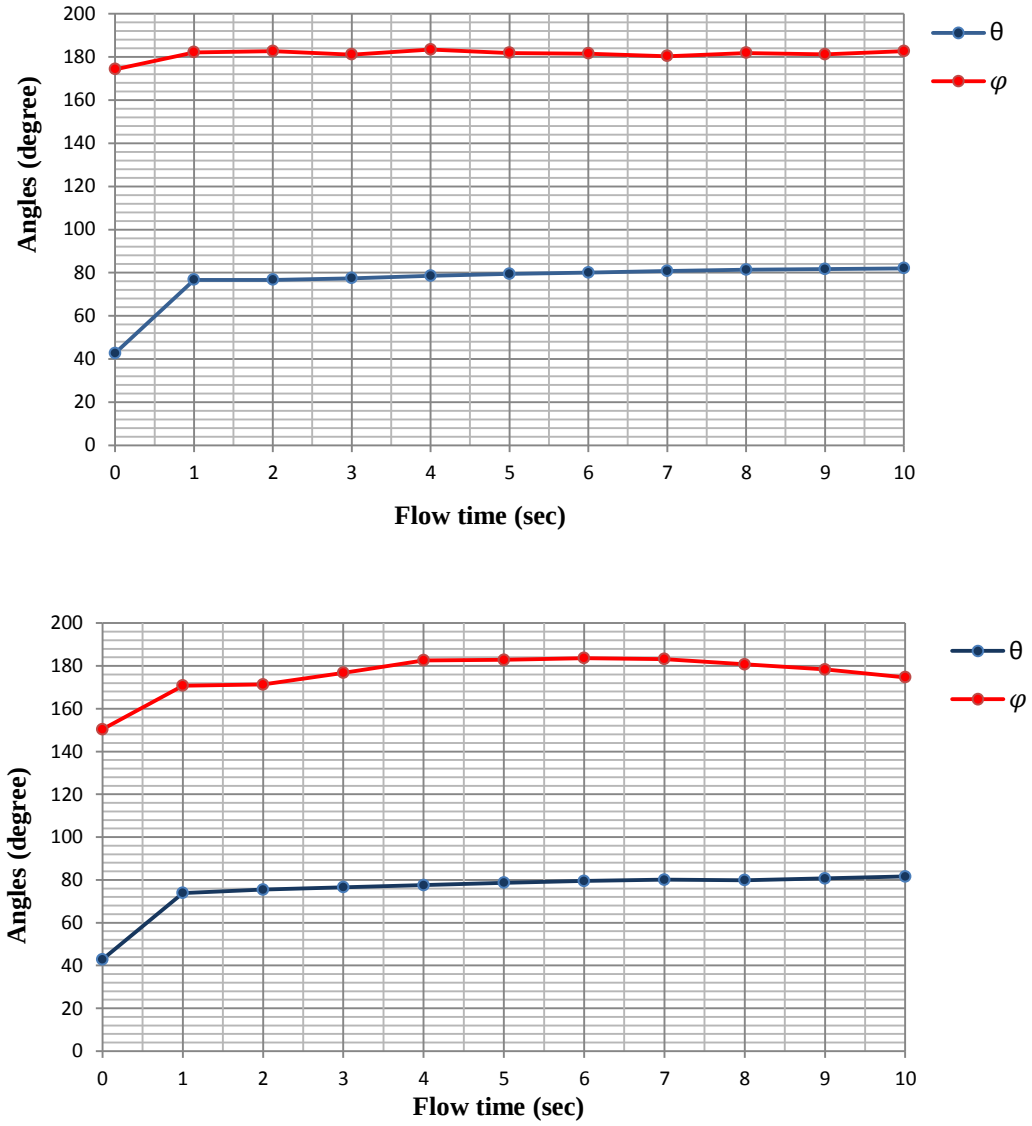

Figure 6.17: The mean values of angles θ and φ for Mix 8 (top) and Mix 6 (bottom) in slump test

From the above results, it is clear that fibres align themselves with the flow such that the mean angle of orientation with respect to the horizontal direction of flow is only $(90\text{-}\theta) \approx 8^{o}$ after 10 s, irrespective of the volume fraction of fibres. This is in agreement with the probability density function $f(\theta)$ which is skewed to the right (Figures 6.9 , 6.11). The fibre orientation is therefore mainly dictated by the fluid flow of the homogeneous SCC mix rather than the mass of fibres, and this confirms the assumption made in the SPH simulation that the positions of the particles

representing a fibre are largely controlled by the fluid particles surrounding them. The fibres however remain randomly distributed in the circumferential direction as attested by the probability density function $f(\varphi)$ which remains nearly a uniform distribution throughout the flow (Figures 6.10 , 6.12) with the mean φ deviating from the anticipated 180^o by less than 6^o in Mix 6 (low volume fraction of fibres) and by less than 3^o in Mix 8 (high volume fraction of fibres) (Figures 6.17) after 10 s.

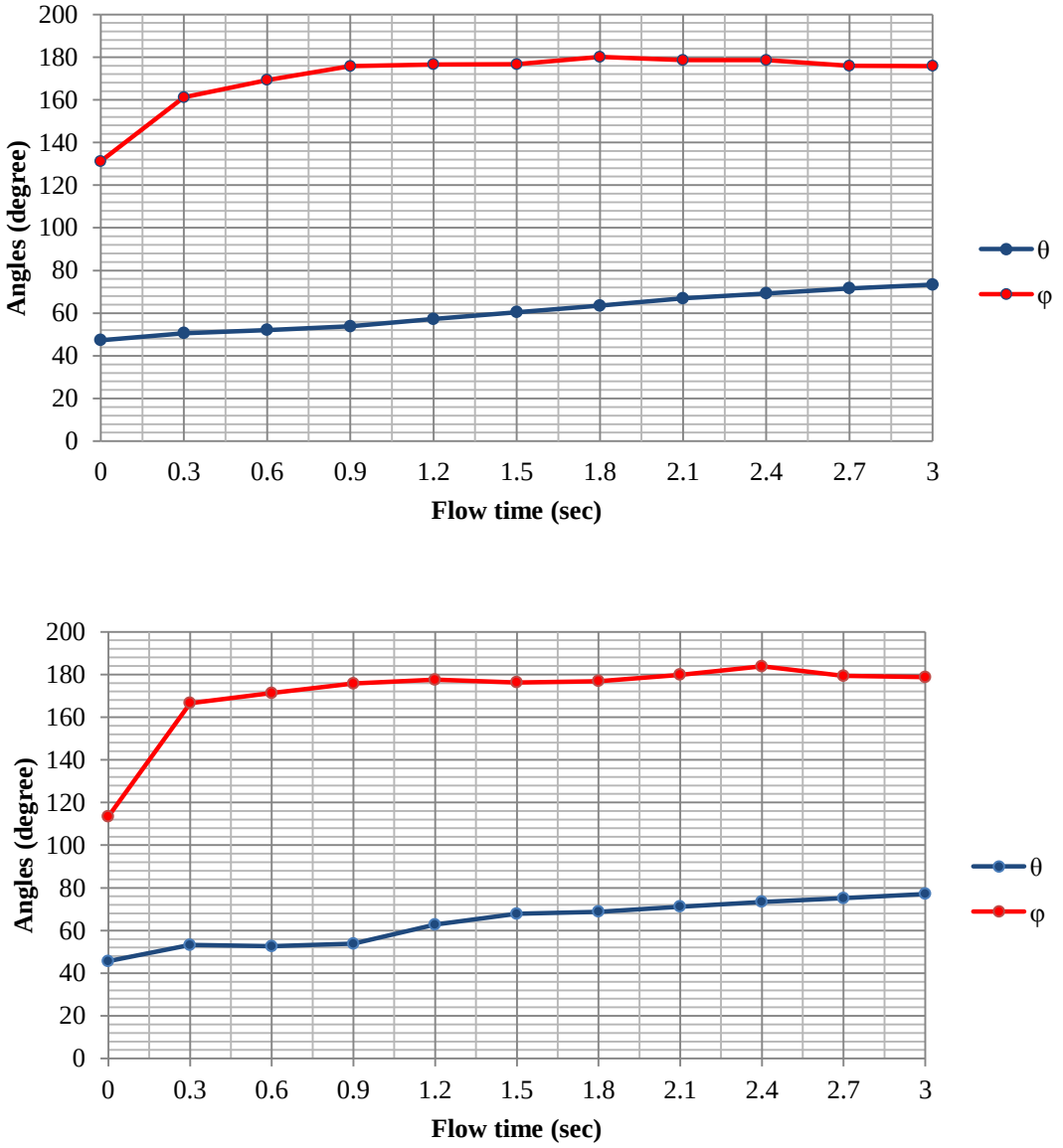

Figure 6.18: The mean values of angles θ and φ for Mix 8 (top) and Mix 6 (bottom) in L-box test

Similar results were found for L-box test; the fibres again aligned themselves predominantly with the principal direction of flow and the mean angle of orientation with respect to the horizontal direction of flow is only $(90\text{-}\theta) \approx 13^o$ after 3 sec for Mix 6 and $(90\text{-}\theta) \approx 17^o$ for Mix 8. The deviation is more than that observed above in the slump test because the flow in the L-box is more three-dimensional than in the slump flow where it is mostly two dimensional.

6.4.1 Determination of fibre orientation in a cross-section

In practice, the fibre orientation is often assessed by image analysis on cut sections of a hardened concrete structural element. A cylindrical fibre with diameter *d* and length *l* cut by a plane will appear as a circle (with diameter *d*) if the plane is perpendicular to the fibre, as an ellipse if the plane is inclined to the fibre (with the aspect ratio dependent on the angle of inclination), or as a rectangle (width *d* and length *l*) if it lies in the plane (Figure 6.19).

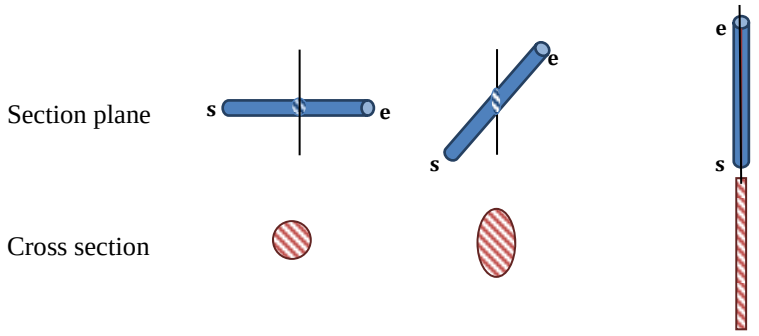

Figure 6.19: Possible cross-sections of a fibre cut by a vertical plane.

By cutting the slump flow by a plane at any time during the flow, we can calculate exactly the number and cross-sectional shapes of the fibres lying in this plane or cut by it. For this, we need to calculate the centre of intersection between a cylindrical fibre and the cutting plane, say the horizontal plane *xy* at *z* = 100 mm for the slump cone. Let us denote the coordinates of the centre of intersection as (x_{ci}, y_{ci}, z_{ci}). These coordinates are calculated from the coordinates of the ends of a fibre (Figure 6.7) and the plane *z* = 100 mm

$$x_{ci} = x_{si} + ((x_{ei} - x_{si})(z_{ci} - z_{si})/(z_{ei} - z_{si})) \tag{6.7}$$

$$y_{ci} = y_{si} + ((y_{ei} - y_{si})(z_{ci} - z_{si})/(z_{ei} - z_{si})) \tag{6.8}$$

$$z_{ci} = 100 \tag{6.9}$$

The shape of the cross-section of the fibre cut by a horizontal plane is decided as follows:

It is rectangular (with width = d and length = l) if $z_{si} = z_{ei}$, as both ends of the fibre will appear in the plane;

It is circular (with diameter = d) if z_{si} is not equal to z_{ei} and θ_i is equal to 0 (Figure 6.7);

It is elliptical if z_{si} is not equal z_{ei} and θ_i is not equal to 0. The semi major and semi minor axes of the ellipse are calculated once the angle θ_i is known (it spans between 0 and 90 degrees)

The semi-major (a_i) and semi-minor (b_i) are given by

$$a_i = r / \cos\theta_i \tag{6.10}$$

where the fibre radius $r = d/2 = 0.275$ mm, and θ_i can be calculated from Equation (6.2), and

$$b_i = r \tag{6.11}$$

At this stage all the required geometrical data for the ellipses are known, namely the centre c_i (x_{ci}, y_{ci}, z_{ci}), the semi-major a_i, and the semi-minor b_i.

The major axis of the ellipse may also be rotated by an angle φ_i (spanning between 0 and 360 degrees with respect to y-axis as illustrated in Figure 6.7 which can be calculated from Equation (6.3). Figure 6.20 shows how the steel fibres are oriented in a horizontal section (100 mm above the base of the cone) of the self-compacting concrete mixes (Mix 8 and Mix 6) at the start of the slump cone test.

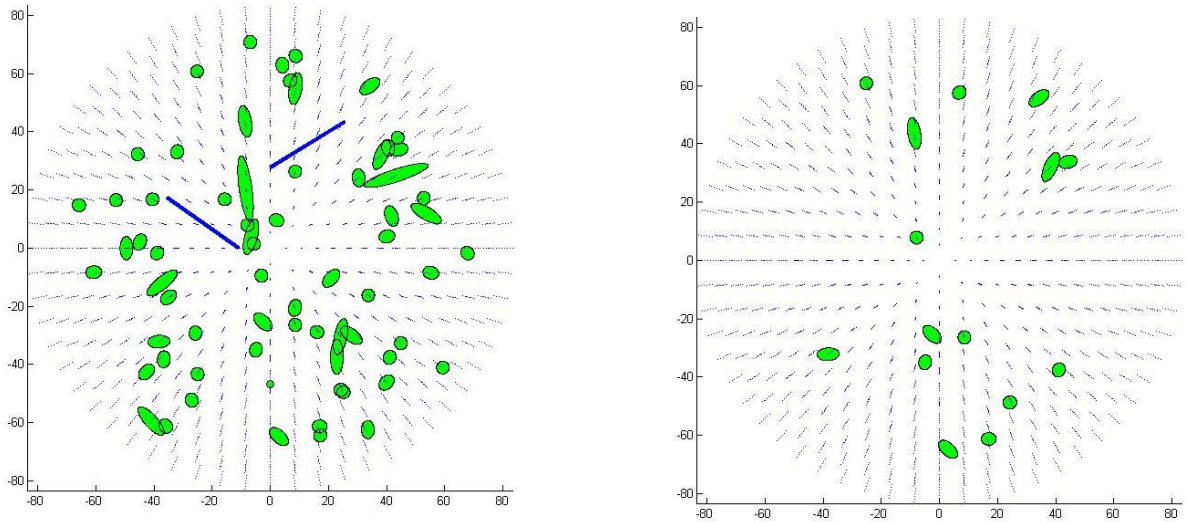

Figure 6.20: Horizontal cross-section of slump cone at the initiation of flow; Mix 8 (left) and Mix 6 (right)

In a similar manner the slump flow can be cut by a vertical plane parallel to the *xz*-plane, as we shall do below and the same steps as described above for the horizontal plane followed to calculate the number and cross-sectional shapes of fibres lying in the vertical cross-section or cut by it. In this case however, θ is measured from the *y*-axis. Angles θ and φ and the co-ordinates of the point of intersection are again given by Equations (6.7) to (6.9), after swapping *y* and *z*.

Figures 6.21-6.25 illustrate how the steel fibres are oriented in a vertical section of the self-compacting concrete mixes (Mix 8 and Mix 6) at various times during the slump flow test. Figure 6.21 shows a diametrical section of the slump cone at the initiation of flow when the fibres are nearly randomly distributed in the mixes. For clarity of presentation, the sizes of the ellipses, circles, and rectangles are exagerated several times compared to the cross section dimensions of the cone. Note that the coordinates of the particles representing the ends of the fibres are continuously monitored throughout the simulation from which the cross-sectional shapes of the fibres cut by the vertical sections are calculated as described above.

It should be mentioned that the end particles representing the fibres are randomly distributed, but as the distance between these particles is fixed, a number of degrees of freedom are suppressed. Referring to Table 6.1, this means that 118 degrees of freedom out of a possible 70743 are suppressed in Mix 6; the corresponding figures in Mix 8 are 590 out of 70743. In the L-box test, based on Table 6.3, 298 degrees of freedom out of a possible 178704 are suppressed in Mix 6 and 1490 in Mix 8.

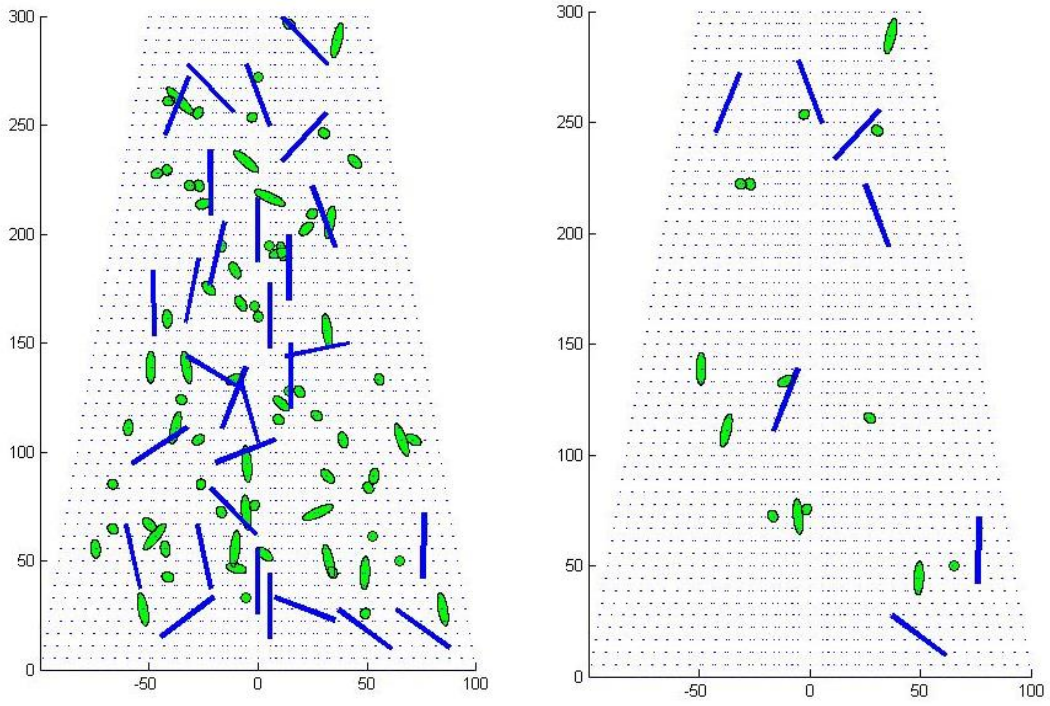

Figure 6.21: Vertical cross section of slump cone at the initiation of flow for Mix 8 (left) and Mix 6 (right)

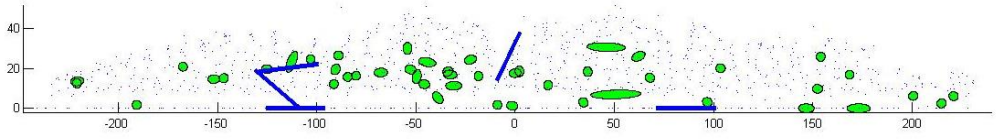

Figure 6.22: Vertical cross section of slump flow after 3 sec (Mix 8)

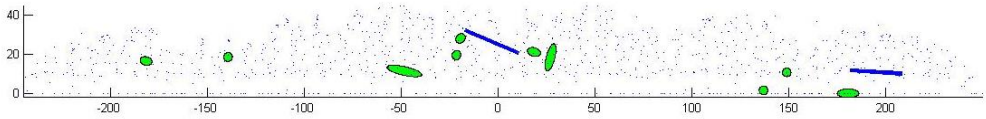

Figure 6.23: Vertical cross section of slump flow after 3 sec (Mix 6)

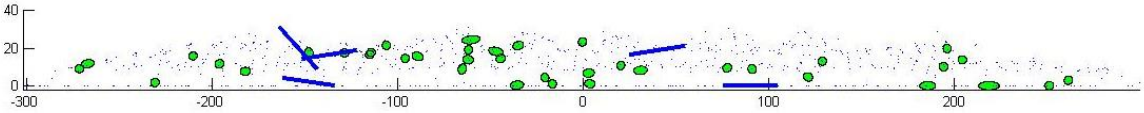

Figure 6.24: Vertical cross section of slump flow after 10 sec (Mix 8)

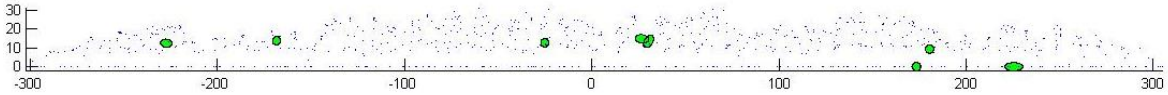

Figure 6.25: Vertical cross section of slump flow after 10 sec (Mix 6)

It can be seen from Figures 6.21-6.25 that the number of fibres lying in the vertical section (plane *xz*) or cut by it decreases as the flow time increases and the surface area of cut section reduces.

In a similar manner, the L-box can be cut by a vertical plane perpendicular to the flow direction following the same steps as described above for the slump test to calculate the number and cross-sectional shapes of fibres lying in the vertical cross-section or cut by it. Two vertical sections will be taken; the first one at 200 mm from the vertical leg of the L-box (see Figure 6.6) and the second at 300 mm.

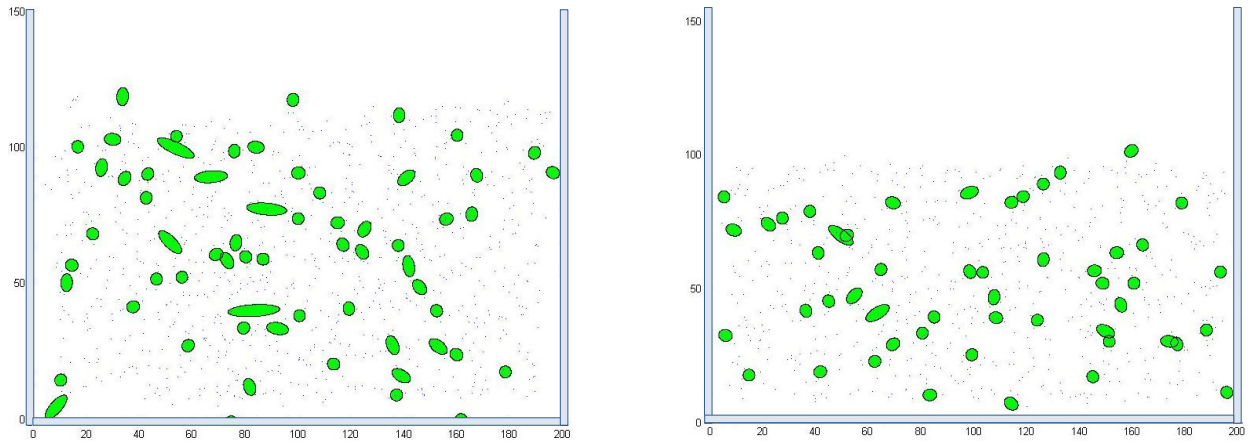

Figure 6.26: Vertical cross sections at 200 mm (left) and 300 mm (right) in the L-box after 2 sec (Mix 8)

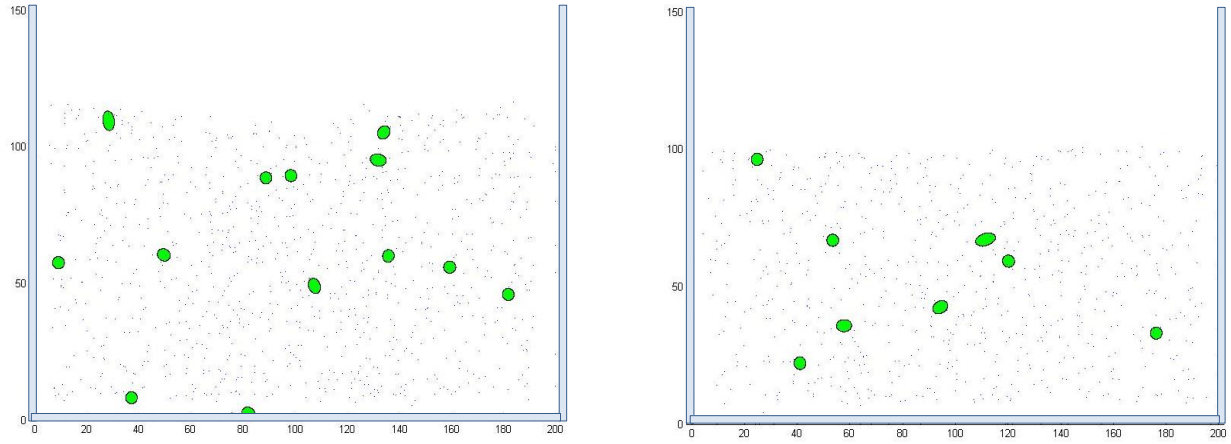

Figure 6.27: Vertical cross sections at 200 mm (left) and 300 mm (right) after 2 sec in L-box test (Mix 6)

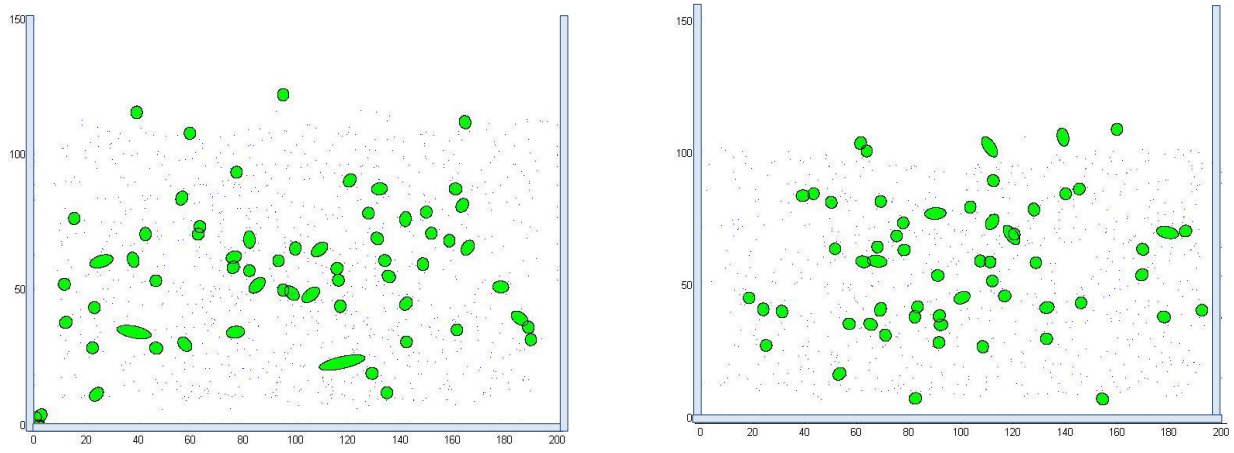

Figure 6.28: Vertical cross sections at 200 mm (left) and 300 mm (right) in the L-box after 3 sec (Mix 8)

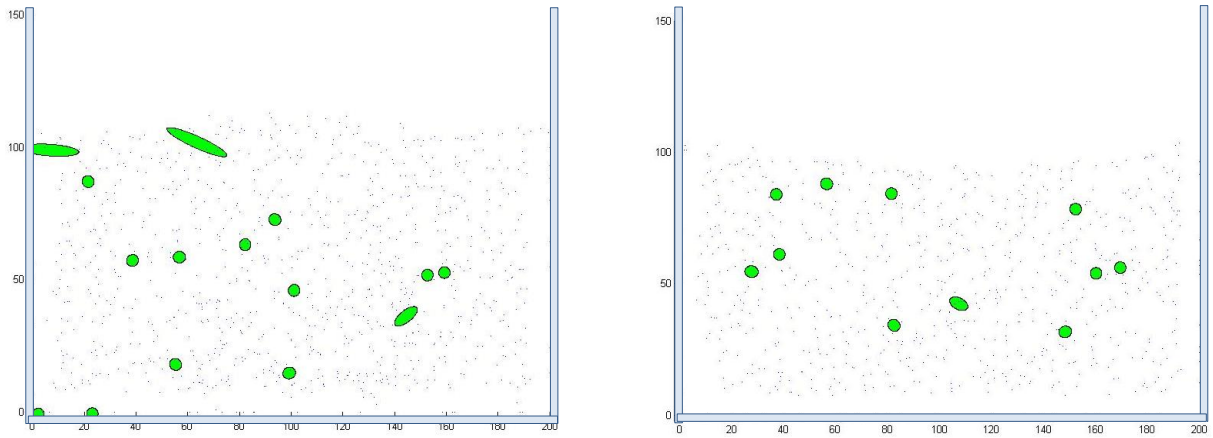

Figure 6.29: Vertical cross sections at 200 mm (left) and 300 mm (right) after 3 sec in L-box test (Mix 6)

It can be seen from Figures 6.26-6.29 that the number of fibres cut by the vertical section decreases as the flow time increases and the surface area of cut section reduces, exactly as in the slump cone test. It should be mentioned that in the case of L-box, when the flow stops, the surface area of all cut sections should be almost the same, therefore the number of fibres should be same in all the vertical cross sections. These results are not available because of the long computational time needed for the flow to stop.

For a random distribution of fibres in a volume, the number of fibres lying in section of a certain area or cut by it can be calculated exactly using the theory of geometric probability, or more precisely from the solution of the so-called Buffon problem (Solomon, 1978; Crofton, 1885). The solution is

$$l\frac{E(h)}{E(c)} = 4\frac{\sum \text{volumes}}{\sum \text{surface areas}} \tag{6.12}$$

The solution is obtained by dividing the volume of the container into smaller cells, say 40 mm cubes and then calculating the number of fibres of equal length that either fall into interior of the cells or are cut by one of its surfaces. The cell size has to be greater than the length of the fibre. However, it shouldn't be too large to affect the accuracy, nor should it be too small so that a fibre can cut two surfaces. Here, $E(c)$ is the number of fibres of length l that are cut by one of the surfaces of the cells , and $E(h)$ is the number of times each of the two ends of the fibres fall in the interior of the cells.

- **Slump test**

For Mix 8 containing 2.5% volume fraction of 30 mm long steel fibres with 0.55 mm diameter, the total number of fibres in the volume of the truncated slump cone is

$$N_f = \frac{V_c}{V_f} * 2.5\% = \frac{5497787.144}{7.127} * 2.5\% = 19285 \tag{6.13}$$

where V_c is the volume of truncated cone and V_f is the volume of each fibre. By dividing the cone volume into 40 mm cubical cells (there are nearly 86 such cells in the cone) we have

$$\sum volume = 5497787 mm^3 \; ; \; \sum surface \text{ areas } = \left(\frac{5497787.144}{64000} \right) * 1600 * 6 = 824668 mm^3 \tag{6.14}$$

From Equation (6.12) it follows that

$$30 \frac{E(h)}{E(c)} = 4 \frac{5497787}{824668} \tag{6.15}$$

$$\frac{E(h)}{E(c)} = \frac{8}{9} \tag{6.16}$$

The total number of fibres in the interior of each cell or cut by one of its surfaces is

$$E(c) + E(h) = \frac{V_{cube}}{V_f} * 2.5\% = \frac{40 * 40 * 40}{7.127} * 2.5\% = 224 \tag{6.17}$$

From Equations (6.16) and (6.17) it follows that, the number of fibres cut by a 40x40 mm^2 section is $E(c) = 118$. The diametrical vertical section of the slump cone at the start of the test (Figure 6.21) has a surface area equal to 45000 mm^2, so that the total number of fibres cut by this section is $\frac{118}{40 * 40} * 45000 = 3318$ fibres out of a total of 19285 fibres in the cone (Equation (6.13)). However, as only 590 fibres represent the total number of fibres in the 3D SPH simulation (Table 6.1), the number of fibres that should theoretically be cut by the diametrical section of the slump cone at the start of the test is 590*3318/19285=101 fibres. The actual number in our simulation (Figure 6.21) is 100. The small difference between the theoretical and

simulated numbers is because of the pseudo-random nature of the fibre distribution in the simulations, as explained above.

It is seen from Equation (6.12) that the number of fibres cut by a vertical section $E(c)$ is proportional of the surface area of the section. At the initiation of flow, the surface area was 45000 mm^2, and theoretically 101 fibres should be found in the cut section, while after 10 sec, this number should be only 39 fibres because the area of the vertical section is reduced to approximately 17000 mm^2. The actual number in our simulation is 43 (Figure 6.24). The number of fibres in the cut section in the simulations is compared with the theoretical value in Table 6.5.

Table 6.5. Number of fibres in a vertical cross-section of (Mix 6) and (Mix 8) based on the 3D simulation and Buffon problem

	Flow time (sec)	No. of fibres in the simulation	No. of fibres based on Buffon problem
Mix 6	0	21	21
	10	8	8
Mix 8	0	100	101
	10	43	39

Also, as seen in Figures 6.21 - 6.25, the number of fibres in the cut sections with elliptical cross-sections reduces and those with circular sections increases as the flow time increases. This suggests that more and more fibres are orienting with the dominant flow direction normal to the cutting plane. However, this was to be expected because the cone flow spread is almost planar towards the end of flow reducing in height from 300 mm at initiation (Figure 6.21) to only about 30 mm after 10 sec when the flow is about to stop (Figures 6.24-6.25).

- **L-box test**

By using the theory of geometric probability for Mix 8 containing 2.5% volume fraction of 30 mm long steel fibres with 0.55 mm diameter, the total number of fibres in the volume of the concrete in the L-box is

$$N_f = \frac{V_c}{V_f} * 2.5\% = \frac{12900000}{7.127} * 2.5\% = 45250 \quad (6.18)$$

where V_c is the volume of concrete in the L-box and V_f is the volume of each fibre. By dividing the concrete volume into 40 mm cubical cells (there are nearly 202 such cells) we have

$$\sum volume = 12900000\ mm^3 ; \sum surface\ \text{areas} = \left(\frac{12900000}{64000}\right) * 1600 * 6 = 1935000 mm^3 \qquad (6.19)$$

From Equation (6.12) it follows that

$$30\frac{E(h)}{E(c)} = 4\frac{12900000}{1935000} \qquad (6.20)$$

$$\frac{E(h)}{E(c)} = \frac{8}{9} \qquad (6.21)$$

The total number of fibres in the interior of each cell or cut by one of its surfaces is

$$E(c) + E(h) = \frac{V_{cube}}{V_f} * 2.5\% = \frac{40 * 40 * 40}{7.127} * 2.5\% = 224 \qquad (6.22)$$

Therefore $E(c) = 118$. The vertical section of the L-box at 200 mm (Figure 6.26) has a surface area equal to 25400 mm^2, so that the total number of fibres cut by this section is $\frac{118}{40 * 40} * 25400 = 1873$ fibres out of a total of 45250 fibres in the L-box (Equation (6.18)). As before, the number of fibres that should theoretically be cut by the vertical cross-section at 200 mm of the L-box after 2 sec flow time is 1490*1873/45250 = 62 fibres. Table 6.6 compares the numbers of fibres in a vertical cross-section based on the 3D simulations with the Buffon problem solution. Again, the small difference between the theoretical and simulated numbers is because of the pseudo-random nature of the fibre distribution in the simulations. The distribution is pseudo-random because some of the degrees of freedom of the fibre end particles are suppressed, as explained above.

Table 6.6. Number of fibres in a vertical cross-section of (Mix 6) and (Mix 8) in L-box test based on the 3D simulation and Buffon problem

	Flow time (sec)	No. of fibres in the simulation		No. of fibres based on Buffon problem	
Section (mm)		200	300	200	300
Mix 6	2	13	8	13	10
	3	16	11	13	11
Mix 8	2	63	51	62	49
	3	64	58	62	56

6.4.2. Fibre orientation factor

A fibre orientation factor $\eta(0 \le \eta \le 1)$ is used to assess the orientation state of fibres in a given cross-section (Johnson, 1949). If this orientation factor can be controlled and predicted effectively, then the partial safety factor reflecting the fibre orientations can be chosen close to unity thus allowing the superior properties of fibre reinforced self-compacting concrete to be exploited to the full extent (FIB, 2010). It was first proposed by Soroushian and Lee (1990) as the ratio of the number of fibres actually counted in a given cross-section (N) to the average theoretical number of fibres in such a cross-section(N_{th}), assuming that all the fibres are perpendicular to the cut surface. The theoretical number of fibres was chosen equal to the area of all fibres in the cross section ($A_c * V_f$) divided by the area of one fibre (A_f) , where (A_c) is the area of the cross-section and V_f is the volume fraction of fibres (Martinie & Roussel, 2011). The lower this factor, the larger is the average deviation of the fibres from the perpendicular direction to the cut surface.

There are two drawbacks of this definition of the fibre orientation factor. Firstly, the N_{th} calculated in the approximate manner described above overestimates the actual theoretical number of fibres in a cross section. This number can however be exactly calculated using the theory of geometric probability described above (Solomon, 1978). Secondly, N does not reflect the actual inclination of the fibres relative to the section, and thus does not reflect the effectiveness of a fibre; a fibre is most effective if it is perpendicular to the cross-section; it is completely ineffective if it lies in the section; a fibre inclined to the section is partially effective depending on its angle of inclination.

Therefore, a new orientation factor is introduced here. It is defined as the ratio of the projected length along the normal to the (vertical) cut plane (*y*-axis for vertical plane *xz*) to the actual length *l* of the fibre (Lee et al., 2002; Liu et al., 2011). This ratio is nothing but the cosine of the angle between the fibre and the *y*-axis. This definition is consistent with the fibre probability density function introduced above. The orientation factor in the vertical cut plane is:

$$\overline{\eta} = \frac{1}{n}\sum_{i=1}^{n}\cos\theta_i = \frac{1}{n}\sum_{i=1}^{n}\frac{r}{a_i} \tag{6.23}$$

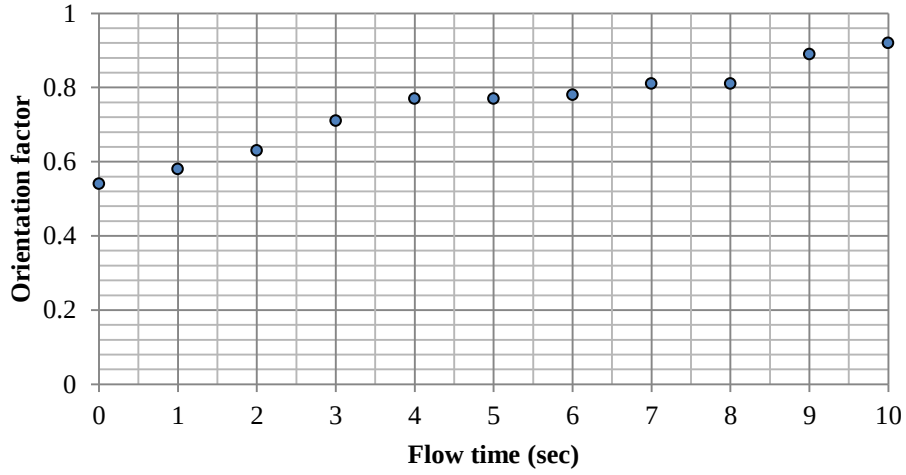

Figure 6.30: Fibre orientation factor in a vertical cut section (Mix 6) in the slump test

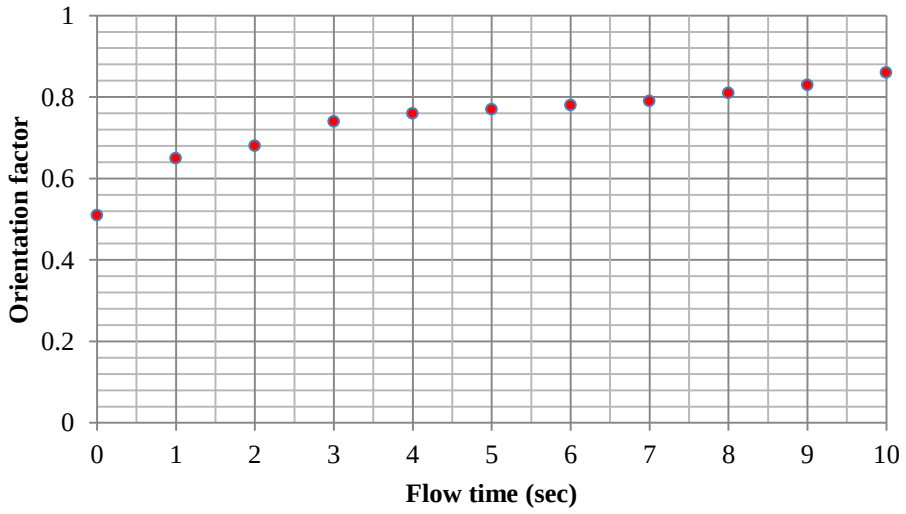

Figure 6.31: Fibre orientation factor in a vertical cut section (Mix 8) in the slump test

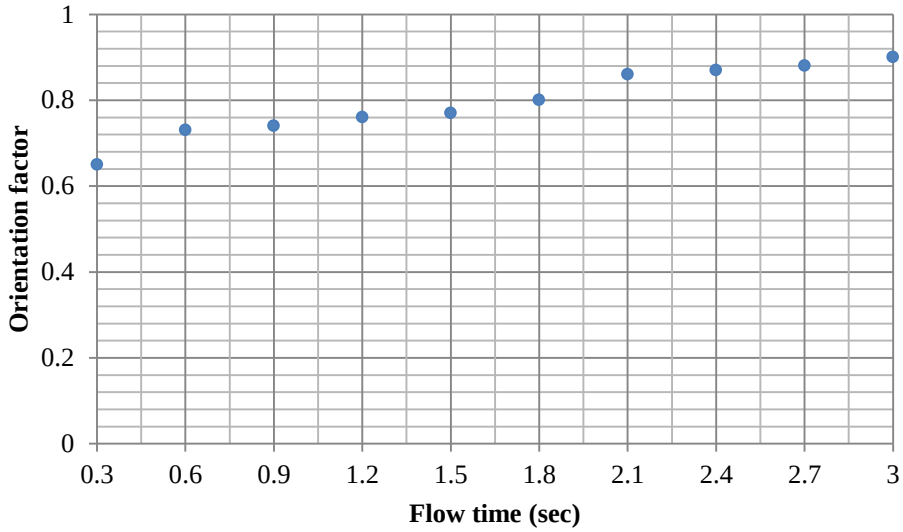

Figure 6.32: Fibre orientation factor in a vertical cut section at 100 mm (Mix 6) in the L-box

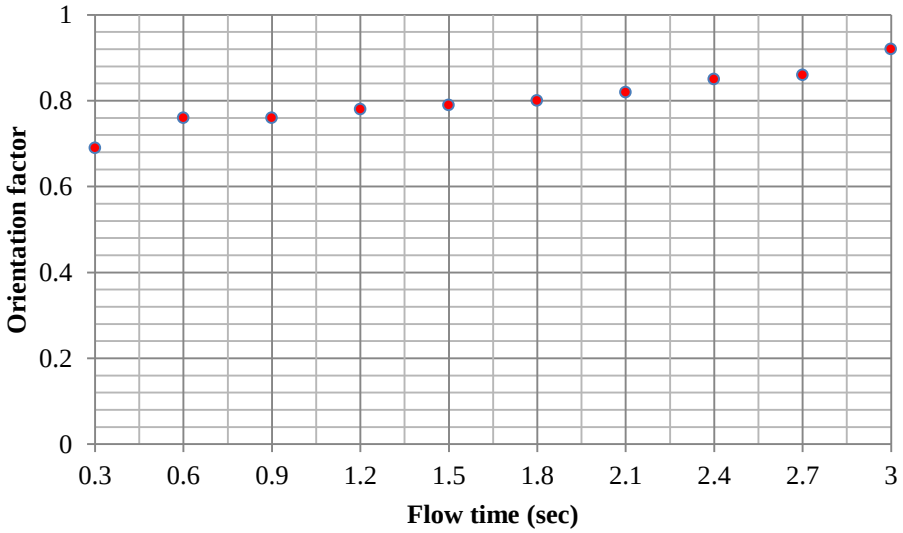

Figure 6.33: Fibre orientation factor in a vertical cut section at 100 mm (Mix 8) in the L-box

It is clear from Figures 6.30 and 6.31 that the fibres tend to orient themselves with the direction of flow. This is reflected in the high fibre orientation factor in the *xz*-plane, irrespective of the fibre volume fraction. In a slump cone spread test, it is more appropriate to consider the fibre distribution in the *xy*-plane. As noted above, the fibres are still distributed randomly in the circumferential direction. Note that at the beginning of slump cone test the fibres are oriented nearly randomly with the mean angle θ equal to about 42.7^{o} (for perfect random distribution the

mean angle would be 45^o), so that the fibre orientation factor in the *xy*-plane is about 0.68. The fibres start to reorient themselves with the direction of flow and after 10 sec the mean angle θ has increased to about 82^o , corresponding to a fibre orientation factor of about 0.99, irrespective of the fibre volume fraction. Such a high orientation factor for the slump flow is not surprising, given that after 10 sec the flow spread is nearly two-dimensional lying in the *xy*-plane with the maximum height in the z-direction only 30 mm. In a real concrete structural element the fibre orientation factor in a cut section is likely to be smaller because the flow spread is three-dimensional. In the case of L-box, the fibres also reorient themselves with the direction of flow (Figures 6.32 and 6.33); the mean angle θ has increased from 45^o to about 77^o for Mix 6 and from 47^o to about 73^o for Mix 8 after 3 sec flow, corresponding to a fibre orientation factor of about 0.92 and 0.9, respectively.

By comparison, according to the definition of Soroushian and Lee (1990) the fibre orientation factor for Mix 6 would be (21/32) = 0.66 at the start of slump cone test and (8/12) = 0.67 after 10 s flow. The corresponding values for Mix 8 are (101/158) = 0.64 and (39/60) = 0.65. In other words, the fibre orientation factor hardly changes from the start of the flow until it stops, i.e. the fibres do not reorient with the principal flow direction at all which is clearly unexpected and counterintuitive in SCC mixes. In calculating the fibre orientation factor according to Soroushian and Lee (1990) we have used N_{th}, as explained above and N according to the solution of the Buffon problem (Table 6.5).

Finally, it should be mentioned that in practice it may not be possible or practicable to perform the full three-dimensional simulation of the flow of fibre-reinforced SCC into the formwork and thus to determine the angles of inclination of fibres θ_i needed for the calculation of the fibre orientation factor. In such instances, it is necessary to measure the major axis of all elliptical sections of fibres in the cut section, and together with all fibres with circular sections in the cut plane, used to determine the fibre orientation factor using the second Equation (6.23). Note that the fibres that lie in the plane along which the specimen is cut, and which are thus likely to come loose and fall off during cutting, make a negligibly small contribution to the fibre orientation factor, Equation (6.23).

6.5 Concluding remarks

A Lagrangian SPH method has been used to simulate the 3-dimensional flow of SCC mixes containing 0.5 or 2.5 % by volume of 30mm steel fibres in the slump cone and L-box configurations. Notably, the numerical results of slump test are in excellent agreement with test results and therefore can confirm the capability of the 3D SPH methodology of predicting accurately the flow of SCC with fibres. In the L-box simulations, although the simulation results was able to predict accurately the distribution of fibres and there orientations during the flow, there was an unavoidable delay in the flow time measured in the laboratory due to the difficulty of opening the gate in a single lift. This delay should be considered when analysing the filling ability of L-box test.

The orientation and the distribution of the steel fibres have been monitored throughout the flow and the change in orientation has been described by the Johnson SB distribution function. It is shown that the fibres tend to align themselves with the principal direction of flow but remain mostly randomly distributed perpendicular to this direction. The reorientation of the fibres during the flow has been used to estimate the fibre orientation factor (FOF) in a cross section perpendicular to the principal direction of flow. This estimation procedure involves the number of fibres cut by the section and their inclination to the cutting plane. It is shown that the number of fibres cut by the plane as monitored in the SPH simulation is in excellent agreement with the theoretically expected value, thus confirming the validity of the definition of FOF introduced in this Chapter.

Chapter 7

Mix proportioning of self-compacting normal and high strength concretes

7.1 Introduction

Over the last two decades, self-compacting concrete (SCC) mixes of varying strengths and performance have been proportioned on a trial and error basis using time-consuming laboratory tests, such as the slump cone, J-ring, and L-box. An alternative method has recently been proposed by Karihaloo and Ghanbari (2012) for proportioning self-compacting high performance concrete (SCHPC) and ultra-high performance concrete (SCUHPC) mixes with and without steel fibres (with characteristic cube strength between 140 and 160 MPa). This method is based on an extensive investigation of the flow characteristics of such mixes using computational simulations, thus avoiding time-consuming laboratory tests. However, the mixes they proportioned contained no coarse aggregate which has a significant effect on the flow characteristics. This Chapter will extend their method to the proportioning of self-compacting concrete mixes that contain traditional coarse aggregate and whose characteristic cube strength varies between 35 and 100 MPa.

Part of this chapter has been published in the journal 'Magazine of Concrete Research' (see publication 4 in the list in Chapter 1).

7.2 Mix Proportioning

Over the last decade, extensive research has been conducted on achieving self-compactability of concrete. Unlike normal vibrated concrete for which there are different standards around the world for selecting the mix proportions for plain and reinforced concrete (DoE, 1988; ASTM C938 - 10, 2010; Indian_Standard, 2009), there are still no clear rules for proportioning SCC mixes. This lack of rules is intimately connected with the very special flow characteristics of SCC. In Chapters 5 and 6, we have numerically simulated the flow of pre-designed SCC mixes with and without fibres in moulds of different geometries. Here in this Chapter, we are going to show that these simulations are useful for proportioning SCC mixes at the design stage.

A method for mix proportioning of self-compacting high and ultra-high performance concrete mixes with and without short steel fibres having the right flow and passing ability was developed by Karihaloo and Ghanbari (2012). These mixes did not contain any conventional coarse aggregates. This method will be extended here to conventional normal and high

strength self-compacting mixes (Mixes 1-6 in Tables 4.1 and 4.2). It will provide an alternative tool to the heuristic mix proportioning of SCC thus avoiding expensive and time consuming laboratory tests. The mix proportioning procedure involves the following three steps.

Firstly, the slump cone flow is simulated numerically using the technique described in Chapters 5 and 6 to obtain t_{500} time for a given target plastic viscosity of the mix ranging from 6 Pa.s to 14 Pa.s because of the large aggregates used in the mixes. It is useful to point out that the range was only from 2 Pa.s to 6 Pa.s for self-compacting ultra-high performance concretes which need to be less viscous to accommodate the large amount of steel fibres (Karihaloo and Ghanbari, 2012). The simulated t_{500} time will be compared with the measured t_{500} from Tables 4.1 to 4.3.

Secondly, the flow of the mixes is numerically simulated in the L-box configuration to obtain the t_{200}, t_{400} and level off times.

Finally, guidance is given for mix proportioning a range of mixes that would attain the target plastic viscosity, and t_{500}, t_{200}, t_{400} and level off times and thus satisfy the flow and passing ability criteria.

7.3 Slump flow simulation

The slump flow simulation of a series of mixes was carried out using the technique described in Chapters 5 and 6 to obtain t_{500} that gives an indication of the flow-ability of the SCC mix. The target plastic viscosity was chosen in the range 6 – 14 Pa.s for mixes 1- 6.

Table 7.1 gives the slump flow times (t_{500}) of this series of mixes obtained using the simulation technique.

Table 7.1. Slump flow time (t_{500}) for SCC mixes with different target plastic viscosity

SCC type	Plastic viscosity of mix without fibres (Pa.s)	Plastic viscosity of mix with fibres (Pa.s)	t_{500} (s)
Mix 1	6	-	1.90
	8	-	2.10
	10	-	2.50
	12	-	2.75

	14	-	3.20
Mix 2	6	-	1.90
	8	-	2.20
	10	-	2.55
	12	-	2.80
	14	-	3.30
Mix 3	6	-	1.80
	8	-	2.00
	10	-	2.40
	12	-	2.70
	14	-	3.10
Mix 4	6	-	1.70
	8	-	1.90
	10	-	2.20
	12	-	2.50
	14	-	2.90
Mix 5	6	-	1.60
	8	-	1.80
	10	-	2.10
	12	-	2.40
	14	-	2.80
Mix 6 (0.5% steel fibres)	6	25.89	2.10
	8	34.52	2.40
	10	43.15	3.00
	12	51.78	3.20
	14	60.32	3.40

Figure 7.1 illustrates the relation between the plastic viscosity of the mixes reported in Table 7.1 and the corresponding flow time (t_{500}). It can be seen that the flow time and the plastic viscosity of the above mixes are reasonably correlated.

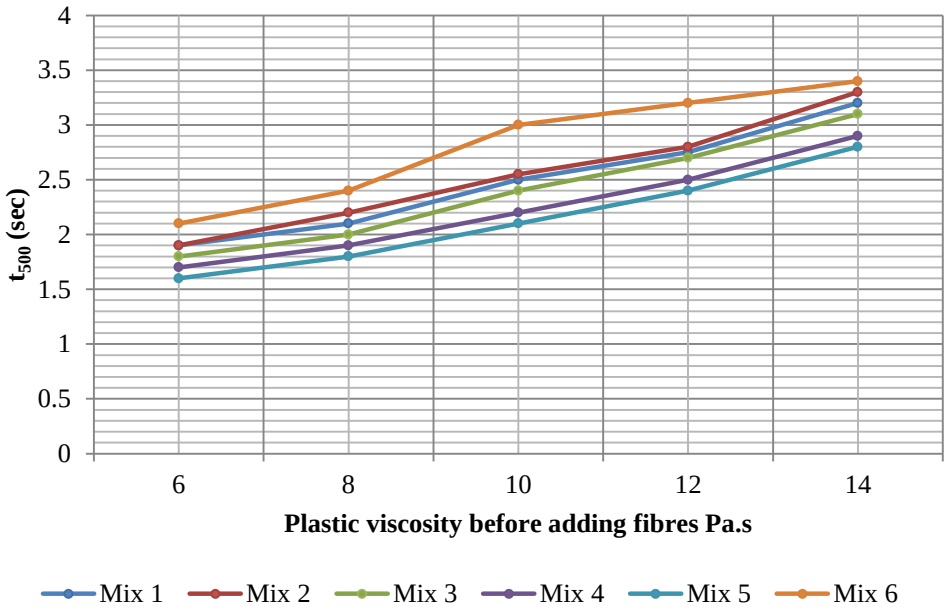

Figure 7.1: Relationship between the plastic viscosity and t_{500} of SCC mixes

7.4 L-box simulation

The next step is the flow simulation of the above mixes in the L-box configuration. The remarks made previously on the inaccuracies of the two-dimensional simulation need again to be borne in mind. Therefore, for more accurate results the 3D simulations of L-Box should be conducted. However, because of the excessive computational time involved in the 3D simulation of the L-box and the large number of mixes involved, the simulations will be only performed on a 2D configuration of the L-box.

Table 7.2. L-box flow times (t_{200}, t_{400} and level-off time) for mixes with different target plastic viscosity

SCC type	PV of mix without fibres (Pa.s)	PV of mix with fibres (Pa.s)	t_{200} (s)	t_{400} (s)	Level-off time (sec)
Mix 1	6	-	0.22	0.57	5.90
	8	-	0.25	0.61	6.60
	10	-	0.29	0.70	7.30
	12	-	0.33	0.81	8.60
	14	-	0.40	0.91	10.10
Mix 2	6	-	0.22	0.58	6.00
	8	-	0.26	0.63	6.70
	10	-	0.30	0.72	7.70
	12	-	0.34	0.83	8.90
	14	-	0.41	0.95	10.80
Mix 3	6	-	0.20	0.55	5.70
	8	-	0.23	0.61	6.50
	10	-	0.27	0.69	7.20
	12	-	0.31	0.79	8.20
	14	-	0.38	0.90	9.30
Mix 4	6	-	0.18	0.53	5.70
	8	-	0.21	0.58	6.30
	10	-	0.25	0.65	6.90
	12	-	0.29	0.74	7.90
	14	-	0.35	0.87	9.20
Mix 5	6	-	0.18	0.50	5.30
	8	-	0.21	0.55	5.40
	10	-	0.24	0.60	5.90
	12	-	0.28	0.70	6.70
	14	-	0.32	0.81	7.10
Mix 6 (0.5% steel fibres)	6	25.89	0.30	1.20	30.00
	8	34.52	0.35	1.50	33.00
	10	43.15	0.50	1.60	38.00
	12	51.78	0.55	2.00	40.00
	14	60.32	0.60	2.20	42.00

The data in Table 7.2 show that t_{200}, t_{400}, and level-off times correlate well with the plastic viscosity for all the mixes. This is clearly seen from Figures 7.2 and 7.3 which illustrates t_{200}, t_{400} for all 6 mixes.

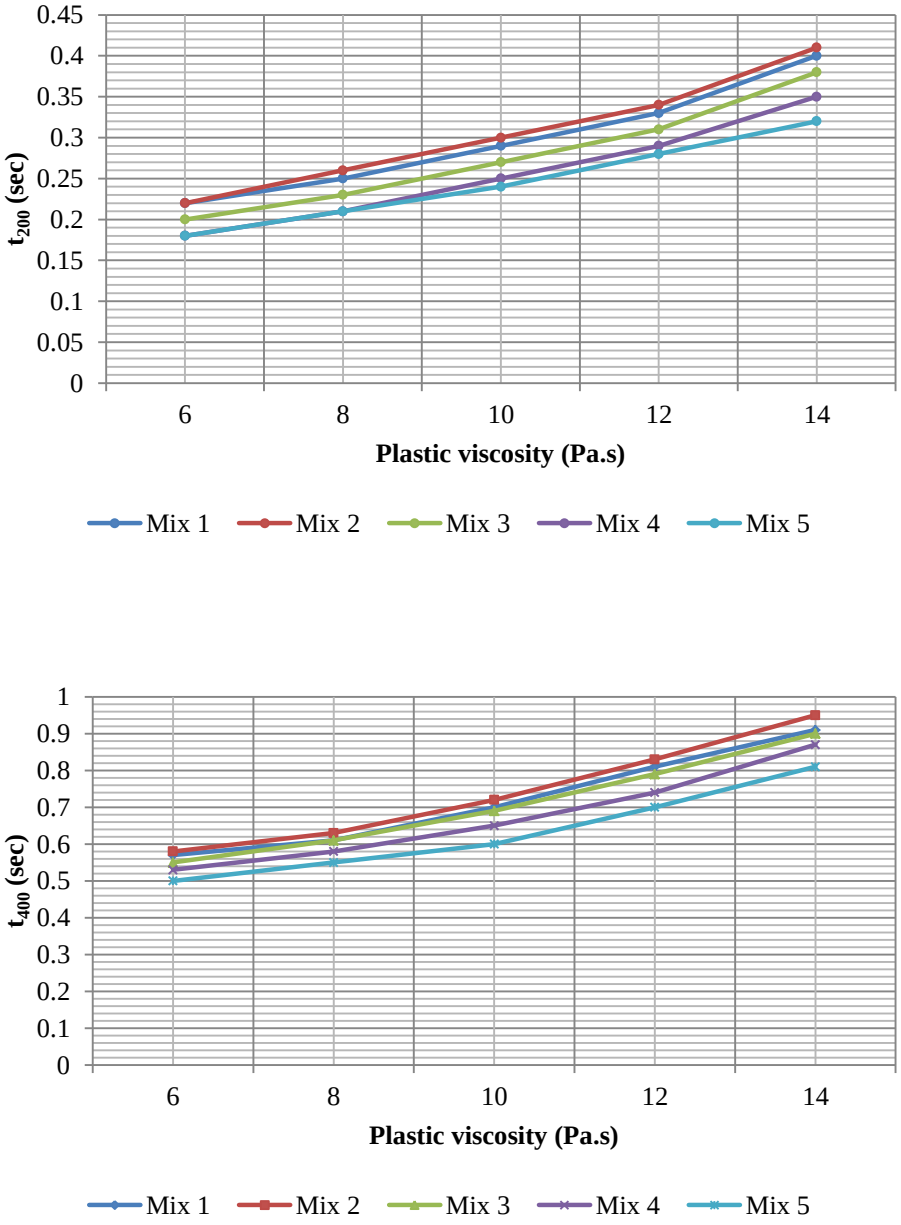

Figure 7.2: t_{200}, t_{400} vs. the plastic viscosity of mixes 1-5

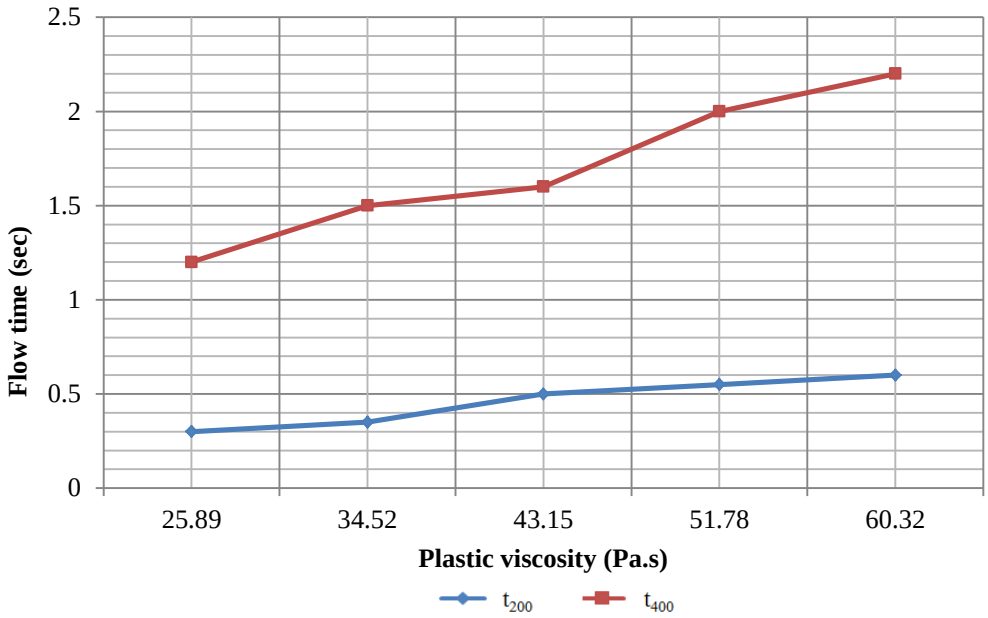

Figure 7.3: t_{200}, t_{400} vs. the plastic viscosity of Mix 6

7.5 Mix proportioning

The final step is to choose the mix proportions that meet the flow-ability (slump flow) and passing ability (flow in L-box) requirements. This is done as follows.

1. Assume the amount of cement and use the initial water and super-plasticiser contents of, say Mix 4 in Table 4.2;
2. Estimate the volume fractions of solid particles (explained below);
3. Calculate the amount of the finest solid particles suspended in the previous liquid suspension (in the first step it is the cement paste) according to its volume fraction;
4. Repeat step 3 until the amounts of all solid constituents in the mix have been calculated;
5. Adjust the water content such that the water to binder ratio is the same as in Table 4.2;
6. Adjust the super-plasticiser content to the same value as in Table 4.2;
7. Estimate the plastic viscosity of new cement paste (cement, water and super-plasticiser) (Sun et al., 2006);
8. Calculate the plastic viscosity of the new mix, based on the two-phase liquid-solid suspension model;
9. Compare the plastic viscosity calculated at step 8 with the one used in the simulations. If the error is more than 5% repeat steps 3 to 8 after altering the volume fractions of solid phases;

10. Estimate t_{500}, t_{200}, t_{400} and the level-off time from their correlations with the plastic viscosity.

7.5.1 Estimating the volume fractions of solid phases

The plastic viscosity of the SCC mixes without fibres is calculated from

$$f_i(\phi_i) = f_1(\phi_1) f_2(\phi_2) \ldots f_n(\phi_n) \tag{7.1}$$

where $f_i(\phi_i)$ can be replaced by its equivalent, relative plastic viscosity i.e. plastic viscosity of SCC mix without fibre η_{NF} divided by the plastic viscosity of paste η_{paste}.

Therefore Equation (4.1) can be rewritten as

$$\eta_{NF} = \eta_{paste}\{f_1(\phi_1) f_2(\phi_2) \ldots f_n(\phi_n)\} \tag{7.2}$$

where *n* is the total number of solid phases in the mix, such as coarse aggregate, sand, and cement replacement materials;

η_{paste} is the plastic viscosity of the cement paste;

η_{NF} is the plastic viscosity of SCC mix without fibres.

The Krieger and Dougherty equation is the most suitable for cement pastes. Therefore, it is used here to obtain $f_i(\phi_i)$.

For a given η_{NF} and η_{paste}, and the value of [η] = 2.5 and ϕ_m = 0.63 are used.

Equation (7.2) can be rewritten as

$$(0.63-\phi_1)(0.63-\phi_2)(0.63-\phi_3)\ldots(0.63-\phi_n) = u \tag{7.3}$$

where *u* is a constant number.

The value of ϕ_i is given by

$$\phi_i = 0.63 - t_i x \tag{7.4}$$

where $x = \sqrt[n]{u}$ and t_i is a factor such that

$$t_1 \times t_2 \times t_3 \times \ldots \times t_n = 1 \tag{7.5}$$

7.5.2 Example of mix proportioning

As an example of the application of the mix proportioning method described in Section 7.5, let us calculate the mix proportions of a SCHPFRC mix (Mix 6 in Table 4.2) with $\phi_f = 0.5\%$ assuming that the viscosity of the base SCUPHC mix without fibres is η_{NF} = 10 Pa.s (Based on the Figures 7.1 and 7.2 and guided by Table 4.2) and that of the cement paste is η_{paste} = 0.40 Pa.s

1. The amount of cement (c) is assumed to be 500 kg. The initial amount of water (w) and super-plasticiser (sp) are the same as in Table 4.2 i.e. 138 kg and 19.32 kg, respectively.
2. In order to estimate the volume fractions of micro-silica ϕ_{MS}, limestone ϕ_{LS}, fine aggregates ϕ_{FA} and coarse aggregates ϕ_{CA} we proceed as per the algorithm above. We first use Equation (7.2) as follows

$$\begin{aligned}\eta_{NF} &= \eta_{paste}\times\left(1-\frac{\phi_{MS}}{0.63}\right)^{-2.5\times0.63}\times\left(1-\frac{\phi_{LS}}{0.63}\right)^{-2.5\times0.63}\times\left(1-\frac{\phi_{FA}}{0.63}\right)^{-2.5\times0.63}\times\left(1-\frac{\phi_{CA}}{0.63}\right)^{-2.5\times0.63}\\ &= \frac{\eta_{paste}}{\left((0.63)^4\right)^{-2.5*0.63}}\left[(0.63-\phi_{MS})(0.63-\phi_{LS})(0.63-\phi_{FA})(0.63-\phi_{CA})\right]^{-2.5*0.63}\end{aligned} \tag{7.6}$$

Substituting η_{NF} = 10 Pa.s and η_{paste} = 0.4 Pa.s into (7.6) yields

$$u = (0.63-\phi_{MS})(0.63-\phi_{LS})(0.63-\phi_{FA})(0.63-\phi_{CA}) = 0.02041 \tag{7.7}$$

$$x = \sqrt[4]{u} = 0.37795$$

Using (7.4) i.e. $\phi_i = 0.63 - t_i x$ with t_1 = 1.5, t_2 = 1/1.5, t_3 = 0.87 and t_4 = 1/0.87 (note that $t_1 \times t_2 \times t_3 \times t_4 = 1$), Equation (7.7) gives the following volume fractions of solid phases

ϕ_{MS} = 0.0631

ϕ_{LS} = 0.3780

ϕ_{FA} = 0.3013

ϕ_{CA} = 0.1953

There is an infinite choice in the selection of t_i, as mentioned before.

3. The amount of finest solid particle i.e. micro-silica (MS) suspended in cement paste is calculated according to its volume fraction (ϕ_{MS}) to give

$$\phi_{MS} = \frac{\dfrac{MS}{\rho_{ms}}}{\left(\dfrac{c}{\rho_c} + \dfrac{w}{\rho_w} + \dfrac{sp}{\rho_{sp}}\right) + \dfrac{MS}{\rho_{ms}}} \tag{7.8}$$

Using ρ_c = 2950 kg/m^3, ρ_w = 1000 kg/m^3, ρ_{sp} = 1070 kg/m^3 and ρ_{ms} = 2200 kg/m^3 in (7.8) gives the amount of micro-silica as MS = 48.20 kg/m^3.

4. Step 3 is repeated until all the solid contents in the mix have been calculated i.e. limestone (LS), fine aggregates (FA) and coarse aggregates (CA). The amounts of LS (ρ_{ls} = 2400 kg/m^3), FA (2650 kg/m^3) and CA (2800kg/m^3) work out to be LS = 506.83 kg, FA = 793.73 kg and CA = 379.73 kg.
5. The amount of water is adjusted such that water-binder ratio is 0.24. Therefore w = 131.57 kg.
6. The amount of super-plasticiser is adjusted such that SP-water ratio is 0.14. Therefore sp = 18.42 kg.
7. The value of plastic viscosity of cement paste in relation to the original cement paste used is estimated to be 0.4 Pa.s.
8. The plastic viscosity of SCC mix without fibres is calculated according to the stepwise procedure described in Chapter 4. This gives η_{NF} =11.16 Pa.s.
9. This value of plastic viscosity is compared with the one used in the simulation (i.e. η_{NF} =10 Pa.s). This gives an error in η_{NF} > 5% which is not acceptable. Therefore steps 3 to 8 have to be repeated with a lower trial amount of cement in order to reduce the plastic viscosity.

- 3 (repeat): try cement = 495 kg/m^3, giving MS = 47.96 kg.
- 4 (repeat): calculate corresponding LS = 504.24 kg, FA = 652.40 kg and CA = 511.45 kg.
- 5 (repeat): the amount of water is w =130.31 kg.
- 6 (repeat): the amount of super-plasticiser is sp =18.24 kg.

- 7 (repeat): viscosity of cement paste is calculated as 0.41 Pa.s which is a slight increase on the first trial because of the reduction in the *w/c* ratio.
- 8 (repeat): the plastic viscosity of new mix will be η_{NF} = 10.44 Pa.s.
- 9 (repeat): the error in the plastic viscosity is less than 5%, the acceptable error.
- The plastic viscosity of the mix after adding fibres is 45.04 Pa.s with error again less than 5% as compared with the one used in the simulation (i.e. η_{wF} =43.15 Pa.s).

Table 7.3. SCHPFRC mix constituents

	Mix 1
Cement (kg)	495.00
Micro-silica (MS) (kg)	47.96
Limestone (LS) (kg)	504.24
Coarse aggregate (CA) (kg)	652.40
Sand (FA) (kg)	511.45
Water(kg)	130.31
Super-plasticiser (kg)	18.24
Fibres 0.5% (kg)	39.00
SP/water	0.14
Water/Binder	0.24
w/c	0.26
η_{NF} (Pa.s)	10.44
η_{wF} (Pa.s)	45.04
η_{NF} (error%)	4.40
t_{500} (Slump flow test) (sec)	3.05
t_{200} (L-box test) (sec)	0.52
t_{400} (L-box test) (sec)	1.62
Level-off time (L-box test) (sec)	38.00

7.5.3 Typical mix proportions of normal and high strength SCC mixes

Tables 7.4 to 7.9 give proportions of typical normal and high strength SCC mixes obtained using the procedure described above for prescribed target plastic viscosity.

For each strength grade, the plastic viscosity that achieves the t_{500}, t_{200} and t_{400} that are closest to the experimental values (Tables 4.1 and 4.2) is chosen as the target value. For example, for normal strength SCC Mix 1, the t_{500}, t_{200} and t_{400} (Tables 7.1 and 7.2) are closest to the experimental values (Table 4.1) when the plastic viscosity is 10 Pa s. Therefore, many other mixes (theoretically infinitely many because t_1, t_2, ... t_n above can be chosen arbitrarily as long as their product equals unity) can be proportioned with the same plastic viscosity η_{NF} within an acceptable 5% error that will have the same nominal strength (35 MPa) and meet the flow-ability and passing ability criteria. In the tables below four typical mix proportions for each strength grade are shown.

Table 7.4 Typical mix proportions of 35 MPa SCC mixes

35 MPa				
Constituents	**Mix 1**	**Mix 2**	**Mix 3**	**Mix 4**
Cement (kg)	220.0	233.0	233.4	207.2
(GGBS) (kg)	134.6	117.9	117.3	152.2
Limestone(kg)	508.1	517.5	514.3	484.4
Coarse aggregates(kg)	556.1	451.1	547.6	540.2
Sand(kg)	708.4	789.7	697.7	709.0
Water(kg)	200.0	200.0	197.2	202.4
SP(kg)	1.80	1.80	1.80	1.80
SP/water	0.009	0.009	0.009	0.009
Water/Binder	0.56	0.56	0.56	0.56
w/c	0.91	0.86	0.84	0.98
η_{NF} (Pa.s)	10.45	10.41	10.51	10.1
η_{NF} (error%)	4.31	3.94	4.91	0.99
t_{500} (Slump flow test)(sec)	2.50	2.50	2.50	2.45
t_{200} (L-Box test)(sec)	0.25	0.25	0.25	0.24
t_{400} (L-Box test)(sec)	0.70	0.70	0.70	0.65
Level-off time (L-Box test)(sec)	6.70	6.70	6.70	6.10

Table 7.5. Typical mix proportions of 45 MPa SCC mixes

45MPa				
Constituents	**Mix 1**	**Mix 2**	**Mix 3**	**Mix 4**
Cement (kg)	315.1	315.8	314.1	316.2
(GGBS) (kg)	51.9	48.0	51.9	44.0
Limestone(kg)	771.3	776.8	770.8	781.9
Coarse aggregates(kg)	186.7	221.6	296.7	564.8
Sand(kg)	735.2	704.7	632.2	383.3
Water(kg)	201.9	200.1	201.8	198.1
SP(kg)	4.30	4.31	4.29	4.3
SP/water	0.02	0.02	0.02	0.02
Water/Binder	0.55	0.55	0.55	0.55
w/c	0.64	0.63	0.64	0.62

η_{NF} (Pa.s)	11.36	11.52	10.89	11.54
η_{NF} (error%)	3.3	4.7	0.9	4.9
t_{500} (Slump flow test)(sec)	2.65	2.68	2.62	2.68
t_{200} (L-Box test)(sec)	0.33	0.34	0.32	0.34
t_{400} (L-Box test)(sec)	0.78	0.78	0.78	0.78
Level-off time (L-Box test)(sec)	8.40	8.40	8.30	8.40

Table 7.6. Typical mix proportions of 60 MPa SCC mixes

60MPa				
Constituents	**Mix 1**	**Mix 2**	**Mix 3**	**Mix 4**
Cement (kg)	296.1	255.1	222.8	237.6
(GGBS) (kg)	82.8	130.6	174.3	146.8
Limestone(kg)	541.5	508.9	421.5	487.8
Coarse aggregates(kg)	437.0	693.1	785.6	543.1
Sand(kg)	766.7	531.4	517.1	686.5
Water(kg)	191.0	193.9	201.0	194.1
SP(kg)	3.30	3.30	3.40	3.30
SP/water	0.02	0.02	0.02	0.02
Water/Binder	0.50	0.50	0.50	0.50
w/c	0.79	0.79	0.79	0.79
η_{NF} (Pa.s)	9.54	10.19	10.37	10.37
η_{NF} (error%)	4.82	1.86	3.57	3.57
t_{500} (Slump flow test) (sec)	2.20	2.30	2.30	2.30
t_{200} (L-box test) (sec)	0.25	0.26	0.26	0.26
t_{400} (L-box test) (sec)	0.62	0.65	0.66	0.66
Level-off time (L-box test) (sec)	6.10	6.20	6.30	6.30

Table 7.7. Typical mix proportions of 80 MPa SCHPC mixes

80MPa				
Constituents	**Mix 1**	**Mix 2**	**Mix 3**	**Mix 4**
Cement (kg)	403.8	405.0	407.4	400.0
(MS) (kg)	194.4	196.3	195.1	194.3
Limestone(kg)	396.6	400.4	397.9	396.3
Coarse aggregates(kg)	788.2	795.7	790.9	787.6
Sand(kg)	434.0	433.7	435.5	433.7
Water(kg)	145.2	144.3	145.5	143.0
SP(kg)	20.50	20.20	20.40	20.00
SP/water	0.14	0.14	0.14	0.14
Water/Binder	0.24	0.24	0.24	0.24
w/c	0.36	0.36	0.36	0.36
η_{NF} (Pa.s)	10.07	10.3	10.04	10.36
η_{NF} (error%)	0.70	2.91	0.40	3.47
t_{500} (Slump flow test) (sec)	2.10	2.20	2.10	2.20
t_{200} (L-box test) (sec)	0.24	0.25	0.24	0.25
t_{400} (L-box test) (sec)	0.61	0.68	0.61	0.68
Level-off time (L-box test) (sec)	6.10	6.30	6.10	6.30

Table 7.8. Typical mix proportions of 100 MPa mixes with 0.5% fibres

100 MPa with 0.5%fibres				
Constituents	Mix 1	Mix 2	Mix 3	Mix 4
Cement (kg)	403.8	405.0	407.4	400.0
(MS) (kg)	194.4	196.3	195.1	194.3
Limestone(kg)	396.6	400.4	397.9	396.3
Coarse aggregates(kg)	788.2	795.7	790.9	787.6
Sand(kg)	434.0	433.7	435.5	433.7
Water(kg)	145.2	144.3	145.5	143.0
SP(kg)	20.50	20.20	20.40	20.00
Fibres%	0.50	0.50	0.50	0.50
SP/water	0.14	0.14	0.14	0.14
Water/Binder	0.24	0.24	0.24	0.24

w/c	0.36	0.36	0.36	0.36
η_{NF} (Pa.s)	10.07	10.3	10.04	10.36
η_{wF} (Pa.s)	43.39	44.38	43.26	44.64
η_{NF} (error%)	0.55	2.77	0.25	3.34
t_{500} (Slump flow test) (sec)	3.00	3.03	3.00	3.05
t_{200} (L-box test) (sec)	0.50	0.51	0.50	0.52
t_{400} (L-box test) (sec)	1.60	1.62	1.60	1.62
Level-off time (L-box test) (sec)	38.00	38.00	38.00	38.00

Table 7.9. Typical mix proportions of 100 MPa mixes without steel fibres

100 MPa				
Constituents	**Mix 1**	**Mix 2**	**Mix 3**	**Mix 4**
Cement (kg)	428.5	389.0	420.5	430.7
(MS) (kg)	136.8	137.6	137.6	160.4
Limestone(kg)	450.2	452.9	452.9	448.4
Coarse aggregates(kg)	560.2	563.5	689.9	958.4
Sand(kg)	690.6	694.8	564.1	268.4
Water(kg)	130.6	137.7	130.0	134.6
SP(kg)	15.70	16.50	16.80	17.30
SP/water	0.12	0.12	0.12	0.12
Water/Binder	0.23	0.23	0.23	0.23
w/c	0.30	0.35	0.30	0.31
η_{NF} (Pa.s)	11.93	11.95	12.46	11.68
η_{NF} (error%)	0.58	0.41	3.69	2.74
t_{500} (Slump flow test) (sec)	2.70	2.70	2.80	2.70
t_{200} (L-box test) (sec)	0.27	0.27	0.29	0.27
t_{400} (L-box test) (sec)	0.78	0.78	0.80	0.78
Level-off time (L-box test) (sec)	7.90	7.90	8.10	7.90

7.6 Conclusions

Different grades of normal and high strength SCC mixes with and without steel fibres that contain traditional coarse aggregate and whose characteristic cube strength varies between 35 and 100 MPa were developed. The maximum size of the coarse aggregate in all the SCC mixes reported above was 10 mm. This was the same as in the corresponding VC mixes prepared in the same laboratory. The procedure described above for proportioning the SCC mixes can of course be also applied if larger size coarse aggregate (say, 20 mm) is used, especially in mixes with compressive strength up to 60 MPa. It is however necessary to maintain the paste to solids ratio given in Table 4.4. The plastic viscosities of the mixes were estimated from the measured plastic viscosity of the paste using a micromechanical constitutive model (Ghanbari and Karihaloo, 2009).

Slump flow and L-box numerical simulations were then performed on the mixes to test their flow-ability and passing ability as measured by t_{500} for the slump test, t_{200} ,t_{400} and level-off time for the L-box test.

Guidelines for proportioning self-compacting normal strength concrete (SCNSC) and high strength concrete (SCHSC) mixes with and without steel fibres that would attain the target plastic viscosity were given (Karihaloo and Ghanbari, 2012). This method is based on an extensive investigation of the flow characteristics of such mixes using computational simulations, thus avoiding time-consuming laboratory tests.

It provides an alternative tool to the heuristic mix proportioning of SCC thus avoiding expensive and time consuming laboratory tests. It should be noted that for a given viscosity of the paste, there are many (theoretically infinitely many) mix combinations that will lead to the desired viscosity of the SCC mixes.

Chapter 8

Conclusions and Recommendations for Future Research

8.1 Conclusions

From the research work embodied in Chapters 4 to 7, the following major conclusions can be drawn:

- The development of self-compacting concrete mixes is a complex process requiring the resolution of conflicting demands of flow-ability and non-segregation which can be achieved by increasing the paste content and decreasing the large aggregate volume. Self-compacting normal, high-strength and ultra-high-performance concrete mixes without fibres may be designed to satisfy only the flow-ability and cohesiveness (i.e. resistance to segregation) criteria using the slump cone flow test. The resistance to segregation was checked visually only.
- Adding long steel fibres with crimped ends to the self-compacting concrete mix can improve the ductility, toughness, flexural and shear strengths of cement-based materials by bridging the micro- and macro-cracks and preventing their coalescence. However, the addition of fibres compromises the ability of the mix to flow smoothly through gaps in the reinforcement and to cause segregation of the fibres. Therefore, in the mixes with fibres, it is additionally necessary to check that the mixes meet the passing ability criterion using the J-ring and L-box tests. Our investigations show that although the mixes with fibres meet the flow-ability criterion and are resistant to segregation, as judged by the slump flow test, they may not meet the passing ability criterion. These mixes need to be more flow-able than required by the slump flow test, in order to satisfy the passing ability test (Chapter 4).
- The measurement of the plastic viscosity of heterogeneous SCC, especially those containing long fibres using the rheometers often gives inaccurate results with a large scatter. The viscosity of SCC mixes with and without fibres produced in Chapter 4 can be accurately estimated using a micromechanical procedure based on the measured viscosity of the cement paste alone, and the mix proportions. The 30 mm long, 0.55 mm diameter steel fibres with crimped ends significantly increase the viscosity of SCC mixes with fibres (Chapter 4).
- The plastic viscosity of SCC mixes with and without fibres so developed is accurately estimated using a micromechanical procedure based on the measured viscosity of the cement paste and the mix proportions.

- ❖ A corrected incompressible mesh-less Lagrangian SPH method was implemented to simulate the flow of the non-Newtonian self-compacting concrete with and without fibres whose behaviour is described by a Bingham-type model. This SPH approach offers considerable potential as a numerical method for modelling problems involving large deformations (Chapters 6 and 7). The simulations of the SCC mixes developed in Chapter 4 emphasised the distribution of large aggregate particles of different sizes throughout the flow in the 3D configuration. On the other hand, the simulation of high strength SCC mixes (compressive strengths in the range 100-160 MPa) which contain between 0.5 and 2.5% by volume steel fibres focused on the distribution of fibres and their orientations during the flow in 3D configuration. The capabilities of this methodology were validated by comparing the simulation results with the slump flow and L-box tests carried out in the laboratory. The numerical results were in excellent agreement with test results and confirmed that the SPH methodology is capable of predicting accurately the SCC flow with and without fibres (Chapters 6 and 7).
- ❖ The orientation and the distribution of the steel fibres have been monitored throughout the flow and the change in orientation has been described by the Johnson SB distribution function. It is shown that the fibres tend to align themselves with the principal direction of flow but remain mostly randomly distributed perpendicular to this direction. The reorientation of the fibres during the flow has been used to estimate the fibre orientation factor (FOF) in a cross section perpendicular to the principal direction of flow.
- Several powder-type SCC mixes with different plastic viscosity with and without steel fibre were proportioned using the SPH simulations as a mix design tool. This method is based on an extensive investigation of the flow characteristics of such mixes using computational simulations, thus avoiding time-consuming laboratory tests (Chapter 7).

8.2 Recommendations for future research

- In L-box laboratory test, there was an inevitable delay in manually lifting the gate to release the mix thus increasing the measured times. The delay is the more, the larger the content of coarse aggregate and/or fibres in the mix. This problem needs to be solved by providing an alternative method for opening the gate in a single lift.

- The passing ability of SCC mixes was tested using J-ring and L-box tests. In this thesis, only the simulation of flow in confined spaces (L-box) was implemented in 3D configuration. For a full understanding of the passing ability of SCC with or without fibres in unconfined spaces, a 3D simulation of SCC mixes in J-ring test is needed.

- The lengthy computational time can be significantly reduced either by using high specification serial computers or by using high performance parallel computers. Since the particle methods such as SPH method are eminently suited for parallelisation, larger 3D configurations can be simulated within a reasonable computational time by the developed algorithms after appropriately parallelising them.

- The maximum size of the coarse aggregate in all the SCC mixes reported in Chapter 4 was 10 mm. The procedure described in Chapter 7 for proportioning the SCC mixes can of course be also applied if larger size coarse aggregate (say, 20 mm) is used, especially in mixes with compressive strength up to 60 MPa. It is however necessary to maintain the paste to solids ratio given in Table 4.4.

References

Amini, Y., Emdad, H., Farid, M., (2011). A new model to solve fluid–hypo-elastic solid interaction using the smoothed particle hydrodynamics (SPH) method. European Journal of Mechanics - B/Fluids, 30(2), pp. 184-194.

Assaad, J., Khayat, K., Mesbah, H., (2003). Assessment of the Thixotropy of Flowable and Self-Consolidating Concrete. ACI Materials Journal, 100(2), pp. 99-107.

ASTM C938–10, Standard Practice for Proportioning Grout Mixtures for Preplaced-Aggregate Concrete, DOI: 10.1520/C0938-10.

Banfill, P. B. G., Beaupré, D., Chapdelaine, F., de Larrard, F., Domone, P. L., Nachbaur, L., Sedran, T., Wallevik, J. E., Wallevik, O., (2001). In Comparison of concrete rheometers: International tests at LCPC, Ferraris, C. F. and Brower, L. E. (eds), NISTIR 6819, National institute of standards and technology, Nantes, France.

Banfill, P. B. G., (2006). Rheology of fresh cement and concrete. The British Society of Rheology, School of the Built Environment, Heriot-Watt University, Edinburgh. pp. 61-130.

Bartos, P. J. M., Marrs, D. L., (1999). Development and testing of self-compacting grout for the production of SIFCON. In Proceedings of international workshop on high performance fibre reinforced cement composites, Reinhardt, H. W. and, Maaman, A. E. (eds), Germany, pp. 171-180.

Batchelor, G. K., (1967). An introduction to fluid dynamics. 1st ed. Cambridge: Cambridge University Press. ISBN: 0-52166396-2

Bayasi, Z., Kaiser, H., (2003). Flexural Behavior of Composite Concrete Slabs Using Carbon Fiber Laminate Decks. Material journal, 100(4), pp. 274-279.

Bayraktar, S., Güdükbay, U. , Özgüç, B.,(2009). GPU-Based Neighbor-Search Algorithm for Particle Simulations. Journal for Graphics, 14(1), pp. 31-42.

Becker, M., Teschner, M., (2007). Weakly compressible SPH for free surface flows. San Diego, Eurographics/ ACM SIGGRAPH Symposium on Computer Animation, pp. 1-8.

Bennenk, I. H. W., (2005). Self-compacting concrete - Five years of experience with SCC in the Netherlands. In Proceedings of the 18th BIBM International Congress, Amsterdam, pp. 211-218.

Benson, S. D. P. , Karihaloo, B. L., (2005a). CARDIFRC®-Development and mechanical properties. Part I: Development and workability. Magazine of Concrete Research, 57(6), pp. 347-352.

Benson, S. D. P. , Karihaloo, B. L., (2005b). CARDIFRC®-Development and mechanical properties. Part III: Uniaxial tensile response and other mechanical properties. Magazine of Concrete Research, 57(8), pp. 433-443.

Benson, S. D. P., Nicolaides, D. , Karihaloo, B. L., (2005). CARDIFRC®-Development and mechanical properties. Part II: Fibre distribution. Magazine of Concrete Research, 57(7), pp. 421-432.

Benz, W., Asphaug, E., (1994). Impact Simulations with Fracture. I. Method and Tests. Icarus, 107(1), pp. 98–116.

Bernasconi, A., Cosmi, F. , Hine, P., (2012). Analysis of fibre orientation distribution in short fibre reinforced polymers: A comparison between optical and tomographic methods. Composites Science and Technology, 72(16), pp. 2002-2008.

Bezerra, E. M., Joaquim, A. P., Savastano, H., (2004). Some properties of fibre-cement composites with selected fibres. In Conferência Brasileira de Materiais e Tecnologias NãoConvencionais: Habitações e Infra-Estrutura de Interesse Social, Brasil, pp. 33-43.

Billberg, P., (1999). Self-compacting concrete for civil engineering structures- The Swedish experience, Report no 2:99. Swedish Cement and Concrete Research Institute, Stockholm.

Blask, O., Honert, D., (2003). The Electrostatic Potential of Highly Filled Cement Suspension Containing Various Superplasticizers. In Seventh CANMET/ACI International Conference on Superplasticizers and Other Chemical Admixtures in Concrete, Germany, Berlin, pp.87-102.

Bonen, D., (2004). The Effects of Formulation on the Properties of Self- Consolidating Concrete. In International RILEM Symposium on Concrete Science and Engineering, A Tribute to Arnon Bentur. RILEM Publications SARL, North America, Evanston, IL. pp. 43-56.

Bonet, J., Peraire, J., (1991). An alternating digital tree (ADT) algorithm for 3D geometric searching and intersection problems. International Journal for Numerical Methods in Engineering, 31(1), pp. 1-17.

Bonet, J., Lok, T. S. L., (1999). Varational and momentum aspects of smooth particle hydrodynamics formulations. Computer Method in Applied Mechanics and Engineering, 180(1-2), pp. 97-115.

Bonet, J., Kulasegaram, S., (2000). Correction and stabilization of smooth particle hydrodynamic methods with application in metal forming simulations. International Journal of Numerical Methods in Engineering, 47(6), pp. 1189-1214.

Boukendakdjia, O., Kadrib, E. H., Kenaic, S., (2012). Effects of granulated blast furnace slag and superplasticizer type on the fresh properties and compressive strength of self-compacting concrete. Cement and Concrete Composites, 34(4), pp. 583–590.

Boulekbachea, B., Hamrata, M., Chemroukb, M., Amzianec, S., (2010). Flowability of fibre-reinforced concrete and its effect on the mechanical properties of the material. Construction and Building Materials, 24(9), pp. 1664-1671.

Brouwers, H. J. H., Radix, H. J., (2005). Self-Compacting Concrete: Theoretical and experimental study. Cement and Concrete Research, 35 (11), pp. 2116–2136.

Bouzoubaa, N., Lachemib, M., (2001). Self-compacting concrete incorporating high-volumes of class F fly ash: preliminary results. Cement and Conrete Research, 31(3), pp. 413-420.

BS EN 12350-8, (2010). Testing fresh concrete, Part 8: Self-compacting concrete- Slump test flow, British Standards publication.

BS EN 206-9, (2010). Concrete, Part 9: Additional rules for self-compacting concrete (SCC), British Standards publication.

BS EN 12350-10, (2010). Testing fresh concrete, Part 10: Self-compacting concrete- L-box test, British Standards publication.

BS EN 12350-12, (2010). Testing fresh concrete, Part 12: self-compacting concrete-J-ring test, British Standard Publications.

Bui, H. H., Fukagawa, R., Sako, K., Ohno, S., (2008). Lagrangian meshfree particles method (SPH) for large deformation and failure flows of geomaterial using elastic–plastic soil constitutive model. International journal for numerical and analytical methods in Geomechanics, 32(12), pp. 1537-1570.

Burj Khalifa, (2010) [Online] Available at: http://www.burjkhalifa.ae/en/ [Accessed 10/11/2010]

Burke, D. R., Tabrizi, S. M., Smy, T. J., (2010). Simulation of inhomogeneous models using the finite cloud method. Simulation inhomogener Modelle unter Benutzung der Finite-Wolken-Methode. Advanced Computational Engineering and Experimenting, 41(5), pp. 336–340.

Bury, M. A., Christensen, B. J., (2002). Role of innovative chemical admixtures in producing self-consolidating concrete. In 1st North American Conference on the Design and Use of Self-Consolidating Concrete, Chicago, IL, ACBM, pp.137-141.

Carlsward, J., Emborg, M., Utsi, S., Oberg, P., (2003). Effects of constituents on the workability and rheology of self-compacting concrete, The 3rd International RILEM Symposium on Self-Compacting Concrete, RILEM Publications S.A.R.L, Bagneux, France, pp. 143-153.

Castro, A. d., Liborio, J., (2006). Initial rheological description of high performance concretes. Materials Research, 9 (4), pp. 405-410.

Chan, K. D., Ong, K. C. G, Tan, C. T., (2010). Passing ability of SCC- Improved method based on the J-ring. In 35th Conference on our world in concrete and structures, Singapore.

Chaniotis, A. K., Poulikakos, D., Koumoutasakos, P., (2002). Remeshed smoothed particle hydrodynamics for the simulation of viscous and heat conducting flows. Journal of Computational Physics, 182(1), pp. 67-90.

Chen, J. K., Beraun, J. E., Jih, C. J., (1999). An improvement for tensile instability in smoothed particle hydrodynamics. Computational Mechanics, 23(4), pp. 279-287.

Chorin, A. J., (1968). Numerical solution of the Navier-Stokes equations. Mathematics of Computation, 22(104), pp. 745-762.

Cleary, P., Ha, J., Alguine, V., Nguyen, T., (2002). Flow modelling in casting processes. Applied Mathematical Modelling, 26(2), pp. 171-90.

Colagrossi, A., Landrini, M., (2003). Numerical simulation of interfacial flows by smoothed particle hydrodynamics. Journal of Computational Physics, 161(2), pp. 448-475.

Collepardi, M., (2005). Chemical admixtures today. Proceedings of Second International Symposium on Concrete Technology for Sustainable February - Development with Emphasis on Infrastructure, Hyderabad, India, pp. 527-541.

Crofton, M. W., (1885). Probability. Encyclopedia Brittanica, 9th ed., 19, pp. 768-788.

Cummins, J. S., Rudman. M, (1999). An SPH projection method. Journal of Computational Physics, 152(2/1), pp.584–607.

Cussigh, F., (1999). Self-compacting concrete stability, Proceedings of First RILEM International Symposium on Self Compacting Concrete. Stockholm, Å. Skarendahl 13-15 September.

Dalrymple, R., Knio, O., (2001). SPH Modelling of Water Waves. Coastal Dynamics, 1, pp. 779-787.

Deeb, R., Ghanbari, A., Karihaloo, B. L., (2012). Development of self-compacting high and ultra high performance concretes with and without steel fibres. Cement and Concrete Composites, 34(2), pp. 185–190.

Deeb, R., Karihaloo, B. L., (2013). Mix proportioning of self-compacting normal and high strength concretes, Magazine of Concrete Research, 65(9), pp.546–556

Deeb, R., Kulasegaram, S., Karihaloo, B. L., (2013a). 3D modelling of the flow of self-compacting concrete with or without steel fibres. Part I: slump flow test, Computational Particle Mechanics (submitted).

Deeb, R., Karihaloo, B. L., Kulasegaram, S., (2013b). Reorientation of short steel fibres during the flow of self-compacting concrete mix and determination of the fibre orientation factor, Cement and Concrete Research (accepted).

Dinakar, P., Sethy, K. P., Sahoo, U. C., (2013). Design of self-compacting concrete with ground granulated blast furnace slag. Materials and Design, 43, pp. 161-169, ISSN 0261-3069, 10.1016/j.matdes.2012.06.049.

Dilts, G. A., (1999). Moving least square particle hydrodynamics-I: consistency and stability. International Journal for Numerical Methods in Engineering, 44(8), pp. 1115-1155.

Dilts, G. A., (2000). Moving least square particle hydrodynamics - II: conservation and boundaries. International Journal for Numerical Methods in Engineering, 48(10), pp. 1503–1524.

DoE (1988), Design for Normal Concrete Mixes. HMSO, London Department of Environment.

Domone, P. L. and Thurairatnam, H., (1988), The effect of water/cement ratio, plasticizers and temperature on the rheology of cement grouts, Advances in Cement Research, 1(4), pp. 203–214.

Domone, P. L, (2003). Fresh Concrete. In: Advanced Concrete Technology: Concrete properties. Newman, J. and Choo, B., (eds). Oxford: Elsevier Ltd, pp. 20-30.

Domone, P. L, (2006). Self-compacting concrete: An analysis of 11 years of case studies. Cement and Concrete Composites, 28(2), pp. 197–208.

Domone, P. L, Illston, J. M., (2010). Construction Materials: Their Nature and Behaviour. 4th ed. Taylor and Francis Publication, ISBN. 041546515X, pp.590.

Douglas, R. P., (2004). Properties of Self-Consolidating Concrete Containing Type F Fly Ash, M.Sc. Thesis, Northwestern University.Evanston, Illinois, SN. 2619.

Dragon Bridge, (2012), [Online] Available at: http://www.ulmaconstruction.cn/eng/case_info.asp?id=62&lx=8, [Accessed 07/12/2012].

Dransfield, J., (2003). Admixtures for concrete, mortar and grout. In: Newman, J. and Choo, B. S. (eds.). Advanced Concrete Technology: Constituent Materials. Oxford: Elsevier, pp. 162-195.

Dufour, F., Pijaudier-Cabot, G., (2005). Numerical modelling of concrete flow: homogeneous approach. International Journal for Numerical and Analytical Methods in Geomechanics, 29(4), pp. 395–416.

Dupont, D., Vandewalle, L., (2005). Distribution of steel fibres in rectangular sections. Cement and Concrete Composite, 27(3), pp. 391-398.

Duval, R., Kadri, E., (1998). Influence of silica fume on the workability and the compressive strength of high-performance concretes. Cement and Concrete Research, 28(4), pp. 533-547.

Dyka, C. T., Randles, P. W., Ingel, R. P., (1997). Stress points for tension instability in SPH. International Journal for Numerical Methods in Engineering, 40(13), pp. 2325-2341.

EFNRC, (2005). The European Guidelines for Self-Compacting, Specification, Production and Use. [Online] Available at: www.efnarc.org [Accessed 07/12/2012]

Ferreira, J. P. J. G., Branco, F. A. B, (2007). The use of glass fiber–reinforced concrete as a structural material, Experimental Techniques, 31(3), pp. 64-73.

Feys, D., Heirman, G., De Schutter, G., Verhoeven, R., Vandewalle, L., Van Germet, D., (2007), Comparison of two concrete rheometers for shear thickening behaviour of SCC, In 5th International RILEM Symposium of self-compacting concrete, Ghent, Belgium, pp. 365-370.

FIB, (2010). Draft Code. The International Federation for Structural Concrete, 2, pp. 312.

Fonseca, T. F., Marques, C. P., Parresol, B., (2009). Describing maritime pine diameter distributions with Johnson's SB distribution using a new all-parameter recovery approach. The Society of American Foresters, 55(4), pp. 367-373.

Frankel, N. A., Acrivos, A., (1967). On the viscosity of a concentrated suspension of solid spheres, Chemistry and Engineering Science, 22(6):pp. 847-853

Fulk, D. A., Quinn, D. W., (1996). An analysis of 1-D smoothed particle hydrodynamics kernels. Journal of Computational Physics,126(1), pp. 165-180.

Gaimster, R., Dixon, N., (2003), Self-compacting concrete, in Advanced concrete technology, Newman, J., Choo, B. S. (eds), Elsevier, 3, pp. 202-223.

Ghanbari, A., Karihaloo, B. L. (2009). Prediction of the plastic viscosity of self-compacting steel fibre reinforced concrete. Cement and Concrete Research, 39(12), pp. 1209-1216.

Ghanbari, A., (2011). Self-compacting high and ultra-high performance concretes, PhD Thesis, Cardiff University, UK.

Gingold, R. A., Monaghan, J. J., (1977). Smoothed particle hydrodynamics: theory and application to non-spherical stars. Monthly Notices of the Royal Astronomical Society, 181, pp. 375-389.

Gram, A., (2009). Numerical Modelling of Self-Compacting concrete flow-Discrete and Continuous Approach, PhD Thesis, Royal Institute of Technology, Sweden.

Gram, A., Silfwerbrand, J., (2011). Numerical simulation of fresh SCC flow: applications. Materials and structures, 44(4), pp. 805-813.

Grünewald, S., Walraven, J. C., (2003). Rheological measurements on self-compacting fibre reinforced concrete. France, eds. Wallevik Ó. and Níelsson I. S.A.R.L, pp. 49-58.

Grünewald, S., (2004), Performance-based design of self-compacting fibre reinforced concrete, Ph.D. Thesis, Delft university, Netherlands.

Grünewald, S., Walraven, J. C., (2009). Transporting Fibres as Reinforcement in Self-Compacting Concrete. HERON, 54(2/3), pp. 101-126.

Grzeszczyk, S., Lipowski, G., (1997). Effect of content and particle size distribution of high-calcium fly ash on the rheological properties of cement pastes. Cement and Concrete Research, 27(6), pp. 907-916.

Heirman, G., Vandewalle, L., Van Gemert, D. , Wallevik, Ó. ,(2008). Integration approach of the Couette inverse problem of powder type self-compacting concrete in a wide-gap concentric cylinder rheometer, Journal of Non-Newtonian Fluid Mechanics ,150(2/3),pp. 93-103.

Indian_Standard. (2009). B. o. Indian Standards concrete mix proportioning -Guidelines. IS 10262. New Delhi, India.

Johnson, N., (1949). Systems of frequency curves generated by methods of translation. Biometrika, 36(1), pp. 149-176.

Johnston, C. D., (1996), Proportioning, mixing and placement of fibre-reinforced cements and concretes, Production Methods and Workability of Concrete, Bartos, P., Marrs, D. L. and Cleland, D. J.,(eds) E&FN Spon, London. pp. 155-179.

Kalssen, R., (2002). Astrophysikalishes institute potsdam. [Online] Available at: http://www.ita.uniheidelberg.de/research/klessen/people/klessen/publications/presentations/2002-04-26-SPH-lecture-cardiff.pdf [Accessed 13/ 04/ 2013].

Karihaloo, B. L., (2012). Influence of micro-structural parameters and thermal cycling on the properties of CARDIFRC. Sadhana, Indian Academy of Sciences, 37(1), pp. 125-132.

Karihaloo, B. L., Ghanbari, A., (2012). Mix proportioning of Self-Compacting High and Ultra-high Performance concretes with and without steel fibres. Magazine of Concrete Research, 64(12), pp.1089-1100.

Katkhuda, H., Hanayneh, B., Shatarat, N., (2010). Effect of Microsilica and Water Proofer on Resistance of Concrete to Phosphoric Acid Attack. Jordan Journal of Civil Engineering, 4(4), pp. 426-438.

Kelecy, F., Fletcher, R., (1997). The development of a free surface capturing approach for multidimensional free surface flow in closed container. Journal of Computational Physics, 138(2), pp. 939-980.

Kennedy, C. T., (1940). The Design of Concrete Mixes. American Concrete Institute, 36, pp. 373-400.

Khayat, K. H., (1995). Effects of Antiwashout Admixtures on Fresh Concrete Properties. ACI Materials Journal, 92(2), pp. 164-171.

Khayat, K. H., Guizani, Z., (1997). Use of viscosity-modifying admixture to enhance stability of fluid concrete. American Concrete Institute Materials Journal, 94(4), pp. 332-340.

Khayat, K. H., (1999). Workability, testing, and performance of self-consolidating concrete. ACI Materials Journal, 96(3), pp. 339-346.

Khayat, K. H., (2000). Optimization and performance of air-entrained, self-consolidating concrete. Materials Journal, 79(5), pp. 526-535.

Khayat, K. H., Hu, C., Monty, H., (1999). Stability of self-consolidating concrete, advantages, and potential applications. In 1st International RILEM Symposium on Self-Compacting Concrete, Skarendahl, Å. and Petersson, Ö. (eds), Stocknolm, Sweden. pp. 143-152.

Kim, J. K., Han, S. H., Park, Y. D., Noh, J. H., Park, C. L., Kwon, Y. H. and Lee, S. G., (1996), Experimental research on the material properties of super flowing concrete, In: Bartos P. J. M., Marrs, D. L., Cleland, D. J. (eds), Production Methods and Workability of Concrete, E&FN Spon, pp.271-284

Kitaoji, H., Tanigawa, Y., Mori, H. , Kurokawa, Y. , Urano, S. , (1996). Flow simulation of fresh concrete cast into wall structure by viscoplastic divided space element method. Transactions of the Japan Concrete Institute, 16, pp. 45-52.

Koehler, E. P., Fowler, D. W., (2003). Summary of Concrete Workability Test Methods., Aggregates Foundation for Technology: Research and Education, Washington, Research report ICAR-105-1, pp. 92.

Koehler, E. P., Fowler, D. W., (2007). ICAR Mixture Proportioning Procedure for SCC. Aggregates Foundation for Technology: Research and Education, University of Texas, Austin, Research report ICAR-108-1, pp. 21.

Koehler, E. P., Fowler, D. W., Foley, E. H., Rogers, G. J., Watanachet, S., Jung, M. J., (2007). Self-Consolidating Concrete for Precast Structural Applications: Mixture Proportions, Workability, and Early-Age Hardened Properties, Aggregates Foundation for Technology: Research and Education, University of Texas, Austin, CTR Technical Report: 0-5134-1, pp.348.

Koshizuka, S., Oka, Y., Tamako, H., (1995). A particle method for calculating splashing of incompressible viscous fluid. Proc. Int: International Conference on Mathematics and Computations, Reactor Physics and Environmental Analysis, 2, pp. 1514-1521.

Koshizuka, S., Nobe, A., Oka, Y., (1998). Numerical analysis of breaking waves using moving particle semi- implicit method. International Journal for Numerical Methods in Fluids, 26(7), pp. 751-769.

Krieger, I. M., Dougherty, T. G., (1959). A mechanism for non-Newtonian flow in suspensions of rigid spheres. Journal of Rheology, 3(1), pp. 137-152.

Kulasegaram, S., Karihaloo, B. L., Ghanbari, A., (2011). Modelling the flow of self-compacting concrete. International Journal for Numerical and Analytical Methods in Geomechanics, 35(6), pp. 713-726.

Kulasegaram, S., Karihaloo, B., (2013). Fibre-reinforced, self-compacting concrete flow modelled by SPH. Proceedings of the ICE - Engineering and Computational Mechanics, 166(1), pp. 22-31.

Kurokawa, Y., Tanigawa, Y., Mori, H., Nishinosono, Y., (1996). Analytical study on effect of volume fraction of coarse aggregate on Bingham's constants of fresh concrete. Transactions of the Japan Concrete Institute, 18, pp. 37-44.

Kwan, A. K. H., Ng, I. Y. T., (2010). Improving Performance and Robustness of SCC by Adding Supplementary Cementitious Materials. Construction and Building Materials, 24(11), pp. 2260–2266.

Lachemi, M., Hossain, K., Lambros, V., Bouzoubaa, N., (2003). Development of Cost Effective Self-Consolidating Concrete Incorporating Fly Ash, Slag Cement, or Viscosity-Modifying Admixtures. ACI Materials Journal, 100(5), pp. 419-425.

Lee, E. S. E. S., Moulinec, C., Xu, R., Violeau , D., Laurence , D., Stansby, P. , (2008). Comparisons of weakly compressible and truly incompressible algorithms for the SPH mesh free particle method. 227(18), pp. 8417–8436.

Lee, Y. H., Lee, S. W.,Youn , J. R., Chung, K., Kang T. J., (2002). Characterization of fiber orientation in short fiber reinforced composites with an image processing technique. Materials Research Innovations, 6(2), pp. 65-72.

Lewis, R., Sear, L., Wainwright, P., Ryle, R., (2003). Advanced Concrete Technology-Constituent Materials, Cementitious additions. Newman, J. and Choo, B.S. (Eds). Oxford: Elsevier Ltd, pp. 96-159.

Li, S. F., Liu, W. K., (1996). Moving least square kernel Galerkin method (II) fourier analysis. Computer Methods in Applied Mechanics and Engineering, 139(4), pp. 159-193.

Li, S. F., Liu, W. K., (2002). Meshfree and particle methods and their applications, American Society of Mechanical Engineers, 55(1), pp. 1-34.

Li, C. Z., Feng, N., Li, Y. D., Chen, R. J., (2005). Effects of polyethylene oxide side chains on the performance of polycarboxylate-type water reducers. Cement and Concrete Research, 35(5), pp. 867-873.

Libersky, L. D., Petschek, A. G., Carney, T. C. Hipp, J. R. Allahdadi, F. A., (1993). High Strain Lagrangian Hydrodynamics: A Three-Dimensional SPH Code for Dynamic Material Response, Journal of Computational Physics, 109(1). pp. 67-75.

Liu, G. R., Liu, M. B., (2003). Smooth particle hydrodynamics. Singapore: World Scientific Printers CO. Pte. Ltd. ISBN 981-238-456-1.

Liu , M. B., Liu, G. R., (2010). Smoothed Particle Hydrodynamics (SPH): an Overview and Recent Developments. Archives of Computational Methods in Engineering, 17, pp. 25-76.

Liu, J., Li, C., Liu, J., Du, Z., Cui, G., (2011). Characterization of fiber distribution in steel fiber reinforced cementitious composites with low water-binder ratio. Indian Journal of Engineering and Materials science, 18(6), pp. 449-457.

Lucy, L. B., (1977). A numerical approach to the testing of the fission hypothesis. Astron Journal, 82(12), pp. 1013–1024.

Martys, N., (2005). Study of a dissipative particle dynamics based approach for modelling suspensions. Journal of Rheology, 49(2), pp. 401-424.

Martinie, L., Roussel, N., (2011). Simple tools for fiber orientation prediction in industrial practice. Cement and Concrete Research, 41(10), pp. 933-1000.

Mazloom, M., Ramezanianpour, A. A., Brooks, J., (2004). Effect of Silica Fume on Mechanical Properties of High-Strength Concrete. Cement Concrete Composites, 26(4), pp. 347–357.

Nehdi, M., Rahman, M., (2004). Estimating rheological properties of cement pastes using various rheological models for different test geometry, gap and surface friction. Cement and Concrete Research, 34(11), pp. 1993-2007.

Monaghan, J. J., Gingold, R. A, (1983). Shock simulation by the particle method SPH. Journal of Computational Physics, 52(2), pp. 374-389.

Monaghan, J. J., Lattanzio, J. C., (1985). A refined particle method for astrophysical problems. Astronomy and Astrophysics, 149(1), pp. 135-143.

Monaghan, J. J., (1994). Simulating Free Surface Flows with SPH. Journal of Computational Physics, 110(2), pp. 399-406.

Monaghan, J. J., Thompson, M. C., Hourigan, K., (1994). Simulation of free surface flows with SPH. Lake Tahoe, Proc. of ASME Symposium on Computational Methods in Fluid Dynamics, USA.

Monaghan, J. J., Kocharyan, A., (1995). SPH simulation of multi-phase flow. Computer Physics Communications, 87(1/2), pp. 225-235.

Monaghan, J. J., (1996). Gravity currents and solitary waves. Physica D: Nonlinear Phenomena, 98(2/4), pp. 523-533.

Monaghan, J. J., Kos, A., (1999). Solitary waves on a Cretan beach. Journal of Waterway, Port, Coastal, and Ocean Engineering, 125(3), pp. 145-154.

Monaghan, J. J., (2000). SPH without a tensile instability. Journal of Computational Physics, 159(2), pp. 290-311.

Mori, H., Tanigawa, Y., (1992). Simulation methods for fluidity of fresh concrete. Nagoya University, Memoirs of the school of engineering, pp. 71-133.

Morris, J. P., (1996). A study of the stability properties of SPH, Publications Astronomical Society of Australia, 13(1), pp. 97-102.

Morris, J. P., Fox, P. J., Zhu, Y., (1997). Modelling low Reynolds number incompressible flows using SPH. Journal of Computational Physics, 136(1), pp. 214-226.

Murali, G., Vardhan, C. M. V., Prabu, R., Khan, Z. M. S. A. ,Mohamed, T. A., Suresh, T., (2012). Experimental investigation on fibre reinforced concrete using waste materials. International Journal of Engineering Research and Applications, 2(2), pp. 278-283.

Obla, K. H. H. R. H., Thomas, M., Shashiprakash, S. G., Perebatova, O., (2003). Properties of Concrete Containing Ultra-Fine Fly Ash. ACI Materials Journal, 100(5), pp. 426-433.

Oh, S. G., Noguchi, T., Tomosawa, F., (1997). Evaluation of pass ability of self-compacting concrete by visualization mode.In proceeding of Japan concrete institute, 19(1), pp. 37-42.

Okamura, H., Ozawa, K., (1995). Mix design for self-compacting concrete. Concrete Library of JSCE, 25, pp. 107-120.

Okamura, H., Ouchi, M., Hibino, M., Ozawa, K., (1998). A rational mix-design method for mortar in self-compacting concrete. In the 6th East Asia-Pacific Conference on Structural Engineering and Construction, Taipei, ROC, 2, pp. 1307-1312.

Okamura, H., Ouchi, M., (1999). Self-compacting concrete. Development, present use and future. In 1st International RILEM Symposium on Self-Compacting Concrete, Skarendahl, Å. and Petersson, Ö. , (eds). Stocknolm, Sweden, RILEM, pp. 3-14.

Okamura, H., Ouchi, M., (2003), Self-compacting concrete, Journal of Advanced Concrete Technology, 1(1), pp. 5-15.

Oner, A., Akyuz, S., (2007). An Experimental Study on optimum usage of GGBS for the compressive strength of concrete. Cement and Concrete Composites, 29(6), pp. 505-514.

Ouchi, M., M. Hibino, and H. Okamura, (1997). Effect of Superplasticizer on Self-Compactability of Fresh Concrete, Transportation Research Board of the National Acadimies, ISBN: 0309059739, 1574, pp. 37-40.

Ouchi, M., Nakamura, S., Osterson, T., Hallberg, S. and Lwin, M., (2003), Applications of self-compacting concrete in Japan, Europe and the United States, ISHPC, pp. 2-5.

Ozawa, K., Maekawa, K., Kunishima, M., Okamura, H., (1989). Development of high performance concrete based on the durability design of concrete structures. Proceedings of the 2nd East-Asia and Pacific Conference on Structural Engineering and Construction (EASEC-2), 1, pp. 445-450.

Papanastasiou, T. C., (1987). Flows of materials with yield. Journal of Rheology, 31(5), pp. 385-404.

Park, C. K., Noh, M. H., Park, T. H., (2005). Rheological Properties of Cementitious Materials Containing Mineral Admixtures. Cement and Concrete Research, 35(5), pp. 842-849.

Patzák, B., Bittnar, Z., (2009). Modeling of fresh concrete flow. Computers and Structures, 87(15), pp. 962-969.

PCI (Precast/Prestressed Concrete Institute**)**, (2003). Interim Guidelines for the Use of Self-Consolidating Concrete in Precast/Prestressed Concrete Institute. [Online] Available at: www.pci.org [Accessed 05 12 2012].

Phan-Thien, N., Huilgol, R. R., (1980). A Micromechanic Theory of Chopped-Fibre-Reinforced Materials, Journal of Fibre Science and Technology, 13(6), pp. 423-433.

Ramachandran, V. S., Feldman, R. F. and Beaudoin, J. J., (1981). Concrete Science, Heyden and Son Ltd, ISBN: 0855017031.

Ramachandran, V. S., Beaudoin, J. J., (2001). Techniques in concrete science and technology. Principles, techniques and applications, William Andrew & Noyes Publications, USA. ISBN-13: 978-0815514374.

Rao, G. A., (2003). Investigations on the performance of silica fume-incorporated cement pastes and mortars. Cement and Concrete Research, 33(11), pp. 1765–1770.

Rennolls, K., Wang, M., (2005). A new parameterization of Johnson's SB distribution with application to fitting forest tree diameter data. Canadian Journal of Forest Research, 35(3), pp. 575–579.

Richardson, A., Dave, U., (2008). The effect of polypropylene fibres within concrete with regard to fire performance in structures. Structural Survey, Emerald Group Publishing Limited, 26(5), pp. 435 - 444.

Robinson, M., (2009). Turbulence and Viscous Mixing using Smoothed Particle Hydrodynamics, PhD thesis, Monash University, Austratia.

Roussel, N., Coussot, P., (2005). Fifty-cent rheometers for yield stress measurements: from slump to spreading flow. Journal of Rheology, 49(3), pp. 705–718.

Roussel, N., (2006). Correlation between yield stress and slump: Comparison between numerical simulations and concrete rheometers results. Materials and Structures, 39(4), pp. 501-509.

Roussel, N., (2007). Rheology of fresh concrete: from measurements to predictions of casting processes. Materials and Structures, 40(10), pp. 1001-1012.

Roussel, N., Geiker, M. R., Dufour,F.,Thrane, L. N., Szabo, P. (2007). Computational modeling of concrete flow: General overview. Cement and Concrete Research. 37(9), pp. 1298–1307.

Roussel, N., Nguyen, T., Yazoghli, O., Coussot, P., (2009). Passing ability of fresh concrete: A probabilistic approach. Cement and Concrete Research, 39(3), pp. 227-232.

Roziere, E., Granger, S., Turcry, P., Loukili, A., (2007). Influence of Paste Volume on Shrinkage Cracking and Fracture Properties of Self Compacting Concrete. Cement and Concrete Composites, 29(8), pp. 626-636.

Russel, W. B., (1997). High performance concrete-from buildings to bridges. Concrete International, 19(8), pp. 62-63.

Sahmaran, M., Yurtseven, A., Yaman, I. O., (2005). Workability of hybrid fiber reinforced self-compacting concrete. Building and Environment, 40(12), pp. 1672-1677.

Schutter, D., (2005). The European Guidelines for Self-Compacting, Specification, Production and Use. [Online] Available at: www.efnarc.org. [Accessed 7/10/2012].

Shadle, R., Somerville, S., (2002). The Benefits of Utilizing Fly Ash in Producing Self-Compacting Concrete. In 1st North American Conference on the Design and Use of Self-Consolidating Concrete, Chicago, pp. 217-222.

Shao, S., Lo, E. Y. M., (2003). Incompressible SPH method for simulating Newtonian and non-Newtonian flows with a free surface. Advances in Water Resources, 26(7), pp. 787-800.

Siddique, R., Khan, M. I., (2011). Supplementary Cementing Materials: Silica Fume. Engineering Materials, Ch:2. Springer-Verlag Berlin Heidelberg, , pp. 67-119. ISBN: 978-3-642-17865-8.

Sodra Lanken , (1997), [Online] Available at: http://publikationswebbutik.vv.se/upload/3267/89043_Sodra_lanken_a_new_traffic_route_in_Stockholm.pdf. [Accessed 7/9/2012].

Solenthaler, B., Pajarola,R., (2009). Predictive-Corrective Incompressible SPH. ACM Transactions on Graphics, 28(3), pp. 1-6.

Solomon, H., (1978). Geometric probability. Society for Individual and Applied Mathematics. USA: SIAM.

Sonebi, M., (2004). Medium Strength Self-Compacting Concrete Containing Fly Ash: Modeling Using Statistical Factorial Plans. Cement and Concrete Research, 34(7), pp. 1199-1208.

Soroushian, P., Lee, C. D., (1990). Distribution and Orientation of fibres in steel fibre reinforced concrete. ACI Materials Journal, 87(5), pp. 433-441.

Spangenberg, J. , Roussel, N., Hattel, J. H., Thorborg, J., Geiker, M. R., Stang, H., Skocek, J., (2010). Prediction of the Impact of Flow-Induced Inhomogeneities in Self-Compacting Concrete (SCC). Khayat, K. H.; Feys, D. (eds.), In: Proceedings of the 2010 International

RILEM Symposium on Self-Compacting Concrete. Design, Production and Placement of Self-Consolidating Concrete, pp. 209-214, Canada.

Stamatelos, F. G., Anagnostopoulos, J. S., (2008). Simulation of Viscous Flows with a Gridless Particle Method. Wseas Transactions on Fluid Mechanics, 3(4), pp. 379-389.

St George Wharf,(2004), [Online] Available at: http://projects.bre.co.uk/ConDiv/concrete%20frame/ProjectOverview.pdf, [Accessed 7/10/2012].

Struble, L., Sun, G. K., (1995). Viscosity of Portland cement paste as a function of concentration. Advanced Cement Based Materials, 2(2), pp. 62-69.

Su, N., Hsu, K., Chai, H., (2004). A simple mix design method for self-compacting concrete. Cement and Concrete Research, 31(12), pp. 1799-1807.

Su, N., Miao, B., (2003). A new method for the mix design of medium strength flowing concrete with low cement content. Cement and Concrete Composites, 25(2), pp. 215-222.

Sun, Z., Voigt, T., Shah, S. P., (2006). Rheometric and ultrasonic investigations of viscoelastic properties of fresh Portland cement pastes. Cement and Concrete Research, 36(2), pp. 278-287.

Surabhi, C. S., Soman, M., Prakash, V. S., (2009). Influence of limestone powder on properties of self-compacting concrete. 10th National Conference on Technological Trends (NCTT09), pp. 159-164. Kerala, India.

Svec, O., Skocek, J., Stang, H., Geiker, M. R., Roussel, N., (2012). Free surface flow of a suspension of rigid particles in a non-Newtonian fluid: A lattice Boltzmann approach. Journal of Non-Newtonian Fluid Mechanics, 179/180, pp. 32-42.

Swegle, J. W., Hicks, D. L., Attaway, S. W., (1995). Smoothed particle hydrodynamics stability analysis. Journal of Computational Physics, 116(1), pp. 123-134.

Takeda, H., Miyama, S. M., Sekiya, M., (1994). Numerical Simulation of Viscous Flow by Smoothed Particle Hydrodynamics. Progress of Theoretical Physics, 92(5), pp. 939-960.

Tattersall, H., (1991). Workability and quality control of concrete. Taylor & Francis publication, London. pp. 262. ISBN: 0419148604.

Taylor, M., (1997). Characterisation of normal and high-strength plain and fibre-reinforced concretes by means of strength fracture and combined fracture/relaxation tests, PhD Thesis, Cardiff University.UK.

Thrane, L., Szabo, P., Geiker, M., Glavind, M. and Stang, H., (2004), Simulation of the test method “L-box” for self-compacting concrete, Annual Transactions of the Nordic Rheology Society, 12, pp. 47-54.

Thrane, L. N., (2007), Form filling with self-compacting concrete. Ph.D. Thesis, Danish Technological Institute. ISBN 97-8877-8772-473.

Tregger, N., Ferrara, L. and Shah, S. P., (2007), Empirical relationships between viscosity and flow time measurements from mini-slump tests for cement pastes formulated from SCC, Proceedings of the 5th International RILEM Symposium-SCC 2007, pp. 273-278. Ghent, Belgium.

Tviksta, L. G., (2000). Guidlines- Task 9-End product, Brite EuRam Proposal No. BE96-3801.

Utsi, S., Emborg, M and Carlsward, J., (2003), Relation between workability and rheological parameters, In: Proceedings of the 3rd International RILEM Symposium, Pro 33, Wallevik, O., Nielsson, I. (eds). RILEM: Cachan, pp. 154-160.

Uysal, M., Sumer, M., (2011). Performance of self-compacting concrete containing different mineral admixtures. Construction and Building Materials, 25(11), p. 4112–4120.

Vandewalle, L., (1993). Fibre reinforced concrete ,Special types of concrete and applications. Belgium, Bouwkunde, D. B. (ed.). Katholieke Universiteit Leuven.

Valizadeh, A., Shafieefar, M.,Monaghan,J. J., Salehi, S. A. A. N., Neyshaboori, (2008). Modeling Tow-Phase Flows Using SPH Method. 8(21), pp. 3817-3826.

Vasilic, K., Roussel, N., Meng, B., Kühne, H. C., (2010). Computational modeling of SCC flow through reinforced sections in self-compacting concrete (SCC). Canada, In: Proceedings of the 2010 International RILEM Symposium on Self-Compacting Concrete.Design, production and placement of self-consolidating concrete eds. Khayat, K. H. and Feys, D., pp. 187-195.

Vesenjak, M., Ren, Z., (2007). Application Aspects of the Meshless SPH Method. Journal of the Serbian Society for Computational Mechanics, 1(1), pp. 74-86.

Vikan, H. and Justnes, H., (2003), Influence of silica fume on rheology of cement paste, Proceeding of international symposium. Self-Compacting Concrete, Reykjavik, Iceland.

Welton, W., (1998). Two-dimensional PDF/SPH simulation of compressible turbulent flows. Journal of Computational Physics, 139(2), pp. 410-443.

Wróblewski, P., Kopeć, M., Boryczko, K., (2007). SPH – a comparison of neighbor search methods based on constant number of neighbors and constant cut-off radius. Task Quarterly, 11(3), pp. 273-283.

Xiong, S., Liu, W. K., Cao, J., Li, C. S., Rodrigues, J. M. C., Martins, P. A. F., (2005). Simulation of bulk metal forming processes using the reproducing kernel particle method. Computers & Structures, 83(8/9), pp. 574‑587.

Yahiaa, A., Tanimurab, M., Shimoyama, Y., (2005). Rheological properties of highly flowable mortar containing limestone filler-effect of powder content and w/c ratio. Cement and Concrete Research, 35(3), pp. 532-539.

Yang, C. T., (2013). Application of reproducing kernel particle method and element-free Galerkin method on the simulation of the membrane of capacitive micromachined microphone in viscothermal air. Computational Mechanics, 51(3), pp. 295-308

Zak, G., Park, C., Benhabib, B., (2001). Estimation of three-dimensional fibre-orientation distribution in short-fibre composites by a two-section method. Journal of Composite Materials, 35(4), pp. 316-339.

Zheng, X., Duan, W. -W., (2010). Numerical simulation of dam breaking using smoothed particle hydrodynamics and viscosity behavior. Journal of Marine Science and Application, 9(1), pp. 34-41.

Zhu, Y., Fox, P. J., Morris, J. P., (1999). A pore-scale numerical model for flow through porous media. International Journal for Numerical and Analytical Methods in Geomechanics, 23(9), pp. 881–892.

Appendix A

A.1 Substantial derivative

The substantial derivative or the total time derivative is an important physical concept in fluid dynamics. Let us consider the infinitesimal fluid cell moving with the flow (Figure A.1) at two time instants, t_1 and t_2.

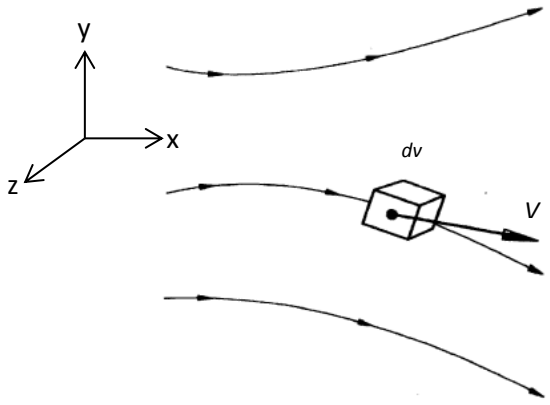

Figure A.1: Infinitesimal fluid element approach with moving control element

The scalar density field at time t_1 is given by;

$$\rho_1 = \rho(x_1, y_1, z_1, t_1) \tag{A.1}$$

At a later time, t_2 this field becomes:

$$\rho_2 = \rho(x_2, y_2, z_2, t_2) \tag{A.2}$$

The function (A.2) is expanded in a Taylor's series around first point $t_1$to give

$$\rho_2 = \rho_1 + (\frac{\partial \rho}{\partial x})_1 (x_2 - x_1) + (\frac{\partial \rho}{\partial y})_1 (y_2 - y_1) + (\frac{\partial \rho}{\partial z})_1 (z_2 - z_1)$$
$$+ (\frac{\partial \rho}{\partial t})_1 (t_2 - t_1) + (\text{higher order terms}) \tag{A.3}$$

Dividing both sides of (A.3) by $(t_2 - t_1)$ gives

$$\frac{\rho_2-\rho_1}{t_2-t_1}=(\frac{\partial\rho}{\partial x})_1(\frac{x_2-x_1}{t_2-t_1})+$$
$$(\frac{\partial\rho}{\partial y})_1(\frac{y_2-y_1}{t_2-t_1})+(\frac{\partial\rho}{\partial z})_1(\frac{z_2-z_1}{t_2-t_1})+(\frac{\partial\rho}{\partial t})_1 \quad (A.4)$$

The left hand side of (A.4) is physically the average time rate of change in density of the fluid element as it moves from point 1 to point 2. If t_2 approaches t_1, then

$$\lim_{t_2\to t_1}(\frac{\rho_2-\rho_1}{t_2-t_1})\equiv\frac{D\rho}{Dt} \quad (A.5)$$

Examining (A.5), it can be realized that in a physical sense $\frac{D\rho}{Dt}$ is the time rate of change of the fluid element, i.e. the change of density as it moves through point one as opposed to $\frac{\partial\rho}{\partial t}$ which is the time rate of change of density at the fixed point 1. By taking the limit of the right hand side of (A.4) as t_2 approaches t_1, we have

$$\lim_{t_2\to t_1}(\frac{x_2-x_1}{t_2-t_1})\equiv v_x$$
$$\lim_{t_2\to t_1}(\frac{y_2-y_1}{t_2-t_1})\equiv v_y$$
$$\lim_{t_2\to t_1}(\frac{z_2-z_1}{t_2-t_1})\equiv v_z \quad (A.6)$$

Therefore (A.4) becomes

$$\frac{D\rho}{Dt}\equiv v_x\frac{\partial\rho}{\partial x}+v_y\frac{\partial\rho}{\partial y}+v_z\frac{\partial\rho}{\partial z}+\frac{\partial\rho}{\partial t} \quad (A.7)$$

By considering (A.7), a general expression can be obtained for a substantial derivative

$$\frac{D}{Dt}\equiv\frac{\partial}{\partial t}+v_x\frac{\partial}{\partial x}+v_y\frac{\partial}{\partial y}+v_z\frac{\partial}{\partial z} \quad (A.8)$$

Denoting

$$\nabla\equiv\vec{i}\frac{\partial}{\partial x}+\vec{j}\frac{\partial}{\partial y}+\vec{k}\frac{\partial}{\partial z} \quad (A.9)$$

in Cartesian co-ordinates, (A.8) can be written as

$$\frac{D}{Dt} \equiv \frac{\partial}{\partial t} + (\mathbf{v} \cdot \nabla) \tag{A.10}$$

$\mathbf{v} \cdot \nabla$ is called the convective derivative, which in physical terms defines the time rate of change as the fluid element moves from one location to another in the flow field. The substantial derivative can be used for any flow field variables, e.g. pressure.

A.2 Physical meaning of $\nabla \cdot \mathbf{v}$

The divergence of the velocity is a term that appears frequently when dealing with fluid dynamics problems. Consider a moving control volume in a flow field; this control volume contains the same particles as it moves through the flow. As the control volume moves to a different location of the fluid, its volume V and control surface S will change because at its new position a different value of ρ might exist. The moving control volume with a constant mass is continuously changing its volume and shape depending on the characteristics of the flow. Consider an infinitesimal element moving at the local velocity $\mathbf{v}$, with surface dS and volume ΔV. Figure A.2 shows the change in the volume of the control volume ΔV over a time increment Δt.

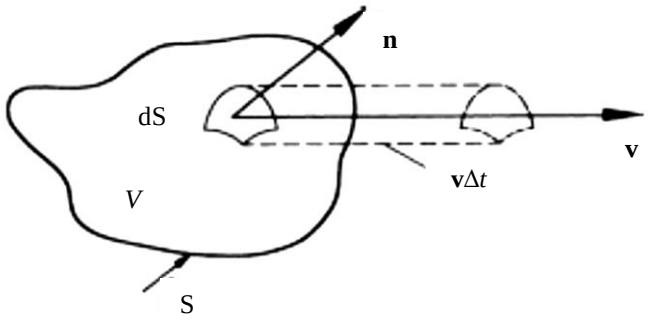

Figure A.2: Physical meaning of the divergence of velocity

From Figure A.2, the change in volume is equal to the volume of the cylinder with the base area dS and height $(\mathbf{v}\Delta t) \cdot \mathbf{n}$, where $\mathbf{n}$ is a unit vector perpendicular to the surface. This change in volume is equal to

$$\Delta V = [(\mathbf{v}\Delta t) \cdot \mathbf{n}]\,\mathrm{dS} \tag{A.11}$$

The total volume change of the entire control volume is the integral over the control surface S

$$\Delta V = \int_S \mathbf{v}\Delta t \cdot \mathbf{n}\, \mathrm{dS} \tag{A.12}$$

Dividing both sides of (A.12) by Δt and applying the divergence theorem yields

$$\frac{\Delta V}{\Delta t} = \int_V \nabla \cdot \mathbf{v}\, \mathrm{d}V \tag{A.13}$$

where ∇ is the divergence operator (A.9).

Note that the left side of (A.13) is the substantial derivative of *V*, since this case is dealing with the time rate of change of the control volume as the volume moves with the flow.

If the control volume is shrunk to an infinitesimal fluid element with volume δV, (A.13) becomes

$$\frac{\Delta(\delta V)}{\Delta t} = (\nabla \cdot \mathbf{v}) \int_V d(\delta V) = (\nabla \cdot \mathbf{v})\delta V \tag{A.14}$$

Finally, the velocity divergence is given by;

$$\nabla \cdot \mathbf{v} = \frac{1}{\delta V} \frac{D(\delta V)}{Dt} \tag{A.15}$$

The right hand side of (A.15) explains physically the divergence of the velocity. It expresses the fact that $\nabla \cdot \mathbf{v}$ is the time rate of change of the volume of a moving fluid element per unit volume.

Appendix B (After: Bonet and Lok (1999))

B.1 Corrected SPH integration

The basic SPH approximations as given by Equation (3.44) or (3.47) do not accurately reproduce or approximate the functions $f(\mathbf{x})$ and $\nabla f(\mathbf{x})$. Therefore, in the past, corrected SPH equations were developed to address these issues (Bonet and Lok, 1999; Bonet and Kulasegaram, 2000). The main aim of the correction techniques is to satisfy the conservation of angular momentum which, unlike the linear momentum, is not automatically satisfied.

B.1.1 Preservation of momentum

In the absence of external forces, the motion of a number of particles must be such that the total linear and angular momentum are preserved. The motion of each particle is integrated from the instantaneous acceleration vector $\boldsymbol{a}$, which is govern by Newton's second law

$$m_a \boldsymbol{a}_a = \boldsymbol{F}_a - \boldsymbol{T}_a \tag{B.1}$$

where $\boldsymbol{F}_a$ represents the external forces acting on a particle 'a', and $\boldsymbol{T}_a$ denotes the internal forces due to the state of stress inside the material. The most common expression used in the literature for the internal forces is

$$\boldsymbol{T}_a = \sum_{b=1}^{N} V_a V_b \left(p_b \pm p_a\right) \nabla W_a(\mathbf{x}_b) \tag{B.2}$$

where the isotropic stress tensor $\sigma = p\mathbf{I}$, with p as the mean stress and $\mathbf{I}$ the identity tensor.

B.1.1.1 Linear momentum

The total linear momentum of a system of particles is given by

$$G = \sum_{a=1}^{N} m_a v_a \tag{B.3}$$

Combining the time derivative of this equation with Newton's second law as given by (B.1) in the absence of external forces gives the rate of change of the total linear momentum as

$$\dot{G} = \sum_{a=1}^{N} m_a \boldsymbol{a}_a = -\sum_{a=1}^{N} \boldsymbol{T}_a \tag{B.4}$$

Hence the condition for preservation of linear momentum is

$$\sum_{a=1}^{N} \boldsymbol{T}_a = 0 \tag{B.5}$$

In general the internal forces on particle *a* are equal to

$$\boldsymbol{T}_a = \sum_{b=1}^{N} \boldsymbol{T}_{ab} \tag{B.6}$$

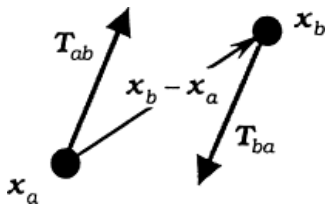

Figure B.1: Interaction forces between two particles

Based on Equation (B.2) and given that $\nabla W_a(\mathbf{x}_b) = -\nabla W_b(\mathbf{x}_a)$, it is clear that $\boldsymbol{T}_{ab} = -\boldsymbol{T}_{ba}$ and consequently the total sum of the all interaction pairs will vanish and Equation (B.4) will be satisfied.

B.1.1.2 Angular momentum

Similarly, the total angular momentum of the system with respect to the origin is given by

$$H = \sum_{a=1}^{N} \mathbf{x}_a \times m_a v_a \tag{B.7}$$

And the time differentiation in the absence of the external forces gives

$$\dot{H} = \sum_{a=1}^{N} \mathbf{x}_a \times m_a \boldsymbol{a}_a = -\sum_{a=1}^{N} \mathbf{x}_a \times \boldsymbol{T}_a \tag{B.8}$$

Consequently, the angular momentum will be preserved provided that the total moment of the internal forces about the origin vanishes, that is

$$\sum_{a=1}^{N} \mathbf{x}_a \times \boldsymbol{T}_a = 0 \tag{B.9}$$

The total moment of the two interacting forces as seen in Figure (B.1) about the origin can be found as

$$\mathbf{x}_a \times \boldsymbol{T}_{ab} + \mathbf{x}_b \times \boldsymbol{T}_{ba} = -(\mathbf{x}_b - \mathbf{x}_a) \times \boldsymbol{T}_{ab} \tag{B.10}$$

where again $\boldsymbol{T}_{ab}$=-$\boldsymbol{T}_{ba}$ has been used. This expression will vanish whenever the interaction force is collinear with the vector ($\mathbf{x}_b$ - $\mathbf{x}_a$) that joins the two particles, which is not always satisfied. Therefore, the preservation of angular momentum cannot be proved by the above simple procedure and a more general derivation is required.

Alternatively, it is simpler to show that the invariance of the potential energy with respect to rigid body rotations leads to the preservation of angular momentum. In order to examine that, consider a rigid body rotation about the origin described by a set of velocities given in terms of an angular velocity vector $\boldsymbol{w}$ with components $[w_x, w_y, w_z]^T$; the velocity vector at any given point is

$$\mathbf{v}(\mathbf{x}) = \boldsymbol{w} \times \mathbf{x} \tag{B.11}$$

And the gradient of this velocity is found by simple derivation to give

$$\nabla \mathbf{v} = \boldsymbol{W} \tag{B.12}$$

$$\boldsymbol{W} = \begin{bmatrix} 0 & -w_z & w_y \\ w_z & 0 & -w_x \\ -w_y & w_x & 0 \end{bmatrix} \tag{B.13}$$

Note that the rate of deformation tensor $\dot{\boldsymbol{\varepsilon}}$ given by Equation (B.14) vanishes given the skew symmetric nature of $\boldsymbol{W}$

$$\dot{\boldsymbol{\varepsilon}} = \frac{1}{2}\left(\nabla \mathbf{v} + \nabla \mathbf{v}^T\right) \tag{B.14}$$

In the absence of approximations introduced by discretization, the total potential energy would be independent of rigid body translations. However, if the SPH approximation is used, the gradient of the velocity is evaluated as

$$\nabla \mathbf{v}_a = \sum_{b=1}^{N} V_b \left(\boldsymbol{W}\mathbf{x}_b - \boldsymbol{W}\mathbf{x}_a\right) \otimes \nabla W_b(\mathbf{x}_a) \tag{B.15}$$

The correct skew symmetric tensor is only obtained if the following matrix condition is satisfied by the gradient of kernel function

$$\sum_{b=1}^{N} V_b(\mathbf{x}_b - \mathbf{x}_a) \otimes \nabla W_b(\mathbf{x}_a) = \mathbf{I} \tag{B.16}$$

where $\mathbf{x}_a$ and $\mathbf{x}_b$ are the position vectors of particles *a* and *b*, respectively.

Unfortunately, the standard SPH algorithm does not generally meet this condition and therefore, the angular momentum will not be preserved.

In order to overcome this shortcoming a number of correction techniques can be used. Either the gradient of the kernel is addressed directly (Bonet and Lok, 1999) or the kernel function itself is modified (Li and Liu, 1996). Another possible way is to mix the kernel and gradient corrections (Bonet and Kulasegaram, 2000; Bonet and Lok, 1999). In following these methods are discussed in more detail.

B.2 Gradient correction

The kernel gradient is modified by introducing a correction matrix **L** such that

$$\tilde{\nabla} W_b(\mathbf{x}) = \mathbf{L} \nabla W_b(\mathbf{x}) \tag{B.17}$$

In (B.16), if general SPH equation (for any particle i.e. without subscript *a*) is used and the term $\nabla W_b(\mathbf{x})$ is replaced by its corrected one (B.17), we have

$$\sum_{b=1}^{N} \frac{m_b}{\rho_b} (\mathbf{x}_b - \mathbf{x}) \otimes \mathbf{L} \nabla W_b(\mathbf{x}) = \mathbf{I} \tag{B.18}$$

Therefore, **L** is given by

$$\mathbf{L} = \left(\sum_{b=1}^{N} \frac{m_b}{\rho_b} \nabla W_b(\mathbf{x}) \otimes (\mathbf{x}_b - \mathbf{x}) \right)^{-1} \tag{B.19}$$

B.1.2 Kernel correction

The kernel can be modified to ensure that polynomial functions up to a given degree are exactly interpolated. The linear kernel correction is given by

$$\tilde{W}_b(\mathbf{x}) = W_b(\mathbf{x}) \alpha(\mathbf{x}) \{1 + \boldsymbol{\beta}(\mathbf{x})(\mathbf{x} - \mathbf{x}_b)\} \tag{B.20}$$

For any linear field, such as velocity, the correction formulation is

$$\mathbf{v}_0 + \mathbf{v}_1\mathbf{x} = \sum_{b=1}^{N} \frac{m_b}{\rho_b}\left(\mathbf{v}_0 + \mathbf{v}_1\mathbf{x}_b\right)\tilde{W}_b(\mathbf{x}) \tag{B.21}$$

The following completeness conditions must be satisfied

$$\sum_{b=1}^{N} \frac{m_b}{\rho_b}\tilde{W}_b(\mathbf{x}) = 1 \tag{B.22}$$

$$\sum_{b=1}^{N} \frac{m_b}{\rho_b}\left(\mathbf{x} - \mathbf{x}_b\right)\tilde{W}_b(\mathbf{x}) = 0 \tag{B.23}$$

The vector parameter, $\boldsymbol{\beta}(\mathbf{x})$ is obtained by substituting (B.20) into (B.23)

$$\boldsymbol{\beta}(\mathbf{x}) = \frac{\sum_{b=1}^{N} \frac{m_b}{\rho_b}\left(\mathbf{x} - \mathbf{x}_b\right)W_b(\mathbf{x})}{\sum_{b=1}^{N} \frac{m_b}{\rho_b}\left(\mathbf{x} - \mathbf{x}_b\right)\otimes\left(\mathbf{x} - \mathbf{x}_b\right)W_b(\mathbf{x})} \tag{B.24}$$

Substituting (B.20) into (B.22) gives the scalar parameter, $\alpha(\mathbf{x})$ as

$$\alpha(\mathbf{x}) = \frac{1}{\sum_{b=1}^{N} \frac{m_b}{\rho_b}\left\{1 + \boldsymbol{\beta}(\mathbf{x})\left(\mathbf{x} - \mathbf{x}_b\right)\right\}W_b(\mathbf{x})} \tag{B.25}$$

As can be seen from (B.24) and (B.25) both $\alpha(\mathbf{x})$ and $\boldsymbol{\beta}(\mathbf{x})$ are functions of $\mathbf{x}$ and therefore make this correction expensive in terms of the computational time. A possible way to make the correction less time consuming is by ignoring $\boldsymbol{\beta}(\mathbf{x})$, i.e. the kernel is corrected by using a constant rather than a linear correction. Therefore the interpolation of the field function $\mathbf{v}(\mathbf{x})$ becomes

$$\mathbf{v}(\mathbf{x}) = \sum_{b=1}^{N} \frac{m_b}{\rho_b}\mathbf{v}_b\tilde{W}_b(\mathbf{x}) \tag{B.27}$$

where

$$\tilde{W}_b(\mathbf{x}) = \frac{W_b(\mathbf{x})}{\sum_{b=1}^{N} \frac{m_b}{\rho_b}W_b(\mathbf{x})} \tag{B.28}$$

B.1.3 Combined kernel and gradient correction

Another possible correction technique is by mixing the kernel and gradient corrections described above. The corrected gradient of the corrected kernel is given by

$$\tilde{\nabla}\tilde{W}_b(\mathbf{x}) = \mathbf{L}\nabla\tilde{W}_b(\mathbf{x}) \tag{B.29}$$

$\nabla\tilde{W}_b(\mathbf{x})$ can be obtained by differentiation of (B.28) to give

$$\nabla\tilde{W}_b(\mathbf{x}) = \frac{\nabla W_b(\mathbf{x}) - \varepsilon(\mathbf{x})}{\sum_{b=1}^{N} \frac{m_b}{\rho_b} W_b(\mathbf{x})} \tag{B.30}$$

where

$$\varepsilon(\mathbf{x}) = \frac{\sum_{b=1}^{N} \frac{m_b}{\rho_b} \nabla W_b(\mathbf{x})}{\sum_{b=1}^{N} \frac{m_b}{\rho_b} W_b(\mathbf{x})} \tag{B.31}$$

Similar to (B.19), the correction matrix **L** is given by

$$\mathbf{L} = \left(\sum_{b=1}^{N} \frac{m_b}{\rho_b} \nabla\tilde{W}_b(\mathbf{x}) \otimes \mathbf{x}_b \right)^{-1} \tag{B.32}$$

Note that in (B.32), the term $\mathbf{x}$ is no longer required since only the constant kernel is used instead of a linear one. Using the corrected gradient of the corrected kernel, the SPH Equations (3.34) and (3.35) can be rewritten as

$$f(\mathbf{x}) = \sum_{b=1}^{N} \frac{m_b}{\rho_b} f(\mathbf{x}_b) \tilde{W}_b(\mathbf{x}) \tag{B.33}$$

$$\nabla f(\mathbf{x}) = \sum_{b=1}^{N} \frac{m_b}{\rho_b} f(\mathbf{x}_b) \tilde{\nabla}\tilde{W}_b(\mathbf{x}) \tag{B.34}$$